The University Of Sheffield.

Pulsed Optical Driving of Cavity-Coupled Open Quantum Systems

Samuel John Sheldon

Submitted for the degree of Doctor of Philosophy

Department of Physics and Astronomy
University of Sheffield
March 2022

Abstract

Cavity coupled solid-state systems have shown great promise for the physical realisation of scalable, on-chip optical quantum technologies. Using ultra-fast optical pulses the states of such systems can be manipulated on extremely short timescales. However, while these quantum systems have demonstrated atomic-like properties, strong interactions with the solid-state environment introduce additional processes not found in purely atomic systems. This thesis considers the control of open quantum systems (namely Quantum Dots (QDs)) through pulsed optical driving, and the impact of coupling to the environment.

While the effects of this environmental coupling on the emission properties ($g^{(1)}(t)$ and $g^{(2)}(t)$) of QDs are well-known under Continuous-Wave (CW) driving, there has been relatively little work studying these properties in the pulsed driving regime. Using the polaron formalism we show the asymmetry in the emission spectra under CW driving is enhanced under pulsed optical driving, in addition to the Mollow satellite peaks that appear in the spectrum in this limit. Furthermore, by extending the variational polaron model to include pulsed optical driving, we present a formalism describing the QD-phonon coupling that remains valid in the limits of long pulse duration and strong driving, where the traditional weak-coupling and polaron formalisms respectively break down.

Additionally, by performing full Cavity Quantum Electrodynamics (cQED) calculations, we consider how the configuration of optical cavity structures may be optimised to improve the fidelity of the initialisation and readout of single charge-carrier spins confined to semiconductor QD in a single Voigt geometry magnetic field. We show an optical cavity with a single, linearly polarised cavity mode is able to support both high-fidelity spin initialisation and readout, and always out-performs bi-modal cavities in realistic driving regimes. Moreover, we experimentally characterise a potential cavity candidate, demonstrating a flexible design with the ability to form single- or bi-modal cavities with directional cavity emission.

Acknowledgements

There are many people I would like to thank for their assistance, guidance, and friendship that has gotten me to this point despite the unusual challenges that we have all encountered over the last few years. I will start by thanking all of my academic colleagues in the LDSD group and the wider physics department for making my time as an undergraduate and PGR student at Sheffield so enjoyable. I would particularly like to thank my supervisor Prof. Mark Fox, as well as Dr. Alistair Brash and Dr. Catherine Phillips whom I have had the pleasure of working closely with over the past few years. Our regular chats and daily coffee breaks have been regular highlights throughout my time as a PGR student. I would also like to give my thanks to Dr. René Dost for fabricating the optical nano-structures studied in the later chapters of this thesis, and Dr. Ed Clarke and the rest of the team in EEE and the National Epitaxy Facility for growing the QD samples on which my optical structures were fabricated. Additionally I would like to give my thanks to the technical staff that support all of our research efforts. My experiments would not have been possible without the liquid helium provided by Chris Vickers, Phil Taylor, and Thomas Ball. The workshop staff have been excellent at providing high-quality, unique, and intricate components required to perform various measurements despite my sometimes rather dubious CAD drawings. For all of their help with my masters year and FDTD simulations I would also like to thank Dr. Andrew Foster and Dr. Dominic Hallett.

I must also give special thanks to Dr. Jake Iles-Smith for stepping in as my unofficial second supervisor, and selflessly giving his help and guidance with the open quantum systems theory I have presented in this thesis. I am immeasurably grateful for the vast number of questions (both insightful and not so insightful) that you have answered over a countless number of emails and video calls that have helped get a significant portion of my work to the state it is presented here. Given the number of considerable challenges that have presented themselves throughout the course of my PhD, including (but

not limited to) a global pandemic, I can honestly say my thesis and time as a PGR student would have been vastly different and more stressful without all of your help. At the start of our collaboration you promised to drag me from experimental physics to the 'dark side' that is theoretical physics, and I think you have been successful in your mission.

I would like to thank my examiners, Prof. Pieter Kok and Dr. Egor Muljarov, for a thoroughly enjoyable and intellectually stimulating viva.

Outside of my colleagues I would like to thank my parents, and the rest of my family for all of their continued support and encouragement. Last but by no means least I would like to thank my fiancée Tamara who has always been a bright ray of sunshine on even the darkest of days.

This page is intentionally left otherwise blank.

List of Figures

This page is intentionally left otherwise blank.

Contents

Chapter 1

Introduction

1.1 Quantum Information Processing

The field of Quantum Information Processing (QIP) encompasses three main areas, namely Quantum Cryptography, Quantum Computing, and Quantum Teleportation. Here we shall give a brief overview of the former two as part of the motivation for the work presented in the later chapters of the thesis.

1.1.1 Quantum Computing

We are currently living through an exciting time in the development of quantum technologies. In the realm of quantum computing, a number of publications have claimed to have reached a so-called quantum computational advantage[1], and there have also been claims of reaching quantum primacy[2], using few Quantum Bit (qubit) quantum computers [1–3].

The principles of quantum computing were first proposed by Richard Feynman as a potential method for simulating complex quantum mechanical systems in an efficient manner [4], with the universal quantum computer first being proposed by David Deutsch in 1985 [5]. Quantum computers are based on the properties of so-called qubits. Qubits, the quantum analogue of the classical bit, are quantum systems consisting of two quantised eigenstates that may be used to encode information. Using the principles of quantum superposition, and quantum entanglement allows a quantum computer to perform a number of classes of problems exponentially faster than a classical computer.

[1] Quantum computational advantage is the point at which quantum computers surpass their classical counterparts in performing a given task.

[2] Quantum primacy is the point at which quantum computers perform tasks that would be infeasible for a classical computer to perform.

This makes quantum computing particularly attractive in sectors such as finance [6], research and medicine [4, 7–9], and cryptography [10].

To understand how quantum computers are able to perform given tasks faster than their classical counterparts, let us consider the example of two classical bits (that may take value 0 or 1) versus two quantum bits (with basis states $\{|0\rangle, |1\rangle\}$). Although the two classical bits can exist in four different combinations (00, 01, 10, 11), a full description of the information held by these classical bits only requires knowledge of two values, the value of the first bit and the value of the second bit. However, a single qubit can exist in a superposition of both eigenstates simultaneously. Hence, according to the superposition principle, an arbitrary state of two entangled qubits is given by $|\psi\rangle = \alpha|00\rangle + \beta|01\rangle + \delta|10\rangle + \gamma|11\rangle$. From this we see that a complete description of two entangled qubits requires four values, α, β, δ, and γ, known as amplitudes [11]. This scales exponentially with the number of qubits. To contain the same information as N qubits would require 2^N classical bits[3]. Therefore the performance advantage of a quantum computer is not derived from the speed of each individual step in a given calculation, but from the requirement for an exponentially reduced number of steps to perform such calculations by using this increase in held information to run parallel processes.

While the amplitudes in the entangled qubit state may contain a large amount of information, when a measurement of the system is performed the state must collapse to one of the basis states (e.g. $|01\rangle$), and thus most of this information is lost upon measurement [11]. To take advantage of the improvement in computing performance, numerous quantum algorithms have been developed that use the parallelism provided by the superposition state, while maximising the probability of returning the basis state representing the desired outcome. For example, Shor's algorithm for factorising large prime numbers, and Grover's algorithm for searching through unsorted databases, are two quantum algorithms that have already been developed [12–14].

The implementation of a quantum computer may be achieved with only two types of gate; a single-qubit gate, and a two-qubit gate e.g. CNOT gate [15–17], or controlled phase gate [18]. It is possible to realise a single-qubit phase shift gate using only classical linear optics [19], while two-qubit gates require non-linear behaviour at the single-phonon level [18]. Charged Quantum Dots (QDs) (discussed further in Chapter 3) are one potential system for realising

[3]In a physical quantum computer this ratio is not quite accurate as some qubits are required solely for error correction, but it is not far off.

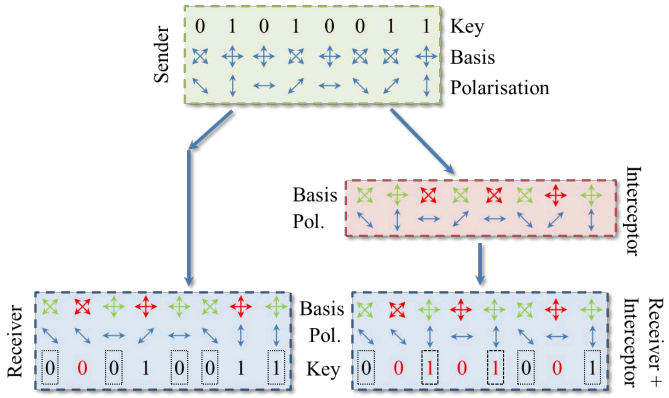

Figure 1.1: A diagram of the BB84 protocol, including the effects of potential interception of the exchanged key. The sender encodes their key into the polarisation of single photons using a random selection of polarisation bases. The receiver then measures polarisation of the received photons using another random selection of orthogonal polarisation bases. The values where the two bases were aligned are kept, while wherever orthogonal bases were employed by the sender and receiver the values are discarded. Here, in the absence of interception, there are no errors in the exchanged values which can be confirmed by publicly exchanging a small subset of the key's digits. However, when the exchanged key is intercepted, the error rate in the remaining values increases which can be used to detect the presence of the eavesdropper.

such single- and two-qubit gates [20–22].

1.1.2 Quantum Communication: Quantum Key Distribution

Quantum systems can also be used in the encryption and secure transmission of confidential information, a task which has become essential in our society. The field of quantum cryptography covers a range of different cryptographic tasks, but in this short introduction we shall focus on Quantum Key Distribution (QKD). The most secure method of communication known to date is the One-Time Pad (OTP), providing, theoretically at least, a completely secure method of transmitting data. This method relies on the ability to securely exchange a randomly generated 'secret key' between the sender and receiver that has the same length as the message, and as the name suggests is used only once. Using classical methods, the main hurdle in ensuring this technique is indeed 100% secure is the exchange of the secret key. The rapid advancement of classical technology is gradually eroding the security of existing protocols for secure key exchange, and with the dawn of quantum computing even the most secure existing classical methods of communication could be rendered entirely

ineffective. However, by utilising the fundamental laws of quantum mechanics QKD provides a solution to this.

The first QKD protocol was proposed in the early 1980s, and is known as the BB84 protocol [10, 11, 23]. Utilising the polarisation state of single photons, the BB84 protocol provides a method for detecting attempted interception of the secret key when transmitted via public communication channels. The BB84 protocol is outlined in Figure 1.1. Firstly information is encoded in the polarisation of the transmitted photons using a random selection of non-commuting bases (e.g. rectilinear and diagonal). The receiver then measures the photons in another random sequence of the bases, and the lists of bases used are shared via a public communication channel. A process called key-sifting is then applied whereby the sender and receiver only retain the results of the measurements where the same basis was applied by both parties, crucially without communicating the actual measurement result in these cases. Using a subset of these results any attempted interception of the transmitted key can be detected, as each attempted interception perturbs the quantum state, owing to the no-cloning theorem, introducing detectable errors. When an attempted interception of the key is detected through an increase in the error rate, either a smaller subset of the data may be used as the key or repeated transmission attempts can be made (via different channels if required) until there is certainty that the key has remained secure.

Since the development of the BB84 protocol, numerous other techniques for encrypting data using quantum mechanical properties have been developed. For example variations of BB84 protocol using two states [24] or six states [25] have been developed, and cryptography using entangled states in the Ekert protocol has been demonstrated [26]. These schemes can be realised using optimised QD single-photon sources. In Chapters 4 and 5 we explore the properties of QDs, a candidate single-photon source, when coupled to their solid-state environment, and in Chapter 6 we discuss how one can optically control the states of these quantum systems.

1.2 Quantum Metrology

In addition to information processing, quantum systems have potential applications in metrology, the science of measurement. That is, quantum systems may be employed to perform measurements with a higher statistical precision than is achievable using classical techniques. Such improved precision has

potential benefits in many applications including, but not limited to: gravitational wave detection, measurements on biological systems, spectroscopy, microscopy, navigation, thermometry, and magnetometry [27–29]. For more detailed discussions of quantum metrology than given here see [27, 30, 31].

In general, metrology can be broken down into three stages: probe preparation, interaction between the probe and the system of interest, and readout of the probe state after the interaction [27, 30, 31]. The aim of metrology is to maximise the amount of information determined about a system by optimising both the readout method and choice of probe to maximise the information that can be encoded on, and determined from, the state of the probe. For a given parameter, θ, of interest, when performing a measurement using N non-entangled particles, it can be shown the best achievable precision is the *shot-noise* limit [30]

$$\Delta\theta \approx N^{-\frac{1}{2}}. \tag{1.1}$$

However, with the same number of entangled particles it can be shown that it is theoretically possible to reach [30]

$$\Delta\theta \approx N^{-1}, \tag{1.2}$$

known as *Heisenberg scaling*.

One example of a quantum metrology scheme is the use of N00N states as an input in a Mach-Zender interferometer [27, 30, 32]. The N00N state ($|\psi\rangle = (|N,0\rangle + |0,N\rangle)/\sqrt{2}$) describes the situation in which N single photons enter one input port of the interferometer while the input at the second interferometer port is the vacuum state. Such states are optimised for phase (ϕ) measurements, yielding output states $(e^{-i\phi N/2}|N,0\rangle + e^{i\phi N/2}|0,N\rangle)/\sqrt{2}$ where the phase is functionally multiplied by N [27, 30]. A number of experiments have demonstrated precision beyond the shot-noise limit using N00N states in optical systems [33–36], including the generation of a 2002 state using a QD single-photon source [37]. While N00N states are sensitive to loss mechanisms, they should be able to tolerate a certain level of loss and still return quantum features [38] with small N.

1.3 Overview and Scope of the Thesis

The main focus of this thesis is to study the effect of pulsed optical driving on open quantum systems, i.e. quantum systems that experience some coupling to

their environment. This is considered in two contexts: the effects of coupling to a phonon-bath on the properties of a QD driven in the ultra-fast pulsed excitation regime, and the application of optical pulses in the preparation, control, and readout of single cavity-coupled charge-carrier spin states.

The thesis is structured as follows. Chapter 2 introduces the background theory required in later chapters. This includes an introduction to the density matrix formalism, and a derivation of the second-order Born-Markov and Lindblad master equations. In Chapter 3 the properties of QDs are introduced, including the effects of situating QDs in external fields. The Lindblad master equation approach is then used to study the optical properties of a classically driven Two-Level System (2LS), approximating a QD, under Continuous-Wave (CW) and pulsed excitation. Chapter 3 also contains an introduction to Cavity Quantum Electrodynamics (cQED) that is used in later chapters.

In Chapter 4 the effects of coupling to a phonon bath on the emission properties of a QD when driven by an optical pulse are studied. Given the solid-state nature of QDs, they naturally couple strongly to the quantised lattice vibrations (phonons) of the host material which impacts both the QD system dynamics and emission properties. Using a time-dependent Markovian polaron master equation, we calculate the time-dependent and time-integrated emission spectra of a QD coupled to a phonon bath. Using this master equation approach, we demonstrate an asymmetry in these emission spectra that is not accounted for by a simple pure dephasing model. Additionally, in Chapter 5 we explore the limits of the (non-Markovian) polaron and weak-coupling models under pulsed excitation. For given driving parameters, under pulsed excitation it is possible for the states of the system to evolve on time-scales approximately equal to, or faster than, the evolution of the bath. In this limit the polaron model breaks down. Conversely, the weak-coupling model is inadequate for capturing phonon effects when the coupling to the phonon bath is strong. To describe the system dynamics accurately in these limits, we derive a non-Markovian time-dependent variational polaron model that remains valid over a wide range of driving parameters.

The focus of Chapter 6 is the optical preparation, control, and readout of single charge-carrier spins confined to QDs coupled to an optical cavity in a single applied magnetic field geometry. The ability to initialise, control, and readout the state of a single charge-carrier spin confined to a QD using all-optical methods is an attractive proposition as this would be compatible with the development of scalable on-chip optical circuits for QIP and Quantum

Communication (QC) applications. Such circuits could then use optical pulses to control the stationary (spin) qubits, while simultaneously using single photons as flying qubits propagating through the same on-chip optical components. In the chapter we consider the impact the cavity configuration (single-mode or bi-modal) has on the spin initialisation and readout fidelities, along with the ability to coherently control the spin state after the initialisation stage.

Chapter 7 introduces the theoretical and experimental methods used to design, and characterise the optical cavity structures studied in Chapter 8. This begins with an overview of Maxwell's equations, and their application in the Finite-Difference Time-Domain (FDTD) simulations of electromagnetic waves propagating through a medium. The chapter then concludes with an overview of the principles behind diodes, and the fabrication of photonic structures as well as diode structures. Chapter 8 then presents the measurements characterising optical cavity structures. We show the potential suitability of these cavity structures for testing the theory set out in Chapter 6, and also demonstrate additional properties of the cavities that could make them suitable for applications in on-chip quantum technologies.

Chapter 9 presents a summary of the work presented in the thesis, along with potential further work that could be performed to build upon the results presented.

This page is intentionally left otherwise blank.

Chapter 2

Open Quantum Systems

In this chapter we shall explore the foundational theoretical concepts used in later chapters. We will begin with an introduction to the density matrix formalism, before moving on to discuss the time evolution of composite systems. We shall then use these concepts to derive a method for studying the dynamics of *open quantum systems* coupled to an environment with a large number of degrees of freedom. In Chapter 3 we shall apply these concepts to the simplest example of a quantum system, and cavity coupled quantum systems.

2.1 The Density Matrix Formalism

2.1.1 Introduction to the Density Matrix Formalism

The mathematical framework of quantum mechanics is founded on a number of postulates that allow one to map physical systems and their properties to mathematical structures. One of these postulates states that any physical system may be described by a state in a given Hilbert space, $\mathscr{H}$, where the state of the system is a ray[1], $|\psi\rangle$, with norm $\||\psi\rangle\| = \sqrt{\langle\psi|\psi\rangle} = 1$ in $\mathscr{H}$. A further postulate states that the time evolution (dynamics) of quantum systems is governed by unitary transformations such that

$$|\psi(t)\rangle = U(t, t_0)\,|\psi(t_0)\rangle\,, \tag{2.1}$$

where $U(t, t_0)$ is a unitary operator ($UU^\dagger = U^\dagger U = \mathbf{I}$) that evolves the state of the quantum system, $|\psi\rangle$, from time t_0 to time t. For a time-dependent

[1]The difference between a vector and a ray is that while the former has a direction and magnitude, the latter extends indefinitely in a given direction from a given starting point.

Hamiltonian, $H(t)$, this unitary operator is given by

$$U(t,t_0) = \boldsymbol{\mathcal{T}} \exp\left\{-i \int_{t_0}^{t} dt' H(t')\right\}, \tag{2.2}$$

where $\boldsymbol{\mathcal{T}}$ is the time-ordering operator that orders the products of operators with a time-dependence such that the earliest times appear at the right. This unitary operator simplifies to $U(t,t_0) = \exp\{-iH(t-t_0)\}$ if the Hamiltonian is time-independent. Taking the derivative of Eq. 2.1 with respect to time produces the Schrödinger equation

$$\frac{\partial}{\partial t} |\psi(t)\rangle = -iH(t) |\psi(t)\rangle , \tag{2.3}$$

where we have set $\hbar = 1$ as will be standard practice throughout the thesis. This description of quantum mechanics is known as the state-vector formalism. The state vector formalism provides a complete description of the dynamics of *closed quantum systems*, i.e. quantum systems isolated from their environment. However, physical quantum systems will often have some form of coupling to the environment around them. Such systems are known as *open quantum systems*, and cannot be adequately described by the state vector formalism [39]. The system-environment interaction introduces classical uncertainties to the reduced state of the system (tracing out the environment) which the state vector formalism is not suited to accurately accounting for. Instead, to fully describe open quantum systems we must move to the density matrix formalism.

The density matrix describing the state of a quantum system with a set of N basis states $\{|\psi_i\rangle\}$ is defined as

$$\rho = \sum_{i=1}^{N} p_i |\psi_i\rangle\langle\psi_i| , \tag{2.4}$$

where p_i is the classical probability of the system being in state $|\psi_i\rangle$. The state described by Eq. 2.4 is known as a *mixed state*. However, in the case where $p_{i=j} = 1$ and $p_{i\neq j} = 0$ Eq. 2.4 reduces to a *pure state*, $\rho = |\psi_j\rangle\langle\psi_j|$. From Eq. 2.4 we see a valid density matrix has a number of properties [40].

1. The density matrix is Hermitian, i.e. $\rho^\dagger = \rho$.
2. The density matrix is normalised, i.e. $\mathrm{Tr}\{\rho\} = \sum_i^N p_i = 1$.
3. The density matrix is positive semi-definite, i.e. $\rho \geq 0$, as its eigenvalues are probabilities and are thus either positive or zero.

There are two other important properties of the density matrix that we shall use in later chapters [40].

1. The expectation value of an operator $\mathbf{A}$ can be calculated using $\langle \mathbf{A} \rangle = \mathrm{Tr}\{\rho \mathbf{A}\} = \sum_i p_i \langle \psi_i | \mathbf{A} | \psi_i \rangle$.

2. The purity of a state described by a density matrix is given by $P(\rho) = \mathrm{Tr}\{\rho^2\}$ where $P(\rho) = 1$ for a pure state and $P(\rho) < 1$ for a mixed state.

In general the diagonal elements of the density matrix ($\rho_{i,i}$) are referred to as populations as they give the probability of the system existing in that given state. The off-diagonal elements ($\rho_{i,j\neq i}$) on the other hand are known as coherences as they quantify the relative phases between different components of the superposition.

2.1.2 Time Evolution of the Density Matrix

The Schrödinger Picture

Just as in the state vector formalism, the temporal evolution of the density matrix describing a quantum state is determined by unitary transformations. The time-evolution of a density matrix describing a system starting in a state $|\psi(t_0)\rangle$ is given by

$$\rho(t) = U(t, t_0) \, |\psi(t_0)\rangle\langle\psi(t_0)| \, U^\dagger(t, t_0). \tag{2.5}$$

Differentiating Eq. 2.5 with respect to time we obtain the density matrix formalism equivalent of the Schrödinger equation, known as the *Liouville-von Neumann equation* or simply the *von Neumann equation* [39, 40]

$$\frac{\partial}{\partial t}\rho(t) = -i\big[H(t), \rho(t)\big]. \tag{2.6}$$

The more general form is given by

$$\frac{\partial}{\partial t}\rho(t) = \mathcal{L}\rho(t), \tag{2.7}$$

where $\mathcal{L}$ is a Liouvillian super-operator, an epithet indicating that $\mathcal{L}$ is an operator that acts on another operator [39].

This formulation of quantum mechanics, where the time-dependence of the system is included in the density matrix while leaving the operators representing physical observables time-independent, is known as the *Schrödinger pic-*

ture. However, this is not the only manner in which time-dependence may be accounted for in quantum mechanics. There are two other formalisms known as the *Heisenberg*, and *Interaction pictures* that also do this. In the *Heisenberg picture* the time-dependence is moved from the density matrix to the operators (O) representing observables such that $\langle O(t)\rangle = \mathrm{Tr}\{O(t)\rho(t_0)\}$ where $O(t) = U^\dagger(t,t_0)OU(t,t_0)$ [39–41]. This picture is not overly relevant to the work done in this thesis, and thus will not be discussed in further detail here. For a good discussion of the Heisenberg picture see [39–41].

The Interaction Picture

The interaction picture, also referred to as the Dirac picture, lies in-between the Schrödinger and Heisenberg pictures, with time-dependence in both the density matrix and operators [39]. In many cases using either the Schrödinger picture or Heisenberg picture makes developing perturbative methods challenging. Moving to the interaction picture provides a solution to this. To perform this transformation from the Schrödinger picture to the interaction picture one must first spilt the Hamiltonian into two components

$$H(t) = H_0(t) + H_I(t), \tag{2.8}$$

where $H_0(t)$ is trivial to solve while $H_I(t)$ is non-trivial. Splitting the Hamiltonian in such a way allows the contribution from H_0 to be moved to the time-evolution of the operators by performing the appropriate unitary transformation

$$\langle \mathbf{O(t)}\rangle = \mathrm{Tr}\{\mathbf{O}\rho(t)\} = \mathrm{Tr}\big\{\mathbf{O}U(t,t_0)\rho(t_0)U^\dagger(t,t_0)\big\}, \tag{2.9}$$

where $\langle \mathbf{O}\rangle$ is the expectation value of some observable $\mathbf{O}$, which is assumed to have no intrinsic time dependence. Using this transformation guarantees the invariance of the expectation values between the different pictures as required [41]. This unitary operator, $U(t,t_0)$, can then be decomposed into two parts

$$U(t,t_0) = U_0(t,t_0)U_I(t,t_0), \tag{2.10}$$

where $U_0(t,t_0) = \boldsymbol{\mathcal{T}}\exp\Big\{-i\int_{t_0}^{t} dt' H_0(t')\Big\}$. Making the substitution back into Eq. 2.9 yields

$$\langle \mathbf{O(t)}\rangle = \mathrm{Tr}\{\mathbf{O}\rho(t)\} = \mathrm{Tr}\Big\{\mathbf{O}U_0(t,t_0)U_I(t,t_0)\rho(t_0)U_I^\dagger(t,t_0)U_0^\dagger(t,t_0)\Big\}. \tag{2.11}$$

We can now make use of the cyclic nature of the trace ($\mathrm{Tr}(ABC) = \mathrm{Tr}(CAB) = \mathrm{Tr}(BCA)$) to rewrite Eq. 2.11 as

$$\langle \mathbf{O(t)} \rangle = \mathrm{Tr}\{\mathbf{O}_I(t)\rho_I(t)\}, \tag{2.12}$$

where the operator in the interaction picture, $\mathbf{O}_I(t)$, is defined as

$$\begin{aligned} \mathbf{O}_I(t) =& U_0^\dagger(t,t_0)\mathbf{O}U_0(t,t_0) \\ =& \exp\{iH_0(t-t_0)\}\mathbf{O}\exp\{-iH_0(t-t_0)\}, \end{aligned} \tag{2.13}$$

and

$$\rho_I(t) = U_I(t,t_0)\rho(t_0)U_I^\dagger(t,t_0) = U_I^\dagger(t,t_0)\rho(t)U_I(t,t_0). \tag{2.14}$$

is the density matrix in the interaction picture. Accordingly we see the time evolution of operators in the interaction picture is indeed determined by H_0, while the density matrix evolves according to H_I. Differentiating equation 2.14 with respect to time, and making use of Eq. 2.6, reveals that the time evolution of the density matrix in the interaction picture is still determined by a von Neumann equation

$$\frac{\partial}{\partial t}\rho_I(t) = -i\big[H_I(t), \rho_I(t)\big]. \tag{2.15}$$

The only difference here is $H_I(t) = U_0(t,t_0)H_IU_0(t,t_0)$ appears in the commutator on the right-hand side of the equation, rather than the total Hamiltonian as in Eq. 2.6. From Eq. 2.15 it can also be seen that $U_I(t,t_0)$ takes the same form as the unitary operator in Eq. 2.2.

2.1.3 Composite Systems

In addition to the properties of single quantum systems, we are often interested in the effects resulting from interactions between multiple quantum systems. For this reason, now that we have a description of an individual isolated quantum system, it will be useful to consider how one mathematically describes two distinguishable interacting quantum systems. If the first quantum system is described by Hilbert space $\mathscr{H}_1$, and the second by a Hilbert space $\mathscr{H}_2$, then the total Hilbert space describing the full composite system, $\mathscr{H}$, is given by the tensor product of the two sub-spaces

$$\mathscr{H} = \mathscr{H}_1 \otimes \mathscr{H}_2. \tag{2.16}$$

The states of a composite system generally fall into two categories: separable, and inseparable. Assuming the individual quantum systems have basis states $\{|\psi\rangle_i\}$ and $\{|\phi\rangle_j\}$ in their respective Hilbert sub-spaces, and assuming the two systems do not interact, a state is defined as separable when it can be written as the sum of the tensor product of the pure states of the individual sub-systems, i.e.

$$|\Psi\rangle = \sum_{ij} a_{ij} |\psi\rangle_i \otimes |\phi\rangle_j \tag{2.17}$$

which can naturally be extended to the density matrix formalism as

$$\rho = |\Psi\rangle\langle\Psi| = \sum_{ij} c_{ij} |\psi\rangle\langle\psi|_i \otimes |\phi\rangle\langle\phi|_j = \sum_{ij} c_{ij} \rho_i \otimes \rho_j. \tag{2.18}$$

The classical correlations found in mixed states (described by Eq. 2.4) fall into the separable category. We can retrieve the state of a single sub-system (known as the reduced state of the system) by tracing over all others. For example, if we wish to know the reduced state of the first quantum system in Eq. 2.18 ($|\psi\rangle$) we can take the partial trace over the second sub-system ($|\phi\rangle$). If the sub-systems are in a separable state this will result in a pure state

$$\begin{aligned} \rho_1 &= \mathrm{Tr}_2\big(\rho_1 \otimes \rho_2\big) = \mathrm{Tr}_2\big(|\psi\rangle\langle\psi| \otimes |\phi\rangle\langle\phi|\big) \\ &= |\psi\rangle\langle\psi| \,\mathrm{Tr}\big(|\phi\rangle\langle\phi|\big) = |\psi\rangle\langle\psi| \,. \end{aligned} \tag{2.19}$$

However, if there is an interaction between the two sub-systems then the total state is entangled and thus we can no longer write the total state as the tensor product of two pure states. Instead the state may be decomposed as

$$|\Psi\rangle = \sum_{ij} a_{ij} |\psi, \phi\rangle_{ij} \;\text{ or }\; \rho = \sum_{ijkl} c_{ijkl} |\psi, \phi\rangle\langle\psi, \phi|_{ijkl} \,. \tag{2.20}$$

In this case taking the partial trace over the degrees of freedom of one of the sub-systems will not lead to a pure state, but a mixed state instead. We can see this by considering two qubits that are initially prepared in a pure entangled state

$$|\Psi\rangle = \alpha |0,1\rangle + \beta |1,0\rangle \,, \tag{2.21}$$

where $|\alpha|^2 + |\beta|^2 = 1$. From the superposition principle we know $|\Psi\rangle$ is a valid quantum state since both $|0,1\rangle$ and $|1,0\rangle$ are also valid quantum states. The

density matrix describing this state is then given by

$$\rho = \alpha^2 \left|0,1\right\rangle\!\left\langle 0,1\right| + \beta^2 \left|1,0\right\rangle\!\left\langle 1,0\right| + \alpha\beta\big(\left|0,1\right\rangle\!\left\langle 1,0\right| + \left|1,0\right\rangle\!\left\langle 0,1\right|\big). \tag{2.22}$$

We can again take the partial trace over the second qubit to give the reduced state of the first qubit

$$\rho_1 = \mathrm{Tr}_2(\rho) = \alpha^2 \left|0\right\rangle\!\left\langle 0\right| + \beta^2 \left|1\right\rangle\!\left\langle 1\right|, \tag{2.23}$$

as $\mathrm{Tr}\{\left|1\right\rangle\!\left\langle 0\right|\} = \mathrm{Tr}\{\left|0\right\rangle\!\left\langle 1\right|\} = 0$. It turns out that even though the composite system was in a pure state, the reduced states of the individual qubits are mixed. If $\alpha = \beta = \frac{1}{\sqrt{2}}$ we actually find the states of the sub-systems (qubits) are maximally mixed with a purity $P(\rho_1) = \frac{1}{2}$. In taking the partial trace we have lost some information from the composite state that is not found in the states of the individual sub-systems. As discussed in Chapter 1, it is this property of the entangled system to hold more information than the individual sub-systems that makes quantum entanglement useful in quantum information processing applications.

2.2 Second-Order Master Equations

Using the density matrix formalism it is possible to derive a microscopic description of the interaction between two distinct quantum systems. However, an open quantum system will typically be coupled to an environment with a large number of degrees of freedom. This makes a complete description of an open quantum system too complex to perform exactly using the von Neumann equation. We must therefore find a simpler method of calculating the dynamics of the reduced state of the quantum system that we are interested in that does not explicitly track the degrees of freedom of the environment. To do this we will derive a second-order master equation that treats the interaction between the quantum system, S, and the environment, E, as a perturbation. This will allow us to evolve the state of the composite system, which we assume to be a closed quantum system, and then take the partial trace over the environment degrees of freedom to find the temporal evolution of the reduced density matrix of the open system of interest. In addition to this, utilising a master equation approach will then allow us to calculate experimentally important quantities such as correlation functions and emission spectra as will be discussed later.

There are a number of different methods that have been used to derive such

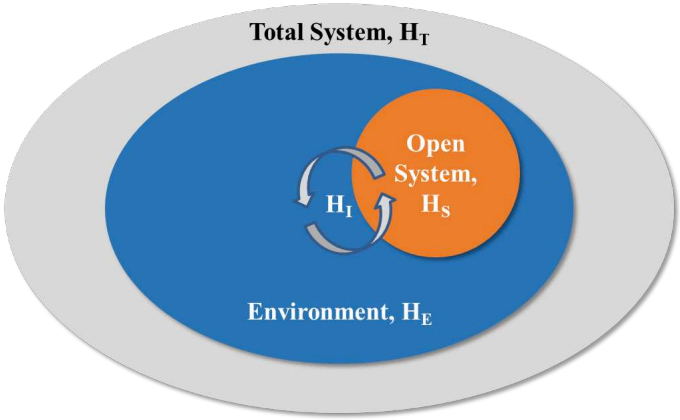

Figure 2.1: A schematic representation of an open quantum system described by the Hamiltonian H_S coupled to its environment, H_E. The interaction between the open system and the environment is governed by the Hamiltonian H_I. The composite system formed by the open system and environment is itself a closed system referred to as the total system.

an approximate master equation, including mathematically rigorous derivations based on the projection operator method, first introduced by Nakajima and Zwanzwig [42, 43]. However, in this thesis we shall use a less mathematically rigorous derivation that highlights the physical nature of the various assumptions that must be made on the way to deriving a master equation second-order in the interaction Hamiltonian [44].

A schematic of the system we wish to derive a master equation for is shown in Figure 2.1. We shall again begin with a general Hamiltonian of the form

$$H = H_0 + H_I. \tag{2.24}$$

While the Hamiltonian given here has no explicit time-dependence, this derivation does hold in the time-dependent case. We shall now go a step further than we did studying the interaction picture by expanding the first term on the right-hand-side of the equation to $H_0 = H_S + H_E$ to give the total Hamiltonian

$$H = H_S + H_E + H_I. \tag{2.25}$$

Here H_S describes the open quantum system degrees of freedom S, H_E generates the environment degrees of freedom E, and H_I characterises the interaction between the two. We can also assume H_I is the only term involving both S and E. Moving to the interaction picture with respect to H_0, H_I becomes

$$\tilde{H}_I(t) = U_0^\dagger(t) H_I U_0(t) = \exp\{i(H_S + H_E)t\} H_I \exp\{-i(H_S + H_E)t\}, \tag{2.26}$$

following the form of Eq. 2.13 with $t_0 = 0$ for simplicity. Here the tilde represents an operator in the interaction picture. As we have assumed the total system is itself a closed system, the density operator describing the composite system will evolve according to the von Neumann equation in the interaction picture

$$\frac{\partial}{\partial t}\tilde{\rho}(t) = -i\big[\tilde{H}_I(t), \tilde{\rho}(t)\big]. \tag{2.27}$$

Integrating Eq. 2.27 produces the formal solution

$$\tilde{\rho}(t) = \tilde{\rho}(0) - i\int_0^t dt' \big[\tilde{H}_I(t'), \tilde{\rho}(t')\big], \tag{2.28}$$

and substituting this solution back into Eq. 2.27 returns

$$\frac{\partial}{\partial t}\tilde{\rho}(t) = -i\big[\tilde{H}_I(t), \tilde{\rho}(0)\big] - \int_0^t dt' \Big[\tilde{H}_I(t), \big[\tilde{H}_I(t'), \tilde{\rho}(t')\big]\Big]. \tag{2.29}$$

2.2.1 The Born-Markov Master Equation

At first glance it would seem that we have not improved our situation much. Eq. 2.29 is still exact, and thus still as challenging to solve as the von Neumann equation we started with. However, we are now in a position to make a number of useful approximations. Before we do this, as we are only interested in the evolution of S, we can take the partial trace over the environment degrees of freedom to find the reduced density operator for S

$$\frac{\partial}{\partial t}\tilde{\rho}_S(t) = -i\,\mathrm{Tr}_E\big[\tilde{H}_I(t), \tilde{\rho}(0)\big] - \int_0^t dt'\,\mathrm{Tr}_E\Big[\tilde{H}_I(t), \big[\tilde{H}_I(t'), \tilde{\rho}(t')\big]\Big]. \tag{2.30}$$

From here we can introduce the first of our assumptions, starting by setting $-i\,\mathrm{Tr}_E\big[\tilde{H}_I(t), \tilde{\rho}(0)\big] = 0$. This condition can be ensured by moving a term $\mathrm{Tr}_E[\tilde{H}_I(t), \tilde{\rho}(0)]$ from the interaction Hamiltonian to the system Hamiltonian [44]. Next we may assume there are no correlations between the sub-systems S and E before a given starting time t_0, which we set to $t_0 = 0$ for simplicity. This allows the initial density matrix of the composite system to be factorised as $\rho(0) = \rho_S(0) \otimes \rho_E(0)$. From here we can make a further approximation, known as the *Born approximation*, and assume the density matrix factorises at all times such that $\tilde{\rho}(t) \approx \tilde{\rho_S}(t) \otimes {\rho_E}$[2]. In other words we assume the environment density matrix is time-independent. This approximation relies on the interaction between the two sub-systems (S and E) being weak, and

[2]We assume the environment density matrix is in a Gibbs state.

E being sufficiently large that the effect of the coupling to S on the state of the environment is negligible. Assuming a weak interaction between E and S also allows us to ignore higher order terms that could be found by repeating the process used to derive Eq. 2.30. Applying all these approximations to Eq. 2.30 yields

$$\frac{\partial}{\partial t}\tilde{\rho_S}(t) = -\int_0^t dt' \, \mathrm{Tr}_E\Big[\tilde{H}_I(t), \big[\tilde{H}_I(t'), \tilde{\rho_S}(t') \otimes \rho_E\big]\Big]. \tag{2.31}$$

This form of the master equation can be shown to be a perturbative expansion in the interaction Hamiltonian. We must now make a further approximation known as the *Markov approximation*. Although we are now closer to the final form of our master equation, the time evolution of the reduced density matrix is still dependent on its history via the $\tilde{\rho}_S(t')$ term. We can make the substitution $\tilde{\rho}_S(t') \to \tilde{\rho}_S(t)$ on the right-hand side of our equation if the memory time of E is exceedingly short relative to the memory time of S. This is consistent with the Born approximation we made earlier which assumed E was large enough to remain unaffected by its interaction with S. The master equation in the Born-Markov approximation then becomes

$$\frac{\partial}{\partial t}\tilde{\rho_S}(t) = -\int_0^t dt' \, \mathrm{Tr}_E\Big[\tilde{H}_I(t), \big[\tilde{H}_I(t'), \tilde{\rho_S}(t) \otimes \rho_E\big]\Big]. \tag{2.32}$$

To make this master equation truly Markovian [3], we need to make one more approximation. In its present form, this master equation still contains a reference to a starting time, $t_0 = 0$, in the lower limit of the integral. Making the substitution $t' \to t - \tau$ we can extend the limit of the integral to infinity, taking the starting time to minus infinity, again using the justification of separation of time scales between the system and environment. Making this substitution yields

$$\frac{\partial}{\partial t}\tilde{\rho_S}(t) = -\int_0^\infty d\tau \, \mathrm{Tr}_E\Big[\tilde{H}_I(t), \big[\tilde{H}_I(t-\tau), \tilde{\rho_S}(t) \otimes \rho_E\big]\Big]. \tag{2.33}$$

This is the full form of the weak-coupling Born-Markov master equation that approximately describes the evolution of an open system in the interaction picture. It can be shown that this master equation is second-order in the interaction Hamiltonian, H_I.

[3] A Markovian process is one where the future state of the system is only dependent on its present state and not it's previous states.

2.2.2 The Lindblad Master Equation and the Secular Approximation

Unfortunately we cannot guarantee the density matrix produced by Eq. 2.33 will always be physical. That is, the density operator given by the Born-Markov master equation can have negative eigenvalues and $\mathrm{Tr}(\rho_S) \neq 1$. We shall now continue from the weak-coupling Born-Markov master equation in Eq. 2.33 to derive the Lindblad master equation. To do this we now decompose the interaction Hamiltonian into system (S_j) and environment (E_j) operators such that

$$\tilde{H}_I(t) = \sum_j S_j(t) \otimes E_j(t), \tag{2.34}$$

and substitute this into the Born-Markov master equation. Expanding the commutators we find

$$\begin{aligned}\frac{\partial}{\partial t}\tilde{\rho_S}(t) = -\sum_{ij}\int_0^\infty d\tau \Big(&\big[\tilde{S}_i(t), \tilde{S}_j(t-\tau)\tilde{\rho}_s(t)\big]\langle \tilde{E}_i(t)\tilde{E}_j(t-\tau)\rangle \\ &- \big[\tilde{S}_i(t), \tilde{\rho}_s(t)\tilde{S}_j(t-\tau)\big]\langle \tilde{E}_j(t-\tau)\tilde{E}_i(t)\rangle\Big),\end{aligned} \tag{2.35}$$

where we have defined the environment two-time correlation functions as

$$\begin{aligned}\langle \tilde{E}_i(t)\tilde{E}_j(t-\tau)\rangle &= \mathrm{Tr}_E\big(E_i(t)E_j(t-\tau)\rho_E\big), \\ \langle \tilde{E}_j(t-\tau)\tilde{E}_i(t)\rangle &= \mathrm{Tr}_E\big(E_j(t-\tau)E_i(t)\rho_E\big),\end{aligned} \tag{2.36}$$

and again made use of the cyclic nature of the trace. If we decompose the system Hamiltonian as $H_S = \sum_i \lambda_i |\lambda_i\rangle\langle\lambda_i|$ where λ_i is an eigenvalue of H_S given by the eigenvalue equation $H_S|\lambda_i\rangle = \lambda_i|\lambda_i\rangle$, then the system operator can also be written in this basis as

$$S_k(t) = \sum_{ij} \langle\lambda_i| S_k(t) |\lambda_j\rangle |\lambda_i\rangle\langle\lambda_j| . \tag{2.37}$$

In the interaction picture this is given by

$$S_k(t) = e^{iH_S t} S_k e^{-iH_S t}, \tag{2.38}$$

in accordance with Eq. 2.13. Making the substitution we find

$$S_k(t) = \sum_{i,j} e^{i(\lambda_i - \lambda_j)t} \langle\lambda_i| S_k |\lambda_j\rangle |\lambda_i\rangle\langle\lambda_j| = \sum_\omega e^{i\omega t} S_k(\omega), \tag{2.39}$$

with

$$S_k = \sum_{\omega} S_k(\omega) = \sum_{\omega} S_k^\dagger(\omega), \tag{2.40}$$

where $\omega = \lambda_i - \lambda_j$ and the operators $S_i(\omega)$ and $S_i^\dagger(\omega)$ obey the commutation relations

$$\big[H_S, S_k(\omega)\big] = -\omega S_k(\omega) \text{ and } \big[H_S, S_k^\dagger(\omega)\big] = \omega S_k^\dagger(\omega). \tag{2.41}$$

Substituting this into Eq. 2.35 yields

$$\begin{aligned}\frac{\partial}{\partial t}\tilde{\rho_S}(t) = &-\sum_{\omega,\omega'}\sum_{ij}\int_0^\infty d\tau\Big(e^{i\omega' t}e^{-i\omega(t-\tau)}\big[\tilde{S}_i(\omega'), \tilde{S}_j(\omega)\tilde{\rho}_s(t)\big]\langle\tilde{E}_i(t)\tilde{E}_j(t-\tau)\rangle \\ &- e^{-i\omega' t}e^{i\omega(t-\tau)}\big[\tilde{S}_i(\omega'), \tilde{\rho}_s(t)\tilde{S}_j(\omega)\big]\langle\tilde{E}_j(t-\tau)\tilde{E}_i(t)\rangle\Big) \\ = &-\sum_{\omega,\omega'}\sum_{ij}\Big(e^{i(\omega-\omega')t}\Gamma_{ij}(\omega)\big[\tilde{S}_i(\omega'), \tilde{S}_j(\omega)\tilde{\rho}_s(t)\big] \\ &- e^{-i(\omega-\omega')t}\Gamma_{ji}^*(\omega)\big[\tilde{S}_i(\omega'), \tilde{\rho}_s(t)\tilde{S}_j(\omega)\big]\Big),\end{aligned} \tag{2.42}$$

with $\Gamma_{ij}(\omega) = \int_0^\infty d\tau e^{i\omega\tau}\langle\tilde{E}_i(t)\tilde{E}_j(t-\tau)\rangle$ when $[H_E, \rho_E] = 0$. Assuming the total system evolves on much shorter time scales than the reduced state of the open quantum system we can use the *secular approximation*. This allows us to only consider the resonant terms ($\omega = \omega'$) in Eq. 2.42 as the non-resonant terms lead to rapid oscillations which average out on the open system timescales. From here we can divide the dynamics of the system into real and imaginary components by defining $\Gamma_{ij}(\omega) = \frac{1}{2}\gamma_{ij}(\omega) + i\pi_{ij}(\omega)$ such that

$$\gamma_{ij} = \Gamma_{ij}(\omega) + \Gamma_{ji}^*(\omega) \text{ and } \pi_{ij} = \frac{1}{2i}\big(\Gamma_{ij}(\omega) - \Gamma_{ji}^*(\omega)\big). \tag{2.43}$$

Using these definitions we can re-write Eq. 2.42 as [44]

$$\begin{aligned}\frac{\partial}{\partial t}\tilde{\rho}_S = &-i\big[H_{LS}, \rho_S(t)\big] \\ &+ \sum_{\omega}\sum_{ij}\gamma_{ij}(\omega)\Big(S_j(\omega)\rho_S(t)S_i^\dagger(\omega) - \frac{1}{2}\big\{S_i^\dagger(\omega)S_j(\omega), \rho_S(t)\big\}\Big),\end{aligned} \tag{2.44}$$

where $H_{LS} = \sum_\omega \sum_{ij} \pi_{ij}(\omega) S_i^\dagger(\omega) S_j(\omega)$ is the Lamb shift Hamiltonian, arising from $\mathrm{Im}[\Gamma_{ij}(\omega)]$, that results in a renormalisation of the system energy levels due to the interaction with the environment [44]. Transforming back to the

Schrödinger picture using

$$\frac{\partial}{\partial t}\rho_S(t) = -i[H_S, \rho_S(t)] + e^{-iH_S t}\Big(\frac{\partial}{\partial t}\tilde{\rho}_S(t)\Big)e^{iH_S t}, \tag{2.45}$$

yields [44]

$$\begin{aligned}\frac{\partial}{\partial t}\tilde{\rho}_S &= -i\big[H_S + H_{LS}, \rho_S(t)\big] \\ &\quad + \sum_{\omega}\sum_{ij}\gamma_{ij}(\omega)\Big(S_j(\omega)\rho_S(t)S_i^{\dagger}(\omega) - \frac{1}{2}\big\{S_i^{\dagger}(\omega)S_j(\omega), \rho_s(t)\big\}\Big).\end{aligned} \tag{2.46}$$

Re-writing the master equation in the diagonal form gives [39, 44]

$$\begin{aligned}\frac{\partial}{\partial t}\rho_S(t) &= -i\big[H_S + H_{LS}, \rho_S(t)\big] \\ &\quad + \frac{1}{2}\sum_{\omega,k}\Big(2L_k(\omega)\rho(t)L_k^{\dagger}(\omega) - \big\{L_k^{\dagger}(\omega)L_k(\omega), \rho_S(t)\big\}\Big) \equiv \mathscr{L}\rho_S(t),\end{aligned} \tag{2.47}$$

which reduces to

$$\begin{aligned}\frac{\partial}{\partial t}\rho_S(t) &= -i\big[H_S + H_{LS}, \rho_S(t)\big] \\ &\quad + \frac{1}{2}\sum_{k}\Big(2L_k\rho(t)L_k^{\dagger} - \{L_k^{\dagger}L_k, \rho_S(t)\}\Big) \equiv \mathscr{L}\rho_S(t),\end{aligned} \tag{2.48}$$

when there is only a single relevant frequency. This is the final form of the Lindblad Master equation. The coherent lossless dynamics of the quantum system are described by the commutator $[H_S+H_{LS}, \rho_S(t)]$, while the incoherent dynamics are incorporated by the collapse operators, $L_k = \sqrt{\gamma_k}S_k$, with rates γ_k derived from the real component of $\Gamma_{ij}(\omega)$. To reach this point we have assumed the system and environment have no interactions before the given starting time, the interaction between the system and environment is weak and the environment is large enough to remain unaffected by the quantum system (Born approximation), the state of the open quantum system evolves rapidly relative to the state of the S (Secular approximation), and the memory time of the environment is very short (Markov approximation).

This page is intentionally left otherwise blank.

Chapter 3

Quantum Dots and The Classically Driven Two-Level System

3.1 Introduction

There are numerous examples of different simple quantum systems whose evolution may be described by the Lindblad master equation we derived in Chapter 2. The simplest of these examples is the Two-Level System (2LS)[1] which consists of a ground state $|g\rangle$ and an excited state $|e\rangle$ separated by an energy $\hbar\omega_e$. While the 2LS may be a simple example of a quantum system, it can prove to be an extremely useful approximation when studying physical quantum systems.

The semiconductor QD is one example of a physical quantum system that is often approximated as a 2LS. In Chapters 4 and 5 we shall consider the effects of pulsed driving on a QD coupled to a large bath of quantum harmonic oscillators, approximating the QD as a 2LS. Furthermore, in Chapter 6 we shall extend the classically driven 2LS model to a Four-Level System (4LS) picture with pulsed excitation. It will therefore be useful to explore the electronic properties of QDs, and examine the properties of a classically driven 2LS under Continuous-Wave (CW) and pulsed optical driving in the absence of coupling to a thermal bath using the Lindblad master equation. Additionally we shall explore the impact of pure dephasing mechanisms, and coupling to an optical cavity on the properties of the 2LS.

[1] The two-level system may also be referred to as a two-level atom or two-level emitter.

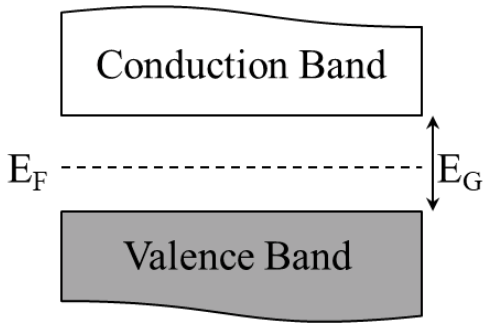

Figure 3.1: A simple representation of the edges of the conduction and valence bands of a semiconductor. The bands are separated by a band gap of energy E_G in which lies the Fermi level at energy E_F. At $T = 0$ K the valence band is fully occupied while the conduction band is empty.

3.2 The Properties of Semiconductor Quantum Dots

In this section we shall give a brief overview of the properties of QDs, and the effects resulting from the application of external fields. For more in-depth discussions see [11, 45, 46].

3.2.1 Band Structure of Bulk Semiconductors

Within the crystal lattice of a bulk solid the constituent atoms are situated in close proximity to one another. Because of this, the outer valence orbitals of the atoms forming the crystal have a significant overlap, and thus strongly interact [45, 46]. To preserve the Pauli exclusion principle that states no two Fermions may simultaneously possess the same quantum state within a quantum system, the interacting orbitals must broaden into electronic bands [2]. Each band maintains some characteristics of the atomic orbitals from which it originated, and the energy width of each band is determined by the magnitude of the overlap between these orbitals [46]. Depending on the material and band configuration, this finite width can result in the emergence of gaps between the bands in which there are no allowed electronic energy levels.

Of the bands that form the band structure of a crystal lattice, it is those lying closest to the Fermi level that are of the most interest. The Fermi level defines the highest energy an electron may possess in the material at a temperature of zero Kelvin. That is, at zero Kelvin electronic states below

[2]Each band actually consists of a series of discrete energy levels. However, the large number of these discrete levels (proportional to the number of atoms in the lattice) means their energy separation is small enough for each band to be considered as continuous.

the Fermi level will be occupied whereas the states above the Fermi level will remain unoccupied [46]. In a semiconductor, the material type most relevant to the work presented in this thesis, the Fermi level lies within a band gap. The lowest energy unoccupied band above the Fermi level is referred to as the conduction band, and the highest energy fully occupied band below the Fermi level is known as the valence band [45] as shown in Figure 3.1. Electrons may be promoted across the band gap from the valence band to the conduction band by absorbing a quanta with energy greater than the band gap energy, E_G [45]. This process of inter-band absorption leaves behind a *hole*, a spin-3/2 quasi-particle[3] with an effective positive charge and mass resulting from the absence of an electron, in the valence band [46].

3.2.2 Quantum Confinement

The band structure of a material may be engineered to confine charge carriers (electrons and holes) to a desired spatial region. By surrounding one type of semiconductor material (e.g. InAs) with another possessing a larger band gap (e.g. GaAs), discontinuities appear in the valence and conduction bands forming a potential well as shown in Figure 3.2. If along a given axis the spatial dimension of the potential well is smaller than the de Broglie wavelength of a charge carrier, the charge carrier will no longer be free to move along that given confinement axis [11, 46]. Specifically, on these scales the confinement of the charge carrier will begin to exhibit quantum properties, and the charge carriers will occupy discrete energy levels defined along the confinement axes while remaining free to move along any unconfined axes. We can therefore classify quantum confined structures according to the number of spatial dimensions along which any trapped charge carriers remain free to move. Quantum wells are formed by confining the motion of electrons and holes along a single spatial dimension, while allowing free motion along the other two dimensions, and are thus referred to as two dimensional structures. On the other hand, quantum wires confine charge carriers in all but one of the spatial dimensions. Because of this they are referred to as 1D structures. In a QD charge carriers are spatially confined along all three axes [4], and thus have zero dimensions along which any confined charge carriers may freely move. As QDs are the most relevant quantum confined structure to this thesis we shall neglect the other

[3]Holes with spin-3/2 are known as heavy-holes. Holes can also have spin-1/2, known as light-holes, but these are not extensively considered in the thesis as the quantum confinement in the QD lifts the degeneracy of the light- and heavy-hole valence bands.

[4]The growth process of Self-Assembled Quantum Dots (SAQDs) is discussed in Chapter 7.

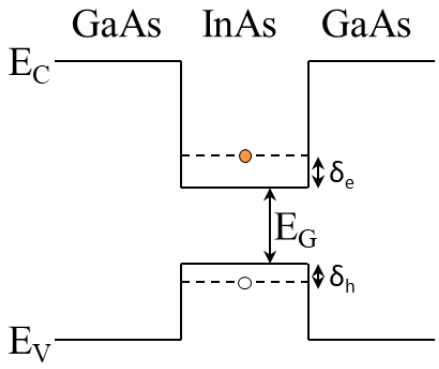

Figure 3.2: A simple band diagram of a quantum confined structure (e.g. a Quantum Dot (QD)) formed from InAs surrounded by GaAs. The band gap of InAs (E_G) is smaller than that of GaAs resulting in the confinement of the charge carriers to the InAs region. This confinement shifts the discrete energy levels of the charge carriers away from the band edges of the bulk material by $\delta_{e(h)}$.

types of quantum confined structures in our discussions from here on. The energy of charge carriers confined to a QD is fully quantised giving rise to atom-like properties. Each further dimension of confinement has the additional effect of shifting the band edge in the structure away from the band edge of the material by the confinement energy [46] as can be seen in Fig 3.2.

3.2.3 Neutral States: Excitons and Biexcitons

When discussing the band structure of solid materials we briefly mentioned that promoting an electron to the conduction band leaves a quasi-particle referred to as a hole in the valence band. Under the right conditions these two oppositely charged particles can be bound together by their mutual Coulomb interaction to form a further quasi-particle known as an *exciton* [45, 46].

As the exciton is formed from a negatively charged electron and positively charged hole it has no overall net charge. However, excitons do possess a net spin derived from the spin of their component particles. Excitons can be split into two categories based on the magnitude of their spin. *Bright excitons* have a spin magnitude of one, i.e. the spins of the electron and hole are anti-parallel ($|\uparrow\Downarrow\rangle, |\downarrow\Uparrow\rangle$). These excitons are referred to as bright as they are able to be created by the absorption of, and recombine via the emission of, a single photon with angular momentum ± 1. In *dark excitons* the electron and hole spins are parallel resulting in an exciton spin of ± 2. As a result the recombination of a dark exciton is optically forbidden.

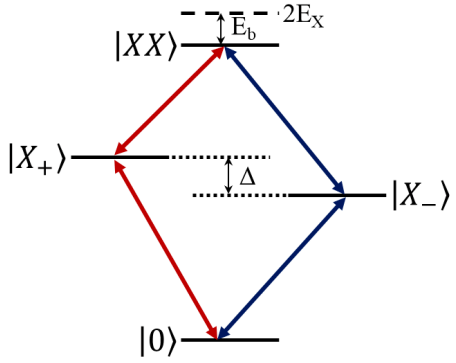

Figure 3.3: The energy level structure of the biexciton cascade written in the linear basis. Here $|X_{\pm}\rangle = \frac{1}{\sqrt{2}}\big(|{\downarrow}{\Uparrow}\rangle \pm |{\uparrow}{\Downarrow}\rangle\big)$, and $|XX\rangle = |{\uparrow}{\Downarrow}{\downarrow}{\Uparrow}\rangle$. The exciton eigenstates $|X_{\pm}\rangle$ are split by the fine structure splitting, Δ, caused by an asymmetry in the Quantum Dot (QD) coupling the bright excitonic states via the electron-hole exchange interaction [47].

Excitons can be further categorised based on the strength of the interaction between the electron and hole. *Frenkel excitons* are usually formed in materials with small dielectric constants, and thus have a large binding energy and small spatial extent on the order of the lattice constant of the bulk material [46]. *Wannier-Mott excitons*, on the other hand, are typically formed in materials with a large dielectric constant such as semiconductors [46], and are therefore the more relevant type of exciton to this thesis. The large dielectric constant reduces the binding energy between the electron and hole resulting in a large exciton radius extending over multiple lattice periods. When excited in a bulk material the binding energy of Wannier-Mott excitons is so small that above cryogenic temperatures the thermal vibrations of the crystal lattice provide enough energy to overcome the binding energy and dissociate the electron and hole. However, exciting an electron-hole pair within a QD increases the exciton binding energy. This is due to the spatial confinement of the charge carriers increasing the overlap of their wave functions resulting in a stronger Coulomb interaction and smaller spatial extent.

Just as it is possible to excite a single exciton, the nature of the electronic bands allows for two excitons with opposite spin configurations to be simultaneously excited. The Coulomb interaction between the components of the two neutral states can then also bind them to form an exciton molecule known as a biexciton. The biexciton energy is then given by

$$E_{XX} = 2E_X - E_b, \tag{3.1}$$

where E_X is the exciton energy, and E_b is the biexciton binding energy. It is this difference in energy between the exciton and biexciton transitions (i.e. E_b) that allows us to approximate neutral QDs as 2LSs assuming that any optical driving is also far enough detuned from the biexciton energy. The formation of a biexciton results in an energy structure referred to as the biexciton cascade shown in the linear basis in Figure 3.3. This can be employed as a source of entangled photon pairs, emitted when the biexciton relaxes to the ground state via the intermediate exciton states [48–52].

3.2.4 Charged States: Trions

In addition to neutral exciton states, it is also possible to confine single charge carriers (electrons or holes) inside QDs. This is considerably more challenging to achieve than confining excitonic states, as it is not possible to photo-excite a single charge carrier as it is with single excitons. There are a number of methods for isolating single charge carriers in QDs including ionising an exciton, deterministically charging the confined structure with an applied electric field, or including a dopant whose concentration is controlled to give a unity mean charge carrier occupancy [5]. These methods often require the use of diode structures, which will be discussed in the next section.

It is also possible to excite an exciton in a charged QD. Although the exciton possesses no overall charge, the Coulomb interaction between the constituent charge carriers of the exciton and the single charge carrier, combined with the wave function overlap resulting from the quantum confinement, results in the formation of a charged quasi-particle known as a trion, often labelled as X^+ or X^- (or equivalently T^+ or T^-) depending on the charge. The overall charge of the trion depends on the charge of the single charge carrier initially occupying the QD, with a single hole producing a positively charged trion ($|\Uparrow\Downarrow\uparrow\rangle$ or $|\Downarrow\Uparrow\downarrow\rangle$) and a single electron resulting in a negatively charged trion ($|\uparrow\Uparrow\downarrow\rangle$ or $|\downarrow\Downarrow\uparrow\rangle$). These charged exciton states will form an important part of the work presented in Chapter 6.

3.2.5 The Quantum Confined Stark Effect

Now we have discussed the electronic properties of QDs in the absence of any external fields, we can extend our discussion to explore the effect of situating a QD in an external field. We shall begin by considering the application of

[5] The epitaxial growth of semiconductor QDs is discussed in Chapter 7.

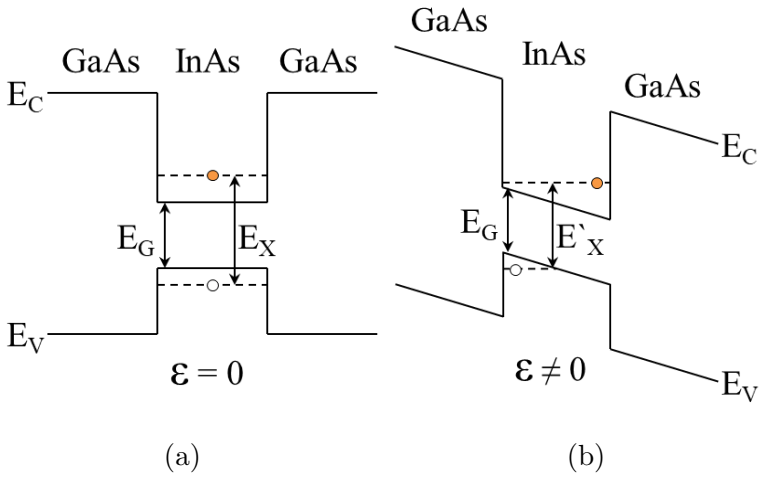

Figure 3.4: The conduction and valence bands of a quantum confined structure with (a) no applied electric field, and (b) a non-zero applied electric field. Applying an electric field tilts the bands altering the potential in which the charge carriers are confined. This shifts the position of the electron and hole wave functions to opposite sides of the confinement well reducing the wave function overlap and thus also reducing the exciton binding energy ($E'_X < E_X$).

an external electric field to a QD, the result of which is described by the Quantum-Confined Stark Effect (QCSE) [45, 46].

One may apply an external direct-current electric field to a QD by situating it within a diode structure (for more information on diodes see Chapter 7). When an electric field is applied to a QD containing an exciton, the constituent electron and hole are forced to move in opposite directions owing to their opposing charges. In the absence of any quantum confinement the exciton would be torn apart by this field. However, in a QD the quantum confinement of the charge carriers prevents the exciton from being dissociated. Instead the applied field moves the two charge carriers to opposing sides of the potential well as the band structure is modified (see Figure 3.4), reducing their wave function overlap and the strength of their mutual Coulomb interaction. This results in a red-shift of the photons emitted when the exciton eventually recombines (see spectra in Section 8.3.3). For a QD, the magnitude of this shift is given by [53, 54]

$$\Delta E_{QCSE} = pF + \beta F^2, \tag{3.2}$$

where in this instance F is the applied electric field strength, p is the electric dipole moment of the QD, and β is the polarisability [53, 54]. From this we can see that the largest shift occurs when the electric field is aligned with the electric dipole of the QD. The principle application of the QCSE is the

tuning of the exciton energy, and, by extension, the emission energy. This can be done, for example, to bring two QDs situated in independent electric fields into resonance, or (as shall be demonstrated in Chapter 8) to bring a QD into resonance with an optical cavity mode. However, if the applied field is large enough, and the band structure is suitable, the QD can be ionised or completely depleted by the application of an electric field as one or both of the charge carriers tunnel out of the structure.

3.2.6 The Zeeman Effect

One may also apply an external magnetic field to a QD, in addition to the external electric fields we have discussed. The results of applying a weak magnetic field to a QD, and any atomic system in general, are described by the Zeeman effect [45]. This effect plays a central role in the work performed in Chapter 6. Depending on the origin, the Zeeman effect may be split into two categories. The normal Zeeman effect describes the results of applying an external magnetic field to a system with no net spin [45]. On the other hand, the anomalous Zeeman effect originates from systems with a non-zero net spin and is thus a purely quantum effect [45]. As we are mainly interested in charge-carriers confined to QDs it is the latter effect that is most relevant since the charge carriers do possess a net spin as we have previously discussed.

When an external magnetic field is applied to a charge carrier spin system, the spin will begin to precess about the magnetic field. The interaction between the spin-system and the magnetic field is characterised by the energy [45]

$$E_z = g\mu_B B, \tag{3.3}$$

where g is the g-factor quantifying the strength of the interaction, μ_B is the Bohr magneton, and B is the applied magnetic field strength. The orientation of the magnetic field also impacts the resulting behaviour of the system as discussed further in Chapter 6. The application of a weak magnetic field to a neutral exciton will also produce a quadratic diamagnetic shift [46, 55]. This diamagnetic shift is characterised by the diamagnetic coefficient γ_2 leading to the total energy shift of an exciton in the presence of an applied magnetic field to be [55]

$$\Delta E = \gamma_1 B + \gamma_2 B^2, \tag{3.4}$$

where γ_1 characterises the Zeeman energy shift.

3.3 The Dipole Approximation

Before we move on to apply the Lindblad master equation to the example of an optically driven 2LS, we first must discuss how one includes classical driving in the system Hamiltonian. In this thesis we consider optically driven atomic-like systems whose spatial extent is much smaller than the wavelengths of the light with which they interact [6]. In this case we may make an approximation, known as the *dipole approximation*, that allows us to simplify the semi-classical Hamiltonian describing the optical driving of a quantum system by a classical source. To make this approximation we can consider a charged particle situated in an external electromagnetic field. The electric and magnetic components of an electromagnetic field may be derived from both a scalar (Φ) and vector ($\boldsymbol{A}$) potential ($\boldsymbol{E} = -\nabla\Phi - \partial_t \boldsymbol{A},\ \boldsymbol{B} = \nabla \times \boldsymbol{A}$). Using this notation the Hamiltonian of a charged particle in an electromagnetic field may be written as [56]

$$H(\boldsymbol{r}, t) = \frac{1}{2m}\big(\boldsymbol{p} - q\boldsymbol{A}(\boldsymbol{r}, t)\big)^2 - q\Phi(\boldsymbol{r}, t), \tag{3.5}$$

where $q,\ m,\ \boldsymbol{p}$ are the charge, mass, and momentum of the charged particle respectively. As the size of the quantum systems we are interested in is much smaller than the wavelengths with which they interact, we may approximate the vector potential as being position independent, i.e. $\boldsymbol{A}(\boldsymbol{r}, t) \to \boldsymbol{A}(t)$. From here we can perform a gauge transformation. This will allow us to simplify the potentials $(\Phi, \boldsymbol{A})$ without changing the fields derived from them. As $\boldsymbol{B} = \nabla \times \boldsymbol{A}$ we may add the gradient of a scalar field ($\nabla\Lambda$) to the vector potential without changing the magnetic field as $\nabla \times (\nabla\Lambda) = 0$. However, to maintain the invariance of the electric field under this gauge transformation we must add the time-derivative of Λ to the scalar field Φ. Our transformed potentials are then given by [57, 58]

$$\begin{aligned} \Phi(\boldsymbol{r}, t) \to \Phi'(\boldsymbol{r}, t) =& \Phi(\boldsymbol{r}, t) - \partial_t \Lambda(\boldsymbol{r}, t), \\ \boldsymbol{A}(\boldsymbol{r}, t) \to \boldsymbol{A}'(\boldsymbol{r}, t) =& \boldsymbol{A}(\boldsymbol{r}, t) + \nabla\Lambda(\boldsymbol{r}, t). \end{aligned} \tag{3.6}$$

Choosing the gauge $\Lambda(\boldsymbol{r}, t) = -\boldsymbol{A}(t) \cdot \boldsymbol{r}$ our new scalar and vector fields may be written as

$$\begin{aligned} \Phi'(\boldsymbol{r}, t) =& \Phi(\boldsymbol{r}, t) - \partial_t \boldsymbol{A}(t)\boldsymbol{r} = \Phi(\boldsymbol{r}, t) + \boldsymbol{r} \cdot \big(\boldsymbol{E} + \nabla\Phi(\boldsymbol{r}, t)\big), \\ \boldsymbol{A}'(\boldsymbol{r}, t) =& \boldsymbol{A}(\boldsymbol{r}, t) - \nabla(\boldsymbol{A}(t) \cdot \boldsymbol{r}) = 0. \end{aligned} \tag{3.7}$$

[6] In the case of QDs a few nanometres compared to wavelengths on the order of 10^3 nm.

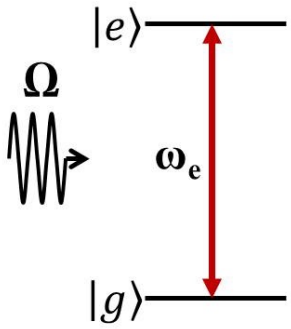

Figure 3.5: A depiction of a 2LS consisting of a ground state $|g\rangle$ and excited state $|e\rangle$ separated by an energy $\hbar\omega_e$. Here the system is driven on resonance with a continuous wave source with Rabi frequency Ω.

Taking the Coulomb gauge, where $\Phi = 0$ [57, 58], and making the substitution into the Hamiltonian yields

$$H(\boldsymbol{r}, t) = \frac{1}{2m}\big(\boldsymbol{p}\big)^2 - q\boldsymbol{r}\cdot\boldsymbol{E}(t) = \frac{1}{2m}(\boldsymbol{p})^2 - \boldsymbol{d}\cdot\boldsymbol{E}(t), \tag{3.8}$$

where $\boldsymbol{d} = -q\boldsymbol{r}$ is the dipole operator, and the final term of the Hamiltonian describes the coupling between a classical electric field and an electric dipole. While the dipole approximation is generally applicable to QDs under a vast majority of circumstances, there are regimes where it breaks down [59, 60].

3.4 Driven Two-Level System Hamiltonian

Using the dipole approximation, and choosing the ground state to have zero energy, the Hamiltonian describing a classically driven 2LS depicted in Figure 3.5 may be written as

$$H = \omega_e \left|e\right\rangle\!\left\langle e\right| - \hat{d}\cdot\boldsymbol{E}(t), \tag{3.9}$$

where $\hat{d}$ is the transition dipole operator, and $\boldsymbol{E}(t)$ is the time-dependent electric field vector. This field vector may be re-written as $\boldsymbol{E}(t) = \boldsymbol{E}_0(t)\cos\omega_l t$ where $\boldsymbol{E}_0 = E_0(t)\boldsymbol{\epsilon}$ is the vector electric field strength which incorporates the polarisation vector $\boldsymbol{\epsilon}$, and ω_l is the laser frequency. One can write the spectral decomposition of the dipole operator in the basis states of the 2LS as $\hat{d} = \langle g|\,\hat{d}\,|e\rangle\,(|g\rangle\!\langle e| + |e\rangle\!\langle g|)$.[7] The diagonal matrix elements are not present as the parity transition selection rules tell us these elements are zero (see

[7] Ordinarily $\hat{d} = \sum_{i,j=e,g}\langle i|\,\hat{d}\,|j\rangle\,|i\rangle\!\langle j|$. The parity transition rules show $\langle i|\,\hat{d}\,|j=i\rangle = 0$ and thus $\hat{d} = \sum_{i,j\neq i=e,g}\langle i|\,\hat{d}\,|j\rangle\,|i\rangle\!\langle j|$.

Appendix A). Making these substitutions, the Hamiltonian describing the coherent dynamics of a classically driven 2LS can be written as

$$H = \omega_e \left|e\right\rangle\!\left\langle e\right| + \frac{\Omega(t)}{2}\left(e^{i\omega_l t} + e^{-i\omega_l t}\right)\left(\left|e\right\rangle\!\left\langle g\right| + \left|g\right\rangle\!\left\langle e\right|\right). \tag{3.10}$$

Here we have defined $\Omega(t) = -\left\langle g\right| \hat{d} \cdot \boldsymbol{E}_0(t) \left|e\right\rangle$ as the Rabi frequency that quantifies the strength of the coupling between the 2LS and coherent driving field modulated by some time-dependent envelope function. The CW limit can then be recovered by choosing $\Omega(t) = \Omega \ \forall \ t$. In the time-dependent driving limit the choice of pulse envelope is arbitrary[8], but here we shall assume the 2LS is driven by a Gaussian optical pulse of the form

$$\Omega(t) = \frac{\Theta}{\sqrt{2\pi w^2}} \exp\Big\{-\frac{(t-t_0)^2}{2w^2}\Big\}, \tag{3.11}$$

where $\Theta = \int_0^\infty \Omega(t)$ is the pulse area, w is the Gaussian width, and t_0 is the time at which the peak of the pulse, i.e. the peak Rabi frequency, occurs. The Gaussian width is related to the electric field Full-Width Half Maximum (FWHM) of the pulse, $\Delta\tau_E$, by

$$w = \frac{\Delta\tau_E}{2\sqrt{2\ln 2}}, \tag{3.12}$$

which in turn is related to the intensity FWHM that is measured in experiment by $\Delta\tau_E = \Delta\tau_I\sqrt{2}$.

3.4.1 Unitary Transformations to a Rotating Frame of Reference

While the Hamiltonian in Eq. 3.10 does describe the dynamics of a 2LS driven by a classical source, the time-dependence in the exponential terms makes the theoretical treatment challenging and computationally expensive. It is possible to remove this time dependence by performing a transformation from the so-called *lab-frame* to a reference frame rotating at an arbitrary frequency of our choice, ω_R. We have already encountered a transformation changing the frame of reference moving from the Schrödinger picture to the Interaction picture. However, we now need to derive a more general transformation that will allow us to find the relationship between an arbitrary Hamiltonian describing

[8] In later chapters we shall make use of different envelope functions.

a quantum system in the lab frame ($H(t)$) and the Hamiltonian describing the same system in an arbitrary rotating frame ($\tilde{H}(t)$).

The state vector of the system in the rotating frame can be found by applying a unitary operator to the lab-frame state vector such that

$$|\tilde{\psi}(t)\rangle = U(t)\,|\psi\rangle\,. \tag{3.13}$$

Here $|\psi\rangle$ is the state vector describing the system in the lab-frame, $|\tilde{\psi}(t)\rangle$ is the state of the system in the rotating frame, and $U(t)$ is a unitary operator whose form is chosen for convenience. The Schrödinger equation must apply in the rotating frame just as it does in the lab-frame, i.e. we may write the Schrödinger equation in the rotating frame as

$$\frac{\partial}{\partial t}\,|\tilde{\psi}(t)\rangle = -i\tilde{H}(t)\,|\tilde{\psi}(t)\rangle\,. \tag{3.14}$$

Substituting Eq. 3.13 into Eq. 3.14, and using the product rule, yields

$$\frac{\partial}{\partial t}\,|\tilde{\psi}(t)\rangle = \Big(\frac{\partial}{\partial t}U(t)\Big)\,|\psi\rangle + U(t)\Big(\frac{\partial}{\partial t}\,|\psi\rangle\Big) = -i\tilde{H}(t)\,|\tilde{\psi}(t)\rangle\,. \tag{3.15}$$

From this we see the second term in the centre is the left-hand side of the Schrödinger equation in the lab-frame pre-multiplied by $U(t)$. We can therefore substitute in the Schrödinger equation to find

$$\Big(\frac{\partial}{\partial t}U(t)\Big)\,|\psi\rangle - iU(t)H(t)\,|\psi\rangle = -i\tilde{H}(t)\,|\tilde{\psi}(t)\rangle\,. \tag{3.16}$$

Using $|\psi\rangle = U^{\dagger}(t)\,|\tilde{\psi}(t)\rangle$ we can re-write this equation to find the final relationship between the Hamiltonians describing a given quantum system in two different frames of reference

$$\tilde{H}(t) = U(t)H(t)U^{\dagger}(t) + i\Big(\frac{\partial}{\partial t}U(t)\Big)U^{\dagger}(t). \tag{3.17}$$

One can show this agrees with the results found when transforming between the Schrödinger and Interaction pictures by substituting in the Hamiltonian $H = H_0 + H_I$ from Eq. 2.8, and choosing $U(t) = \exp\{iH_0t\}$. This yields

$$\tilde{H}(t) = U(t)\big(H_0 + H_I\big)U^{\dagger} - i\big(-iH_0\big) = U(t)H_IU^{\dagger}(t) = \tilde{H}_I(t), \tag{3.18}$$

which agrees with our definition of $\tilde{H}_I(t)$ in Eq. 2.15.

3.4.2 The Rotating Wave Approximation

Utilising Eq. 3.17 the Hamiltonian describing a classically driven 2LS can be transformed into a reference frame rotating at an arbitrary frequency ω_R using the unitary operator

$$U(t) = \exp\{i\omega_R t \left|e\right\rangle\!\left\langle e\right|\}. \tag{3.19}$$

Applying this unitary transformation to our lab-frame Hamiltonian we find the Hamiltonian in the rotating frame is given by

$$\tilde{H}(t) = \big(\omega_e - \omega_R\big) \left|e\right\rangle\!\left\langle e\right| + \frac{\Omega(t)}{2}\big(e^{i\omega_R t} \left|e\right\rangle\!\left\langle g\right| + e^{-i\omega_R t} \left|g\right\rangle\!\left\langle e\right|\big)\big(e^{i\omega_l t} + e^{-i\omega_l t}\big). \tag{3.20}$$

This form of the rotating frame Hamiltonian still contains time-dependent exponential terms which are the computationally challenging terms we are trying to remove by performing this unitary transformation. However, we can now apply the Rotating Wave Approximation (RWA). In doing so we assume $|\omega_R - \omega_l| \ll \omega_R + \omega_l$ which allows us to replace the counter-rotating terms $(\omega_R + \omega_l)$ with their zero time averages. This is a reasonable approximation to make for optical frequencies as the counter-rotating terms would not be experimentally resolvable on the relevant timescales. Transforming to a frame rotating at the laser frequency, that is setting $\omega_R = \omega_l$, removes the remaining time-dependent exponential terms from the rotating frame Hamiltonian

$$\tilde{H}(t) = \big(\omega_e - \omega_l\big) \left|e\right\rangle\!\left\langle e\right| + \frac{\Omega(t)}{2}\big(\left|e\right\rangle\!\left\langle g\right| + \left|g\right\rangle\!\left\langle e\right|\big). \tag{3.21}$$

As a result of transforming to a reference frame rotating at the driving laser frequency and applying the RWA, we now have a semi-classical Hamiltonian describing the coherent dynamics of 2LS driven by a classical field whose only time-dependence arises from the envelope function of the pulse, and therefore vastly reduces the computational resources required to perform calculations. In the CW limit $\Omega(t) \to \Omega$ returns a completely time-independent Hamiltonian.

3.5 The Quantum Optical Master Equation

To model the emission properties of the 2LS we need to account for the interactions with the quantised electromagnetic field. Hence we must derive a master equation that, much like the Lindblad master equation, tracks the degrees of freedom of the 2LS while tracing out the electromagnetic environment. To do this we shall model the electromagnetic field as a continuum of quantum

harmonic oscillators [39]

$$H_E = \sum_k \omega_k \epsilon_k^\dagger \epsilon_k, \tag{3.22}$$

with frequencies ω_k and creation (annihilation) operators $\epsilon_k^\dagger(\epsilon_k)$. The interaction between the field and 2LS is then given by the Hamiltonian

$$H_I = \sum_k \big(g_k \epsilon_k \sigma^\dagger + g_k^* \epsilon_k^\dagger \sigma\big), \tag{3.23}$$

where the coupling strength between the 2LS and k^{th} electromagnetic mode is quantified by g_k, and we have introduced the notation $\sigma = |g\rangle\langle e|$. Transforming the interaction Hamiltonian to the rotating frame into which we transformed the system Hamiltonian yields

$$\tilde{H}_I(t) = \sum_k \big(g_k \epsilon_k \sigma^\dagger e^{i\omega_l t} + g_k^* \epsilon_k^\dagger \sigma e^{-i\omega_l t}\big). \tag{3.24}$$

Assuming the electromagnetic spectral density does not vary significantly over the energy scales relevant to the 2LS, we may take the electromagnetic spectral density to be flat, i.e. $J(\omega) = J \;\forall\; \omega$ [61]. This allows us to transform into the interaction picture using the simple unitary transform

$$U(t) \approx \exp\left\{ i\Big((\omega_e - \omega_l)\sigma^\dagger\sigma + \sum_k \omega_k \epsilon_k^\dagger \epsilon_k\Big)t \right\}, \tag{3.25}$$

where we have redefined H_0 as $H_0 = (\omega_e - \omega_l)\sigma^\dagger\sigma + \sum_k \omega_k \epsilon_k^\dagger \epsilon_k$. This choice of unitary transformation cancels out the $\exp\{\pm i\omega_l t\}$ terms in Eq. 3.24, and thus the interaction picture Hamiltonian is given by

$$\tilde{H}_I(t) = \sum_k \big(g_k \epsilon_k \sigma^\dagger e^{i\omega_e t} e^{-i\omega_k t} + g_k^* \epsilon_k^\dagger \sigma e^{-i\omega_e t} e^{i\omega_k t}\big). \tag{3.26}$$

From here we may explicitly write the components of the decomposition of the interaction Hamiltonian in Eq. 2.34 as

$$\begin{aligned} S_1(t) &= \sigma^\dagger e^{i\omega_e t} \text{ and } E_1(t) = \sum_k g_k^* \epsilon_k e^{-i\omega_k t}, \\ S_2(t) &= \sigma e^{-i\omega_e t} \text{ and } E_2(t) = \sum_k g_k \epsilon_k^\dagger e^{i\omega_k t}. \end{aligned} \tag{3.27}$$

Deriving the full form of our master equation is then a question of substituting these system and environment operators into the master equation given

in Eq. 2.35. Performing the substitutions, and transforming back to the rotating frame of reference in the Schrödinger picture, automatically yields a master equation, known as the *quantum optical master equation*, in the Lindblad form [39]

$$\frac{\partial}{\partial t}\rho_S(t) = -i\Big[\tilde{H}(t), \rho_S(t)\Big] + \frac{\gamma}{2}\Big(2\sigma\rho_S(t)\sigma^\dagger - \Big\{\sigma^\dagger\sigma, \rho_S(t)\Big\}\Big). \tag{3.28}$$

Here $\tilde{H}(t)$ is given by Eq. 3.21, and the spontaneous emission Lindblad operator is given by $L = \sqrt{\gamma}\sigma$, where $\gamma = \pi J/2$ is the decay rate of the exited state of the 2LS given by the inverse of the state lifetime $\gamma = T_1^{-1}$.

As the quantum optical master equation is derived directly from Eq. 2.35, and is in the Lindblad form, it makes the same approximations as the Lindblad master equation. That is, the quantum optical master equation is also a second-order master equation, and uses the Born and Markov approximations assuming the interaction between the system and optical environment is weak such that the two evolve on disparate timescales. Finally, the secular approximation is also used in the derivation of the quantum optical master equation allowing us to only consider resonant terms.

3.6 Coherent Dynamics: Rabi Oscillations

With our simplified rotating frame Hamiltonian we may now use the quantum optical master equation to calculate the temporal dynamics of the 2LS state populations under both CW and pulsed excitation. For the systems described in this chapter, the dynamics (and correlation functions) may be calculated using the Python package QuTiP [62] to computationally solve the master equation at discretised time intervals. Figure 3.6 shows that under CW excitation the population of the 2LS coherently oscillates between the two system eigenstates at frequency Ω when $\Omega \gg \gamma$. The oscillations in the populations under optical excitation are the well-known *Rabi oscillations*, and have been experimentally observed numerous times [63–67]. In the absence of any decoherence mechanisms these oscillations would continue indefinitely (see the grey-dotted line in Figure 3.6a). However, the presence of decoherence in Figure 3.6a, in the form of spontaneous emission, ultimately dampens the oscillations until they are completely suppressed in the long-time limit.

Under pulsed excitation a similar behaviour is observed. During the pulse the state population of the 2LS coherently oscillates between the two system

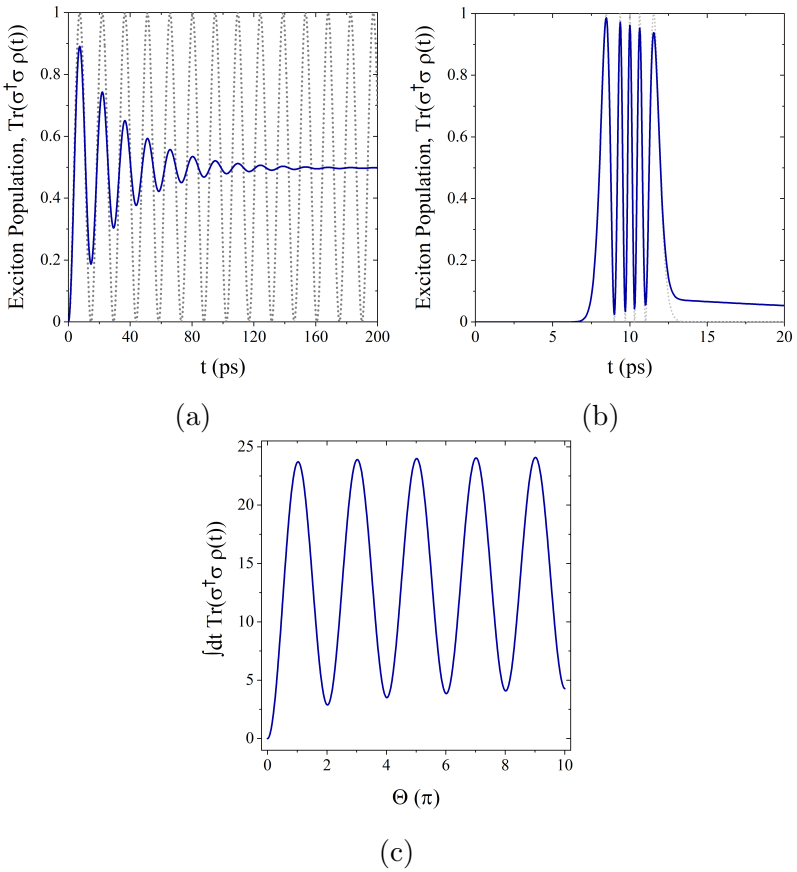

Figure 3.6: The calculated dynamics of the state populations of a Two-Level System (2LS) under (a) Continuous-Wave (CW), and (b,c) pulsed excitation. (c) Under pulsed resonant excitation Rabi rotations are also observed in the state populations sweeping the area of the pulse. The oscillations in (c) do not reach zero due to the use of the time-integrated exciton population rather than the steady-state without spontaneous emission. Parameters used: (blue-solid) $\gamma^{-1} = 23$ ps, (grey-dot) $\gamma = 0$ ps^{-1}, (a) $\Omega = 10\gamma$, (b) $\Theta = 10\pi$, (b,c) $\Delta\tau = 2$ ps.

eigenstates, again damped by spontaneous emission. The number of oscillations in the state populations during the pulse is proportional to Θ/π where $\Theta = \int_0^\infty dt\Omega(t)$ is the pulse area. If we instead plot the time-integrated excited state population as a function of the area of the driving pulse, as shown in Figure 3.6c, we observe Rabi rotations. It is important to note that the Rabi rotations in the time-integrated exciton population with varying pulse area are not equivalent to the time-resolved Rabi oscillations plotted in Figures 3.6a and 3.6b. Rather these Rabi rotations are the result of a phase accumulated during the driving pulse. However, from this we see that, by changing the duration and or peak Rabi frequency to fine-tune the area of the driving pulse, one can adjust the state of the system after the pulse.

3.7 The First-Order Correlation Function and Emission Spectra

Experimentally, information about a classically driven 2LS may be derived from the properties of the light it emits. Thus to make predictions about the properties of a 2LS that can be experimentally tested, we need to relate the system degrees of freedom explicitly tracked by our master equation to the properties of the electric fields measured by detectors in experiments.

One can define the electric field operator measured experimentally as $\boldsymbol{E}(t) = \boldsymbol{E}^{+}(t) + \boldsymbol{E}^{-}(t)$. We may then define the positive component of the electric field operator as $\boldsymbol{E}^{+}(t) = \sum_k E_k \boldsymbol{e}_k \epsilon_k$ where ϵ_k is again the annihilation operator of the k^{th} photonic mode, E_k is the electric field strength, and $\boldsymbol{e}_k$ is the electric field unit vector. The negative field component is then given by $\boldsymbol{E}^{-}(t) = (\boldsymbol{E}^{+}(t))^{\dagger}$. The Wiener-Khinchin theorem tells us that the intensity spectrum is related to the electric field operators by [68]

$$I(\omega) = \int_{-\infty}^{\infty} d\tau \left\langle \boldsymbol{E}^{-}(t)\boldsymbol{E}^{+}(t+\tau) \right\rangle e^{-i\omega\tau}. \tag{3.29}$$

To relate the intensity spectrum to the 2LS creation and annihilation operators we shall consider the Heisenberg equation of motion for one of the quantised field operators which is given by

$$\partial_t \tilde{\epsilon}_k(t) = i\left[\tilde{H}(t), \tilde{\epsilon}_k(t)\right] = -i\left(\omega_k \tilde{\epsilon}_k(t) + g_k \tilde{\sigma}(t)\right). \tag{3.30}$$

Here the tilde now indicates an operator is in the Heisenberg picture such that $\tilde{O}(t) = U^{\dagger}(t) O U(t)$ where $U(t)$ is an arbitrary unitary operator chosen to transform. The terms on the right hand side of Eq. 3.30 originate from the commutators of the environment and interaction Hamiltonians with the photonic annihilation operator respectively. Using

$$\partial_t \left(e^{i\omega_k t}\tilde{\epsilon}_k(t)\right) = i\omega_k e^{i\omega_k t}\tilde{\epsilon}_k(t) + e^{i\omega_k t}\partial_t \tilde{\epsilon}_k(t) = -i g_k \tilde{\sigma}(t) e^{i\omega_k t} \tag{3.31}$$

we can formally integrate Eq. 3.30 giving

$$\tilde{\epsilon}_k(t) = e^{-i\omega_k t}\tilde{\epsilon}_k(0) - i\int_0^t dt' g_k \tilde{\sigma}(t') e^{i\omega_k t'}. \tag{3.32}$$

Substituting this into the positive frequency component of the electric field

operator yields

$$\boldsymbol{E}^{+}(t) = \sum_{k} E_k \left(e^{-i\omega_k t}\tilde{\epsilon}_k(0) - i\int_0^t dt' g_k \tilde{\sigma}(t') e^{i\omega_k t'} \right). \tag{3.33}$$

The first term on the right hand side is the free fields contribution which we take to be the vacuum state, and thus neglect. Taking the continuum limit we can then write

$$\boldsymbol{E}^{+}(t) = -i\int_{-\infty}^{\infty} d\omega \int_0^t dt' g(\omega) E(\omega) \tilde{\sigma}(t') e^{i\omega t'}. \tag{3.34}$$

Just as when we derived the quantum optical master equation, we shall assume the 2LS-environment coupling strength $g(\omega)$ does not vary appreciably over the frequencies of the 2LS. This then allows us to simplify Eq. 3.34 to

$$\boldsymbol{E}^{+}(t) = -igE\int_{-\infty}^{\infty} d\omega \int_0^t dt' \tilde{\sigma}(t') e^{i\omega t'}. \tag{3.35}$$

which, using the relation $\int_0^t d\tau g(\tau) \int_{-\infty}^{\infty} d\omega e^{-i\omega\tau} = 2\pi \int_0^t d\tau g(\tau)\delta(\tau)$, allows us to write the final form of the positive electric field component as

$$\boldsymbol{E}^{+}(t) = C\tilde{\sigma}(t), \tag{3.36}$$

where $C = -iE\sqrt{\pi\gamma/2}$ is a constant. Taking the steady-state limit, the intensity spectrum is given by $I(\omega) \propto S(\omega)$ where

$$S(\omega) = \int_{-\infty}^{\infty} d\tau g^{(1)}(\tau) \exp\{-i(\omega - \omega_l)\tau\}, \tag{3.37}$$

and where in terms of the 2LS raising and lowering operators

$$g^{(1)}(\tau) = \lim_{t\to\infty} \langle \sigma^{\dagger}(t)\sigma(t+\tau)\rangle, \tag{3.38}$$

is the steady-state first-order correlation function quantifying the temporal coherence of the electric fields of the emitted light[9], $\sigma = |g\rangle\langle e|$ is the atomic lowering operator, and ω_l is again the laser frequency.

The emission spectrum has contributions from two distinct components, known as the coherent and incoherent spectra. These arise from the steady-

[9]The first-order correlation function can be measured directly using an optical interferometer such as the Mach-Zehnder or Michelson interferometers. The absolute value of $g^{(1)}(\tau)$ is then given by the visibility of the interference fringes, $v = |g^{(1)}(\tau)|$.

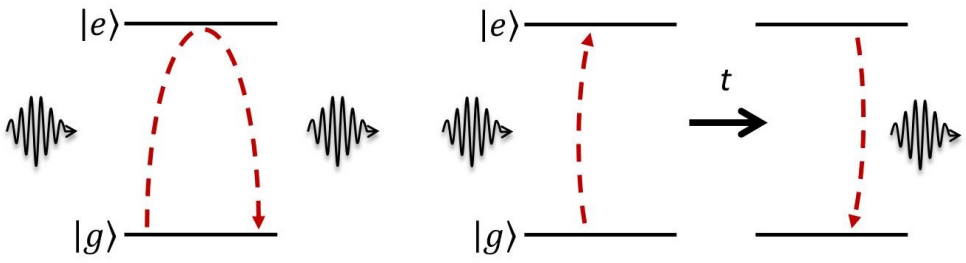

(a) (b)

Figure 3.7: A depiction of coherent (elastic) (a) and incoherent (in-elastic) (b) scattering of incident photons off a Two-Level System (2LS). The excited state of the 2LS is not populated during coherent scattering preserving the first-order coherence of the incident light. Conversely, during incoherent scattering events incident photons are absorbed creating a non-zero excited state population that decays via photon emission after a time period t [69].

state of the correlation function and oscillations in the correlation function respectively. The two spectral components can be written as

$$\begin{aligned} S_{coh}(\omega) &= \int_{-\infty}^{\infty} d\tau g_{coh}^{(1)} \exp\{-i(\omega-\omega_l)\tau\}, \\ S_{inc}(\omega) &= \int_{-\infty}^{\infty} d\tau g_{inc}^{(1)}(\tau) \exp\{-i(\omega-\omega_l)\tau\} \\ &= \int_{-\infty}^{\infty} d\tau (g^{(1)}(\tau) - g_{coh}^{(1)}) \exp\{-i(\omega-\omega_l)\tau\}. \end{aligned} \tag{3.39}$$

Here $S(\omega) = S_{coh}(\omega) + S_{inc}(\omega)$, $S_{coh}(\omega)$ is the coherent contribution to $S(\omega)$, $S_{inc}(\omega)$ is the incoherent contribution to $S(\omega)$, and $g_{coh}^{(1)} = \lim_{\tau\to\infty}\langle\sigma^\dagger(t)\sigma(t+\tau)\rangle = |\langle\sigma_{ss}\rangle|^2$ where $\langle\sigma_{ss}\rangle$ is the steady-state expectation value of σ. As $g_{coh}^{(1)}$ is a (non-zero) constant, assuming the laser coherence time is much greater than the QD coherence time, taking the Fourier transform into the frequency domain yields a delta function at the laser frequency. This corresponds to elastic scattering of the incident laser photons off the 2LS as shown in Figure 3.7a, and as such the scattered light remains first order coherent with the incident laser. Conversely, the incoherent spectrum arises from the inelastic scattering of photons off the 2LS whereby a photon is absorbed and then re-emitted via spontaneous or stimulated emission (see Figure 3.7b). This process results in a change of both the frequency and phase of the photons, and accordingly the incoherent spectrum extends over a range of frequencies with the emitted photons no longer being first-order coherent with the incident light. That is, the incident and emitted light no longer share a constant relative phase.

3.7.1 The Quantum Regression Theorem

As the coherent spectrum reflects the properties of the driving laser [70], we shall consider only the incoherent part of the spectrum in trying to deduce information about the 2LS. However, to do this we must still calculate the two-time correlation function $\langle\sigma^\dagger(t)\sigma(t+\tau)\rangle$. This can be achieved by employing the Quantum Regression Theorem (QRT) which allows one to calculate such correlation functions using the master equation approach.

In our derivation of the Lindblad master equation we saw that one may write the two-time correlation function as

$$C(t,\tau) = \langle A(t)B(t+\tau)\rangle = \mathrm{Tr}\{A(t)B(t+\tau)\rho\}. \tag{3.40}$$

From here the explicit time-dependence can be moved from our operators to unitary operators such that

$$C(t,\tau) = \mathrm{Tr}\big\{U^\dagger(t,0)AU(t,0)U^\dagger(t+\tau,0)BU(t+\tau,0)\rho\big\}. \tag{3.41}$$

Making use of the cyclic nature of the trace and the properties of the unitary operator ($U(t_1,t_2)U(t_2,t_3) = U(t_1,t_3)$ and $U^\dagger(t_1,t_2) = U(t_2,t_1)$) yields

$$\begin{aligned} C(t,\tau) &= \mathrm{Tr}\big\{AU^\dagger(t+\tau,t)BU(t+\tau,t)U(t,0)\rho U^\dagger(t,0)\big\} \\ &= \mathrm{Tr}_S\{BU(t+\tau,t)\rho(t)AU^\dagger(t+\tau,t)\}. \end{aligned} \tag{3.42}$$

Defining a new operator $\Lambda(t+\tau,t) = \mathrm{Tr}_E\{U(t+\tau,t)\rho(t)AU^\dagger(t+\tau,t)\}$, we see the two-time correlation function has a similar form to Eq. 2.11 and accordingly Λ follows a similar equation of motion to $\rho(t)$

$$\frac{\partial}{\partial\tau}\Lambda(t+\tau,t) = \mathscr{L}\Lambda(t+\tau,t). \tag{3.43}$$

The long time limit yields $C(\tau) = \lim_{t\to\infty} C(t,\tau) = \mathrm{Tr}_S\{B\tilde{\Lambda}(\tau)\}$ and therefore

$$\frac{\partial}{\partial\tau}\tilde{\Lambda}(\tau) = \mathscr{L}\tilde{\Lambda}(\tau). \tag{3.44}$$

Hence the two-time correlation function $C(t,\tau)$ can be solved using the master equation as Λ follows the same equations of motion as the density operator used in deriving the master equation. However, the QRT is only valid when the system of interest undergoes strictly Markovian evolution as it requires the complete system-environment density matrix to factorise at all times [71].

3.7.2 CW Driving: The Mollow Triplet

We can now solve Eq. 3.38 using the QRT and our Markovian quantum optical master equation to calculate the incoherent emission spectrum from a 2LS resonantly driven in the CW limit. In the weak-excitation regime ($\Omega \ll \gamma$) one would find this spectrum consists of a single peak centred at the 2LS transition frequency. In the limit of $\Omega \ll \gamma$ light is primarily coherently scattered from the 2LS, and thus the total spectrum is dominated by the single delta function of the coherent spectrum (not calculated here) at the resonance frequency, with an additional smaller and broader incoherent component also centred about this frequency. However, as the excitation strength is increased, Rabi oscillations between the two states of the 2LS begin to occur (see Figure 3.8a). These oscillations are also observed in the first-order correlation function with increasing excitation strength, as shown in Figure 3.8b, with the frequency of these oscillations increasing with the excitation strength.

Taking the Fourier transform of the first-order correlation function yields the emission spectrum. The oscillations in the first-order correlation function result in the emergence of two satellite peaks in the incoherent spectrum. These satellite peaks are separated from the single central peak seen at low excitation strengths by the Rabi frequency (see Figure 3.8c and Figure 3.8d), appearing at $\omega_0 \pm \Omega$. This is the well-known Mollow triplet or Mollow spectrum [72]. At first glance, the mechanism behind the Mollow triplet is not explicitly apparent. Using a classical dipole model one would only ever expect a single Lorentzian line in the emission spectrum regardless of the excitation strength. However, under strong excitation the eigenstates of the 2LS are not the eigenstates of the coupled emitter-drive system. As the semi-classical driving term in our Hamiltonian (Eq. 3.10) is periodic, we may use Floquet's theorem to find the eigenstates and eigenenergies of the coupled laser-2LS system from our semi-classical Hamiltonian [39, 73, 74]. This approach allows us to define a so-called Floquet Hamiltonian, recasting our time-dependent Hamiltonian into an infinite time-independent matrix that can be used in an eigenvalue problem [74]. In the case of zero or small detuning ($\omega_e \approx \omega_l$), it can be shown that this approach returns a series of energy levels with eigenenergies $\lambda_\pm = n\omega_e \pm \Omega/2$ where n in an integer (see Figure 3.8e). The Floquet eigenvectors are then $|\pm\rangle = \frac{1}{\sqrt{2}}\left(|g, n+1\rangle \pm |e, n\rangle\right)$ corresponding to the dressed states from the eigenvalue problem for Eq. 3.21 [75] combined with the Fourier index n. This gives rise to transitions with three unique frequencies. An equivalent picture can be derived by instead considering the drive as a quantised field.

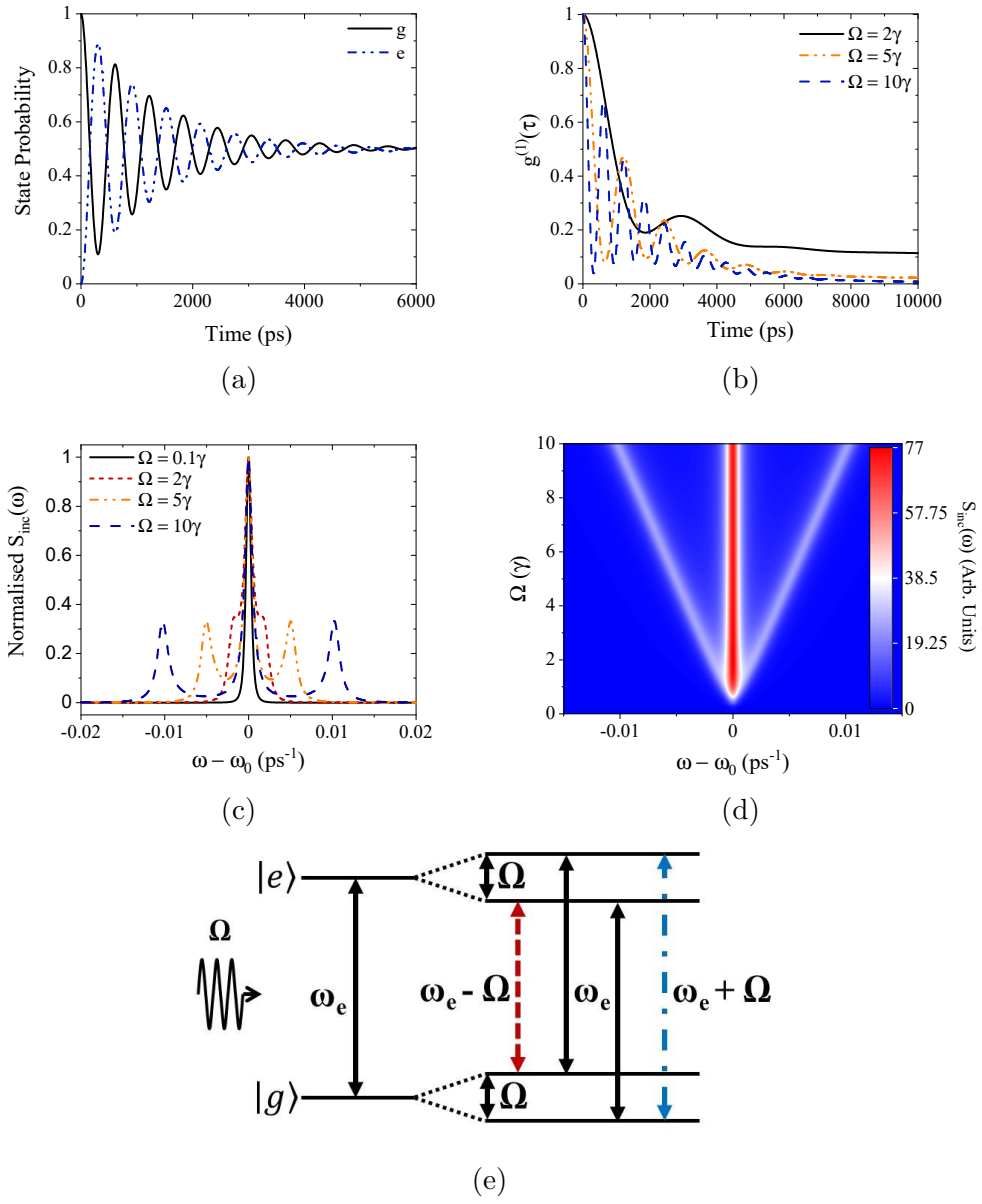

Figure 3.8: The dynamics of the (a) state populations and (b) first-order correlation function of a Two-Level System (2LS) driven by a Continuous-Wave (CW) laser with (a) Rabi frequency $\Omega = 10\gamma$ and (b) three different Rabi frequencies Ω. (c) The normalised incoherent resonance fluorescence spectrum resulting from CW driving of a 2LS for four different Rabi frequencies. (d) A contour plot of the incoherent Mollow spectrum as a function of the Rabi frequency. (e) A depiction of the dressed states picture of the Mollow triplet. The solid black double arrows indicate the transitions at the original frequency ω_e. The dashed orange and dash-dot blue double arrows indicate the transitions with frequencies $\omega_e - \Omega$ and $\omega_e + \Omega$ respectively. Parameters used: $\gamma^{-1} = 971$ ps.

3.7.3 Pulsed Emission Spectrum

Under pulsed excitation the emission spectrum gains a time-dependence and thus has a more complex form given by [76]

$$S(\omega,t,\Upsilon) = 2\Upsilon\,\mathrm{Re}\Big\{\int_0^t dt_2 \exp\big\{\big(-\Upsilon(t-t_2)\big)\big\} \int_0^{t-t_2} d\tau \exp\Big\{\Big(\frac{\Upsilon}{2} - i(\omega-\omega_l)\tau\Big)\Big\}\langle\sigma^\dagger(t_2+\tau)\sigma(t_2)\rangle\Big\}, \quad (3.45)$$

where Υ is the detection bandwidth included to account for time-energy uncertainty [77]. Taking the limit $t \gg t_0 + \Delta\tau$ recovers the time-independent integrated spectrum. Just as in the CW case one must still solve the first-order correlation function using the QRT to calculate the pulsed emission spectrum.

Figure 3.9 shows the resulting TIS and TDS when driving a 2LS with a Gaussian pulse. Driving the system with a single pulse area $\Theta = 7\pi$ reveals the pulsed integrated emission spectrum contains additional Mollow peaks relative to the three peaks found in the Mollow spectrum in the CW limit (see Figure 3.9a). Furthermore, calculating the power dependence of the pulsed TIS by varying Θ reveals the number of Mollow peaks in the pulse spectrum is proportional to the area of the driving pulse as shown in Figure 3.9b. The mechanism behind this is uncovered by the TDS. Figure 3.9c shows the satellite peaks in the TIS evolve from the central spectral peak, with the outer-most Mollow peaks being the first satellite peaks to materialise in the incoherent spectrum. This behaviour is the result of interference between the temporal components of the pulse with corresponding Rabi frequency, i.e. where $\Omega(t_2) = \Omega(t_1 < t_2)$ [78]. The components that constructively interfere produce a Mollow peak in the emission spectrum, while components that destructively interfere have a reduced, or zero, contribution to the spectrum. The effect of coupling to a bath of quantum harmonic oscillators on the dynamics, and TDS and TIS of a 2LS driven by a Gaussian pulse is discussed in Chapters 4 and 5.

3.8 Photon Antibunching: Second-Order Correlation Function

Another important property of the emitted light to consider is the statistical nature of the photons being emitted by the 2LS. When driving the 2LS with

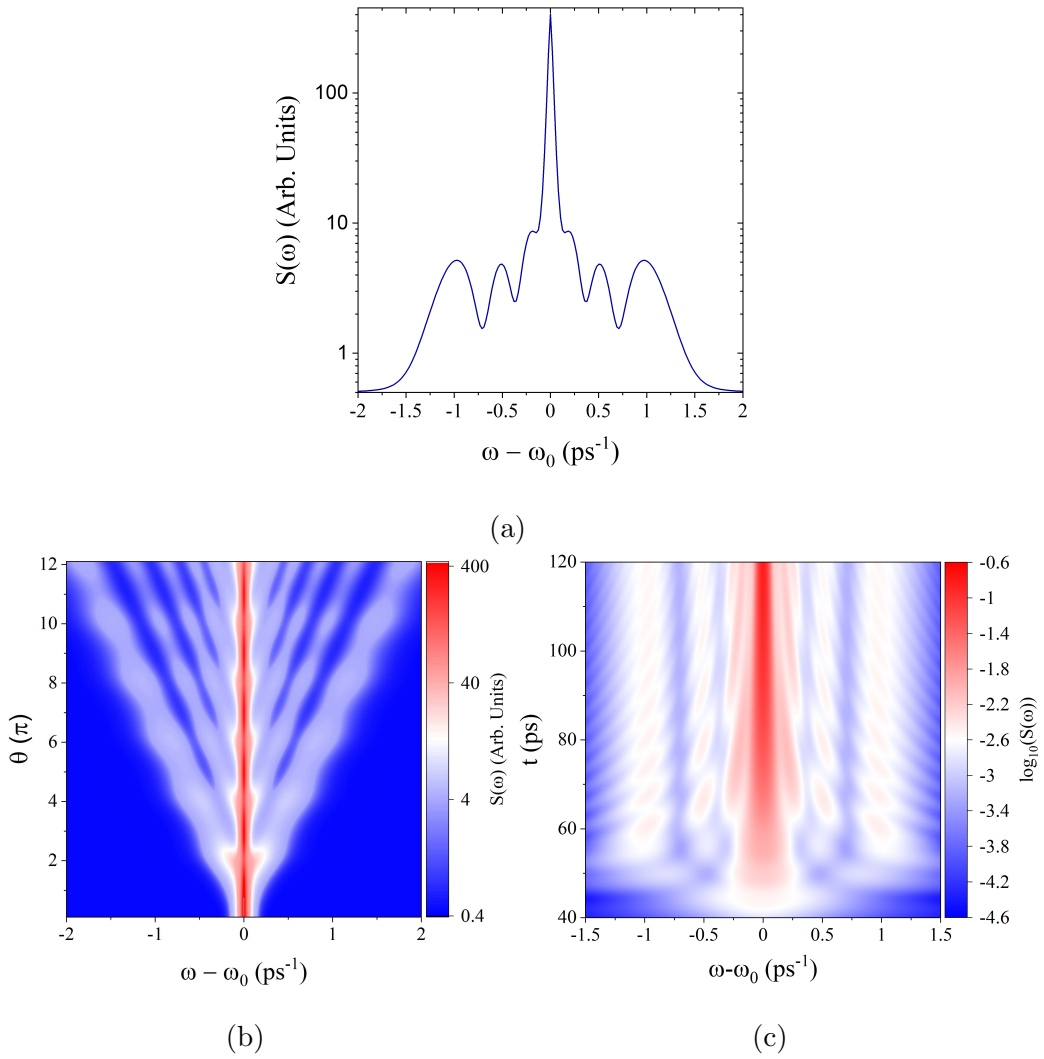

Figure 3.9: (a,b) The Time-Integrated Spectra (TIS) produced when driving a Two-Level System (2LS) with a Gaussian pulse (a) with a single pulse area and width, and (b) sweeping the pulse area for a fixed pulse width. (c) The Time-Dependent Spectra (TDS) produced when driving a 2LS with a Gaussian pulse. Parameters used: (a, c) $\Theta = 7\pi$, (a,b,c) $\Delta\tau = 12$ ps, $\gamma^{-1} = 23$ ps.

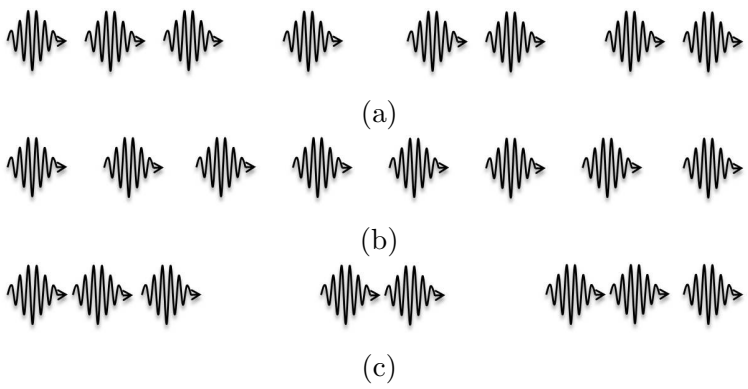

Figure 3.10: An illustration of the emission of photons for different sources. (a) Coherent emission of photons at random time intervals e.g. laser. Coherent light is quantified by $g^{(2)}(\tau) = 1$ for all values of τ (b) Anti-bunched emission of photons. Photons are emitted at regular time intervals quantified by $g^{(2)}(0) < 1$. If the emitter is a single photon source $g^{(2)}(0) = 0$. (c) Bunched emission of photons where photons are emitted in groups or bunches e.g. thermal light. Bunched emission is identified by $g^{(2)}(0) > 1$ and $g^{(2)}(0) > g^{(2)}(\tau \to \infty)$. Adapted from [11].

a CW source, the normalised second-order correlation function is given by

$$g^{(2)}(\tau) = \lim_{t\to\infty} \frac{G^{(2)}(t,\tau)}{|\langle\sigma^\dagger\sigma\rangle|^2}, \tag{3.46}$$

where

$$G^{(2)}(t,\tau) = \langle\sigma^\dagger(t)\sigma^\dagger(t+\tau)\sigma(t+\tau)\sigma(t)\rangle, \tag{3.47}$$

is the un-normalised second-order correlation function that may also be calculated using the QRT. This correlation function quantifies the temporal coherence of intensity fluctuations in a beam of light. Since the intensity of a beam of light is proportional to the number of constituent photons, $G^{(2)}(t,\tau)$ indicates the probability of detecting photons at time $t+\tau$ after a detection event at time t.

Light can be broadly separated into three categories, depicted in Figure 3.10, based on the value of the integrated second-order correlation function at $\tau = 0$, $g^{(2)}(0)$. When $g^{(2)}(0) = 1$ the emitted light is said to be coherent, indicating that single photons are being emitted at random time intervals as shown in Figure 3.10a. If $g^{(2)}(0) < 1$ photons are being emitted from the source at regular intervals (see Figure 3.10b). In this case the light is said to be anti-bunched. When $g^{(2)}(0) < 0.5$ the emitted photon number per given time window is unlikely to be larger than $n = 1$ indicating the emitter is a single-photon emitter. Finally, when $g^{(2)}(0) > 1$ the emitted light is said to

be bunched as in this case photons are more likely to be emitted as groups or bunches than as single photons as shown in Figure 3.10c.

Experimentally, the second-order correlation function is determined by performing a Hanbury-Brown Twiss measurement. A schematic of the experimental set-up is shown in Figure 3.11a. A perfect experiment measuring the second-order correlation function of a perfect single-photon source would find $g^{(2)}(0) = 0$ as shown in Figure 3.11b [10]. A value of $g^{(2)}(0) = 0$ is indicative of a single-photon source as this shows that there is a zero probability of simultaneously detecting two photons from the same source. When driving a 2LS with a small Rabi frequency (and/or spontaneous emission rate) the resulting second-order correlation function appears as a single, broad dip centred around $\tau = 0$ whose width is determined by T_1. The small Rabi frequency results in a slow emission rate from the 2LS, and thus a long delay between successive photons, broadening the $g^{(2)}(\tau)$ dip. Increasing the Rabi frequency (or spontaneous emission rate) increases the rate of photon emission from the 2LS, reducing this delay and resulting in a narrower dip around $\tau = 0$. Larger Rabi frequencies also result in the appearance of Rabi oscillations in the second-order correlation function as shown in Figure 3.11b.

3.9 Pure Dephasing

So far in our examination of a classically driven 2LS, we have assumed the stochastic decay of the excited state population via spontaneous emission is the only dephasing mechanism experienced by the 2LS. However, it is also possible for quantum systems to undergo elastic interactions that do not alter the state populations, but still break the phase of the individual states. Such dephasing mechanisms are referred to as pure dephasing mechanisms to distinguish them from the inelastic dephasing caused by population decay. Pure dephasing can be caused by a number of different physical mechanisms depending on the exact details of the quantum system in question, for example charge fluctuations [79], or phonon-induced dephasing of the Zero Phonon Line (ZPL) [80]. However, all pure dephasing processes can be characterised by a pure dephasing rate Γ and pure dephasing time $T_2^* = \Gamma^{-1}$. From this we can define the total

[10] In reality the detectors used in experiments will have some finite time resolution and thus the measured second-order correlation function will be $g^{(2)}(\tau)$ convolved with the instrument response function.

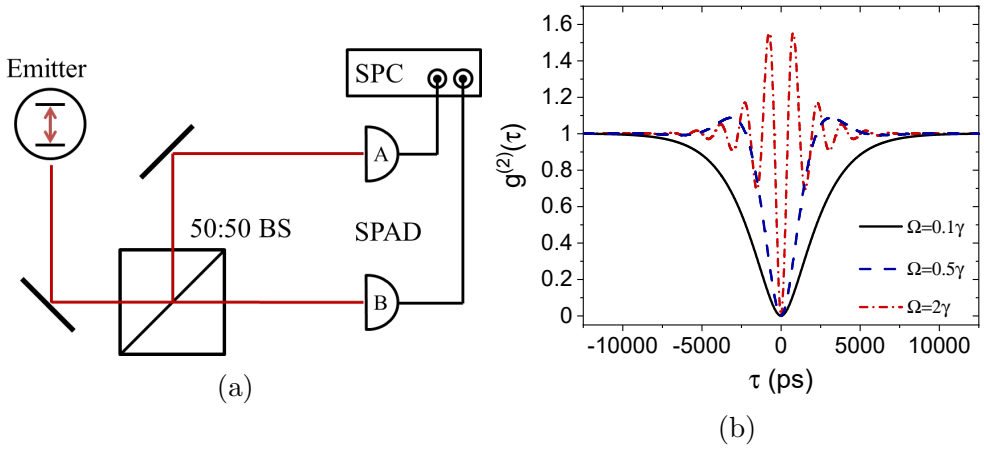

Figure 3.11: (a) A schematic of a typical Hanbury-Brown Twiss (HBT) experiment used to measure the second-order coherence of light. Light from an emitter is directed onto a 50:50 Beam Splitter (BS). Two Single-Photon Avalanche Diodes (SPADs) located at the outputs of the BS detect photons from the emitter with a time delay between the two BS output paths. A Single Photon Counting (SPC) module counts the photon detection events. (b) An example of the second-order correlation function (calculated using the Lindblad master equation and quantum regression theorem) of light emitted by a 2LS resonantly driven by a Continuous-Wave (CW) laser at different powers.

dephasing rate experienced by the quantum system as [11]

$$\frac{1}{T_2} = \frac{1}{2T_1} + \frac{1}{T_2^*}, \tag{3.48}$$

where T_2 is the total dephasing time, and T_1 is the excited state lifetime. To study the effects of pure dephasing on the light emitted by a 2LS we can include an additional Lindblad operator, $L = \sqrt{\Gamma}\sigma^\dagger\sigma$, in the quantum optical master equation in Eq. 3.28. Figure 3.12 shows the effects of pure dephasing on the population dynamics, emission spectra, and second-order correlation function for a number of different pure dephasing rates under CW driving. We shall not consider the effects of pure dephasing under pulsed resonant excitation here as this is addressed in Chapter 4. Comparing Figures 3.12a and 3.12b, it can be seen that the addition of pure dephasing further dampens the Rabi oscillations between the states of the 2LS. In the coherent emission spectrum the effects of pure dephasing can be seen as a broadening of the three Mollow peaks (Figure 3.12c). As pure dephasing does not affect the emission rate of the system, the dip in the second-order correlation function is not broadened, although a suppression of the Rabi oscillations can be seen with increasing pure dephasing rates as shown in Figure 3.12d.

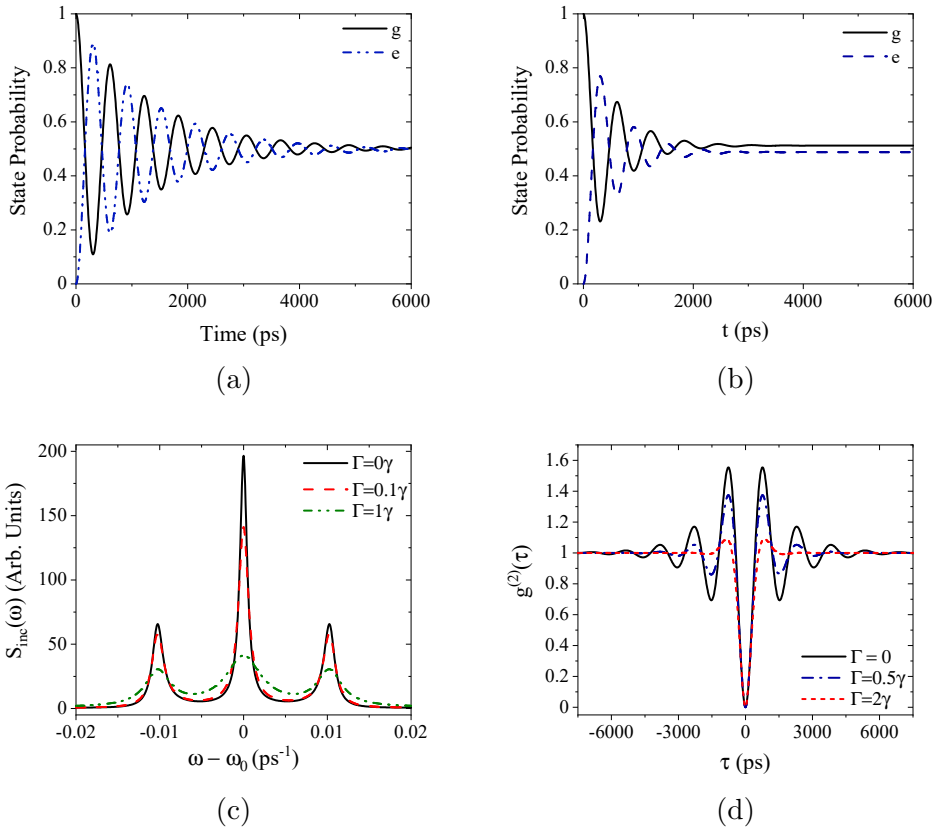

Figure 3.12: Top: The effects of pure dephasing on the population dynamics of a Two-Level System (2LS) driven with a Rabi frequency $\Omega = 10\gamma$ for pure dephasing rates (a) $\Gamma = 0$ and, (b) $\Gamma = \gamma$ calculated using the Lindbald master equation. Bottom: The effects of pure dephasing on the emission properties, namely (c) the incoherent emission spectrum and (d) the second-order correlation function $g^{(2)}(\tau)$, of a 2LS driven with a Rabi frequency $\Omega = 2\gamma$. Parameters used: $\gamma^{-1} = 971$ ps.

3.10 Cavity Quantum Electrodynamics

Now that we have studied the properties of a single 2LS we can add an additional layer of complexity. Thus far in applying our mathematical constructs to physical systems we have discussed only the example of solitary 2LS in free-space. However, it is both possible and frequently useful to modify the optical environment around the 2LS by employing an optical cavity. Indeed the work discussed in later chapters focuses on quantum systems coupled to optical cavities. Therefore we shall now briefly discuss the topic of Cavity Quantum Electrodynamics (cQED), taking the example of a 2LS coupled to an optical cavity with a single quantised bosonic mode, and driven by a classical CW field.

To include the full effects of an optical cavity, we need to make an addition to our 2LS Hamiltonian. We shall now split the lab-frame Hamiltonian into four components such that $H = H_0 + H_I + H_D^{2LS} + H_D^{Cav}$. Here H_0 is given by

$$H_0 = \omega_e \sigma^\dagger \sigma + \omega_c a^\dagger a, \tag{3.49}$$

where ω_e is the frequency of the optical transition of the 2LS as before, ω_c is the frequency of the cavity mode, and $a^\dagger$ and a are the bosonic cavity creation and annihilation operators respectively. The 2LS and cavity couple via a dipole interaction, and therefore one can write the interaction term H_I as

$$H_I = g\big(\sigma + \sigma^\dagger\big)\big(a^\dagger + a\big). \tag{3.50}$$

Here g quantifies the strength of the interaction between the 2LS and cavity. With a cavity coupled 2LS it is possible to drive either the 2LS or cavity separately or simultaneously. Therefore we can further split the driving Hamiltonian into two terms, one for driving the 2LS and one for driving the cavity given by Eq. 3.51 and Eq. 3.52 respectively.

$$H_D^{2LS} = \frac{\Omega}{2}\big(e^{i\omega_l t} + e^{-i\omega_l t}\big)\big(\sigma + \sigma^\dagger\big). \tag{3.51}$$

$$H_D^{Cav} = \frac{\epsilon}{2}\big(e^{i\omega_l t} + e^{-i\omega_l t}\big)\big(a^\dagger + a\big). \tag{3.52}$$

Here Ω is the Rabi frequency as previously defined, and ϵ quantifies the coupling strength between the driving field and cavity mode.

To account for incoherent emission from the cavity mode through the cavity mirrors we require an additional Lindblad operator. This brings the full list

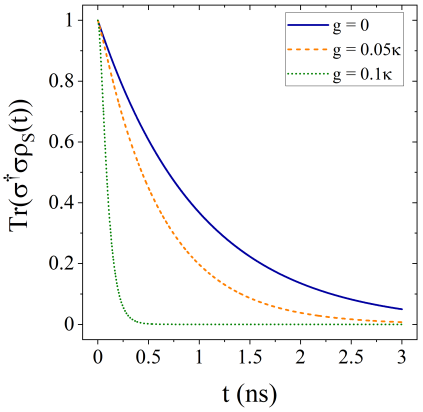

Figure 3.13: The decay of the excited state of a Two-Level System (2LS) weakly coupled on resonance to a single-mode cavity for three different cavity coupling strengths, g. Increasing g increases the rate at which the excited state population decays. Parameters: $\kappa/2\pi = 10$ GHz, and $\gamma^{-1} = 1$ ns.

of Lindblad operators for this total system (not including pure dephasing) to

$$L \in \{\sqrt{\gamma}\sigma, \sqrt{\kappa}a\}, \tag{3.53}$$

where κ is the loss rate from the cavity mode, and γ is again given by the inverse of the excited state lifetime.

3.10.1 Weak-Coupling

There are two coupling regimes relevant to the work done for this thesis. The first is the weak coupling regime where the incoherent decay processes included in the Lindblad collapse operators dominate. Hence this regime is characterised by $g \ll \gamma, \kappa$. In the weak coupling regime the spontaneous emission rate, γ, is enhanced by the Purcell factor [81–83]

$$F_P = \frac{4g^2}{\kappa\gamma} \frac{\kappa^2}{4(\omega_e - \omega_c)^2 + \kappa^2} \frac{|\boldsymbol{\mu} \cdot \boldsymbol{E}(\boldsymbol{r}_0)|^2}{|\boldsymbol{\mu}|^2 |\boldsymbol{E}_{max}|^2}, \tag{3.54}$$

where on the right the central term accounts for detuning between the cavity mode and emitter, and the final term accounts for the spatial overlap between the cavity field $\boldsymbol{E}(\boldsymbol{r})$ and the emitter dipole $\boldsymbol{\mu}$. With $\omega_e = \omega_c$ and perfect dipole positioning and orientation, the Purcell factor is related to the cavity cooperativity C, i.e. the ratio of coupling to loss, by $F_P = 2C$ [82]. The effects of weak cavity-coupling can be clearly seen in Figure 3.13. Initialising a cavity-coupled 2LS in its excited state, it can be seen that increasing the coupling strength g, and thus also the Purcell factor F_P, increases the rate at

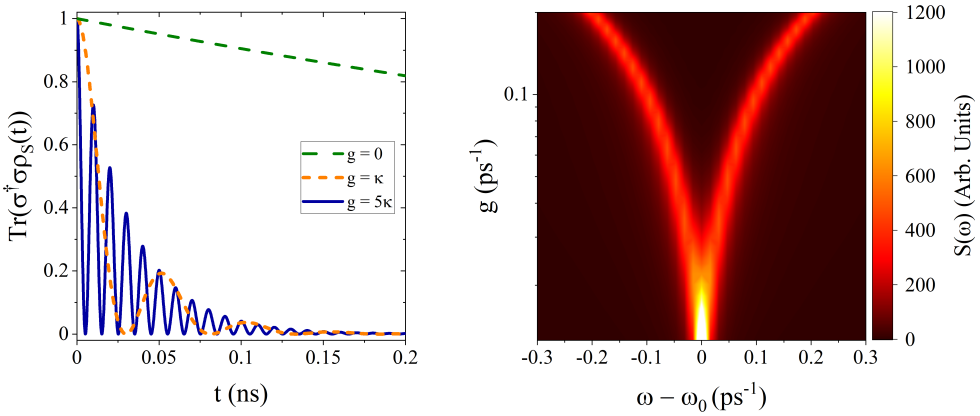

(a) (b)

Figure 3.14: (a) Vacuum Rabi oscillations in the excited state population of a Two-Level System (2LS) strongly coupled to a resonant single-mode cavity. (b)The spectrum of a 2LS coupled to a single-mode cavity as a function of the cavity-2LS coupling strength, g, calculated using the quantum regression theorem. As the 2LS-cavity system moves into the strong coupling regime the spectrum splits into two polaritonic peaks separated by $\Omega_R = 2g$. Parameters used: (a) $\gamma^{-1} = 1$ ns, $\kappa/2\pi = 10$ GHz. (b) $\kappa = 0.063$ ps^{-1}, $\gamma^{-1} = 971$ ps.

which the excited state population decays by F_P.

3.10.2 Strong-Coupling

The second relevant coupling regime is the strong-coupling regime. Here the coherent cavity-2LS coupling dominates indicated by $g \gg \gamma, \kappa$.

Vacuum Rabi Splitting

The strong coupling regime is characterised by the appearance of vacuum Rabi oscillations [84], damped by losses from the cavity, as can be seen in Figure 3.14a. When the 2LS is initialised in the excited state, it cyclically emits photons into, and then re-absorbs photons from, the cavity mode. This results in the formation of polaritons, quasi-particles formed by strongly interacting light and matter. In the case of a 2LS strongly coupled to a single-mode cavity, the ensuing emission spectrum consists of two peaks, corresponding to the polariton states, separated by $\Omega_R = 2g$ [85] (see Figure 3.14b).

Similarly one may also calculate the emission spectrum of the cavity mode from the cavity raising and lowering operators. Following the definition in Eq. 3.38, we can define the first-order coherence of the cavity mode as

$$G_a^{(1)}(t,\tau) = \langle a^\dagger(t) a(t+\tau) \rangle, \tag{3.55}$$

from which the cavity spectrum may be calculated using Eq. 3.37. In this case the cavity and 2LS spectra are (near) identical, and thus only the latter is plotted.

3.11 Summary

In this chapter we have discussed the electronic and optical properties of QDs. Approximating the QD as a 2LS, we have studied the effects of different optical driving regimes on the emission properties of the 2LS. Under strong CW driving we have seen the states of the 2LS become dressed by the interaction with the electromagnetic environment resulting in coherent oscillations between the undressed states, and the emergence satellite peaks in the emission spectrum forming the Mollow triplet. We have also seen the impact of pure dephasing mechanisms under CW driving. Furthermore, under pulsed excitation we have shown additional Mollow satellite peaks are present in the emission spectrum for large pulse areas. Lastly, we have seen how coupling a QD to an optical cavity with a single bosonic mode impacts the system dynamics.

In Chapter 4 we shall extend the 2LS model presented here under pulsed optical excitation to study the effects of coupling to a thermal bath on the time-dependent and time-integrated emission spectra. Chapter 5 then extends this work to present a formalism describing the dynamics of a QD that is valid across wide range of parameter regimes. In Chapter 6 we shall utilise concepts in cQED introduced here to optimise the control of quantum systems using optical pulses.

Chapter 4

Pulsed Resonance Fluorescence from Phonon-Coupled Quantum Dots

4.1 Introduction

In Chapter 3 we briefly discussed some of the properties of semiconductor QDs. The fully quantised, atomic-like, nature of their energy level structure, along with the potential for integration in on-chip semiconductor structures [86] makes QDs exciting candidates for the development of scalable quantum technologies. As such there has been a huge effort to study the optical properties of these structures. To date a number of important phenomena have been experimentally demonstrated using QDs including Mollow triplet spectra [87–90], photon anti-bunching [91–93], and Rabi oscillations [63–67, 84, 94], all of which were discussed in Chapter 3. The experimental observation of these atomic-like properties has demonstrated the potential suitability of QDs for use in quantum technologies. However, despite this, the solid-state nature of QDs provides a fundamental distinction from purely atomic quantum systems. Namely, the strong interaction between the solid-state QD and the quantised lattice vibrations (phonons) of the host semiconductor material introduces decoherence mechanisms that are not experienced in purely atomic systems. While these interactions provide the potential to study system-environment interactions in the solid-state, they must also be mitigated for applications in quantum technologies, making a meaningful understanding of QD-phonon interactions invaluable.

A number of studies (both theoretical and experimental) have already investigated the consequences of this strong coupling between a QD and its environment. For example, an asymmetry in the absorption/emission spectrum of QDs, referred to as the phonon sideband, has been predicted and demonstrated to result from this phonon-coupling [95, 96], persisting regardless of the excitation regime [97–99]. Additionally, the continuation of these phonon effects across different driving conditions has also been experimentally demonstrated to impact the fraction of coherent to incoherent emission from QDs, deviating from the predictions of atomic physics [97–99]. Furthermore, while phonon-coupling has been predicted and demonstrated to lead to a decay of the coherent Rabi oscillations in the system populations when driven with a coherent optical field [100–103], it has been predicted that in the strong driving regime a revival of the coherent scattering processes should occur [104, 105].

Pulsed optical excitation is key to a number of processes useful for the realisation of optical quantum technologies, such as the manipulation of QD spin states as discussed in Chapter 6. A number of studies have moved beyond the CW excitation regime to consider the impact of coupling to Longitudinal Acoustic (LA) phonons on the pulsed excitation dynamics of a QD [106, 107]. Indeed in the limit of ultra-short pulses (i.e.$\Omega(t) = \delta(t)$) exact analytical solutions have been found [108–110]. However, as we are interested in studying the effects of phonon coupling on the emission spectra of a QD coherently driven by resonant excitation pulses of a finite duration, we shall instead use a polaron model approach following the work presented in [106].

4.2 The Polaron Model

While it may be tempting to model the dephasing effects resulting from the QD-phonon coupling using a simple pure dephasing model, such as that discussed in Chapter 3, it has been shown that this approach is inadequate for capturing the full consequences of the QD-phonon coupling [97]. Hence we shall now derive the so-called *polaron model* to describe these interactions, following the work presented in [106]. The result will be an approximate master equation that treats the QD-phonon interaction as a perturbation, and remains valid outside of the weak exciton-phonon coupling regime. We shall then use this master equation to study the effect of the QD-phonon coupling on the pulsed emission spectra, both time-dependent and time-integrated, later in this chapter.

4.2.1 The Polaron Transformed Exciton-Phonon Hamiltonian

To model the effects of exciton-phonon coupling on the optical properties of a QD, we can consider the case of a 2LS linearly coupled to a bath of quantum harmonic oscillators [80, 111–114] neglecting any virtual transitions occurring between states within the phonon-dressed excited state manifold [80, 113, 114]. Here we again define the ground state ($|0\rangle$) of the QD (i.e. the empty QD state) as having zero energy, while the excited exciton state ($|X\rangle$) of the QD has energy $\hbar\omega_X$. We may then describe the modes of the phonon bath in our model with an infinite series of bosonic creation (annihilation) operators $b_k^\dagger$ (b_k). Lastly we shall also assign an explicit time-dependence to the Rabi frequency in the driving term of the Hamiltonian as we are primarily interested in pulsed optical driving. In the laboratory frame of reference, the Hamiltonian describing the coherent dynamics of this total system is given by [106]

$$H(t) = \omega_X |X\rangle\langle X| + \Omega(t)\cos(\omega_l t)\big(|X\rangle\langle 0| + |0\rangle\langle X|\big) + |X\rangle\langle X| \sum_k g_k(b_k^\dagger + b_k) + \sum_k \omega_k b_k^\dagger b_k. \quad (4.1)$$

Here $\Omega(t)$ is the Rabi frequency characterising the laser-QD coupling strength modulated by a time-dependent envelope function, ω_l is the central laser frequency, and g_k characterises the coupling between the bath modes with frequency ω_k and the QD. Following the procedure used in Section 3.4.1, we shall now apply a unitary transformation to the laboratory frame Hamiltonian, and also make use of the RWA, to remove the time-dependent exponential factors originating from the coherent driving term. This transformation yields the RWA Hamiltonian in a reference frame rotating at the laser frequency

$$H_R(t) = (\omega_X - \omega_l)|X\rangle\langle X| + \frac{\Omega(t)}{2}(|X\rangle\langle 0| + |0\rangle\langle X|) + |X\rangle\langle X| \sum_k g_k(b_k^\dagger + b_k) + \sum_k \omega_k b_k^\dagger b_k. \quad (4.2)$$

To fully capture the impact of the phonon coupling on the QD we shall now perform a second unitary transformation to move to the polaron frame [106]. This unitary polaron transformation displaces the phonon bath when the QD is in the excited state $|X\rangle$ as depicted in Figure 4.1. Furthermore, performing this transformation also moves us to a basis that will allow us to to derive a

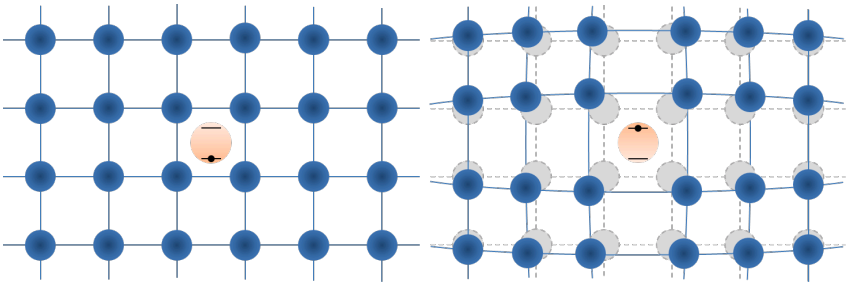

(a) (b)

Figure 4.1: The displacement of a crystal lattice when a Quantum Dot (QD) is excited from the ground (a) to the excited state (b). Figure adapted from [115].

master equation that is non-perturbative in the system-environment coupling strength, and thus is valid even when this coupling strength is large [106]. The polaron-transformed Hamiltonian is given by $H_P(t) = U_{pol} H_R(t) U_{pol}^\dagger$, where

$$U_{pol} = \exp\left\{ \left(|X\rangle\langle X| \sum_k \alpha_k (b_k^\dagger - b_k) \right) \right\} = |0\rangle\langle 0| + |X\rangle\langle X| \prod_k D(\alpha_k). \quad (4.3)$$

Here $\prod_k D(\alpha_k)$ is the product of displacement operators $D(\alpha_k)$ that act on the phonon creation and annihilation operators of the k^{th} bath mode such that

$$D^\dagger(\alpha_k) b_k D(\alpha_k) = (b_k + \alpha_k) \text{ and } D(\alpha_k) b_k D^\dagger(\alpha_k) = (b_k - \alpha_k). \quad (4.4)$$

Applying this transformation to Eq. 4.2, and defining $\sigma_x = \sigma^\dagger + \sigma$ and $\sigma_y = i(\sigma - \sigma^\dagger)$ where $\sigma = |0\rangle\langle X|$, yields the polaron Hamiltonian

$$H_P(t) = \delta_r \sigma^\dagger \sigma + \frac{\Omega_r(t)}{2} \sigma_x + \frac{\Omega(t)}{2} \left(\sigma_x B_x + \sigma_y B_y \right) + \sum_k \omega_k b_k^\dagger b_k + \sigma^\dagger \sigma B_z. \quad (4.5)$$

From this polaron Hamiltonian we can already begin to understand some of the effects resulting from the QD-phonon coupling. Eq. 4.5 shows the coupling to the bath modes gives rise to a time-independent renormalisation of both the Rabi frequency ($\Omega_r(t) = \Omega(t) B$) and QD-laser detuning ($\delta_r = \omega_X - \omega_l - \sum_k \alpha_k (2g_k - \omega_k \alpha_k)$). In Eq. 4.5 we have also defined three bath operators to describe bath-induced fluctuations

$$\begin{aligned} B_x &= \frac{1}{2} \left(B_+ + B_- - 2B \right), \\ B_y &= \frac{1}{2i} \left(B_- - B_+ \right), \\ B_z &= \sum_k (g_k - \omega_k \alpha_k)(b_k^\dagger + b_k). \end{aligned} \quad (4.6)$$

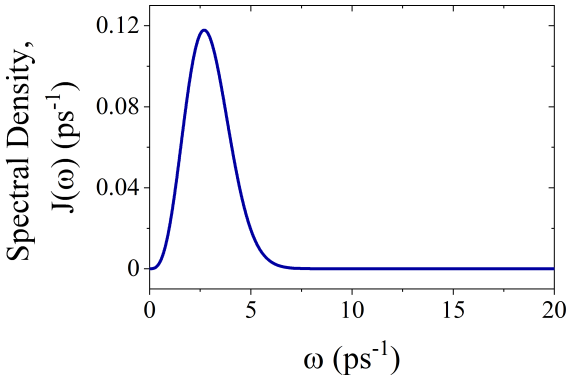

Figure 4.2: The super-Ohmic spectral density function characterising the coupling between the excitonic state of a Quantum Dot (QD) and Longitudinal Acoustic (LA) phonons. Parameters: $\omega_c = 2.2$ ps^{-1}, and $\alpha = 0.027$ ps^2.

In this instance $B = \langle B_\pm \rangle = \exp\{-(1/2)\sum_k |\alpha_k|^2 \coth(\beta\omega_k/2)\}$ is the average displacement of the phonon bath relative to a thermal state, $B_+ = \prod_k D(\alpha_k)$, and $B_- = \prod_k D^\dagger(\alpha_k) = \prod_k D(-\alpha_k)$.

From here we may further simplify the polaron Hamiltonian by setting $\alpha_k = g_k/\omega_k$ [106], which encapsulates the physical displacement of the phonon modes in this model. This also removes the linear coupling term leaving the final form of the polaron transformed Hamiltonian as

$$H_P(t) = \delta_r \sigma^\dagger \sigma + \frac{\Omega_r(t)}{2}\sigma_x + \frac{\Omega(t)}{2}\big(\sigma_x B_x + \sigma_y B_y\big) + \sum_k \omega_k b_k^\dagger b_k. \tag{4.7}$$

In this case the phonon-shifted detuning reduces to $\delta_r = \big(\delta - \sum_k \omega_k \alpha_k^2\big)$ where $\delta = \omega_X - \omega_l$ is the detuning in the absence of any phonon effects.

The coupling between a QD and bulk phonons is completely characterised by a spectral density function. In the case of coupling to bulk LA-phonons, which has been demonstrated to be the dominant phonon coupling component in QDs [116], the spectral density has the phenomenological form [116, 117]

$$J(\omega) = \alpha\omega^3 e^{-(\omega/\omega_c)^2}, \tag{4.8}$$

where α is the coupling constant defining the strength of the bath-system interaction, and ω_c is the phonon cut-off frequency that determines the peak in the spectral density. An example of the spectral density function is plotted in Figure 4.2[1]. Using this spectral density we can redefine the average

[1]The spectral density plotted here is referred to as super-Ohmic as it has the form $J(\omega) \propto \omega^k$ where $k > 1$. Ohmic and sub-Ohmic spectral densities have $k = 1$ and $k < 1$ respectively.

displacement of the phonon bath in the continuum limit as

$$B = \exp\Big\{-\frac{1}{2}\int_0^\infty d\omega \frac{J(\omega)}{\omega^2}\coth\left(\beta\omega/2\right)\Big\}, \tag{4.9}$$

where $\beta = (1/k_B T)$ is the thermodynamic beta factor given by the inverse of the product of the Boltzmann constant (k_B) and temperature (T).

4.2.2 Non-Markovian Polaron Master Equation

From the polaron-transformed Hamiltonian we can now derive a master equation describing the complete dynamics of a driven QD coupled to a phonon bath. The first step in this derivation is to separate the total polaron-transformed Hamiltonian into three components

$$\begin{aligned} H_{P,S}(t) &= \delta_r \sigma^\dagger\sigma + \frac{\Omega_r(t)}{2}\sigma_x \\ &\equiv \frac{\delta_r}{2}\sigma_z + \frac{\delta_r}{2}\mathbf{I} + \frac{\Omega_r(t)}{2}\sigma_x, \\ H_{P,I}(t) &= \frac{\Omega(t)}{2}(\sigma_x B_x + \sigma_y B_y), \\ H_{P,B} &= \sum_k \omega_k b_k^\dagger b_k, \end{aligned} \tag{4.10}$$

describing the QD and driving, the QD-bath interaction (that shall be treated as a perturbation), and the phonon bath respectively. From here we may move into the interaction picture with respect to $H_{P,0} = H_{P,S} + H_{P,B}$ which then allows us to write an interaction picture Hamiltonian in the polaron-transformed interaction picture such that

$$\tilde{H}_{P,I}(t) = U_{P,0}^\dagger(t) H_{P,I}(t) U_{P,0}(t) = U_{P,S}^\dagger(t) e^{iH_{P,B}t} H_{P,I} U_{P,S}(t) e^{-iH_{P,B}t}, \tag{4.11}$$

where $U_{P,S} = \boldsymbol{\mathcal{T}} \exp\Big\{-i\int_0^t d\nu H_{P,S}(\nu)\Big\}$. In this polaron-transformed interaction picture the interaction Hamiltonian can be written as

$$\tilde{H}_{P,I}(t) = \frac{\Omega(t)}{2}\big(\tilde{\sigma}_x(t)\tilde{B}_x(t) + \tilde{\sigma}_y(t)\tilde{B}_y(t)\big). \tag{4.12}$$

Here $\tilde{\sigma}_{x(y)}(t) = U_{P,S}^\dagger(t)\sigma_{x(y)}U_{P,S}(t)$ and $\tilde{B}_{x(y)}(t) = e^{iH_{P,B}t}B_{x(y)}e^{-iH_{P,B}t}$. From here we can substitute this interaction Hamiltonian into the Born-Markov master equation that we derived in Chapter 2 (Eq. 2.32). Making this substitution

yields

$$\frac{\partial}{\partial t}\tilde{\rho}_S(t) = -\frac{\Omega(t)}{4}\int_0^t dt'\Omega(t')\sum_{i=x,y}\Big(\big[\tilde{\sigma}_i(t),\tilde{\sigma}_i(t')\tilde{\rho}_S(t)\big]\Lambda_{ii}(t,t') - \big[\tilde{\sigma}_i(t),\tilde{\rho}_S(t)\tilde{\sigma}_i(t')\big]\Lambda^\dagger_{ii}(t,t')\Big), \quad (4.13)$$

where $\Lambda_{ij}(t,t') = \langle\tilde{B}(t)\tilde{B}(t')\rangle = \langle\tilde{B}_i(\tau)\tilde{B}_j(0)\rangle = \mathrm{Tr}_B\big(\tilde{B}_i(\tau)\tilde{B}_j(0)\rho_B\big)$ for $i = j$ and $\Lambda_{i,j\neq i} = 0$ with $i,j \in \{x,y\}$, $\Lambda^\dagger(\tau) = \Lambda(-\tau)$, and we have defined $\tau = t - t'$. Using the LA-phonon spectral density, $J(\omega)$, the polaron bath correlation functions may be written in the continuum limit as

$$\begin{aligned}\Lambda_{xx}(\tau) &= \frac{B^2}{2}\Big(e^{\phi(\tau)} + e^{-\phi(\tau)} - 2\Big),\\ \Lambda_{yy}(\tau) &= \frac{B^2}{2}\Big(e^{\phi(\tau)} - e^{-\phi(\tau)}\Big),\end{aligned} \quad (4.14)$$

where the phonon propagator is given by

$$\phi(\tau) = \int_0^\infty \frac{J(\omega)}{\omega^2}\Big(\cos(\omega\tau)\coth\Big(\frac{\beta\omega}{2}\Big) - i\sin(\omega\tau)\Big)d\omega. \quad (4.15)$$

A full derivation of the polaron bath correlation functions and average displacement of the bath can be found in Appendix B. Transforming back to the Schrödinger picture, the polaron master equation is given by

$$\begin{aligned}\frac{\partial}{\partial t}\rho_S(t) =& -i\big[\delta_r\sigma^\dagger\sigma + \frac{\Omega_r(t)}{2}\sigma_x,\rho_S(t)\big]\\ &- \frac{\Omega(t)}{4}\sum_{i=x,y}\Big([\sigma_i,\chi_i(\tau)\rho_S(t)] - [\sigma_i,\rho_S(t)\chi_i^\dagger(\tau)]\Big),\end{aligned} \quad (4.16)$$

where we have now defined the system rate operators as

$$\chi_{i=x,y}(\tau) = \int_0^t d\tau\Omega(t-\tau)\sigma_i(t-\tau,t)\Lambda_{ii}(\tau), \quad (4.17)$$

and where we have also defined $\sigma_i(t-\tau,t) = U_{P,S}(t)U^\dagger_{P,S}(t-\tau)\sigma_i U_{P,S}(t-\tau)U^\dagger_{P,S}(t)$.

On timescales relevant to the QD, assuming the electromagnetic spectral density does not vary appreciably over the energy scales of the QD, the spontaneous emission rate remains unaffected by the QD-phonon coupling [104]. Accordingly we may incorporate spontaneous emission from the QD with rate γ in the master equation with the usual Lindblad collapse term $L_k \in \{\sqrt{\gamma}\sigma\}$ [104].

The final form of the non-Markovian polaron master equation incorporating spontaneous emission is then

$$\begin{aligned}\frac{\partial}{\partial t}\rho_S(t) =& -i[\delta_r\sigma^\dagger\sigma + \frac{\Omega_r(t)}{2}\sigma_x, \rho_S(t)] + \frac{\gamma}{2}\Big(2\sigma\rho_S\sigma^\dagger - \big\{\sigma^\dagger\sigma, \rho_S(t)\big\}\Big) \\ &- \frac{\Omega(t)}{4}\sum_{i=x,y}\Big([\sigma_i, \chi_i(t)\rho_S(t)] - [\sigma_i, \rho_S(t)\chi_i^\dagger(t)]\Big) \\ &= \mathcal{L}(t)\rho(t).\end{aligned} \tag{4.18}$$

4.2.3 Markovian Polaron Master Equation

Just as in the derivation of the weak-coupling Born-Markov master equation, we may once again make use of the Markov approximation to simplify the polaron master equation. Assuming the decay of the bath correlation functions is much faster than the dynamics of the 2LS, we can take the upper limits of the integrals in the rate operators to infinity. Doing so removes the time-dependence of the bath rate operators reducing the polaron master equation to

$$\begin{aligned}\frac{\partial}{\partial t}\rho_S(t) =& -i\big[\delta_r\sigma^\dagger\sigma + \frac{\Omega_r(t)}{2}\sigma_x, \rho_S(t)\big] + \frac{\gamma}{2}\big(2\sigma\rho_S\sigma^\dagger - \big\{\sigma^\dagger\sigma, \rho_S(t)\big\}\big) \\ &- \Big(\frac{\Omega(t)}{2}\Big)^2\sum_{i=x,y}\Big(\big[\sigma_i, \chi_i\rho_S(t)\big] - \big[\sigma_i, \rho_S(t)\chi_i^\dagger\big]\Big) = \mathcal{L}(t)\rho(t),\end{aligned} \tag{4.19}$$

where we have made the further substitution $\Omega(t-\tau) \to \Omega(t)$ and moved this factor of the Rabi frequency out of the rate operators. As we have assumed the QD states and bath evolve on disparate timescales, to calculate the rate operators we can make an adiabatic approximation $U(t)U(t-\tau) \approx \exp\{-iH_S(t)\tau\}$ [106], and thus $\sigma_i(t-\tau, t) \to \sigma_i(\tau)$. This allows us to perform a simplified expansion of the system operator in the basis of the system Hamiltonian where $|\psi_k(\tau)\rangle$ are the eigenvectors of $H_s(t) = \delta_r\sigma^\dagger\sigma + \frac{\Omega_r(t)}{2}\sigma_x$, and $\lambda_{ij} = \psi_i - \psi_j$ are the difference in the system eigenvalues. Performing this expansion yields

$$\begin{aligned}\tilde{\sigma}(\tau) &= U_0^\dagger(\tau)\sigma U_0(\tau) = U_0^\dagger(\tau)\mathbf{I}\sigma\mathbf{I}U_0(\tau) = \sum_{lm} U_0^\dagger(\tau)\,|\psi_l\rangle\langle\psi_l|\,\sigma\,|\psi_m\rangle\langle\psi_m|\,U_0(\tau) \\ &= \sum_{lm}\langle\psi_l|\,\sigma\,|\psi_m\rangle\,U_0^\dagger(\tau)\,|\psi_l\rangle\langle\psi_m|\,U_0(\tau) = \sum_{lm}\langle\psi_l|\,\sigma\,|\psi_m\rangle\,e^{i\psi_l(\tau)}\,|\psi_l\rangle\langle\psi_m|\,e^{-i\psi_m(\tau)} \\ &= \sum_{lm} e^{i\psi_{lm}(\tau)}\,\langle\psi_l|\,\sigma\,|\psi_m\rangle\,|\psi_l\rangle\langle\psi_m|\,.\end{aligned} \tag{4.20}$$

This expansion allows one to account for the full eigenstructure of the polaron transformed system, resulting in rate operators given by

$$\chi_{i=x,y} = \sum_{jk} \langle\psi_j| \sigma_i |\psi_k\rangle \int_0^\infty e^{-i\lambda_{jk}\tau} \Lambda_{ii}(\tau) d\tau \, |\psi_j\rangle\langle\psi_k| \,, \tag{4.21}$$

that are computationally simpler to calculate than Eq. 4.17.

4.3 Pulsed Emission Spectra

As we discussed in Chapter 3, one may experimentally determine the properties of quantum systems by measuring the properties of the light they emit. Hence, we wish to understand the impact of the QD-phonon coupling on the properties of the light emitted by the QD under pulsed excitation. As we need to calculate correlation functions to obtain the desired emission spectra, and the QRT is only valid for systems undergoing Markovian dynamics, we shall use the Markovian polaron master equation in Eq. 4.19 rather than the non-Markovian polaron master equation given by Eq. 4.18. Due to the limitations of the polaron formalism, discussed further in Chapter 5, we shall restrict our discussion of the pulsed emission spectra to the long pulse limit to restrict the Rabi frequency at the peak of the pulse.

The two-time first-order correlation function written in terms of the QD operators is given by

$$G^{(1)}(t,\tau) = \langle \sigma^\dagger(t+\tau)\sigma(t)\rangle = \mathrm{Tr}\big(\sigma^\dagger e^{\mathcal{L}\tau}\sigma\rho_S(t)\big), \tag{4.22}$$

where $\rho_S(t)$ is the density matrix of the QD at time t, and $\mathcal{L}$ is the system Liouvillian. To calculate the two-time first-order correlation function, we must first propagate the state of the system along the t axis. To do this we use a standard initial value problem approach with discretised time steps. Starting from an initial state $\rho(t=0)$, this allows us to calculate the system density matrix $\rho(t')$ at a given time time t' in this range of discretised time intervals using a time-dependent Liouvillian $\mathcal{L}(t)$. Using the QRT we can then propagate the density matrix along the τ axis for each discrete time step in t using $\sigma\rho_S(t)$ as the initial states such that $\Lambda(t,\tau) = e^{\mathcal{L}\tau}\sigma\rho(t)$ to find $G^{(1)}(t,\tau)$. The propagation of the states along the τ axis is performed with the same Liouvillian used to initially propagate the state of the system along the t axis, only with a temporally displaced form of the time-dependent Rabi frequency

given by

$$\Omega(t,\tau) = \frac{\Theta}{\sqrt{2\pi w^2}} \exp\left\{ -\frac{\big(\tau - (\tau_0 - t)\big)^2}{2w^2} \right\}, \tag{4.23}$$

where Θ is the pulse area, t_0 is the time at the peak of the pulse, and w is the Gaussian width of the pulse electric field which is related to the electric field Full-Width Half Maximum (FWHM), $\Delta\tau_E$, by

$$w = \frac{\Delta\tau_E}{2\sqrt{2\ln 2}}. \tag{4.24}$$

The electric field FWHM is then related to the intensity FWHM, $\Delta\tau_I$, by $\Delta\tau_E = \Delta\tau_I\sqrt{2}$. As discussed in Chapter 3, we may calculate the TDS from the first-order correlation function using [76]

$$S(\omega,t,\Upsilon) = 2\Upsilon\,\mathrm{Re}\Big\{ \int_0^t dt_2 \exp\big\{ \big(-\Upsilon(t-t_2)\big) \big\} \int_0^{t-t_2} d\tau \exp\left\{ \Big(\big(\frac{\Upsilon}{2} - i(\omega-\omega_l) \big)\tau \Big) \right\} \langle \sigma^\dagger(t_2+\tau)\sigma(t_2)\rangle \Big\}, \tag{4.25}$$

where Υ is the measurement bandwidth accounting for time-energy uncertainty [77]. The TIS is then found in the limit $t \gg t_0 + \Delta\tau_E$.

4.3.1 Time-Dependent Pulsed Emission Spectra

To calculate the emission spectra we shall assume the QD possesses the same excited state lifetime as presented in [82], but we shall take the bad cavity limit such that $\gamma \to F_P\gamma$ where F_P is the Purcell factor (see Chapter 3). Additionally, we choose a laser frequency such that $\delta_r = 0$. Figure 4.3 shows the impact of the QD-phonon coupling on the full time-dependent first-order correlation function, $G^{(1)}(t,\tau)$, as a function of temperature. We find increasing the temperature of the system increases the damping of the Rabi oscillations along the t-axis. Using Eq. 4.25 to calculate the TDS at different temperatures (see Figure 4.4) we find the phonon-coupling results in a broadening of the satellite Mollow peaks of the pulsed emission spectrum (see Section 3.7.3 for more details regarding the pulsed emission spectrum), while the central ZPL and temporal evolution of the satellite peaks remains unaffected. Furthermore, we find the broadening of the satellite peaks increases with increasing temperature until the individual Mollow peaks can no longer be distinguished. The broadening of the satellite peaks results from the pure-dephasing component

of the phonon-coupling [78], while the lack of broadening of the ZPL results from the assumption of a purely linear QD-phonon coupling bath [80].

In addition to the broadening of the satellite Mollow peaks, we find an asymmetry is also induced in the emission spectra that was not observed when using a simple pure dephasing model in either Section 3.9 or [78]. Furthermore, from Figure 4.4 we observe this phonon-induced asymmetry actually decreases with increasing temperature in contrast to the other phonon effects we have seen. This is the result of an imbalance in phonon-mediated photon emission processes. In the limit of low temperature, the number of phonons present in the bath is low. Hence, the probability of the QD emitting a photon with energy $\hbar\omega_\gamma > \hbar\omega_X$ via the absorption of a phonon carrying energy $\hbar(\omega_\gamma - \omega_X)$ is small, suppressing this mechanism. However, the QD may also emit lower energy photons ($\hbar\omega_\gamma < \hbar\omega_X$) by simultaneously emitting a phonon with energy $\hbar(\omega_X - \omega_\gamma)$. Since this latter process does not rely on phonon absorption and thus the existing phonon number, it can occur more readily at lower temperatures. This results in the asymmetry that emerges in the multi-peak QD pulsed emission spectrum when accounting for the full effects of the QD-phonon coupling. When the temperature of the system is increased, the phonon occupation of the bath also increases which in turn increases the rate of phonon scattering balancing the rates of the two phonon-mediated emission processes, and accordingly the asymmetry in the emission spectrum is diminished.

Additional phonon effects can also be observed by considering the power dependence of the TDS and $G^{(1)}(t,\tau)$ in addition to the temperature dependences shown in Figures 4.3 and 4.4. Figure 4.5 shows that increasing the area of the driving pulse simultaneously increases the number of Rabi oscillations in the first-order correlation function $G^{(1)}(t,\tau)$, while also decreasing the magnitude of these oscillations. Moreover, from Figure 4.6 we find increasing the area of the driving pulse, Θ, also increases the number of Mollow side-peaks in the emission spectrum as predicted in [78]. However, it can also be seen that the magnitude of the asymmetry in the spectrum at low temperature also increases with increasing pulse area. In the limit of large pulse area the phonon spectral density, $J(\omega)$, is sampled closer to its peak at ω_c as the peak Rabi frequency $\Omega_r(t_0)$ approaches and exceeds ω_c. This has the effect of increasing the effective phonon coupling strength, and thus magnifies the phonon-coupling effects. Additionally, at larger pulse areas a difference in the evolution of the satellite peaks at $\omega < \omega_l$ and $\omega > \omega_l$ is observed.

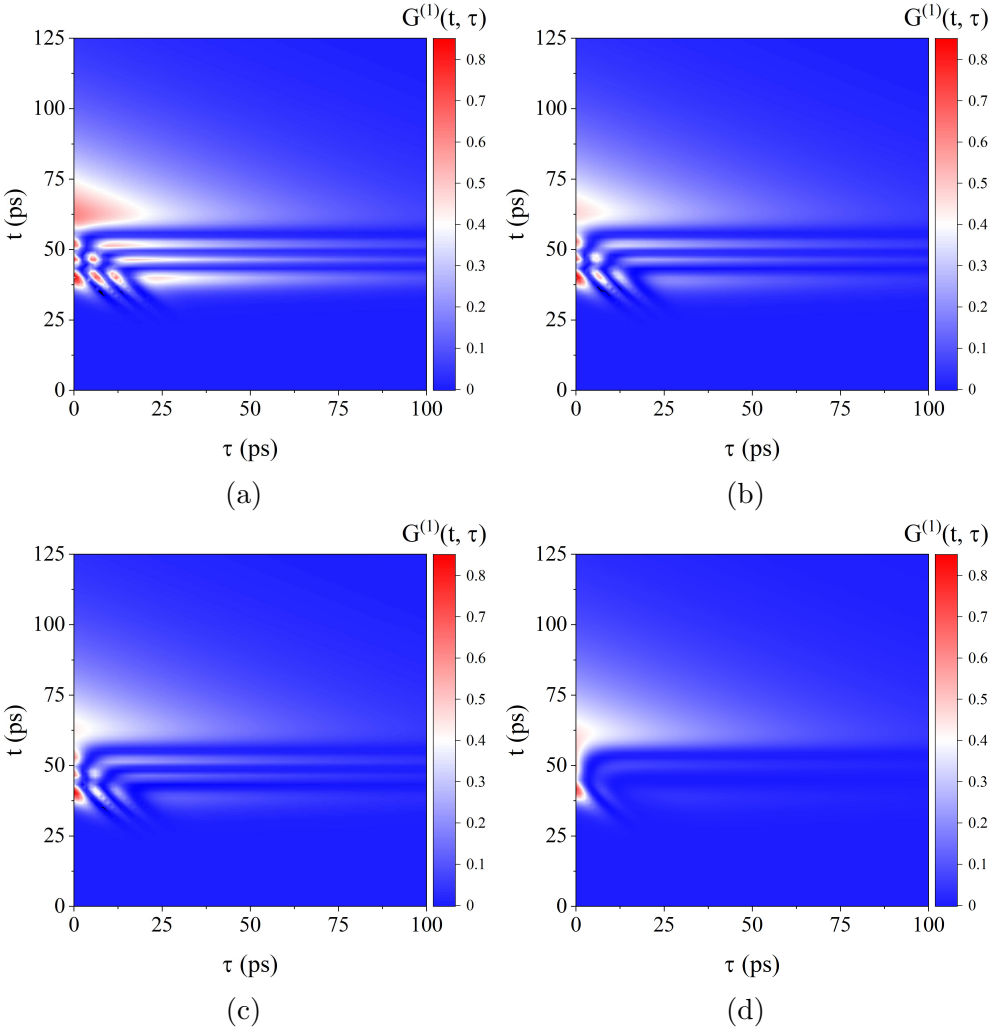

Figure 4.3: The two-time first-order correlation function, $G^{(1)}(t,\tau)$, of the light emitted by a QD coherently driven by a Gaussian optical pulse with (a) no phonon coupling (i.e. $\alpha = 0$ ps^2), and with phonon coupling ($\alpha = 0.027$ ps^2, $\omega_c = 2.2$ ps^{-1}) at temperatures (b) $T = 5$ K, (c) $T = 10$ K, and (d) $T = 50$ K. $G^{(1)}(t,\tau)$ was calculated using the master equation and Quantum Regression Theorem (QRT). Parameters used: $\Theta = 7\pi$, $\Delta\tau_I = 12$ ps, and $t_0 = 4\Delta\tau_I$.

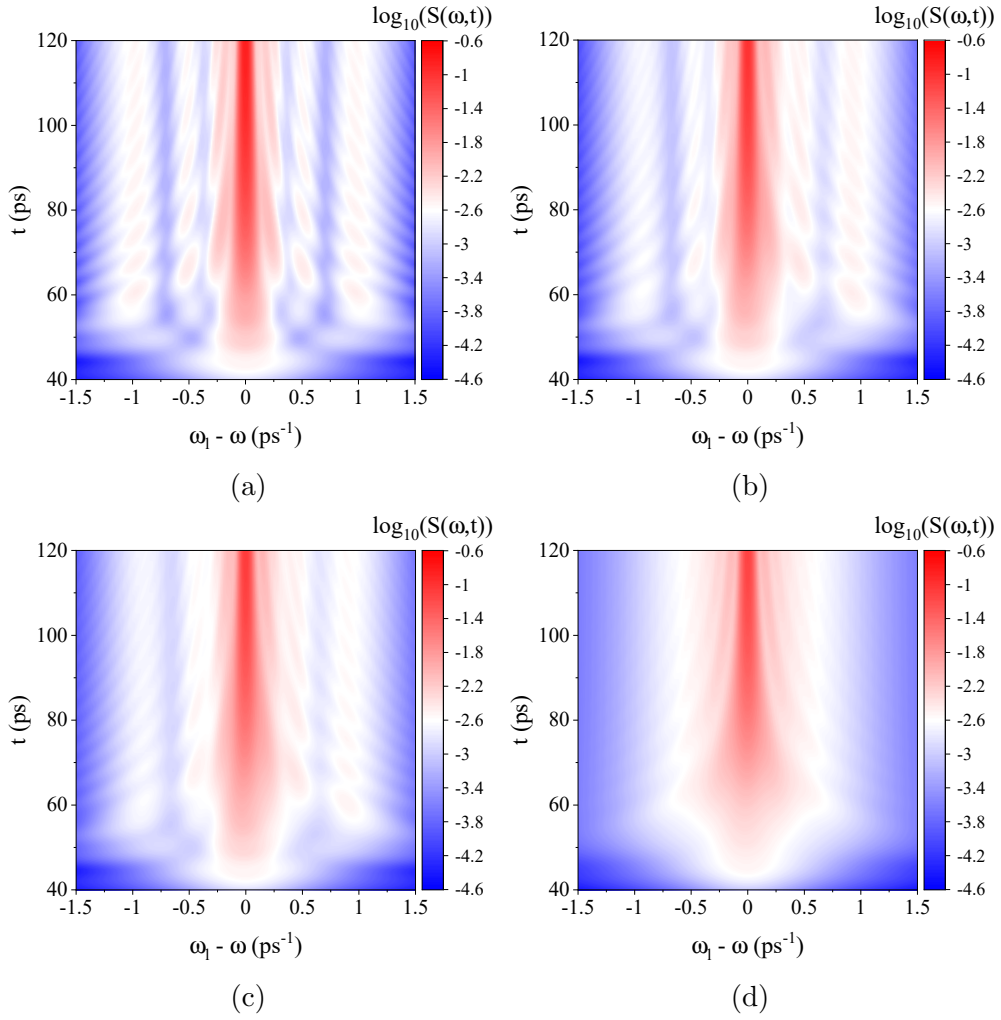

Figure 4.4: The Time-Dependent Spectra (TDS) of the light emitted by a Quantum Dot (QD) coherently driven by a Gaussian optical pulse with (a) no phonon coupling ($\alpha = 0$ ps^2), and with phonon coupling ($\alpha = 0.027$ ps^2, $\omega_c = 2.2$ ps^{-1}) at temperatures (b) $T = 5$ K, (c) $T = 10$ K, and (d) $T = 50$ K. Parameters used: $\Theta = 7\pi$, $\Delta\tau_I = 12$ ps, $t_0 = 4\Delta\tau_I$.

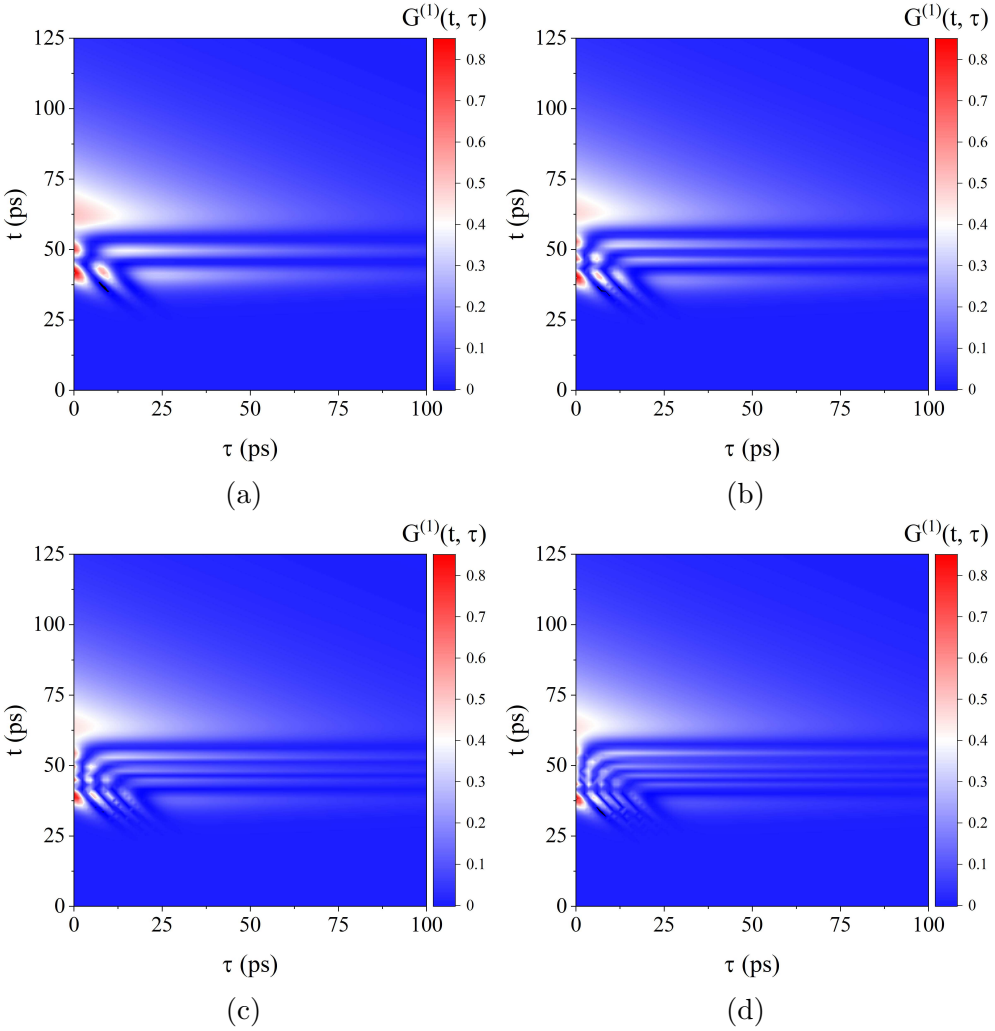

Figure 4.5: The two-time first-order correlation function, $G^{(1)}(t,\tau)$, of the light emitted from a Quantum Dot (QD) coupled to a phonon bath and coherently driven by a Gaussian optical pulse with pulse area (a) $\Theta = 5\pi$, (b)$\Theta = 7\pi$, (c) $\Theta = 9\pi$, and (d) $\Theta = 11\pi$. $G^{(1)}(t,\tau)$ was calculated using the master equation and Quantum Regression Theorem (QRT). Parameters used: $T = 5$ K, $\Delta\tau_I = 12$ ps, $t_0 = 4\Delta\tau_I$, $\alpha = 0.027$ ps^2, $\omega_c = 2.2$ ps^{-1}.

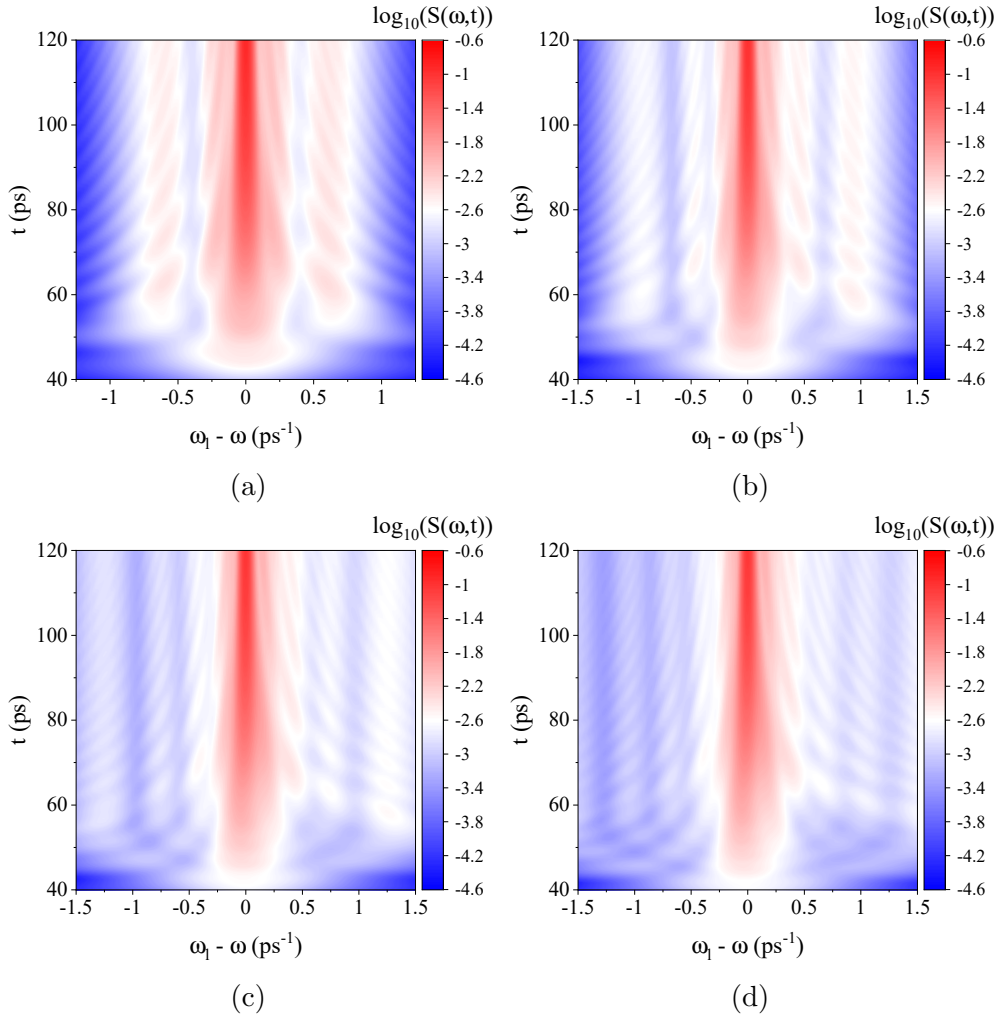

Figure 4.6: The Time-Dependent Spectra (TDS) of the light emitted by a Quantum Dot (QD) coupled to a phonon bath and coherently driven by a Gaussian optical pulse with pulse area (a) $\Theta = 5\pi$, (b) $\Theta = 7\pi$, (c) $\Theta = 9\pi$, and (d) $\Theta = 11\pi$. Parameters used: $T = 5$ K, $\Delta\tau_I = 12$ ps, $t_0 = 4\Delta\tau_I$, $\alpha = 0.027$ ps^2, $\omega_c = 2.2$ ps^{-1}.

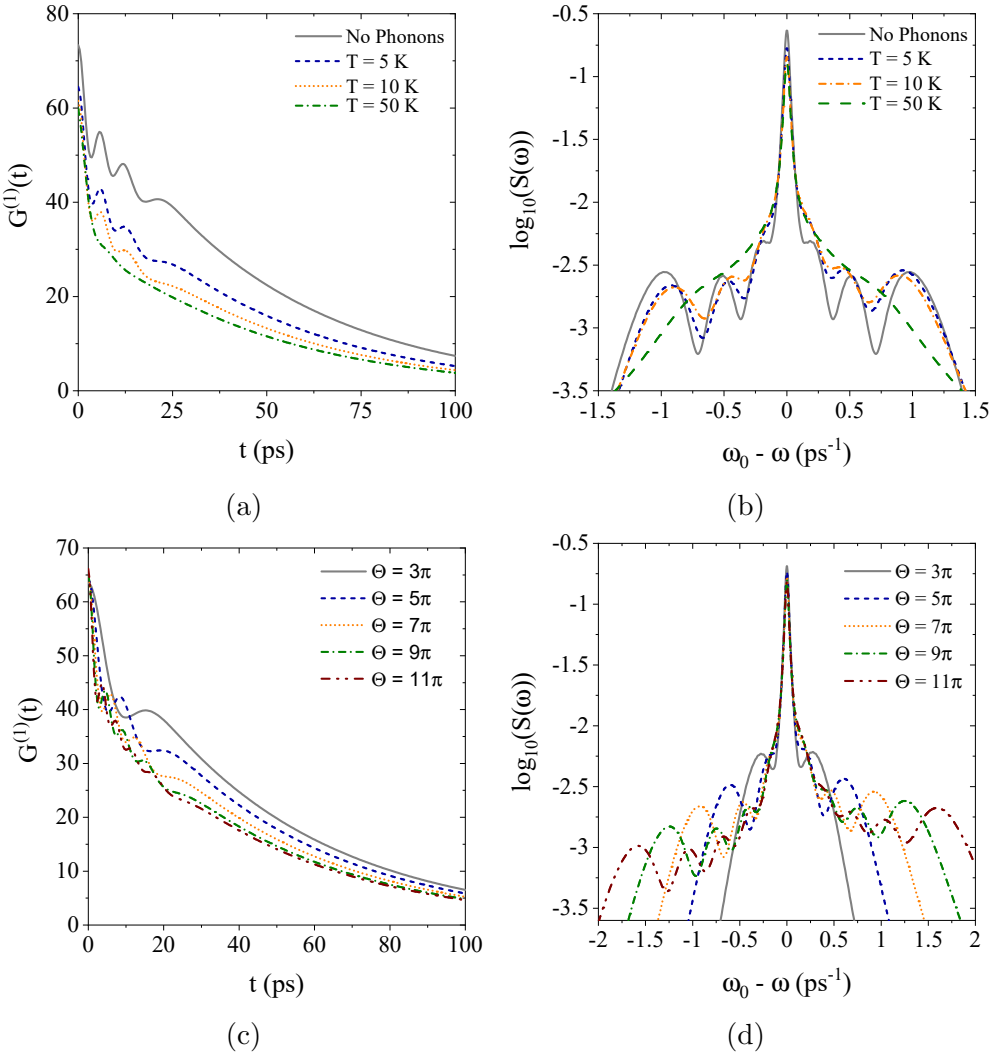

Figure 4.7: (Top) The temperature dependence of the (a) first-order correlation function and (b) Time-Integrated Spectra (TIS) of the light emitted by a Quantum Dot (QD) driven by a Gaussian optical pulse. Phonon effects are included using the Markovian polaron model with parameters: $\Theta = 7\pi$, $\Delta\tau_I = 12$ ps, $t_0 = 4\Delta\tau_I$, $\alpha = 0.027$ ps^{-2}, $\omega_c = 2.2$ ps^{-1}. The expected values in the absence of phonon coupling are also included. (Bottom) The power dependence of the (c) first-order correlation function and (d) TIS from a QD coupled to a phonon bath and driven by a Gaussian optical pulse for a number of different pulse areas. Phonon coupling is included via the Markovian polaron model with parameters: $T = 5$ K, $\Delta\tau_I = 12$ ps, $t_0 = 4\Delta\tau_I$, $\alpha = 0.027$ ps^2, $\omega_c = 2.2$ ps^{-1}

4.3.2 Time-Integrated Pulsed Emission Spectra

The effects on the emission properties of the QD resulting from the phonon coupling can be more clearly seen in the time-integrated first-order correlation function, $G^{(1)}(t) = \int d\tau G^{(1)}(t,\tau)$, and the TIS shown in Figure 4.7. Figures 4.7a and 4.7b show the time-integrated forms of Figures 4.3 and 4.4, that is they show the temperature dependence of $G^{(1)}(t)$ and the TIS. From Figure 4.7a the damping of the oscillations in the first-order correlation function can be clearly seen with increasing temperature. At $T = 50$ K the Rabi oscillations are almost completely damped. In agreement with our findings from the TDS, at low temperatures the QD-phonon coupling results in an asymmetry in the TIS. Increasing the temperature decreases this asymmetry in the TIS, but increases the broadening of the satellite peaks until at $T = 50$ K none of the satellite peaks are individually resolvable. Taking the power dependence we again find an increase in the number of Rabi oscillations and Mollow satellite peaks of the time-integrated first-order correlation function (Figure 4.7c) and TIS (Figure 4.7d) respectively with increasing pulse area. From the TIS shown in Figure 4.7d the increase in the asymmetry of the spectrum with increasing pulse area is clearly visible further to the increased number of satellite peaks.

4.4 Pulsed Second-Order Correlation Function

From the Markovian standard polaron model we may also study the behaviour of the second-order correlation function under pulsed optical driving and the influence of phonon coupling. The second order-correlation function, $G^{(2)}(t,\tau)$ takes a similar form to the first-order correlation function used to calculate the emission spectra

$$G^{(2)}(t,\tau) = \langle \sigma^\dagger(t)\sigma^\dagger(t+\tau)\sigma(t+\tau)\sigma(t)\rangle = \mathrm{Tr}\big(\sigma^\dagger \sigma e^{\mathcal{L}\tau}\sigma\rho_S(t)\sigma^\dagger\big), \qquad (4.26)$$

where again $\mathcal{L}$ is the Liouvillian, and σ is the QD lowering operator. Calculating $G^{(2)}(t,\tau)$ follows the same procedure as calculating $G^{(1)}(t,\tau)$, only $\sigma\rho_S(t)\sigma^\dagger$ are used as the initial states to propagate along the τ axis. Figure 4.8 shows phonon coupling has a minimal impact on the central minimum of the pulsed $G^{(2)}(\tau) = \int dt G^{(2)}(t,\tau)$. As the lifetime of the excited state of the QD is not influenced by the presence of the phonon bath, the widths of the peaks and dips remain unaffected by the QD-phonon coupling. However, as we observed

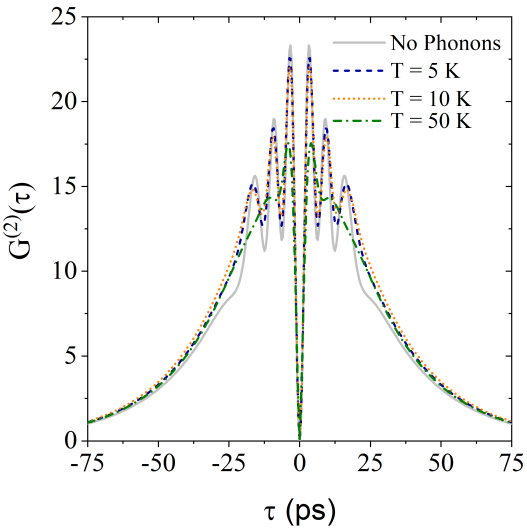

Figure 4.8: The central peak of the pulsed second-order correlation function when driving a Quantum Dot (QD) with a single Gaussian pulse calculated using the quantum regression theorem. $G^{(2)}(\tau)$ is plotted without phonon coupling, and at three different temperatures with phonon coupling. Parameters used: $\Theta = 7\pi$, $\Delta\tau_I = 12$ ps, $\alpha = 0.027$ ps^2, and $\omega_c = 2.2$ ps^{-1}.

with the system dynamics and $G^{(1)}(t, \tau)$, the Rabi oscillations in $G^{(2)}(\tau)$ are increasingly damped as the temperature of the bath is increased.

4.5 Summary

Taking the Markovian limit of the standard polaron model, we have studied the effects of phonon coupling on the emission properties of a QD when driven by a Gaussian optical pulse. We have shown the effects of the QD-phonon coupling manifest themselves in two manners in the emission spectrum. When coupled to a phonon bath the satellite Mollow peaks of the pulsed emission spectrum become broadened, in agreement with a pure dephasing model [78] previously studied. However, an imbalance in phonon-mediated emission processes leads to an asymmetry in the emission spectrum at low temperatures, decreasing in magnitude with increasing temperature, that is not observed when using a pure-dephasing approach alone. Furthermore, we have also shown the phonon-coupling has a minimal impact on the second-order correlation function. This further proves that such models are unable to fully account for the effects of coupling to a phonon bath.

Chapter 5

Time-Dependent Variational Polaron Theory

5.1 Introduction

In deriving the polaron master equation in Chapter 4, we made a number of approximations that naturally limit the regimes in which it is valid. The derivation of the master equation in the polaron transformed frame of reference instantaneously displaces the phonon bath when the QD is driven into its excited state. Therefore we expect the polaron formalism to be valid only when the bath is able to react on timescales shorter than the characteristic timescales of the QD dynamics. In fact, it can be shown that the polaron master equation treats the QD-phonon coupling as a perturbation in the ratio of Ω/ω_c [106], and thus we should only expect the polaron model to be valid in the weak-driving regime where $\Omega/\omega_c \ll 1$ [106]. Additionally, the Markovian limit further restricts the regimes of validity to timescales greater than the inverse of the cutoff frequency [106]. Hence, when driving the system with a Gaussian optical pulse, we expect the polaron model to breakdown in the limits of short pulse duration and/or large pulse area (see Figure 5.1), where the peak Rabi frequency of the pulse approaches and surpasses the phonon cut-off frequency. Therefore, to make accurate predictions of phonon-induced effects in these limits, we must derive a theory that minimises the interaction Hamiltonian even when the ratio Ω/ω_c is large, and is also able to account for the finite reaction time of the bath. To this end we shall now extend the *variational polaron model* [100, 118] to develop a *time-dependent variational polaron model* including pulsed optical driving. While this model still displaces the bath modes according to the charge state of the QD as in the standard polaron

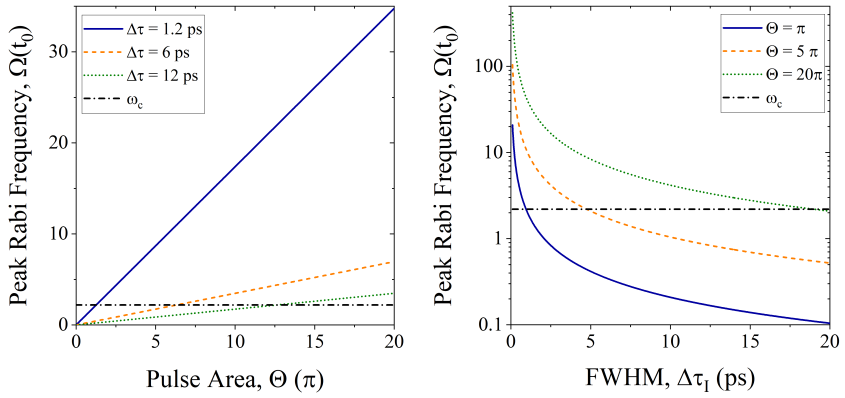

(a) (b)

Figure 5.1: The peak Rabi frequency, $\Omega(t_0)$, of a Gaussian pulse (a) sweeping the pulse area (Θ) for a given Full-Width Half Maximum (FWHM) ($\Delta\tau_I$), and (b) sweeping $\Delta\tau_I$ for a given Θ. The phonon cut-off frequency, $\omega_c = 2.2$ ps^{-2}, is also plotted. The polaron model is only valid when $\Omega(t_0) \ll \omega_c$ [106].

model, it leaves the magnitude of the displacement of each bath mode as a variational parameter chosen to minimise the free-energy of the system [118] at each discretised time step considered. This approach shall allow us to derive a master equation that returns reliable results inside and outside of the optical driving regimes accessible by the weak-coupling and polaron models, and remains valid with environmental interactions that are not governed by super-ohmic spectral densities [118].

5.2 The Variational-Polaron-Transformed Exciton Phonon Hamiltonian

To derive our time-dependent variational polaron master equation we begin with the same rotating frame Hamiltonian[1] that we used to derive the polaron master equation in Chapter 4

$$H_R(t) = (\omega_X - \omega_l)\,|X\rangle\langle X| + \frac{\Omega(t)}{2}(|X\rangle\langle 0| + |0\rangle\langle X|) + |X\rangle\langle X| \sum_k g_k(b_k^\dagger + b_k) + \sum_k \omega_k b_k^\dagger b_k. \quad (5.1)$$

Here $\Omega(t)$ is the Rabi frequency characterising the laser-QD coupling strength modulated by a time-dependent envelope function, ω_l is the central laser fre-

[1] See Chapter 3 for more information on transforming to rotating frames of reference and the Rotating Wave Approximation (RWA).

quency, and g_k characterises the coupling between the bath modes with frequency ω_k and the QD. However, unlike in our derivation of the polaron master equation, we shall now allow the polaron displacement to have some explicit time-dependence i.e. $\alpha_k \to \alpha_k(t)$. Our unitary polaron operator is thus modified from the polaron formalism to

$$U_{vp}(t) = \exp\Big\{|X\rangle\langle X| \sum \alpha_k(t)\big(b_k^\dagger - b_k\big)\Big\} = |0\rangle\langle 0| + |X\rangle\langle X| \prod_k D(\alpha_k(t)). \quad (5.2)$$

This modification results in an additional term in the transformed Hamiltonian from the non-zero time derivative of the unitary operator, $H_V(t) = U_{vp}(t)H_R(t)U_{vp}^\dagger(t) + i\big(\partial_t U_{vp}(t)\big)U_{vp}^\dagger(t)$, modifying the B_z bath operator from the polaron limit such that the bath operators in the time-dependent variational polaron formalism are given by

$$\begin{aligned} B_x(t) &= \frac{1}{2}\big(B_+(t) + B_-(t) - 2B(t)\big), \\ B_y(t) &= \frac{1}{2i}\big(B_-(t) - B_+(t)\big), \\ B_z(t) &= \sum_k h_k(t) b_k^\dagger + \text{h.c.}, \end{aligned} \quad (5.3)$$

where $h_k(t) = \sum_k \big(g_k - \omega_k \alpha_k(t) + i\partial_t \alpha_k(t)\big)$. Comparing these bath operators with those derived in the standard polaron model (Eq. 4.6) we see that the first two maintain the same form as in the polaron limit only now with an additional time dependence. It is also clear that in the variational polaron formalism $B_z(t)$ is an extended version of the B_z operator in the polaron limit, with the first two terms of $h_k(t)$ originating from the polaron model, and the final term arising from the non-zero time derivative of the unitary time-dependent variational polaron operator. Rather than setting the polaron displacement, α_k, to eliminate the linear coupling terms as done in Chapter 4, we now allow it to a be a variational parameter such that $\alpha_k(t) = f_k(t)/\omega_k$ where $f_k(t)$ is the time-dependent variational function [119, 120]. This leaves our time-dependent variational polaron Hamiltonian as $H_V(t) = H_{V,S}(t) + H_{V,B} + H_{V,I}(t)$ where

$$\begin{aligned} H_{V,S}(t) &= \delta_r(t)\sigma^\dagger\sigma + \frac{\Omega_r(t)}{2}\sigma_x, \\ H_{V,I}(t) &= \frac{\Omega(t)}{2}\big(\sigma_x B_x(t) + \sigma_y B_y(t)\big) + \sigma^\dagger\sigma B_z(t), \\ H_{V,B} &= \sum_k \omega_k b_k^\dagger b_k. \end{aligned} \quad (5.4)$$

Here $\delta_r(t) = \delta - \sum_k \omega_k^{-1} f_k(t)\big(2g_k - f_k(t)\big)$, $\sigma = |0\rangle\langle X|$, and σ_x, σ_y, and $\sigma_z = 2(\sigma^\dagger\sigma - 1)$ are the standard Pauli matrices. For each bath mode we choose $f_k(t)$ to minimise the free energy, F, of the system. This ensures that the state of the system relaxes to the true thermal state of the combined system and environment. However, rather than taking the challenging route of explicitly calculating the free energy of the system, we shall instead minimise the Feynman-Bogoliubov upper bound [119, 120] which satisfies $A_B(t) \geq F$, and has the form [111]

$$A_B(t) = \frac{-1}{\beta} \ln\left(\mathrm{Tr}\big\{(e^{-\beta H_0(t)})\big\}\right) + \langle H_I(t)\rangle_{H_0(t)} + \mathcal{O}(\langle H_I^2\rangle_{H_0(t)}). \tag{5.5}$$

Minimising $A_B(t)$ with respect to $f_k(t)$ yields

$$\frac{\partial A_B(t)}{\partial f_k(t)} = \frac{1}{\mathrm{Tr}\{(e^{-\beta H_0(t)})\}}\Big(\frac{\partial H_0(t)}{\partial f_k(t)}\Big) = 0, \tag{5.6}$$

which gives $f_k(t) = F(\omega_k, t)g_k$ where

$$F(\omega_k, t) = \frac{\eta_r(t) - \delta_r(t)\tanh\Big(\frac{\beta\eta_r(t)}{2}\Big)}{\eta_r(t) - \tanh\Big(\frac{\beta\eta_r(t)}{2}\Big)\Big(\delta_r(t) - \frac{\Omega_r(t)^2}{2\omega_k}\coth\Big(\frac{\beta\omega_k(t)}{2}\Big)\Big)}. \tag{5.7}$$

Here $\eta_r(t) = \sqrt{\delta_r(t)^2 + \Omega_r(t)^2}$ is the time-dependent renormalised generalised Rabi frequency. We perform this minimisation for each time-step by self-consistently solving the equations

$$\Omega_r(t) = \Omega(t)\exp\Big(-\frac{1}{2}\int_0^\infty d\omega \frac{J(\omega)F(\omega,t)^2}{\omega^2}\coth\Big(\frac{\beta\omega}{2}\Big)\Big), \tag{5.8}$$

$$\delta_r(t) = \delta + \int_0^\infty d\omega \frac{J(\omega)F(\omega,t)}{\omega}\big(2 - F(\omega,t)\big), \tag{5.9}$$

for the renormalised Rabi frequency and detuning respectively.

5.3 Non-Markovian Variational Polaron Master Equation

From here we follow a similar procedure to the one we used to derive the polaron master equation, once again transforming our Hamiltonian into the interaction picture, now with respect to $H_{V,0}(t) = H_{V,S}(t) + H_{V,B}$, using the unitary operator

$$U_{V,0}(t) = \boldsymbol{\mathcal{T}} \exp\left(-i \int_0^t ds H_{V,0}(s)\right), \tag{5.10}$$

to obtain the interaction Hamiltonian

$$\tilde{H}_{V,I}(t) = \frac{\Omega(t)}{2}\big(\tilde{\sigma}_x(t)\tilde{B}_x(t) + \tilde{\sigma}_y(t)\tilde{B}_y(t)\big) + \tilde{\sigma}^\dagger\tilde{\sigma}(t)\tilde{B}_z(t), \tag{5.11}$$

where operators in the interaction picture are denoted by a tilde and given by $\tilde{S}(t) = U_{V,S}^\dagger(t) S U_{V,S}(t)$ with $U_{V,S}(t) = \boldsymbol{\mathcal{T}} \exp\left(-i \int_0^t ds H_{V,S}(s)\right)$. Substituting Eq. 5.11 into Eq. 2.32 yields

$$\begin{aligned}
&\partial_t \tilde{\rho}_S(t) = \\
&-\int_0^t dt' \Big\{ \sum_{i,j=x,y} \Big([\tilde{\sigma}_i(t), \tilde{\sigma}_j(t')\tilde{\rho}_S(t)]\Lambda_{ij}(t,t') - [\tilde{\sigma}_i(t), \tilde{\rho}_S(t)\tilde{\sigma}_j(t')]\Lambda_{ij}^\dagger(t,t') \Big) \\
&+ \sum_{i=x,y} \Big([\tilde{\sigma}^\dagger\tilde{\sigma}(t), \tilde{\sigma}_i('t)\tilde{\rho}_S(t)]\Lambda_{zi}(t,t') - [\tilde{\sigma}^\dagger\tilde{\sigma}(t), \tilde{\rho}_S(t)\tilde{\sigma}_i(t')]\Lambda_{zi}^\dagger(t,t') \Big) \\
&+ \sum_{i=x,y} \Big([\tilde{\sigma}_i(t), \tilde{\sigma}^\dagger\tilde{\sigma}(t')\tilde{\rho}_S(t)]\Lambda_{iz}(t,t') - [\tilde{\sigma}_i(t), \tilde{\rho}_S(t)\tilde{\sigma}^\dagger\tilde{\sigma}(t')]\Lambda_{iz}^\dagger(t,t') \Big) \\
&+ \Big([\tilde{\sigma}^\dagger\tilde{\sigma}(t), \tilde{\sigma}^\dagger\tilde{\sigma}(t')\tilde{\rho}_S(t)]\Lambda_{zz}(t,t') - [\tilde{\sigma}^\dagger\tilde{\sigma}(t), \tilde{\rho}_S(t)\tilde{\sigma}^\dagger\tilde{\sigma}(t')]\Lambda_{zz}^\dagger(t,t') \Big) \Big\},
\end{aligned} \tag{5.12}$$

where $\Lambda_{ij}(t,t') = \mathrm{Tr}_B\big(\tilde{B}_i(t)\tilde{B}_j(t')\rho_B\big)$ and $\Lambda_{ij}^\dagger(t,t') = \mathrm{Tr}_B\left(\tilde{B}_i(t')\tilde{B}_j(t)\rho_B\right)$ are the correlation functions for $i,j \in \{x,y,z\}$ into which we have now absorbed the time-dependent Rabi frequency terms. The additional bath operator in the variational polaron limit results in a further two correlation functions in addition to the two polaron type correlation functions, a weak-coupling type correlation function $\Lambda_{zz}(t,t')$ and a cross-correlation type function $\Lambda_{yz}(t,t')$. The four unique non-zero variational polaron correlation functions are

$$\Lambda_{xx}(t,t') = \frac{\Omega_r(t)\Omega_r(t')}{8}\big(e^{\phi(t,t')} + e^{-\phi(t,t')} - 2\big), \tag{5.13}$$

$$\Lambda_{yy}(t,t') = \frac{\Omega_r(t)\Omega_r(t')}{8}\big(e^{\phi(t,t')} - e^{-\phi(t,t')}\big), \tag{5.14}$$

$$\begin{aligned}
\Lambda_{yz}(t,t') = \frac{\Omega_r(t)}{2}\int_0^\infty d\omega \frac{J(\omega)F(\omega,t)}{\omega} \Big\{ \big(F(\omega,t')-1\big)\Big(\coth\Big(\frac{\beta\omega}{2}\Big)\sin\big(\omega(t-t')\big) \\
+ i\cos\big(\omega(t-t')\big)\Big) + \frac{\partial_{t'}F(\omega,t')}{\omega}\Big(i\sin\big(\omega(t-t')\big) - \coth\Big(\frac{\beta\omega}{2}\Big)\cos\big(\omega(t-t')\big)\Big)\Big\},
\end{aligned} \tag{5.15}$$

$$\Lambda_{zz}(t,t') = \int_0^\infty d\omega J(\omega)u(\omega,t)u^*(\omega,t')\Big\{\coth\Big(\frac{\beta\omega}{2}\Big)\cos\big(\omega(t-t')\big) - i\sin\big(\omega(t-t')\big)\Big\}. \quad (5.16)$$

Here we define $u(\omega,t) = 1-F(\omega,t)+i\omega^{-1}\partial_t F(\omega,t)$, $J(\omega) = \alpha\omega^3\exp\{-(\omega/\omega_c)^2\}$, and the phonon propagator in the non-Markovian limit of our time-dependent variational polaron formalism is given by

$$\phi(t,t') = \int_0^\infty d\omega \frac{J(\omega)F(\omega,t)F(\omega,t')}{\omega^2}\Big(\cos(\omega(t-t'))\coth\Big(\frac{\beta\omega}{2}\Big) - i\sin\big(\omega(t-t')\big)\Big). \quad (5.17)$$

To maintain the relationship $\Lambda^*(t,t') = \Lambda(t',t)$ to give $\Lambda_{zy}(t,t') = \Lambda^*_{yz}(t',t)$ we define $\Lambda'_{yz}(t,t') = i\Lambda_{yz}(t,t')$. A full derivation of the correlation functions can be found in Appendix C. From here we absorb the correlation functions and integrals into the commutators of the master equation allowing us to define the non-Markovian interaction picture variational bath rate operators as

$$\begin{aligned}
\tilde{\chi}_{j=x,y}(t) &= \int_0^t ds\tilde{\sigma}_j(s)\Lambda_{jj}(t,s),\\
\tilde{\theta}_z(t) &= \int_0^t ds\tilde{\sigma}^\dagger\tilde{\sigma}(s)\Lambda_{zz}(t,s),\\
\tilde{\Xi}_y(t) &= \int_0^t ds\sigma_y(s)\Lambda'_{zy}(t,s),\\
\tilde{\Xi}_z(t) &= \int_0^t ds\tilde{\sigma}^\dagger\tilde{\sigma}(s)\Lambda'_{yz}(t,s),
\end{aligned} \quad (5.18)$$

This yields an interaction picture master equation of the form

$$\begin{aligned}
\frac{\partial}{\partial t}\tilde{\rho}_S(t) = &-\Big([\tilde{\sigma}^\dagger\tilde{\sigma}(t),\tilde{\theta}_z(t)\tilde{\rho}_S(t)] - [\tilde{\rho}_S(t)\tilde{\theta}^\dagger_z(t),\tilde{\sigma}^\dagger\tilde{\sigma}(t)]\Big)\\
&-\Big\{\sum_{i=x,y}\Big([\tilde{\sigma}_i(t),\tilde{\chi}_i(t)\tilde{\rho}_S(t)] + [\tilde{\sigma}_i(t),\tilde{\rho}_S(t)\tilde{\chi}^\dagger_i(t)]\Big)\Big\}\\
&-i\Big([\tilde{\sigma}_y(t),\tilde{\Xi}_z(t)\tilde{\rho}_S(t)] - [\tilde{\rho}_S(t)\tilde{\Xi}^\dagger_z(t),\tilde{\sigma}_y(t)]\Big)\\
&+i\Big([\tilde{\sigma}^\dagger\tilde{\sigma}(t),\tilde{\Xi}_y(t)\tilde{\rho}_S(t)] - [\tilde{\rho}_S(t)\tilde{\Xi}^\dagger_y(t),\tilde{\sigma}^\dagger\tilde{\sigma}(t)]\Big).
\end{aligned} \quad (5.19)$$

The time-ordering operator included in Eq. 5.10 makes analytical solutions extremely difficult if not impossible. Equivalently, we may instead solve the differential equation

$$\partial_t U(t) = -iH_0(t)U(t), \quad (5.20)$$

to calculate the unitary operators while also accounting for time ordering. Additionally, solving this differential equation allows us to perform a unitary transformation back to the Schrödinger picture, naturally simplifying the expectation values we wish to calculate. Our time-dependent variational polaron master equation in the Schrödinger picture is then given by

$$\begin{aligned}\frac{\partial}{\partial t}\rho_S(t) =& -i\big[H_0(t),\rho_S(t)\big] \\ &- \Big\{\sum_{i=x,y}\Big([\sigma_i,\chi_i(t)\rho_S(t)] + [\sigma_i,\rho_S(t)\chi_i^\dagger(t)]\Big)\Big\} \\ &- \Big([\sigma^\dagger\sigma,\theta_z(t)\rho_s(t)] - [\rho_S(t)\theta_z^\dagger(t),\sigma^\dagger\sigma]\Big) \\ &- i\Big([\sigma_y,\Xi_z(t)\rho_S(t)] - [\rho_S(t)\Xi_z^\dagger(t),\sigma_y]\Big) \\ &+ i\Big([\sigma^\dagger\sigma,\Xi_y(t)\rho_S(t)] - [\rho_S(t)\Xi_y^\dagger(t),\sigma^\dagger\sigma]\Big),\end{aligned} \tag{5.21}$$

where, defining $\varrho(t',t) = U(t)U^\dagger(t')\varrho U(t')U^\dagger(t)$ for $\varrho \in \{\sigma_x,\sigma_y,\sigma^\dagger\sigma\}$, the Schrödinger picture rate operators are given by

$$\begin{aligned}\chi_{j=x,y}(t) &= \int_0^t ds\sigma_j(t',t)\Lambda_{jj}(t,t'), \\ \theta_z(t) &= \int_0^t ds\sigma^\dagger\sigma(t',t)\Lambda_{zz}(t,t'), \\ \Xi_y(t) &= \int_0^t ds\sigma_y(t',t)\Lambda'_{zy}(t,t'), \\ \Xi_z(t) &= \int_0^t ds\sigma^\dagger\sigma(t',t)\Lambda'_{yz}(t,t').\end{aligned} \tag{5.22}$$

5.3.1 Recovering the Weak-Coupling and Polaron Models

We can recover both the non-Markovian polaron and weak-coupling models from our time-dependent variational polaron master equation. If we take the limit of $F(\omega,t) = 1\ \forall\ \omega,t$ (i.e. the limit where the bath is always fully displaced) we find that both the weak-coupling type correlation function and cross-correlation functions go to zero. Thus the only remaining non-zero correlation functions are the polaron type correlation functions ($\Lambda_{xx}(t,t')$ and $\Lambda_{yy}(t,t')$). The full time-dependent variational polaron master equation then reduces to the non-Markovian polaron master equation, given by Eq. 4.16, in this limit.

Taking the limit of $F(\omega,t) = 0\ \forall\ \omega,t$ such that the bath is not dis-

placed by the variational polaron transformation, we can recover the non-Markovian weak-coupling model, the non-Markovian form of the master equation in [117, 121]. In this limit only a single correlation function, $\Lambda_{zz}(t,t')$, remains non-zero, and thus the non-Markovian master equation reduces to the weak-coupling master equation in the Schrödinger picture given by

$$\frac{\partial}{\partial t}\rho_S(t) = -i\big[H_0(t),\rho_S(t)\big] - \Big([\sigma^\dagger\sigma,\theta_z(t)\rho_S(t)] - [\rho_S(t)\theta_z^\dagger(t),\sigma^\dagger\sigma]\Big), \quad (5.23)$$

where the weak-coupling rate operator is given by

$$\theta_z(t) = \int_0^t ds\sigma^\dagger\sigma(t',t)\Lambda_{zz}(t,t'). \quad (5.24)$$

5.4 The Variational Function and Renormalisation of the Rabi Frequency

Before investigating the full dynamics of the system, we can gain an initial understanding of the effects captured in the time-dependent variational polaron model by considering the behaviour of both the variational function, $F(\omega,t)$, and the renormalisation of the Rabi frequency. To this end we plot both $F(\omega,t)$ and the time-integrated ratio of the renormalised Rabi frequency to bare Rabi frequency ($\int_0^\infty dt\ \Omega_r(t)/\Omega(t)$) for a range of driving pulse parameters.

To calculate the variational function, renormalisation, and dynamics, we shall assume the system is driven by an optical pulse with a Gaussian envelope such that the time-dependent Rabi frequency of the pulse is given by

$$\Omega(t) = \frac{\Theta}{\sqrt{2\pi w^2}}\exp\left\{-\frac{(t-t_0)^2}{2w^2}\right\}. \quad (5.25)$$

Here Θ is the pulse area, t_0 is the arrival time of the pulse, and w is the Gaussian width of the pulse electric field. The latter quantity is related to the electric field Full-Width Half Maximum (FWHM) by

$$w = \frac{\Delta\tau_E}{2\sqrt{2\ln 2}}, \quad (5.26)$$

where $\Delta\tau_E$ is the electric field FWHM. This is in turn related to the intensity FWHM, $\Delta\tau_I$, measured in experiment, by $\Delta\tau_E = \Delta\tau_I\sqrt{2}$. It is this latter quantity that we shall refer to in this chapter when quoting pulse widths.

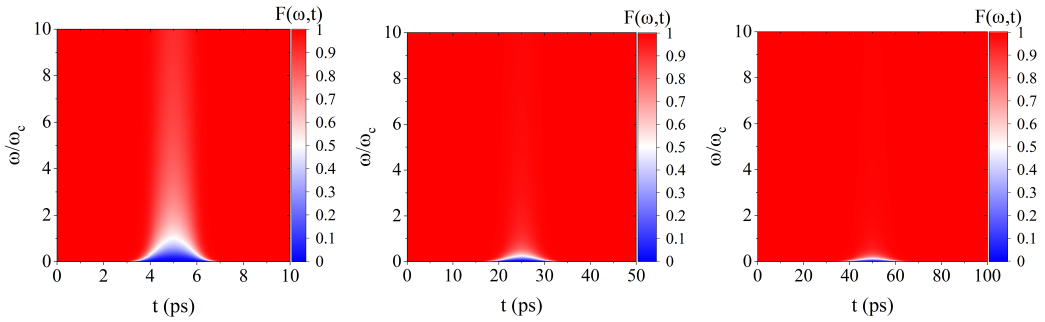

(a) $\Theta = 2\pi,\ \Delta\tau_I = 1$ ps (b) $\Theta = 2\pi,\ \Delta\tau_I = 5$ ps (c) $\Theta = 2\pi,\ \Delta\tau_I = 10$ ps

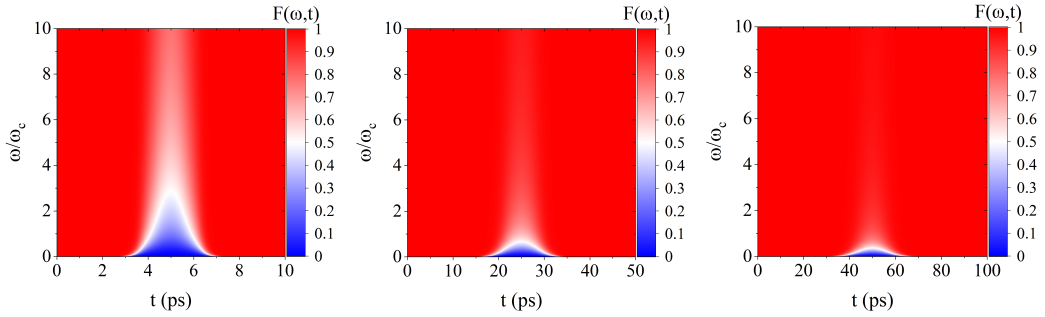

(d) $\Theta = 6\pi,\ \Delta\tau_I = 1$ ps (e) $\Theta = 6\pi,\ \Delta\tau_I = 5$ ps (f) $\Theta = 6\pi,\ \Delta\tau_I = 10$ ps

Figure 5.2: The variational function, $F(\omega, t)$, plotted as a function of time t and the bath mode frequencies as a factor of the cut-off frequency ω_c when driving a QD with a Gaussian. The area (Θ) and Full-Width Half Maximum (FWHM) ($\Delta\tau_I$) of the driving pulse is indicated under each figure. Parameters used: $\omega_c = 2.2$ ps^{-1}, $t_0 = 5\Delta\tau_I$, and $T = 5$ K.

Figure 5.2 shows the time-dependent variational function, $F(\omega, t)$, plotted as a function of both time and the frequencies of the bath modes, for two different Gaussian pulse areas ($\Theta \in \{2\pi, 6\pi\}$) and three different pulse widths ($\Delta\tau_I \in \{1\text{ ps},\ 5\text{ ps},\ 10\text{ ps}\}$). For all of the pulse parameters shown in Figure 5.2, we find $F(\omega, t) = 1\ \forall\ \omega$ before and after the driving pulse. Thus we expect the system to evolve purely according to the standard polaron model with vanishing Rabi frequency. However, during the pulse we find $F(\omega, t) \to 0$ for the lower frequency bath modes, indicating a weak-coupling type interaction between the QD and these phonon modes. Figure 5.2 shows that the range of bath modes that experience this weak-coupling-type interaction during the pulse increases with increasing pulse area, and decreasing pulse duration. Hence, from the form of the variational function, we find that when driving the system with pulses of short duration and large area the QD states primarily evolve according to the weak-coupling model during the pulse. This indicates that the bath modes that evolve on longer characteristic timescales than the QD states are not displaced as in the polaron model.

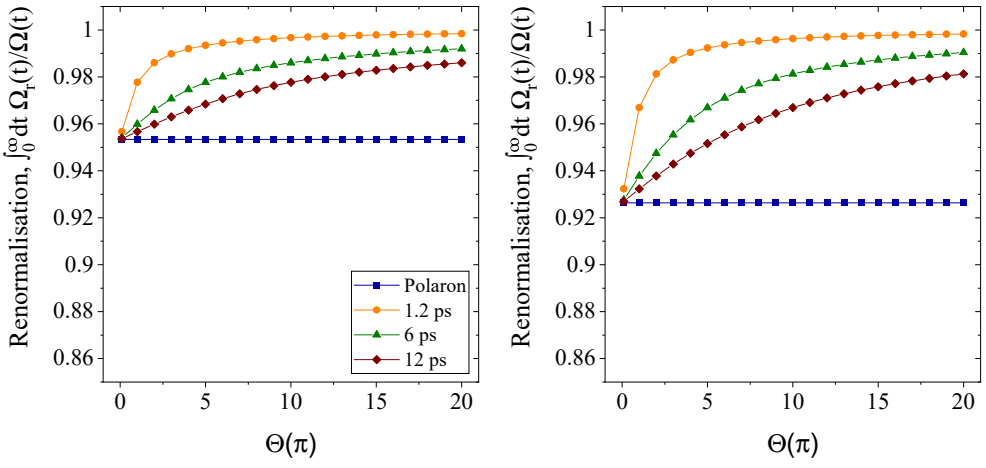

(a) $T = 5$ K (b) $T = 10$ K

(c) $T = 15$ K (d) $T = 20$ K

Figure 5.3: The renormalisation predicted by the polaron (blue squares) and variational polaron models as a function of pulse area for temperatures (a) $T = 5$ K, (b) $T = 10$ K, (c) $T = 15$ K, and (d) $T = 20$ K. The renormalisation calculated using the variational polaron model is also plotted for a number of driving pulse Full-Width Half Maximum (FWHM), namely $\Delta\tau_I = 1.2$ ps (orange circles), $\Delta\tau_I = 6$ ps (green triangles), and $\Delta\tau_I = 12$ ps (burgundy diamonds). Parameters used: $\alpha = 0.027$ ps^2, and $\omega_c = 2.2$ ps^{-1}.

While the variational function does have a temperature dependence through the presence of β in the hyperbolic functions, the effect of increasing temperature on $F(\omega, t)$ is subtle. The effects of varying temperature are more clearly demonstrated through the renormalisation of the Rabi frequency. Figure 5.3 shows the renormalisation, calculated as the time-integrated ratio of the renormalised and bare Rabi frequencies. As expected from Eq. 4.9, the renormalisation of the Rabi frequency predicted by the polaron model is independent of the parameters of the driving pulse, and only changes as a function of temperature. In contrast, the renormalisation of the Rabi frequency returned by the time-dependent variational polaron model shows a strong dependence on both the pulse area and FWHM, in addition to exhibiting a temperature dependence. From Figure 5.3 we expect there to be a reasonable agreement between the polaron and variational polaron models in the limit of small pulse area and large FWHM. However, with increasing pulse area and/or decreasing FWHM the renormalisation of the Rabi frequency predicted by the time-dependent variational polaron model diverges away from the polaron model and towards the weak-coupling regime, returning unity renormalisation. In other words, our time-dependent variational polaron model predicts that the Rabi frequency is not renormalised by the phonon coupling in the limit of large pulse area, i.e. $\Omega_r(t) \to \Omega(t)$ as $\Theta \to \infty$. This further indicates the polaron model breaks down in the limit of large peak Rabi frequency in agreement with the variational function.

5.5 Dynamics Under Resonant Pulsed Excitation

Neglecting spontaneous emission (i.e. setting $\gamma = 0$), we shall now compare the system dynamics predicted by the standard polaron and weak-coupling models under pulsed resonant excitation to those predicted by our time-dependent variational polaron model. The relevant expectation values can be calculated from the time-dependent density matrices produced by each model using

$$\langle \mathbf{O}(t) \rangle = \mathrm{Tr}\{\mathbf{O}\rho_S(t)\}, \tag{5.27}$$

where $\mathbf{O}$ is the Schrödinger picture operator for which we wish to calculate the expectation value. Just as with the polaron model in Chapter 4, we calculate $\rho(t)$ using an initial value problem approach, only now using the time-

dependent variational polaron Liouvillian in the master equation. This allows us to evolve the state of the system over a number of discrete time steps starting from an arbitrary initial state $\rho(t = 0)$.

5.5.1 Time-Resolved Dynamics

To gain an initial understanding of the response of the system dynamics, we first calculate the temporal evolution of the exciton population and coherences, which we plot as the real component of $\sigma_x = \sigma^\dagger + \sigma$, for fixed pulse parameters. Figure 5.4 shows the resulting time-resolved dynamics assuming the bath is held at $T = 5$ K, and the system is driven by a Gaussian pulse with central frequency $\omega_l = \omega_X - \int_0^\infty d\omega \frac{J(\omega)F(\omega,t=0)}{\omega}(2 - F(\omega, t = 0))$, area $\Theta = 10\pi$, and FWHM $\Delta\tau_I \in \{1.2,\ 6,\ 12\}$ ps. Our predictions from the behaviours of the variational function, and renormalisation of the Rabi frequency, are borne out in these dynamics. In the limit of short pulse duration, the exciton dynamics in Figure 5.4a show a close agreement between our time-dependent variational polaron model and the weak-coupling model. On the other hand, in this regime the polaron model overestimates the magnitude of the effects resulting from the QD-phonon coupling. From the coherences calculated with $\Delta\tau_I = 1.2$ ps (Figure 5.4b) we see a closer agreement between our time-dependent variational polaron model and the weak-coupling model than between the former and standard polaron model during the pulse. However, the coherence also clearly demonstrates that the time-dependent variational polaron model predicts the system evolves according to the standard polaron model before and after the pulse. At intermediate pulse widths all three models show a relatively close agreement for the parameters used as can be seen in Figures 5.4c and 5.4d. However, it is again the weak-coupling model that returns the exciton dynamics that most closely agree with those from our time-dependent variational polaron model for the pulse parameters used. On the other hand, it is the two polaron models that show the greater concurrence when considering the coherences. When driving the system with the longest pulse duration studied the reverse is true. In this regime it is now the polaron model that shows greater concurrence with the time-dependent variational polaron model (see Figures 5.4e and 5.4f).

We can further our understanding of this behaviour by considering the bath correlation functions shown in Figures 5.5, 5.6, and 5.7. As we predicted from the variational function, for all pulse widths it is the polaron-type correlation functions that dominate the evolution of the state of the system before the pulse ($t \ll t_0$), with the other correlation functions at or near zero. For pulses

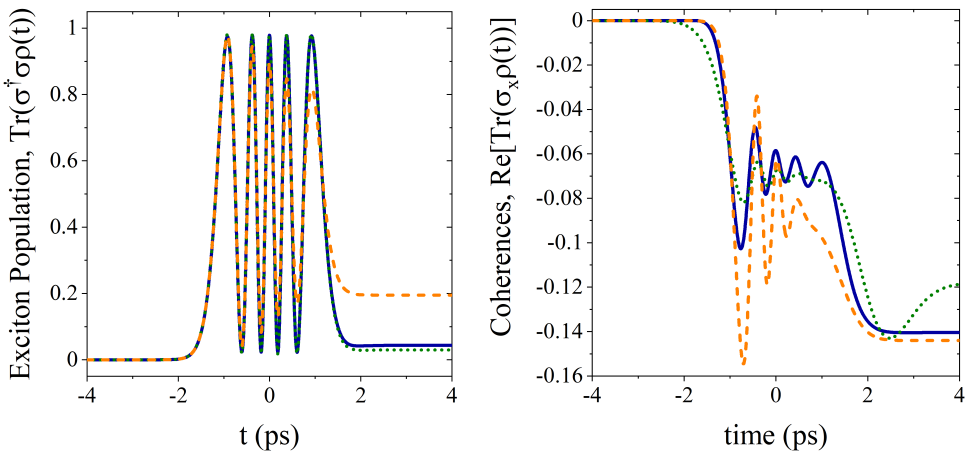

(a) $\Delta\tau_I = 1.2$ ps

(b) $\Delta\tau_I = 1.2$ ps

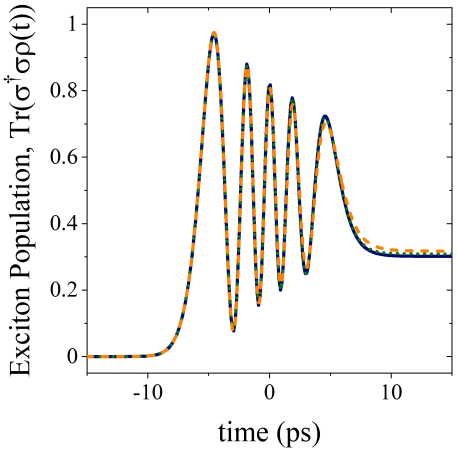

(c) $\Delta\tau_I = 6$ ps

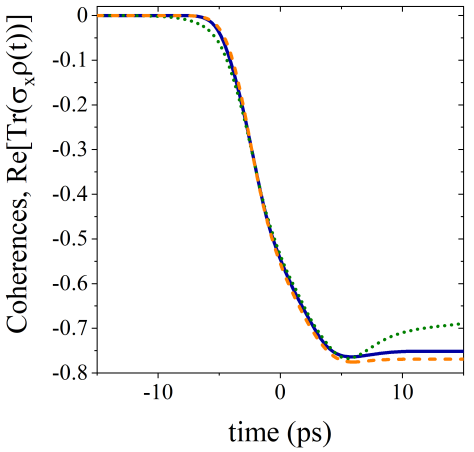

(d) $\Delta\tau_I = 6$ ps

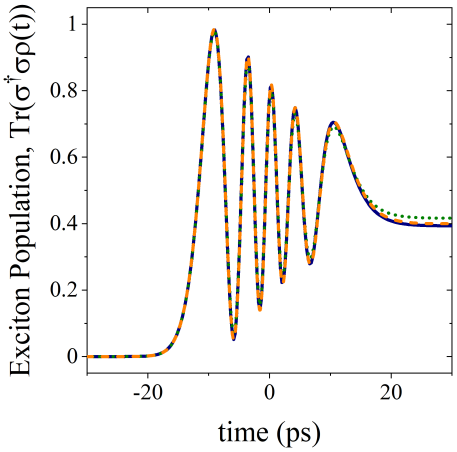

(e) $\Delta\tau_I = 12$ ps

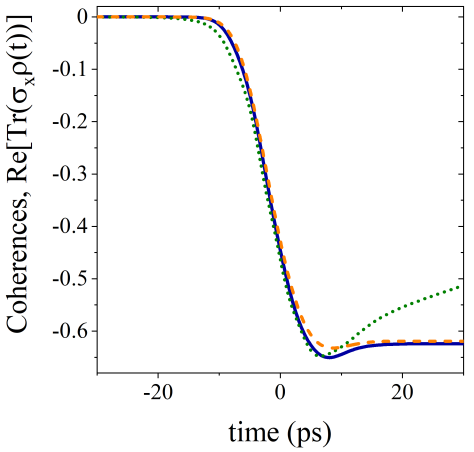

(f) $\Delta\tau_I = 12$ ps

Figure 5.4: The temporal dynamics of the (left) exciton populations, and (right) coherences plotted as the real component of σ_x, centred about the pulse maxima and calculated using the weak-coupling (green dots), full polaron (orange dashed), and time-dependent variational polaron (blue solid) models. The dynamics are calculated for three pulse widths indicated under each sub-figure. Parameters used: $\alpha = 0.027$ ps^2, $\omega_c = 2.2$ ps^{-1}, $\Theta = 10\pi$, $T = 5$ K, and $\omega_l = \omega_X - \int_0^\infty d\omega \frac{J(\omega)F(\omega,t=0)}{\omega}(2 - F(\omega, t = 0))$.

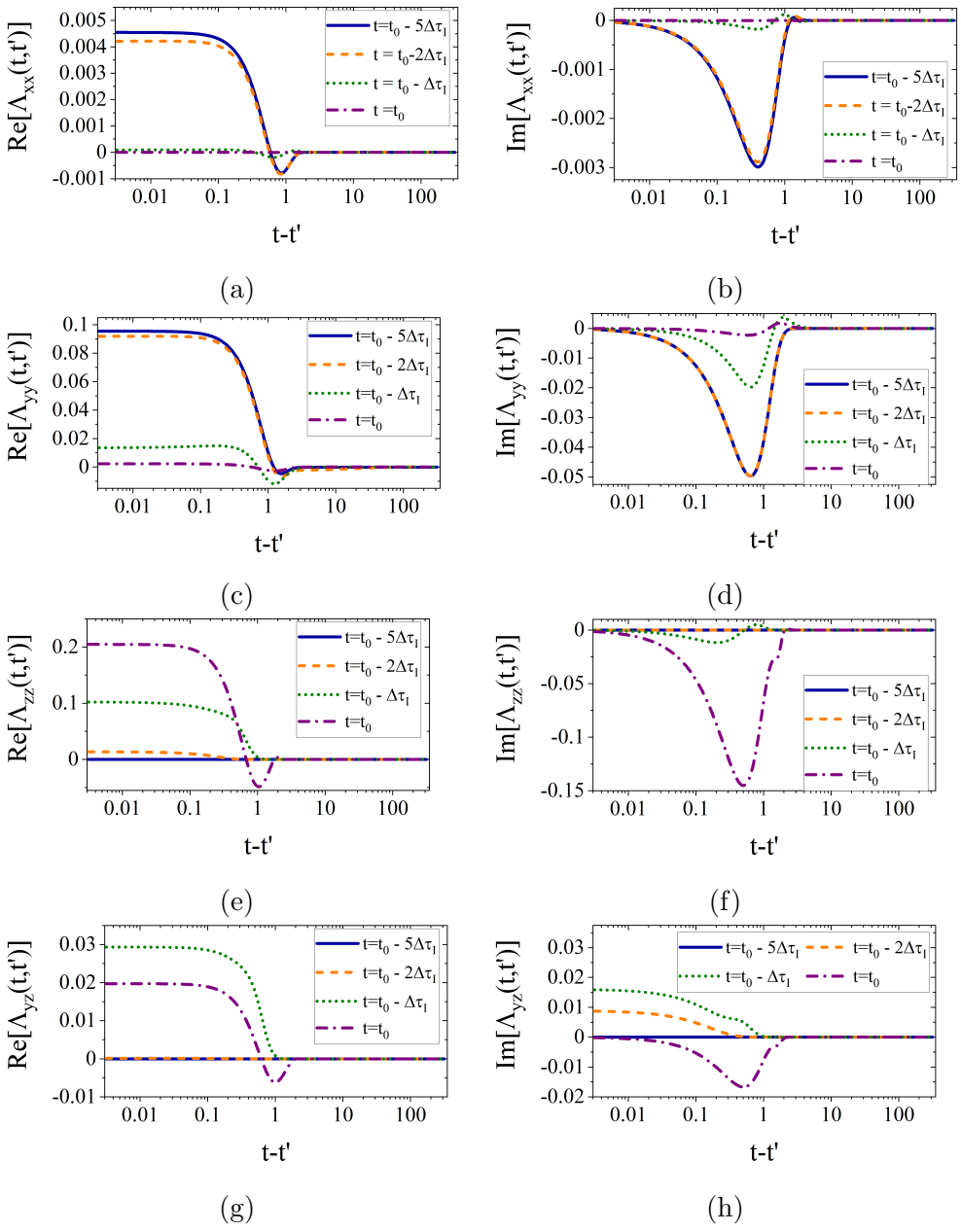

Figure 5.5: The (left) real and (right) imaginary components of the time-dependent variational polaron bath correlation functions calculated when driving a Quantum Dot (QD) with a Gaussian pulse of Full-Width Half Maximum (FWHM) $\Delta\tau_I = 1.2$ ps, and pulse area $\Theta = 10\pi$. Parameters used: $\omega_c = 2.2$ ps^{-1}, $\alpha = 0.027$ ps^2, and $T = 5$ K.

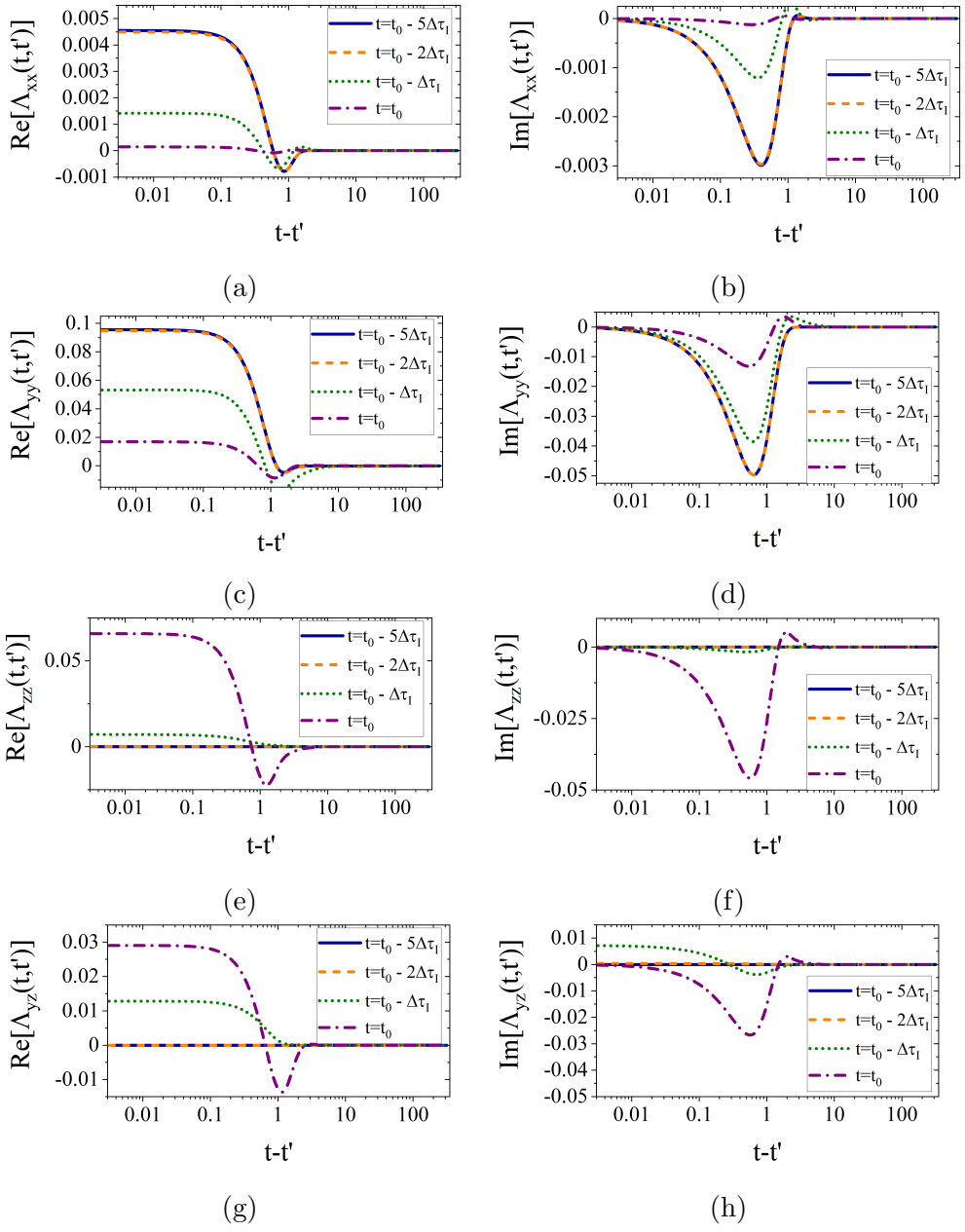

Figure 5.6: The real and imaginary components of the time-dependent variational polaron bath correlation functions calculated when driving a Quantum Dot (QD) with a Gaussian pulse of Full-Width Half Maximum (FWHM) $\Delta\tau_I = 6$ ps, and pulse area $\Theta = 10\pi$. Parameters used: $\omega_c = 2.2$ ps^{-1}, $\alpha = 0.027$ ps^2, and $T = 5$ K.

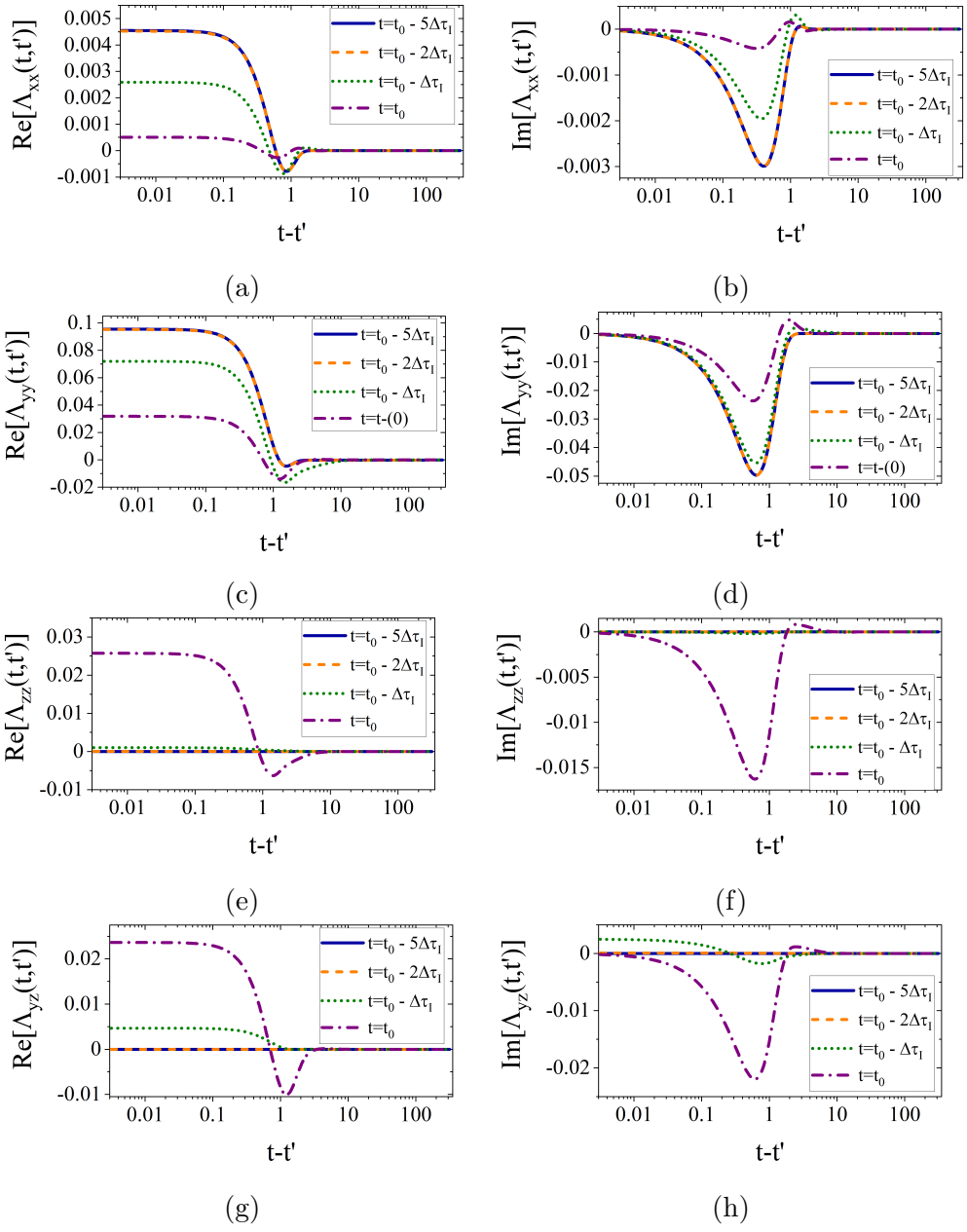

Figure 5.7: The real and imaginary components of the time-dependent variational polaron bath correlation functions calculated when driving a Quantum Dot (QD) with a Gaussian pulse of Full-Width Half Maximum (FWHM) $\Delta\tau_I = 12$ ps, and pulse area $\Theta = 10\pi$. Parameters used: $\omega_c = 2.2$ ps^{-1}, $\alpha = 0.027$ ps^2, and $T = 5$ K.

of short duration, we find the weak-coupling correlation function governs the evolution of the system during the pulse as can be seen in Figure 5.5. During the pulse the polaron-type correlation functions tend to zero, and while there is a non-zero contribution from the cross-correlation function this is an order of magnitude smaller than the weak-coupling correlation function. Figure 5.6 shows that at intermediate pulse widths all of the correlation functions contribute to the system evolution during the pulse. Moving towards the peak of the pulse, the polaron-type correlation functions tend towards zero just as in the short pulse limit, but even at the peak of the pulse a non-zero polaron-type contribution remains. Conversely, the weak-coupling correlation function no longer dominates in this regime as there is a near equal contribution to the dynamics from the cross-correlation function. Finally, in the limit of long pulse duration we find the polaron-type correlation functions overall provide the dominant contribution to the system dynamics as can be seen in Figure 5.7. However, even in this long pulse regime, at the peak of the pulse we find there is still a strong contribution from the weak-coupling correlation and cross-correlation functions for the pulse parameters used. At the FWHM the weak-coupling correlation functions return to (near) zero.

5.5.2 Rabi Rotations

After studying the time-resolved dynamics of the exciton population returned by our time-dependent variational polaron model when driving with a Gaussian pulse with fixed parameters at a fixed temperature, we can move on to study the effects of varying the driving strength and system temperature. To do this we calculate the steady-state exciton population (still assuming $\gamma = 0$ ps^{-1}) sweeping the area of the driving pulse for a range of temperatures and pulse FWHM. Figure 5.8 shows the resulting Rabi rotations for $0\pi \leq \Theta \leq 20\pi$, 5 K $\leq T \leq$ 50 K, and $\Delta\tau_I \in \{1.2, 6, 12\}$ ps.

From the time-dependent variational function and renormalisation of the Rabi frequency, we expect our time-dependent variational polaron model to show a close agreement with the weak-coupling model in the limit of short pulse duration across the range of pulse areas studied. Figures 5.8a and 5.9a show that in the low temperature limit this is indeed true across the range of pulse areas studied with both models returning (nearly) undamped Rabi rotations. On the other hand, we find the polaron model increasingly overestimates the magnitude of the dissipative effects of the QD-phonon coupling with increasing pulse area. When the states of the QD evolve on timescales

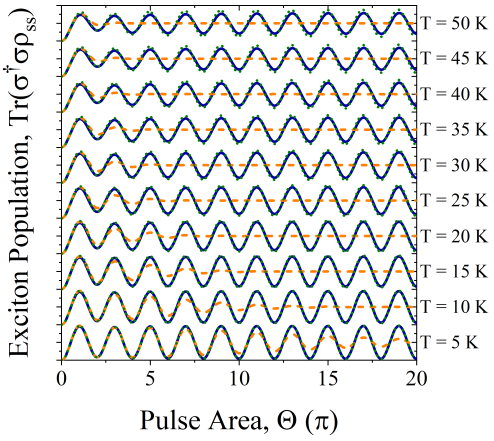

(a) $\Delta\tau_I = 1.2$ ps

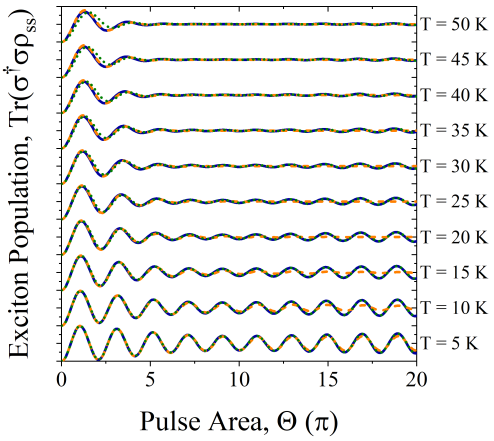

(b) $\Delta\tau_I = 6$ ps

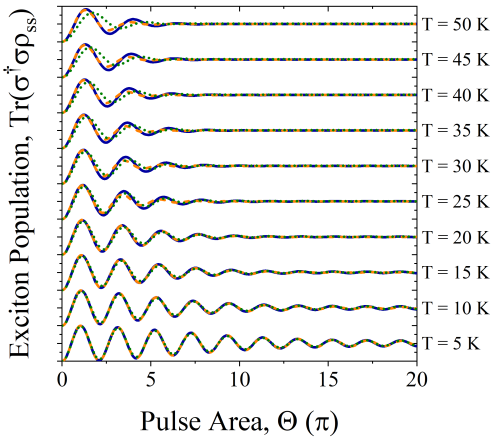

(c) $\Delta\tau_I = 12$ ps

Figure 5.8: The steady-state exciton populations calculated using the weak-coupling (green dot), polaron (orange dash), and time-dependent variational polaron (solid blue) models after driving a Quantum Dot (QD) with a Gaussian pulse, and neglecting spontaneous emission. The final exciton population is plotted as a function of the pulse area for four temperatures, $T \in \{5, 10, 15, 20\}$ K, off-set for clarity. Parameters used: $\omega_c = 2.2$ ps^{-1}, $\alpha = 0.027$ ps^2. $\Omega(t_0) = \omega_c$ at (a) $\Theta = 1.27\pi$, (b) $\Theta = 6.33\pi$, and (c) $\Theta = 12.65\pi$.

shorter than the characteristic timescales of the phonon bath, polarons, quasi-particles formed when a charge carrier displaces the charged atoms of a crystal lattice [46], are unable to form. That is, under such conditions, the exciton recombines before the bath is able to react. Hence the polaron model, which over-estimates the coupling strength to the low-frequency bath modes in this regime and thus assumes a polaron is always formed, increasingly overestimates the phonon effects with increasing pulse area under excitation by short optical pulses. As such, when combined with the fact that the polaron model only remains valid for pulse areas $\Theta \leq 1.27\pi$ in this regime, the polaron model clearly has extremely limited utility at such short pulse durations. At the lower temperatures studied, our Rabi rotation results in the short pulse regime agree with those presented in [122], where the accuracy of the weak-coupling model under excitation with short Gaussian optical pulses ($\Delta\tau_I \approx 1.7$ ps) is experimentally verified at $T = 12.5$ K.

Increasing the system temperature when driving with a short optical pulse we find the standard polaron model increasingly over-estimates the impact of the coupling to the phonon bath (see Figures 5.8a and 5.9b). This over-estimation occurs despite the polaron model increasingly under-estimating the frequency at which the spectral density is sampled compared to our time-dependent variational polaron model as can be seen in Figure 5.3. This under-estimation should return a subsequent under-estimation of the phonon-coupling effects. However, at higher temperatures the number of phonon modes our time-dependent variational polaron modes predicts to weakly-couple to the QD during the pulse increases for this pulse duration. Hence the polaron model actually increasingly over-estimates the phonon effects at higher temperatures. Conversely, the weak-coupling model under-estimates the phonon-coupling effects at high temperatures as shown in Figure 5.9b. From our time-dependent variational polaron model we expect the system to evolve increasingly according to the polaron model as the pulse decays to vanishing Rabi frequency. It is this shift in behaviour from the weak-coupling to polaron models at the end of the pulse that results in the weak-coupling model under-estimating the results of the phonon-coupling at high temperatures.

Under optical driving with Gaussian pulses of intermediate width, we find neither the weak-coupling nor the standard polaron model shows consistent concurrence with the dynamics returned by our time-dependent variational polaron model at $T = 5$ K (see Figure 5.8b and 5.9c). In the limit of small pulse area there is a closer agreement between the standard polaron and

time-dependent polaron models than between the weak-coupling and time-dependent variational polaron models. However, at $\Theta = 6.33\pi$ the peak Rabi frequency, $\Omega(t_0)$, reaches the phonon cut-off frequency and thus the standard polaron model is not valid beyond this pulse area. At these larger pulse areas the standard polaron model overestimates the dissipative effects resulting from coupling to the phonon bath. Conversely, the weak-coupling model begins to show a good agreement with our time-dependent variational polaron model in this regime. While there is no consistent close agreement between the models, all three models studied show a clear revival of the amplitude of the Rabi rotations (qualitatively in agreement with [105]) as the pulse area increases beyond $\Theta \approx 10\pi$. This revival occurs when the period of the time-resolved Rabi oscillations become comparable to, or shorter than, ω_c^{-1} [105].

The inconsistent agreement between the three models under resonant excitation with optical pulses of intermediate width continues at higher temperatures. We find the concurrence between the polaron and time-dependent variational polaron models observed at lower temperatures and pulse areas decreases with increasing temperature. At the highest temperatures studied, neither the weak-coupling nor the polaron model adequately agrees with the dynamics returned by our time-dependent variational polaron model across all pulse areas studied. This can be more clearly seen in Figure 5.9d where there is a clear deviation between the weak-coupling (standard polaron) and time-dependent variational polaron models in the limit of small (large) pulse areas. At higher temperatures the average displacement of the bath, and thus also the renormalisation of the Rabi frequency, is increased (i.e. $B(t)$ is increasingly smaller than unity with increasing temperature) at small pulse areas. Hence at small pulse areas the weak-coupling model increasingly over-estimates the frequency at which the spectral density is sampled with increasing temperatures (i.e. $\Omega(t) > \Omega_r(t)$) [106]. This has the effect of increasing the effective coupling between the QD and phonon bath [106] resulting in this difference between the weak-coupling and time-dependent variational polaron models at small pulse areas. At larger pulse areas the Rabi frequency moves out of the regime in which polaron model is valid, and thus the propensity of the polaron model to over-estimate phonon-coupling effects at large pulse areas continues at high temperatures. We also find that the magnitude of the revival of the Rabi rotations predicted with $\Delta\tau_I = 6$ ps is reduced with increasing temperature for all three models within the pulse area limits studied. While the weak-coupling and time-dependent variational polaron models do both still predict some re-

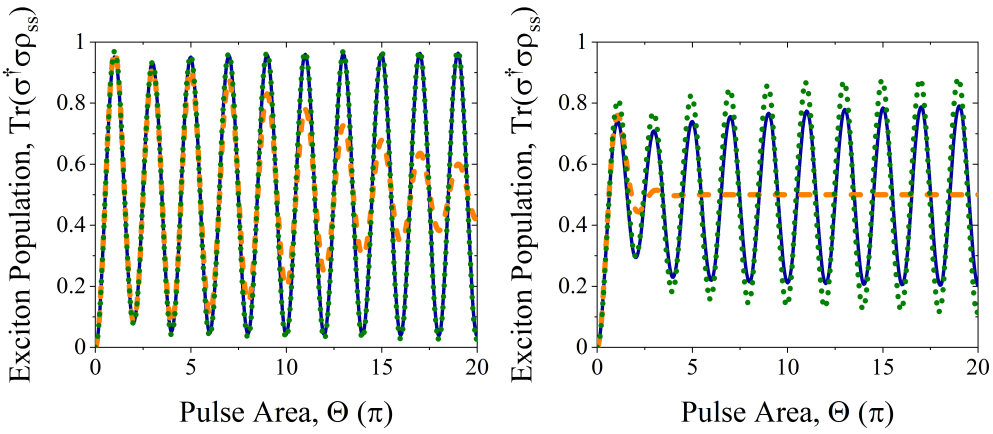

(a) $\Delta\tau_I = 1.2$ ps, $T = 5$ K

(b) $\Delta\tau_I = 1.2$ ps, $T = 50$ K

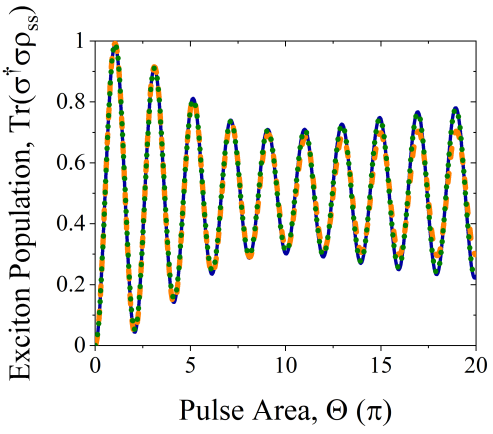

(c) $\Delta\tau_I = 6$ ps, $T = 5$ K

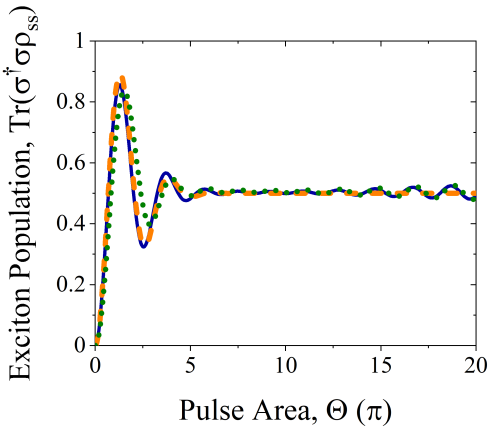

(d) $\Delta\tau_I = 6$ ps, $T = 50$ K

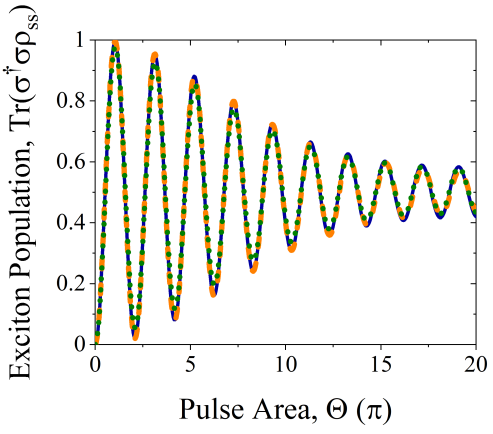

(e) $\Delta\tau_I = 12$ ps, $T = 5$ K

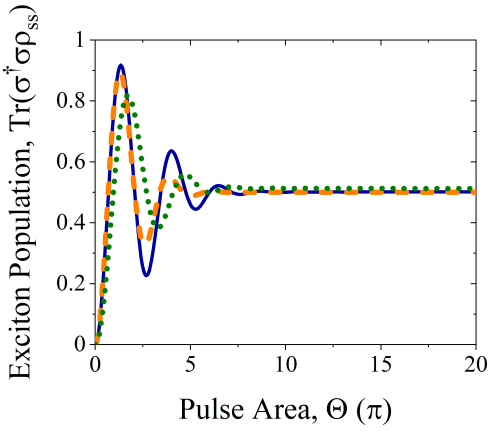

(f) $\Delta\tau_I = 12$ ps, $T = 50$ K

Figure 5.9: The steady-state exciton populations calculated using the weak-coupling (green dot), polaron (orange dash), and time-dependent variational polaron (solid blue) models after driving a Quantum Dot (QD) with a Gaussian pulse. The final exciton population is plotted as a function of the pulse area at (left) $T = 5$ K and (right) $T = 50$ K. Parameters used: $\gamma = 0$ ps^{-1}, $\omega_c = 2.2$ ps^{-1}, $\alpha = 0.027$ ps^2.

vival at larger pulse areas for $T = 50$ K, the polaron model shows no such behaviour in the same regimes.

The long pulse duration limit returns the opposite results of the short pulse limit at low temperatures. From Figures 5.8c and 5.9e we again find that (up to the validity limit of $\Theta = 12.65\pi$) it is the polaron model, rather than the weak-coupling model, that shows a closer concurrence with the time-dependent variational model in agreement with our predictions from the variational function and renormalisation. In this driving regime the QD states evolve on timescales longer than ω_c^{-1}, and thus the phonon bath is able to react to the formation of the exciton, and polarons are able to form. Naturally at the largest pulse areas where the peak Rabi frequency exceeds the phonon cut-off frequency there is a discrepancy between the standard polaron model and our time-dependent variational polaron model, with the former again over-estimating the effects of coupling to the phonon bath. However, as this driving regime lies beyond, but close to, the limit of the regime of validity of the standard polaron model, the magnitude of the discrepancy is not as large as under excitation by short optical pulses. Meanwhile, Figure 5.9e shows the weak-coupling model overestimates the damping of the Rabi rotations in this limit for all pulse areas studied in agreement with [106]. Just as we found in the high temperature and small pulse area limits when driving with a Gaussian pulse of intermediate width, as $\Omega(t) > \Omega_r(t)$ the weak-coupling model samples the phonon spectral density closer to its peak than the two polaron models across the range of pulse areas in this driving width regime [106]. This again results in an increase in the effective coupling strength between the phonon bath and QD states magnifying the phonon-coupling effects returned by the weak-coupling model [106].

With a Gaussian pulse of width $\Delta\tau_I = 12$ ps, studying the dynamics returned by our time-dependent variational polaron model we find the both the standard polaron and weak-coupling models increasingly over-estimate the phonon damping effects with increasing temperature. This can be seen in Figures 5.8c and 5.9f. Just as we found in the intermediate pulse duration regime, we find a significant discrepancy between the dynamics returned by the weak-coupling and time-dependent variational polaron models for high temperatures and small pulse areas as the weak-coupling model continues to under-estimate the renormalisation of the Rabi frequency across all temperatures. Conversely, for the larger pulse areas studied we do find a closer agreement between the two polaron models at $T = 50$ K, although again the polaron model is invalid beyond $\Theta = 12.65\pi$.

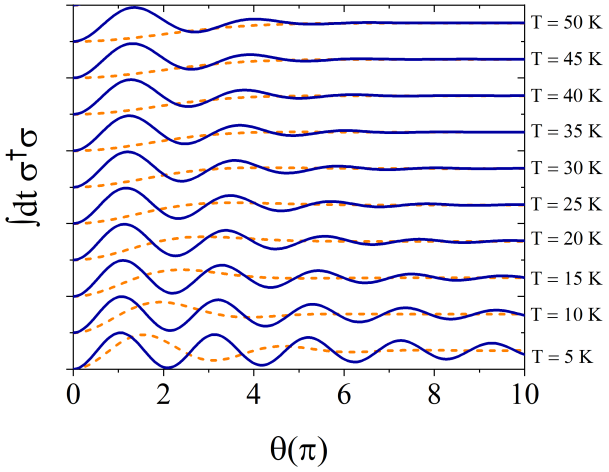

Figure 5.10: The integrated excited state population of a Quantum Dot (QD) coupled to a phonon bath as a function of the driving pulse area for a range of temperatures between 5 K and 50 K calculated using the polaron model. The dynamics are plotted for two different coupling strengths, $\alpha = 0.027$ ps^{-2} (solid blue), and $\alpha = 0.27$ ps^2 (dashed orange). Parameters used: $\omega_c = 2.2$ ps^{-1}, $\Delta\tau_I = 10$ ps, and $\gamma^{-1} = 0.971$ ns.

Through our derivation of the master equation we found the polaron model, and by extension the variational polaron model in the appropriate limits, predicts a renormalisation of the Rabi frequency of the driving pulse that we plotted in Figure 5.3. However, setting $F(\omega, t) = 0$ to recover the weak-coupling model returns $\Omega_r(t) = \Omega(t)$ and as such there is no renormalisation predicted in the weak-coupling limit. While the effects of the renormalisation do manifest in Figure 5.8, they are difficult to observe. Figure 5.10 shows a clearer demonstration of these effects in the polaron limit when sweeping the area of the driving pulse by increasing α. When increasing the temperature of the bath it can be seen that the peaks in the Rabi oscillations shift to larger pulse areas in addition to becoming more heavily damped due to increasing dissipative phonon effects. Note for simplicity we have taken the Markovian limit of the full polaron model, and having reintroduced spontaneous emission calculate the time-integrated (rather than steady-state) exciton population.

5.6 Comparison with Numerically Exact Path-Integral Methods

While our time-dependent variational polaron model shows a clear improvement over the weak-coupling and standard polaron models, the results are

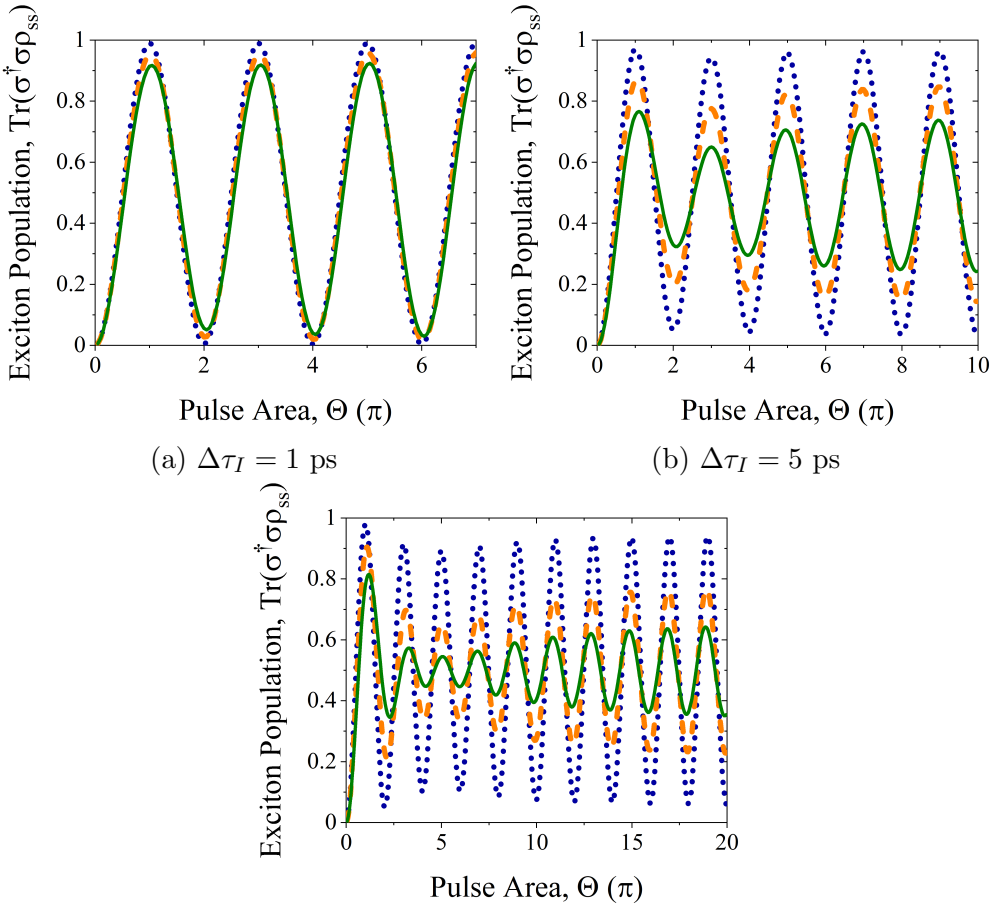

(a) $\Delta\tau_I = 1$ ps (b) $\Delta\tau_I = 5$ ps

(c) $\Delta\tau_I = 10$ ps

Figure 5.11: The steady-state exciton populations calculated using the time-dependent variational polaron model after driving a Quantum Dot (QD) with a Gaussian pulse at temperatures (blue dot) $T = 10$ K, (orange dash) $T = 50$ K, and (solid green) $T = 100$ K. The final exciton population is plotted as a function of the pulse area for three pulse widths, $\Delta\tau_I \in \{1, 5, 10\}$ ps. Parameters used: $\omega_c = 0.725$ ps^{-1}, $\alpha = 0.036$ ps^2.

still approximate due to the treatment of the QD-phonon interaction as a perturbation to second-order. However, there are a number of numerically exact techniques that may be used to calculate the dynamics of a quantum system coupled to a bath of quantum harmonic oscillators. Thus, using the same system parameters, we may compare the dynamics returned by our time-dependent variational polaron model to the dynamics returned by numerically exact methods to determine the accuracy of the behaviours predicted by our model.

Using path-integral methods, numerically exact QD exciton dynamics under pulsed resonant excitation have been calculated [105, 123]. The exciton dynamics presented in [105] assume the system is driven by a square optical

pulse. Owing to the derivative of $F(\omega, t)$ in the correlation functions, our time-dependent variational polaron model is not suited to driving conditions that include discontinuities such as those found in perfectly square pulses. Thus we can only make a qualitative comparison of the dynamics returned by our time-dependent variational polaron model with Gaussian pulses to those presented in [105]. From the deformation potentials and material properties listed in the literature [105, 109], and assuming a spherical QD of radius $r = 5$ nm [105], we calculate the phonon parameters used in our time-dependent variational polaron model to be $\alpha = 0.036$ ps^2 and $\omega_c = 0.725$ ps^{-1}. Figure 5.11 shows the resulting Rabi rotations predicted by our time-dependent variational polaron model for $\Delta\tau_I \in \{1, 5, 10\}$ ps and $T \in \{10, 50, 100\}$ K.

In agreement with [105], we find that when driving a QD with pulses of short duration (Figure 5.11a) there is a minimal damping of the Rabi rotations that, while increasing with increasing temperature, remains small even at higher temperatures. Regardless of pulse duration, our time-dependent variational polaron model predicts a revival of the amplitude of the Rabi rotations with increasing pulse area again agreeing with the results presented in [105]. However, the magnitudes of the damping and revival of these dynamics is not of the same magnitude as the results in [105], which is likely a consequence of using different pulse envelopes [123]. As observed in the literature, we find the revival of the magnitude of the Rabi rotations returned by our time-dependent variational polaron model occurs after a larger number of periods for longer pulse durations.

5.7 Summary

In summary, we have extended the CW variational polaron model to derive a non-Markovian time-dependent variational polaron master equation that accounts for optical driving with (short) pulses. When optically driving a QD in the short pulse regime, we have demonstrated a good agreement between our time-dependent variational polaron model, and the non-Markovian weak-coupling model at low temperatures. In this regime we have shown that the standard polaron model over-estimates the coupling strength to the lower-frequency bath modes resulting in an over-estimation of the phonon induced damping of the Rabi oscillations. Conversely, in the long optical pulse regime our results show it is the standard polaron model that shows a greater concurrence with our time-dependent polaron model at low temperatures. As

the weak-coupling model does not predict a renormalisation of the Rabi frequency, it samples the phonon spectral density closer to its peak which increases the effective coupling to the phonon bath. At high temperatures we have seen that neither the weak-coupling model nor standard polaron model consistently agrees with our time-dependent variational polaron model. Thus we show that our time-dependent variational polaron model remains valid beyond the regimes of validity of both the weak-coupling, and standard polaron models in the pulsed excitation regime. In the short and intermediate pulse width regimes our results also predict a revival of the Rabi oscillations in the exciton population with increasing pulse area. Finally, we have made qualitative comparisons between our time-dependent variational polaron model and the numerically exact dynamics returned by path-integral methods which demonstrate the two approaches return commensurable behaviours. All of these predictions could be tested using experimental Rabi rotation techniques similar to those presented in [121, 122].

Chapter 6

Optical Control and Readout of Single Quantum Dot Spins

In Chapter 3 we discussed the properties of semiconductor QDs, in particular some of the different possible charge states that can be confined to a QD. In this chapter we shall discuss an approach to realising scalable quantum devices by employing charged QDs in on-chip optical structures. Specifically, we shall consider the impact of cavity configuration on the initialisation and readout fidelity of a negatively charged QD by performing full Cavity Quantum Electrodynamics (cQED) calculations. Furthermore, we shall find the optimal cavity parameters to maximise the initialisation and readout fidelities, and demonstrate that coherent optical control is possible with a QD coupled to an optical cavity.

6.1 Introduction

In the absence of any external magnetic field, a single charge carrier confined to a QD possesses a spin degree of freedom with two degenerate basis states $\{|\uparrow\rangle_z, |\downarrow\rangle_z\}$ defined along the QD growth axis. As discussed in Chapter 3, optically exciting the QD introduces an exciton resulting in the formation of a trion which also possesses two degenerate basis states $\{|\uparrow\downarrow, \Uparrow\rangle_z, |\downarrow\uparrow, \Downarrow\rangle_z\}$. When an external magnetic field is applied, the degeneracy of the ground and excited basis states is lifted by the Zeeman interaction. The geometry of the applied field also has an effect on the optical transition selection rules between the ground and excited states as shown in Figure 6.1. In the absence of an applied field, or when a magnetic field is applied in the Faraday geometry along the QD growth axis, only the transitions between the ground and excited states

with the same spin configuration are optically allowed with opposite circular polarisation selection rules [124] (see Figures 6.1a and 6.1b). However, when a magnetic field is applied perpendicularly to the QD growth axis in the Voigt geometry, all four possible transitions become optically allowed with equal decay rates [124]. The optical polarisation transition rules also change from circular to linear with the two outer vertical transitions possessing the orthogonal linear polarisation to the two diagonal transitions [124] (see Figure 6.1c).

Such a spin system has many potential applications in the physical realisation of quantum technologies. Single charge carriers confined to QDs show strong light-matter interactions making them a promising candidate for the implementation of an interface between stationary qubits and flying (single photon) qubits [125]. With experimentally demonstrated lifetimes on the order of milliseconds to seconds [126, 127] and coherence times on the order of microseconds [128, 129], the ability to control the spin state of a charged QD on picosecond timescales [128] provides the potential to perform multiple gate operations within the lifetime of the spin state. This leads to the possibility of developing single-photon transistors [130–132] or generating entangled photonic cluster states [133–136]. Furthermore, situating these QDs in photonic structure can further enhance the strength of the light-matter interactions, and provides the potential for integration into scalable on-chip photonic circuits [86]. This gives rise to the potential for an all optical approach to Quantum Information Processing (QIP) using optical pulses to manipulate stationary qubits, and single photons to act as flying qubits all guided on-chip by optical nanostructures.

The successful implementation of a spin-based device requires the capability to first prepare the system in a simple starting spin-state (a process known as initialisation), and to read out the final state of each individual qubit after any gate operations have been performed. In an all-optical scheme, this would ordinarily require the use of both Voigt and Faraday geometry magnetic fields for control and readout respectively. Spin control using optical pulses requires the presence of optically allowed diagonal transitions between the two excited eigenstates and ground spin eigenstates of opposite spin configuration present when a Voigt geometry magnetic field is applied to the system [137]. The allowed diagonal transitions result in the formation of Λ-systems that provide an effective coupling between the qubit (ground spin) states. The spin state can then be manipulated via a Raman transition using two equally detuned optical pulses driving the two transitions that form the Λ-system [138]. Conversely,

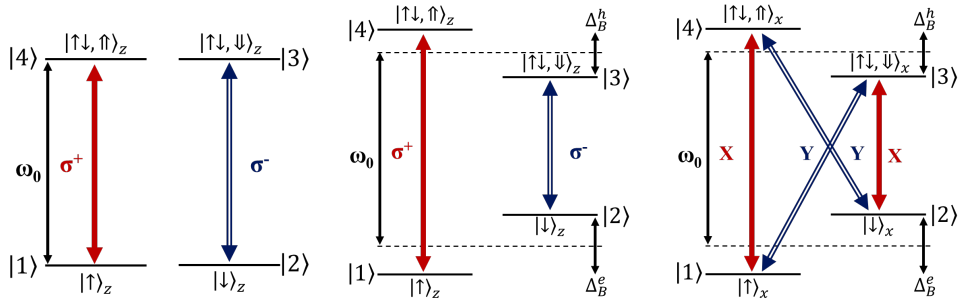

(a) (b) (c)

Figure 6.1: The energy levels and transition selection rules of a single negatively charged Quantum Dot (QD) in: (a) the absence of an applied magnetic field, (b) an applied Faraday geometry magnetic field, and (c) an applied Voigt geometry magnetic field. The spin states are written in the basis parallel to the applied field.

optical readout of the final spin state requires the presence of cycling transitions [139], transitions through which the excited state of the system always decays back to the initial ground state. These cycling transitions are required to produce a detectable readout signal by allowing the system to be probed multiple times without changing the spin state, and are only present when the diagonal transitions are optically forbidden. Optical spin readout thus typically necessitates the application of a Faraday geometry magnetic field as in such a geometry only the outer vertical transitions are optically allowed [1]. Furthermore, while optical spin initialisation has been demonstrated in either field geometry [142–144], they both present significant drawbacks. Optical initialisation performed in the Faraday geometry results in a high initialisation fidelity as the prepared state is completely protected from the driving field by both the optical polarisation selection rules and laser detuning. However, initialisation in this field geometry is slow as the process relies on the diagonal transitions being weakly allowed by light-hole heavy-hole mixing [137, 140, 141]. In the orthogonal Voigt field geometry the spin initialisation process is relatively fast owing to the optically allowed diagonal transitions [140]. The resulting initialisation fidelity, in contrast, is reduced as the prepared state loses the polarisation protection found in the Faraday geometry, and thus must rely on only laser detuning to preserve the prepared state while there is a non-zero

[1] Light-hole heavy-hole mixing experienced in real systems means the diagonal transitions are weakly allowed in a Faraday geometry magnetic field [140, 141].

driving field [140].

However, recent proposals have paved the way for an all-optical implementation of quantum devices using single QD spins situated in a single magnetic field geometry. One such proposal uses higher-order trion states to introduce optically allowed cross-transitions in a Faraday geometry field [145]. Other proposals use optical structures to selectively Purcell enhance the diagonal transitions that are optically allowed in a Voigt geometry magnetic field [146–148]. Selectively Purcell enhancing the diagonal transitions provides a quasi-cycling transition enabling optical spin readout within a Voigt geometry magnetic field. Furthermore, this selective Purcell enhancement also improves the initialisation rate by ensuring a unidirectional flow of the spin population during the initialisation process.

The simplest method of achieving this relative enhancement of the diagonal transitions is through coupling to a photonic structure with a single, linearly polarised mode such as: a slow-light PhC waveguide [149], line-defect PhCCs [150], and single nanobeam cavities [151]. When the cavity mode polarisation is the same as that of the diagonal transitions, the polarisation selection rules ensure the orthogonally polarised vertical transitions are decoupled from the optical mode and therefore not enhanced. However, a number of commonly used photonic cavities naturally possess more than one mode either by design [152–155] or though imperfections in the fabrication process [156, 157]. This bi-modal quality can prove useful when, for example, attempting to suppress any resonant laser background in QD single-photon sources [158, 159]. However, there are still open questions regarding the impact of the cavity configuration on optical spin initialisation and readout of single spins confined to QDs. In this chapter we perform cQED calculations to identify optimal cavity configurations and parameter regimes for maximising spin initialisation and readout fidelities when driving the system with optical pulses.

6.2 Four-Level System Hamiltonian

To answer these open questions, we wish to describe a negatively charged QD coupled to a bi-modal cavity with two orthogonal, linearly polarised cavity modes in the presence of a Voigt geometry magnetic field. First we shall rewrite the spin eigenstates in the basis parallel to the magnetic field (x) axis such that the ground states become $\{|1\rangle = |\uparrow\rangle_x, |2\rangle = |\downarrow\rangle_x\}$ and the excited trion basis states become $\{|3\rangle = |\uparrow\downarrow, \Downarrow\rangle_x, |4\rangle = |\uparrow\downarrow, \Uparrow\rangle_x\}$. To describe this

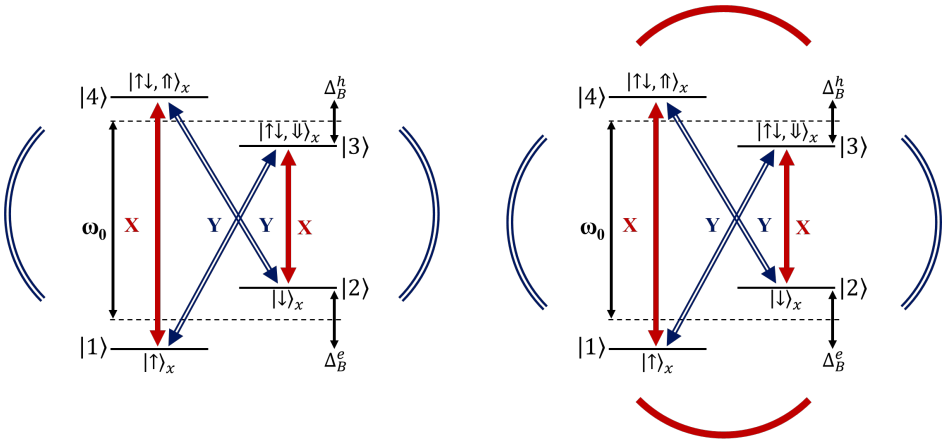

(a) (b)

Figure 6.2: A (a) single-mode and (b) bi-modal cavity coupled to a charged Quantum Dot (QD) in a Voigt geometry magnetic field.

system we can extend the Hamiltonian used in Chapter 3 describing a 2LS coupled to a single-mode cavity to include the additional atomic states and extra cavity mode. In the laboratory frame of reference, the QD and cavity degrees of freedom are generated by the system Hamiltonian

$$H_0 = \frac{\Delta_{\mathrm{B}}^{\mathrm{e}}}{2}(\sigma_{22}-\sigma_{11})+\left(\omega_0-\frac{\Delta_{\mathrm{B}}^{\mathrm{h}}}{2}\right)\sigma_{33}+\left(\omega_0+\frac{\Delta_{\mathrm{B}}^{\mathrm{h}}}{2}\right)\sigma_{44}+\sum_{\lambda=X,Y}\nu_\lambda a_\lambda^\dagger a_\lambda, \quad (6.1)$$

where $\sigma_{ij} = |i\rangle\langle j|$ are the spin operators, ω_0 is the transition frequency in the absence of an applied magnetic field, and a_λ is the operator of the $\lambda = X, Y$ polarised cavity mode with frequency ν_λ. We choose to set the $Y-$polarised cavity mode resonant with the $|2\rangle \rightarrow |4\rangle$ transition while leaving the $X-$polarised cavity mode detuned from the vertical transitions such that $\nu_X = \omega_0$ as this has been shown to maximise the initialisation fidelity with the bi-modal cavity configuration [160]. The Zeeman splitting of the ground (excited) states is given by $\Delta_B^{e(h)} = g_{e(h)}\mu_B B$ where $g_{e(h)}$ is the effective electron (hole) g-factor, μ_B is the Bohr magneton, and B is the applied magnetic field strength. Throughout this chapter we shall assume $g_{e(h)} = 0.5(0.3)$ [140] and $B = 5$ T unless stated otherwise. The interaction between the QD transitions and cavity mode of the same polarisation is characterised by

$$H_I = \sum_{\lambda=X,Y} g_\lambda(a_\lambda + a_\lambda^\dagger)(\sigma_\lambda + \sigma_\lambda^\dagger), \quad (6.2)$$

where g_λ quantifies the cavity-QD coupling strength, and we have defined the collective transition operators $\sigma_X = (\sigma_{14} + \sigma_{23})$ and $\sigma_Y = (\sigma_{13} + \sigma_{24})$.

Optical spin initialisation and control require direct coherent driving of the QD transitions, while optical spin readout is achieved by coherently probing the cavity modes. These two coherent driving processes are included under the dipole approximation in the driving Hamiltonians

$$H_D^{QD}(t) = -\sum_{\lambda=X,Y} \Omega_\lambda(t)\cos(\omega_l t)\sigma_\lambda + \text{h.c.}, \tag{6.3}$$

$$H_D^{C}(t) = -\sum_{\lambda=X,Y} \epsilon_\lambda(t)\cos(\omega_l t)(a_\lambda + a_\lambda^\dagger), \tag{6.4}$$

respectively. Here $\Omega(t)$ and $\epsilon(t)$ are the Rabi frequencies and cavity driving rates of the linearly polarised (X or Y polarised) laser pulses modulated by a time-dependent pulse envelope, and ω_l is the central frequency of each driving laser. The total Hamiltonian describing the coherent dynamics of the cavity-QD system is then given by $H_T(t) = H_0 + H_I + H_D^{QD}(t) + H_D^C(t)$.

The incoherent dynamics of the system, namely spontaneous emission from the QD and loss of photons from the cavity modes, are incorporated in the model via the standard Lindblad master equation approach described in Chapter 2. The collapse operators of the system are thus $L_k \in \{\sqrt{\kappa_\lambda}a_\lambda, \sqrt{\gamma_\lambda}\sigma_\lambda\}$ for $\lambda = X, Y$ where κ_λ are the decay rates of the orthogonally polarised cavity modes and γ_λ are the decay rates of the trion states via the linearly polarised optical transitions. We assume both cavity modes have the same decay rate ($\kappa_{\lambda=X,Y} = \kappa$) and both transition polarisations have the same lifetime such that $\gamma^{-1}_{\lambda=X,Y} = \gamma^{-1} = 1$ ns.

To recover the single-mode cavity configuration from our model we can set $g_X = \kappa_X = \nu_X = 0$ leaving only a single $Y-$polarised cavity mode. We shall not consider the case of a single X-polarised cavity mode. The reason for this will become evident when we move on to discuss the spin initialisation process.

6.2.1 Rotating Frame Transformation for a Cavity-Coupled Four-Level System Hamiltonian

As was the case in Chapter 3, our Hamiltonian contains time-dependent exponential terms originating from the coherent driving of the system. These terms make computations time and resource expensive, and so they need to be removed. To do this we again apply a unitary transform to move to a rotating

frame of reference such that the Hamiltonian in the rotating frame is given by

$$\tilde{H}_{\mathrm{T}}(t) = U(t)H_{\mathrm{T}}(t)U^{\dagger}(t) + i\Big(\frac{\partial}{\partial t}U(t)\Big)U^{\dagger}(t), \tag{6.5}$$

where a tilde represents the Hamiltonian in the rotating frame, and $U(t)$ is the time-dependent unitary operator transforming to a reference frame rotating at frequency ω_R as in Chapter 3. Here the unitary operator is also expanded from that given in Chapter 3 to

$$\begin{aligned} U(t) &= U_C^X(t) \otimes U_C^Y(t) \otimes U_{\mathrm{QD}}(t) \\ &= e^{i\omega_R t\left(a_X^{\dagger}a_X\right)} \otimes e^{i\omega_R t\left(a_Y^{\dagger}a_Y\right)} \otimes e^{i\omega_R t(\sigma_{33}+\sigma_{44})}. \end{aligned} \tag{6.6}$$

Moving to a frame of reference rotating at the laser frequency (i.e. $\omega_R = \omega_l$), and applying the RWA, cancels the time-dependent exponential terms arising from the coherent laser field. The total RWA Hamiltonian in the rotating frame of reference can again be separated into four components, $\tilde{H}_{\mathrm{T}}(t) = \tilde{H}_0 + \tilde{H}_{\mathrm{I}} + \tilde{H}_{\mathrm{D}}^{\mathrm{QD}}(t) + \tilde{H}_{\mathrm{D}}^{\mathrm{C}}(t)$, where

$$\begin{aligned} \tilde{H}_0 = &\frac{\Delta_B^e}{2}(\sigma_{22} - \sigma_{11}) + \Big(\omega_0 - \omega_l - \frac{\Delta_B^h}{2}\Big)\sigma_{33} \\ &+ \Big(\omega_0 - \omega_l + \frac{\Delta_B^h}{2}\Big)\sigma_{44} + \sum_{\lambda=X,Y}(\nu_\lambda - \omega_l)a_\lambda^{\dagger}a_\lambda, \end{aligned} \tag{6.7}$$

$$\tilde{H}_I = \sum_{\lambda=X,Y} g_\lambda a_\lambda^{\dagger}\sigma_\lambda + g_\lambda^* a_\lambda \sigma_\lambda^{\dagger}, \tag{6.8}$$

$$\tilde{H}_D^{QD}(t) = -\sum_{\lambda=X,Y}\frac{\Omega_\lambda(t)}{2}\sigma_\lambda + \mathrm{h.c.}, \tag{6.9}$$

$$\tilde{H}_D^{C}(t) = -\sum_{\lambda=X,Y}\epsilon_\lambda(t)a_\lambda + \epsilon_\lambda^*(t)a_\lambda^{\dagger}. \tag{6.10}$$

In this frame of reference the only remaining time-dependence is that of the pulse envelope. For a full derivation of Eqs. 6.7-6.10 see Appendix D.

6.3 Optical Spin Initialisation

Now we have a suitable Hamiltonian to use in the Lindblad master equation, we first wish to prepare the state of the system in one of the ground basis states with the highest achievable fidelity. To do this we shall drive the vertical, rather than diagonal, transitions with a coherent laser (i.e. $\Omega_X > 0,\ \Omega_Y = 0$)

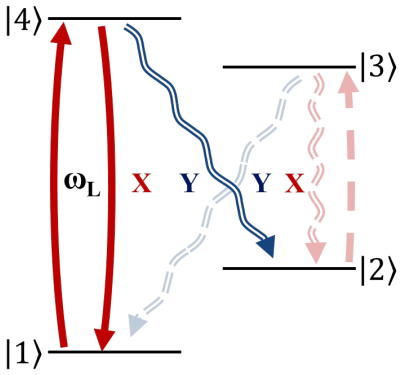

Figure 6.3: A diagram of the initialisation process. The $|1\rangle \rightarrow |4\rangle$ transition is driven with a coherent laser. The decay of the $|4\rangle$ trion state by spontaneous emission via the $|2\rangle \rightarrow |4\rangle$ transition populates the target $|2\rangle$ state. Off-resonant re-pumping of the $|2\rangle$ state through the $|2\rangle \rightarrow |3\rangle$ transition and subsequent decay via the $|1\rangle \rightarrow |3\rangle$ transition limits the initialisation fidelity.

following the protocol presented by [160, 161] and shown in Figure 6.3 . We choose to drive the vertical $|1\rangle \rightarrow |4\rangle$ transition with a resonant $X-$polarised laser such that $\omega_l = \omega_0 + (\Delta_B^e + \Delta_B^h)/2$. Resonantly driving one of the vertical transitions rather than one of the diagonal transitions naturally provides a greater frequency protection to the target state during the initialisation process as the detuning between the vertical transitions is greater than that between the diagonal transitions. In the initialisation process the state of the system is then shelved in the $|2\rangle$ state by the decay of the $|4\rangle$ trion state via the $Y-$polarised diagonal $|4\rangle \rightarrow |2\rangle$ transition.

Previous work studying spin initialisation with a bi-modal cavity assumed the QD was addressed via the cavity mode during the initialisation process [160]. However, to enable a direct, consistent comparison between the two cavity configurations we assume the QD transitions are always directly driven during initialisation. Furthermore, these two driving regimes qualitatively produce the same behaviour, and are unitarily equivalent in the CW driving limit.

Trace Distance

To evaluate the fidelity of the initialisation process we shall use the trace distance [162]

$$T(\rho, \varrho) = \frac{1}{2}\mathrm{Tr}\left\{\sqrt{(\rho - \varrho)^2}\right\}, \tag{6.11}$$

between the prepared (ρ) and target (ϱ) states. The trace distance between the target and prepared states gives a measure of the indisinguishability of the

two using the entirety of the density matrix. Using this metric, $T(\rho = \varrho, \varrho) = 0$ indicates the prepared and target states are completely indistinguishable from one another (i.e. unity initialisation fidelity). However, $T(\rho, \varrho) = 1$ indicates the prepared and target states are orthogonal (i.e. $\mathrm{Tr}(\rho\varrho) = 0$), and thus completely distinguishable. We can show that this is true by considering the spectral decomposition of the two density matrices in a complete orthonormal basis $\{|\psi_i\rangle\}$ such that

$$\rho = \sum_i \alpha_i \, |\psi_i\rangle\langle\psi_i| \;\text{ and }\; \varrho = \sum_i \beta_i \, |\psi_i\rangle\langle\psi_i| \,. \tag{6.12}$$

From this we may then write

$$\sqrt{(\rho - \varrho)^2} = \sum_i |\alpha_i - \beta_i| \, |\psi_i\rangle\langle\psi_i| \,. \tag{6.13}$$

The lower bound is therefore trivial to prove when the two density matrices are identical. In this case $\alpha_i = \beta_i$ and thus $\sqrt{(\rho - \varrho)^2} = 0$. In this same basis only different pure states may be described as orthogonal. That is, for two density matrices to describe orthogonal states it must be true that $\alpha_{i=j} = \beta_{i=k\neq j} = 1$ and $\alpha_{i\neq j} = \beta_{i\neq k} = 0$. This condition can also be seen from $\mathrm{Tr}(\rho\varrho) = 0$ when ρ and ϱ describe orthogonal states. As $\sum_i \alpha_i = \sum_i \beta_i = 1$, when these conditions are met $\mathrm{Tr}\left\{\sqrt{(\rho - \varrho)^2}\right\} = 2$ and thus $T(\rho, \varrho) = 1$. Hence a unity trace distance does indeed indicate the two states are orthogonal.

A number of previous works have used the relative population between the spin ground states as a measure of the initialisation fidelity [160, 163–165]. This approach suffers from the disadvantage of not being able to differentiate between coherent spin superposition states and mixed spin states, something that the trace distance is able to distinguish. Other studies have used the Fidelity , defined as $F(\sigma, \rho) = \mathrm{Tr}\left(\sqrt{\sqrt{\sigma}\rho\sqrt{\sigma}}\right)^2$, to provide a measure of the closeness between the prepared state and target state [140, 148, 166]. While in the case of a pure target state, such as we have defined, this definition of fidelity is equivalent to using the trace distance, it may not always be the case that a pure state is the desired outcome. Hence rather than using $F(\sigma, \rho)$, which is not a true metric[2] on the density matrix space and can be complicated to calculate, we use a more generally applicable metric, namely the trace distance, instead.

[2] A metric, $M(a, b)$, is symmetric $M(a, b) = M(b, a)$ and obeys the triangle inequality $M(a, c) \leq M(a, b) + M(b, c)$ [167].

6.3.1 Steady-State Limit

Using the Lindblad master equation and the trace distance from the $|2\rangle$ ground state we shall begin by considering spin initialisation in the steady state limit with a CW driving term, i.e. $\Omega_X(t) = \Omega_X \ \forall \ t$. While this set-up is not representative of a practical experimental realisation of the spin initialisation process, it will provide a useful insight into the overall behaviour of the system.

Figure 6.4 shows the calculated trace distances as a function of g/κ for a range of cavity linewidths. Just as in Chapter 3, the system dynamics were calculated by solving the master equation at discrete time intervals using the Python package QuTiP [62]. In the limit of small κ both cavity configurations (i.e. single-mode and bi-modal) show the same behaviour. For either cavity configuration, in the narrow cavity linewidth limit, only the $|4\rangle \rightarrow |2\rangle$ transition remains within a cavity mode, and thus (independent of cavity configuration) is the only transition that experiences any Purcell enhancement at such narrow cavity linewidths. In the CW limit it appears that the inclusion of cavity effects negatively impacts the spin initialisation process. In the limit of small g this can be explained as a result of the cavity modifying the lifetime of the trion states. This changes the ratio Ω/γ, and thus as the cavity coupling strength is increased, the fixed driving strength is no longer optimised to achieve the smallest trace distance. As g increases and the system enters the strong coupling regime the QD become hybridised by the cavity-coupling, changing the fundamental eigenstructure of the cavity-QD system.

Figure 6.4a shows that the system evolves to a maximally mixed state with $T(\rho, \sigma_{11}) = T(\rho, \sigma_{22}) = 0.5$, when strongly coupled to a single-mode cavity. However, as shown in Figure 6.4b, when coupled to a bi-modal cavity we instead find the system evolves to $0.1 \leq T(\rho, \sigma_{22}) \leq 0.5$ depending on the cavity linewidth, with narrower cavity linewidths returning smaller trace distances, thus outperforming the single-mode cavity. At first this behaviour may be unexpected. A Purcell enhancement of the $|4\rangle \rightarrow |1\rangle$ transition hinders the spin initialisation process which relies on the flow of spin population via the $|1\rangle \rightarrow |4\rangle \rightarrow |2\rangle$ Λ-system. However, the effect of enhancing the $|4\rangle \rightarrow |1\rangle$ transition only acts to reduce the speed of the initialisation process by increasing the fraction of the $|4\rangle$ state that decays back to the unwanted $|1\rangle$ state. In the CW limit this reduction in speed is less important due to the infinite driving time. Under CW driving, the protection afforded to the prepared state against re-pumping by the Purcell enhancement of the $|3\rangle \rightarrow |2\rangle$ transition outweighs the hindrance caused by the $|4\rangle \rightarrow |1\rangle$ enhancement. This mechanism is ev-

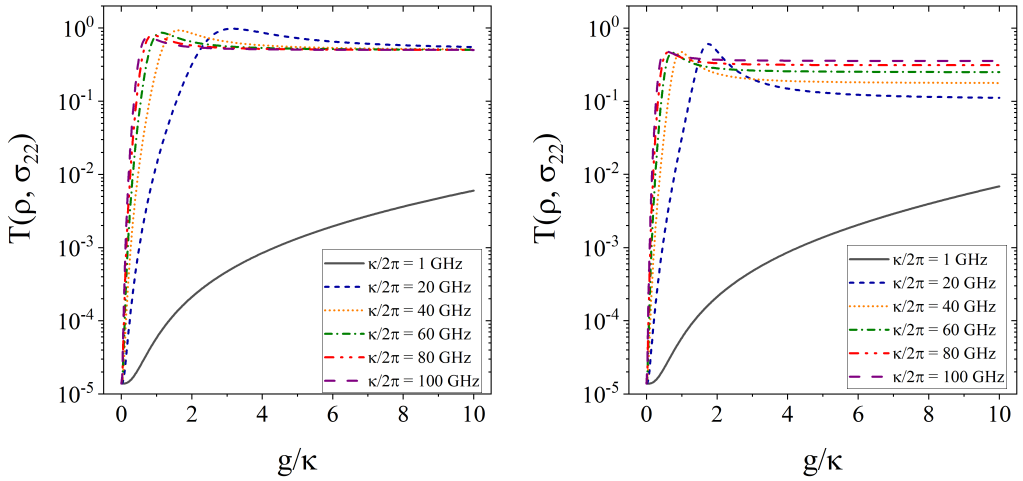

Figure 6.4: The steady-state spin initialisation fidelity driving a Four-Level System (4LS) coupled to a (a) single-mode or (b) bi-modal cavity. Fidelity is quoted as the trace distance, $T(\rho, \sigma)$, between the prepared spin state, ρ, and the steady-state spin-down ground state, σ_{22}, as a function of ratio of the cavity linewidth, κ, and coupling strength, g. Parameters used: $B = 5$ T, $g_{e(h)} = 0.5(0.3)$, $\gamma^{-1} = 1$ ns, $\Omega/2\pi = 0.001$ GHz.

idenced by the decrease in the trace distance shown in Figure 6.4b between $20 \leq \kappa/2\pi \leq 100$ GHz. In a bi-modal cavity with the widest linewidth both the $|3\rangle \rightarrow |1\rangle$ transition and $|3\rangle \rightarrow |2\rangle$ transitions experience equal Purcell enhancement. As the cavity linewidth decreases, the greater detuning between the $|3\rangle \rightarrow |1\rangle$ and $Y-$polarised cavity mode compared to the detuning of the $|3\rangle \rightarrow |2\rangle$ transition and $X-$polarised cavity mode causes an imbalance in the decay rates of the two transitions. This imbalance favours decay back to the $|2\rangle$ state, decreasing the trace distance.

6.3.2 Driving with Finite Optical Pulses

Now that we have a good understanding of the response of the system in the steady-state limit, we can move on to study a more physically realistic approach to spin initialisation, i.e. driving with a finite duration optical pulse. Moving into a more experimentally realistic regime we also choose more experimentally measurable cavity parameters, namely switching to the Purcell enhancement factor ($F_P = 4g^2/\kappa\gamma$ [81–83]) of the $|4\rangle \rightarrow |2\rangle$ transition rather than the cavity-QD coupling strength. We opt to limit the Purcell factor and cavity linewidths to $1 \leq F_P \leq 40$ and $1 \leq \kappa/2\pi \leq 100$ GHz respectively. These limits maintain the enhancement of the optical transitions within lim-

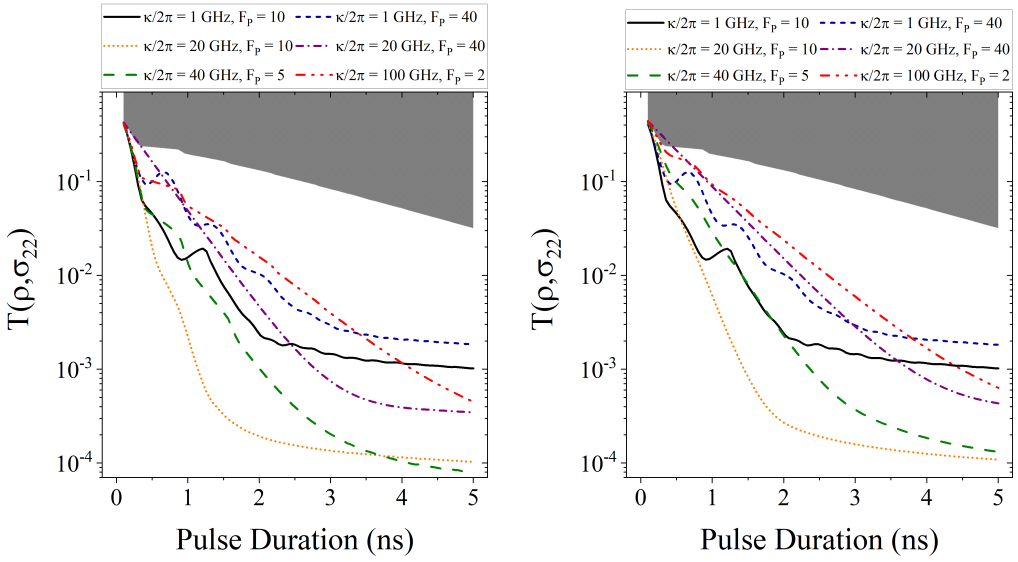

Figure 6.5: The trace distance between the prepared state and target state minimised with respect to the Rabi frequency after the initialisation process as a function of the duration of the square optical driving pulse when coupled to a (a) single-mode cavity, and (b) a bi-modal cavity. The cavity parameters used are indicated in the legends above the plots. The trace distance was minimised with respect to the Rabi frequency sweeping between $0 \leq \Omega \leq 10\gamma$. The shaded region indicates trace distances larger than achievable in the absence of any cavity effects.

its demonstrated experimentally [82] while simultaneously avoiding Purcell suppression ($F_P < 1$), and maintains experimentally accessible [84, 168, 169] cavity quality factors[3]. Assuming the system begins in the maximally mixed ground state (i.e. $\rho_{jj}(t = 0) = 0.5$ for $j \in 1, 2$ with all other elements zero), we again initialise the state of the system by resonantly driving the $|1\rangle \rightarrow |4\rangle$ transition only now using a finite square or Gaussian pulse envelope.

Square Pulse

We begin by studying spin initialisation with a square pulse of finite duration. This pulse takes the form $\Omega_X(t) = \Omega_X(H(t-t_0+\Delta\tau_X/2)-H(t-t_0-\Delta\tau_X/2))$, where $H(x)$ is the Heaviside function, t_0 is the centre of the pulse, $\Delta\tau_X$ is the pulse duration, and Ω_X is the peak Rabi frequency of the pulse. For a selection of cavity parameters and a range of pulse durations, we calculate the minimum trace distance sweeping the Rabi frequency between $0 \leq \Omega_X \leq 10\gamma$, leaving an adequate period of time after the pulse for any remaining excited state

[3] On the order of $10^3 - 10^5$ in the Near Infrared and telecommunications wavelengths.

populations to decay. The results are shown in Figure 6.5.

Overall we see a general trend of decreasing trace distance with increasing pulse duration regardless of cavity configuration. There are a number of reasons for this. The longer pulse duration increases the probability that the entire population of the undesirable ground state is eventually excited by the driving laser. Furthermore, longer duration pulses are also able to re-excite any excited state population that decays back to the undesirable ground state over a number of excited state lifetimes, further increasing the target state population. Increasing the pulse duration has the additional affect of decreasing the bandwidth of the driving laser. This in turn reduces the overlap in frequency between the drive and $|2\rangle \rightarrow |3\rangle$ transition that acts to move the system away from the target state which has the effect of decreasing the distance to the target state.

From Figure 6.5a we see that when the QD is coupled to a single-mode cavity and driven by a square optical pulse the Purcell enhancement of the resonant diagonal transition is the dominant factor in determining the trace distance. From the cavity parameter combinations studied, for all but the narrowest cavity linewidth, the cavity linewidth only appears to have an appreciable effect at longer pulse durations with the pulse duration at which the cavity linewidth has an appreciable effect increasing with decreasing Purcell factor. For $F_P = 10, 40$, outside of the strong coupling regime (i.e. neglecting $\kappa/2\pi = 1$ GHz) we find increasing the cavity linewidth increases the trace distance between the prepared and target states, decreasing the spin initialisation fidelity. On the other hand, for the smaller Purcell factors studied ($F_P = 2, 5$) we find the trace distance is minimised with $\kappa/2\pi = 40$ GHz, increasing for the smaller or larger cavity linewidths studied. Overall we find the smallest trace distance coupled to a single-mode cavity is achieved with $\kappa/2\pi = 20$ GHz and $F_P = 10$ for pulse durations shorter than 4 ns, and $\kappa/2\pi = 40$ GHz and $F_P = 5$ for pulse durations greater than 4 ns. Initially one may expect the largest Purcell factor to produce the smallest trace distance as larger Purcell factors maximise the cyclicity of the $\Lambda-$system. However, the finite duration of the optical pulse increases the bandwidth of the driving field which in turn also increases the strength with which the off-resonant X-polarised vertical transition is driven. Thus, to reduce the probability of a spin-flip away from the prepared state occurring, the Purcell enhancement of the $|3\rangle \rightarrow |1\rangle$ must be reduced by reducing the overall coupling strength between the Y-polarised cavity mode and diagonal transitions.

A similar outcome is found when the QD is coupled to a bi-modal cavity. Figure 6.5b again shows that the Purcell enhancement of the diagonal transition resonantly coupled to the $Y-$polarised cavity mode is the predominant factor in determining the minimum trace distance. However, in general the calculated trace distances are slightly larger than those achieved with a single-mode cavity. Depending on the cavity linewidth, the second cavity mode can Purcell enhance the X-polarised transitions. This increases the probability of the $|4\rangle$ population decaying back to the $|1\rangle$ state rather than to the target $|2\rangle$ state relative to the single-mode case, increasing the trace distance from the target state. Furthermore, when compared to the results from the single-mode cavity configuration, we find the cavity linewidth has a more significant impact at shorter pulse durations, and the calculated trace distances are larger for each given pulse duration reversing the trend seen under CW driving. In the bi-modal configuration we determined increasing the cavity linewidth (again neglecting the narrowest cavity linewidths) increases the calculated trace distance for all Purcell factors studied. However, we find a large overlap of the trace distances for $F_P = 5$ and $F_P = 10$, as well as $F_P = 2$ and $F_P = 40$, with $F_P = 40$ producing the largest trace distances overall. Just as in the single-mode case, we find a combination of $\kappa/2\pi = 20$ GHz and $F_P = 10$ produces the smallest trace distance over the pulse durations studied, but now for all but the smallest pulse durations where $\kappa/2\pi = 1$ GHz achieves this.

For both cavity configurations we find the narrowest cavity linewidth studied ($\kappa/2\pi$) tends to be detrimental to the spin initialisation fidelity. At such narrow cavity linewidths the system quickly enters the strong-coupling regime with increasing Purcell factor. In this regime Rabi oscillations occur as the cavity mode re-excites the system back to the exciton states. In the exciton states there is a finite probability that the system will decay away from the target state thus reducing the initialisation fidelity.

Figure 6.5 shows plateaus in the calculated trace distance. These are the result of small coherent oscillations in the trace distance induced by the coherent driving of the system. Setting an upper bound on the Rabi frequency also limits the number of these coherent oscillations. The edges of the plateaus occur when the pulse duration becomes long enough to encompass the next oscillation in the trace distance that has a smaller local minimum than the previous oscillation. The plateaus disappear at longer pulse durations as the global minimum of these oscillations usually occurs after two or three periods.

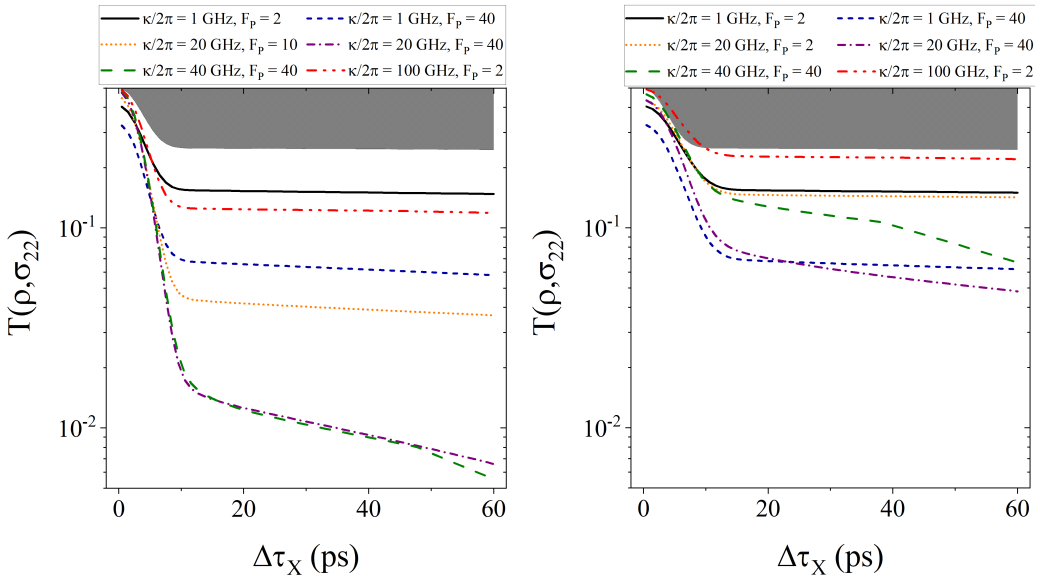

Figure 6.6: The calculated trace distance between the prepared state and target state minimised with respect to the pulse area after the initialisation process as a function of the duration of the Gaussian optical driving pulse when coupled to a (a) single-mode cavity, and (b) a bi-modal cavity. The cavity parameters used are indicated in the legends above the plots. The pulse area was swept between $0.01 \leq \Theta \leq 5\pi$. The shaded region indicates trace distances larger than achievable in the absence of any cavity effects.

Gaussian Pulse

We shall now move on to investigate initialisation with a Gaussian pulse. We define the Gaussian pulse with polarisation $\lambda = X, Y$ as

$$\Omega_\lambda(t) = \frac{\Theta_\lambda}{\sqrt{2\pi w_\lambda^2}} \exp\Big\{-\frac{(t-t_0)^2}{2w_\lambda^2}\Big\}, \tag{6.14}$$

where Θ_λ is the pulse area defined such that a pulse with $\Theta_\lambda = \pi$ would invert the populations of a 2LS, w_λ is the Gaussian width of the pulse related to the intensity FWHM, $\Delta\tau_X$, by

$$w_\lambda = \frac{\Delta\tau_\lambda}{2\sqrt{\ln 2}}, \tag{6.15}$$

and once again t_0 defined the central position of the pulse in time.

To calculate the minimum trace distance we follow the same procedure used when driving the system with a square pulse, only here we sweep the pulse area in the range $0.01\pi \leq \Theta_X \leq 5\pi$ for each $\Delta\tau_X$. Just as we found when driving with a square pulse, when driving with a Gaussian pulse we find it is the Purcell

factor and not the cavity linewidth[4] that has the most significant impact on the trace distance. Again, we find the narrowest cavity linewidth is detrimental to the initialisation fidelity in the single-mode configuration, producing the largest trace distances for each Purcell factor studied. We also find that increasing the cavity linewidth above $\kappa/2\pi = 20$ GHz also increases the trace distance between the prepared and target states. However, unlike when driving with a square pulse, with a Gaussian pulse we find the trace distance decreases with increasing Purcell factor for all cavity linewidths. This is a result of the single-shot nature of initialisation with a Gaussian pulse requiring the maximum Λ-system cyclicity to maximise the initialisation fidelity. As the pulse duration is much shorter than the excited state lifetime (i.e. $\Delta\tau_X \ll \gamma^{-1}$), there is no significant decay of the trion population during the pulse. Consequently, any notable increase in the unwanted ground state population is likely to occur after the driving pulse. Thus a Gaussian pulse is unable to re-excite any non-zero $|1\rangle$ population resulting from the decay of the trion states away from the target state. Accordingly, when driving the system with a pulse of short duration the final trace distance is predominantly determined by the ratio of the rates of the decay paths away from the $|4\rangle$ state. This Purcell factor requirement presents a significant drawback in the physical realisation of spin initialisation as it has often proved challenging to realise large Purcell factors in on-chip, in-plane photonic structures such as Photonic Crystal Cavities (PhCCs).

From the outset it is clear that the Gaussian pulse envelope provides a significant time advantage over the square pulse. Figures 6.6a and 6.6b show that the optimum trace distance for either cavity configuration is achieved in tens of picoseconds rather than the few nanoseconds required when driving with a square pulse. Furthermore, the trace distances achieved by the Gaussian pulse are smaller than those that can be achieved with the shortest ($\Delta\tau_X < 1$ ns) square pulses studied that are unlikely to be experimentally accessible. However, comparing the smallest trace distances achieved by both pulses, it is clear that the square pulse is able to produce trace distances orders of magnitudes smaller than the smallest trace distance achieved when driving with a Gaussian pulse. For Gaussian pulses with $\Delta\tau \lessapprox 15$ ps this a result of the finite bandwidth of the pulse. At these short pulse widths there is a significant spectral overlap with the off-resonant vertical transition which in turn increases the rate at which the system is driven away from the desired ground state.

[4]While the Purcell factor and cavity linewidth are related, the position of the emitter in the cavity field, for example, also impacts the Purcell factor (see Eq. 3.54) and thus we can independently vary the two parameters independently.

However, at longer pulse durations this spectral overlap is minimised, and thus it is the pulse duration limiting the re-excitation of the undesirable ground state after the initial excitation that limits the trace distance in this limit.

Similarly to the square pulse case, we find coupling the QD to a bi-modal cavity significantly increases the trace distances achieved by the initialisation process. Again we find the two cavity configurations produce identical results for the narrowest cavity linewidth studied. However, Figure 6.6b shows that when driving with a Gaussian pulse a number of the cavity parameter combinations may actually provide little benefit when compared to driving the QD in the absence of any cavity effects.

6.3.3 Spin Initialisation Including Pure Dephasing

As we discussed in Chapter 2, the stochastic decay of the populations of the quantum states via spontaneous emission is not the only dephasing mechanism experienced by physical quantum systems. Therefore we now consider the impact of pure dephasing on optical spin initialisation when driving with finite duration optical pulses to determine the resilience of the initialisation process against incoherent processes resulting from elastic interactions with the environment. Assuming both excited trion states experience the same pure dephasing rate, we introduce the additional Lindblad terms $L \in \{\sqrt{\Gamma_{PD}}\sigma_{33}, \sqrt{\Gamma_{PD}}\sigma_{44}\}$ to account for these pure dephasing processes. Here we shall follow the same procedures used in the absence of pure dephasing, sweeping the duration of the optical pulse and minimising the trace distance with respect the either the Rabi frequency or area of the driving pulse. However, we now perform these sweeps for a number of different pure dephasing rates using the single set of cavity parameters that produced the smallest trace distance between the prepared and target states for both pulse shapes when neglecting pure dephasing.

Figure 6.7 shows the resulting trace distances with pure dephasing rates $\Gamma_{PD} \in \{0,\ 0.1\gamma,\ 0.5\gamma,\ \gamma,\ 10\gamma\}$. We find pure dephasing has a minimal impact on the initialisation process when the pure dephasing rate is less than γ. When driving with a square pulse with either cavity configuration, we find the influence of the pure dephasing processes increases with increasing pulse duration, with the largest differences between the calculate trace distances with and without pure dephasing effects occurring at the longest pulse duration (see Figures 6.7a and 6.7b). Even in this limit we find only a minimal increase in the trace distance. When coupled to a single-mode cavity the trace distance

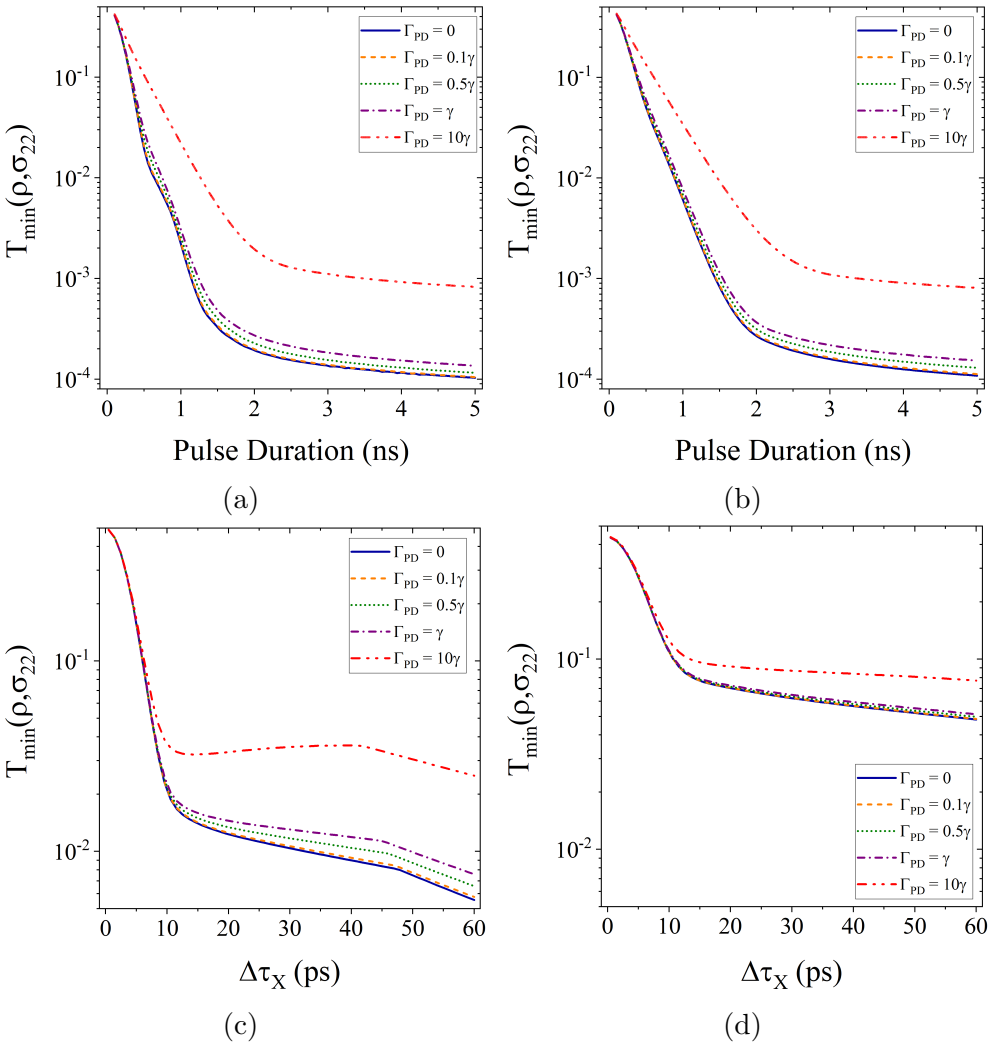

Figure 6.7: The calculated trace distance between the state prepared by the spin initialisation process in the presence of pure dephasing when driving with a QD coupled to a (left: a,c) single-mode or (right: b,d) bi-modal cavity with (top: a,b) square pulse or (bottom: c,d) Gaussian pulse. Parameters used: (a,b) $\kappa/2\pi = 20$ GHz, $F_P = 10$, (c,d) $\kappa/2\pi =$ GHz, $F_P =$, $\gamma^{-1} = 1000$ ps, and $\Gamma_{PD} \in \{0, 0.1, 0.5, 1.0, 10.0\}\gamma$.

increases from $T(\rho, \sigma_{22}) = 1.03 \times 10^{-4}$ in the absence of pure dephasing to $T(\rho, \sigma_{22}) = 1.36 \times 10^{-4}$ (8.25×10^{-4}) at $\Gamma_{PD} = \gamma$ $(\Gamma_{PD} = 10\gamma)$. When coupled to a bi-modal cavity the trace distance increases from $T(\rho, \sigma_{22}) = 1.08 \times 10^{-4}$ when $\Gamma_{PD} = 0$ to $T(\rho, \sigma_{22}) = 1.54 \times 10^{-4}(8.09 \times 10^{-4})$ with $\Gamma_{PD} = \gamma$ $(\gamma_{PD} = 10\gamma)$. We observe a similar behaviour when driving the system with a Gaussian optical pulse shown in Figures 6.7c and 6.7d. Increasing the pure dephasing rate when coupled to a single-mode cavity results in an increase in the trace distance from $T(\rho, \sigma_{22}) = 5.6 \times 10^{-3}$ at $\Gamma_{PD} = 0$ to $T(\rho, \sigma_{22}) = 7.6 \times 10^{-3}$ $(T(\rho, \sigma_{22}) = 2.5 \times 10^{-2})$ at $\Gamma_{PD} = \gamma$ $(\Gamma_{PD} = 10\gamma)$. However, we find coupling the 4LS to a bi-modal cavity and driving with a Gaussian pulse results in the greatest resilience to pure dephasing. In the absence of pure dephasing the smallest trace distance achieved is $T(\rho, \sigma_{22}) = 4.8 \times 10^{-2}$. Increasing the pure dephasing rate to $\Gamma_{PD} = \gamma$ $(\Gamma_{PD} = 10\gamma)$ returns a trace distance of $T(\rho, \sigma_{22}) = 5.1 \times 10^{-2}$ $(T(\rho, \sigma_{22}) = 7.7 \times 10^{-2})$. The robustness of the initialisation process with this cavity configuration and pulse envelope has two origins. The reduced lifetime of the trion states through the Purcell enhancement of all four optical transitions reduces the relative importance of the pure dephasing mechanisms. Additionally, the short duration of the driving pulse further reduces the impact of pure dephasing on the initialisation process.

6.4 Optical Spin Readout

While we now have a selection of cavity parameters that result in high-fidelity optical spin initialisation for either cavity configuration, it is crucial that these cavity parameters are also conducive to high-fidelity optical spin readout for such systems to be used in spin-based optical quantum devices. We shall therefore now study the impact of cavity configuration on spin readout using the method first proposed in [146]. This method, experimentally realised in [147], relies on the spin-dependent cavity transmissivity or reflectivity of the cavity mode resonantly coupled to the QD to determine the spin state of the system. We shall again assume one cavity mode is always resonantly coupled to the $|4\rangle \rightarrow |2\rangle$ transition, conversely to the set-up studied in [146]. To readout the state of the system we weakly probe this transition via the cavity mode using a square pulse turned on at time zero and with some duration τ. If the system is in the $|1\rangle$ ground state the photons will be transmitted. On the other hand, if the system in the $|2\rangle$ spin state it will interact with the driving field and the photons will be reflected. Therefore, by comparing the

number of photons reflected or transmitted with a calculated threshold photon number (k) [146], the ground state occupied by the QD may be determined. If the collected photon number is less than k then the state of the system is $|2\rangle$, otherwise it is $|1\rangle$. This then allows one to write the maximum probability of successfully determining the correct state as $\mathcal{R} = \max_k(q_1 p_1(k) + q_2 p_2(k))$ where q_i is the probability of finding the system in state $|i\rangle$, and p_i is the probability of getting a correct result using the threshold photon number k [146]. As described in [146], if the dead time of the detectors is shorter than the interval between detection events, and the system is driven in the weak driving limit, the probabilities $p_i(k)$ may be described by Poissonian statistics. This then allows the readout fidelity $\mathcal{R}$ to be defined as [146]

$$\mathcal{R}(\tau) = \frac{1}{2} - \frac{1}{2}\sum_{k=0}^{M} \frac{1}{k!}\left([N_1(\tau)]^k\, e^{-N_1(\tau)} - [N_2(\tau)]^k\, e^{-N_2(\tau)}\right), \tag{6.16}$$

where M is the optimal threshold value given by [146]

$$M = \left\lfloor \frac{N_2(\tau) - N_1(\tau)}{\ln[N_2(\tau)] - \ln[N_1(\tau)]} \right\rfloor, \tag{6.17}$$

with $\lfloor x \rfloor$ denoting the largest integer smaller than x, and N_i is the number of photons emitted from the cavity mode when the initial state of the QD is $|i = 1, 2\rangle$. This number can be calculated by integrating the output flux of the cavity mode collected over the duration of the driving pulse [146]

$$N_{i,\lambda}(\tau) = \eta \int_0^\tau dt \left|\mathrm{Tr}\left[\sqrt{\kappa_\lambda} a_\lambda \rho_i(t)\right]\right|^2, \tag{6.18}$$

where η is the photon collection efficiency, and ρ_λ are the system density matrices at time t when the QD starts in the $|i = 1, 2\rangle$ ground state.

This readout method has been demonstrated to work experimentally. A readout fidelity of $\mathcal{R} = 0.61$ was achieved in [147] a with a 75 ns long optical pulse for a QD coupled to a cavity with a cavity linewidth $\kappa/2\pi = 67$ GHz, and enhancement factor $F_P = 62$, and with an optical collection efficiency of $\eta = 4.1 \times 10^{-3}$.

We shall now consider a shorter pulse duration of 35 ns, but still set the cavity driving strength as in [146] at $\epsilon_Y(t) = \sqrt{(0.01 \times 2g_Y^2)}$ for $t \in [0, 35]$ ns to maintain the weak driving regime. The results are shown in Figure 6.8. Assuming $\eta = 1$, we calculate the spin readout fidelity for a range of cavity parameters. When the QD is coupled to a single-mode cavity we find

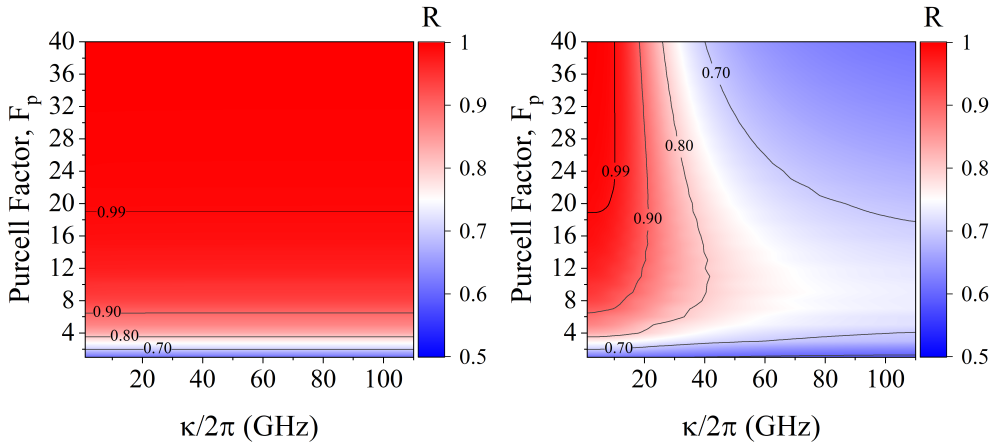

Figure 6.8: The calculated readout fidelity as a function of cavity linewidth and Purcell enhancement of the $2 \rightarrow 4$ transition driving the $Y-$polarised cavity mode of a (a) single-mode and (b) bi-modal cavity with a 35 ns square pulse. A fully optimised readout process returns $\mathcal{R} = 1$, while an un-optimised readout protocol returns $\mathcal{R} = 0.5$.

the most important factor for determining the readout fidelity is the Purcell enhancement of the $|4\rangle \rightarrow |2\rangle$ transition, varying little with respect to κ_Y (see Figure 6.8a). This is the result of the Purcell enhancement increasing the strength of the quasi-cycling transition introduced by the cavity that is required to produce a detectable readout signal. Figure 6.8a shows that an enhancement factor of $F_P = 7$ ($F_P = 19$) gives $\mathcal{R} > 90\%(\mathcal{R} > 99\%)$.

On the other hand, when coupled to a bi-modal cavity both the Purcell enhancement and cavity linewidth have an appreciable impact on the spin readout fidelity. Using this cavity configuration the highest readout fidelities are produced when the cavity modes have a narrow linewidth and the resonant diagonal transition experiences a large Purcell enhancement. The narrow cavity linewidths ensure the vertical transitions are far enough detuned from the cavity mode of the same polarisation that they are not enhanced and thus do not reduce the cyclicity of the Λ-system being probed. To achieve $\mathcal{R} > 99\%$ when coupled to a bi-modal cavity requires $\kappa/2\pi \leq 9.4$ GHz, and $F_P \geq 19$.

While we have so far assumed a 100% collection efficiency, it is important to note that we find $\eta \geq 48\%$ returns $\mathcal{R} \geq 99\%$ when the cavity parameters are optimised for either cavity configuration. Collection efficiencies in this range have already been demonstrated in a number of cavity systems including open-access microcavities [159]. Additionally, for planar cavity systems even higher collection efficiencies could be achieved by direct fibre coupling [170, 171].

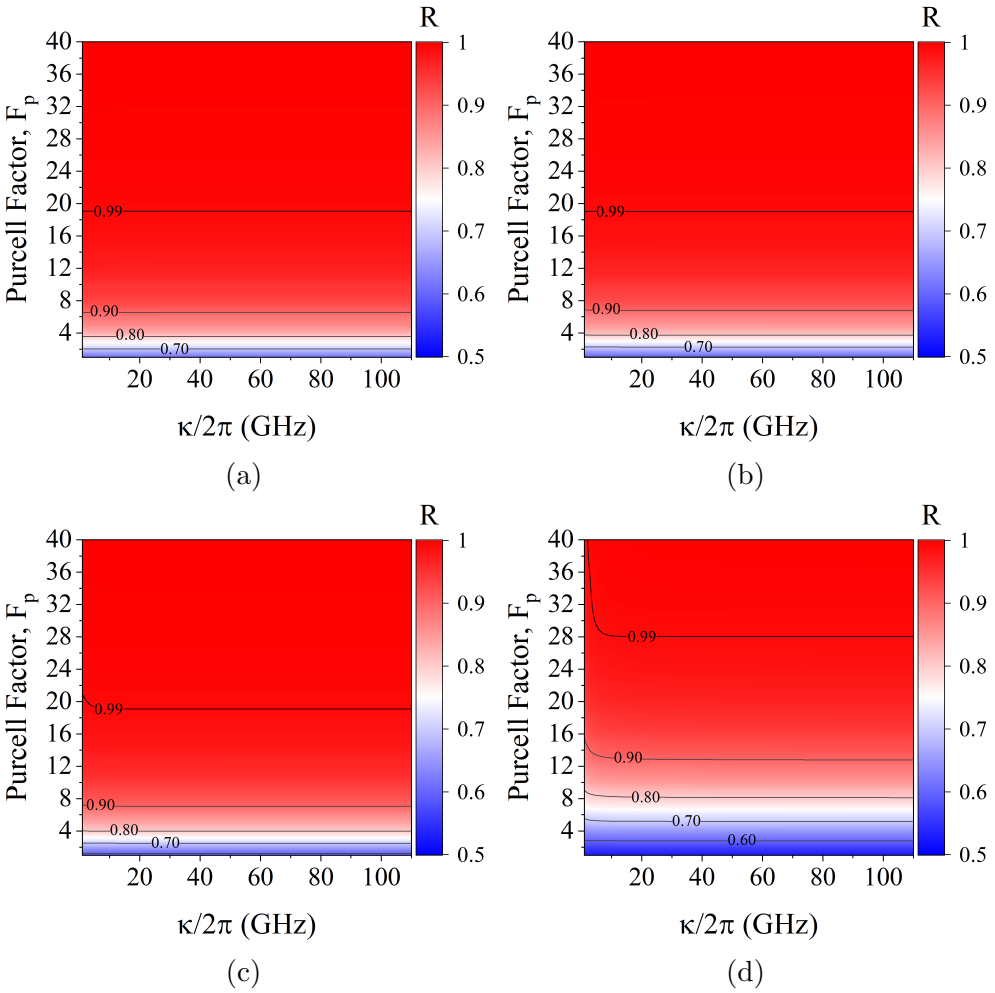

Figure 6.9: The calculated spin readout fidelity as a function of cavity linewidth and the Purcell enhancement of the $2 \rightarrow 4$ transition for a Four-Level System (4LS) coupled to a $Y-$polarised single-mode cavity for four different pure dephasing rates. (a) $\Gamma_{PD} = 0.1\gamma$, (b) $\Gamma_{PD} = 0.5\gamma$, (c) $\Gamma_{PD} = \gamma$, and (d) $\Gamma_{PD} = 10\gamma$. Parameters: $B = 5$ T, $g_{e(h)} = 0.5(0.3)$, $\gamma^{-1} = 1$ ns, $\epsilon = \sqrt{0.01 \times 2g^2}$.

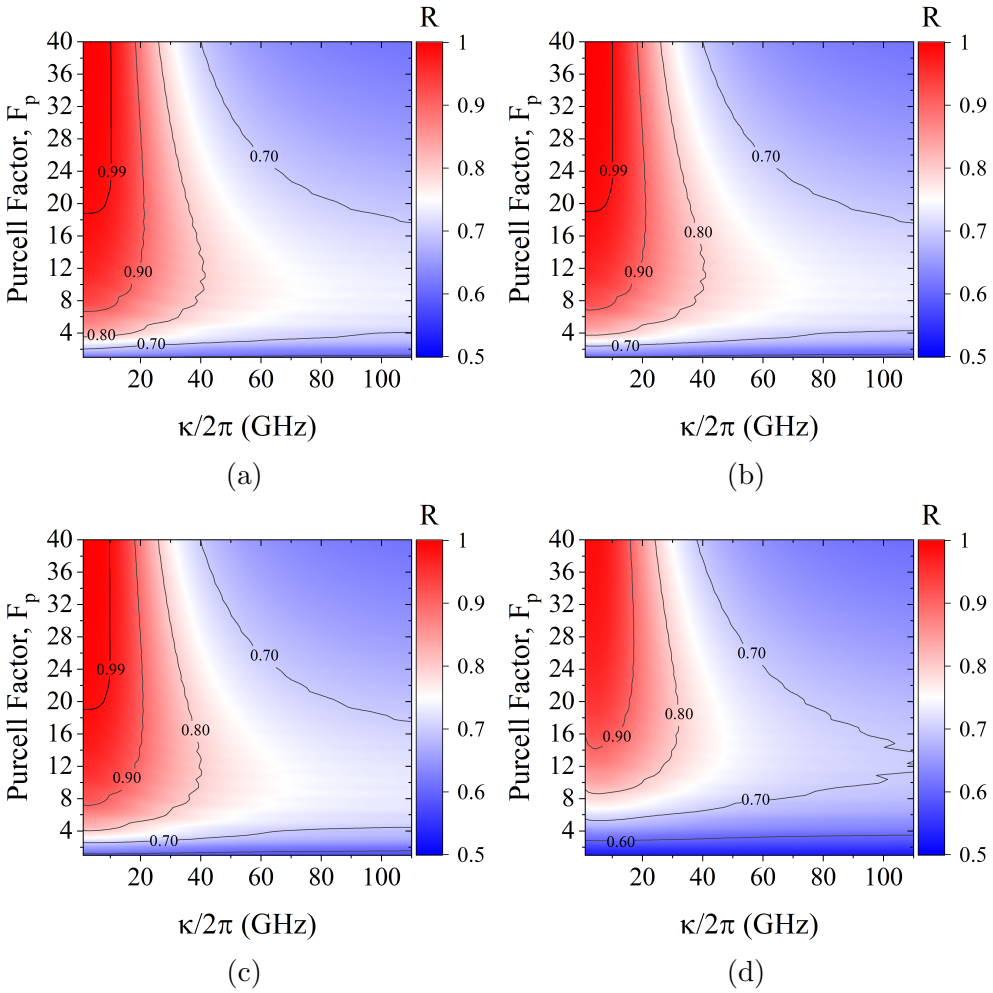

Figure 6.10: The calculated spin readout fidelity as a function of cavity linewidth and the Purcell enhancement of the $2 \rightarrow 4$ transition for a Four-Level System (4LS) coupled to a bi-modal cavity for four different pure dephasing rates. (a) $\Gamma_{PD} = 0.1\gamma$, (b) $\Gamma_{PD} = 0.5\gamma$, (c) $\Gamma_{PD} = \gamma$, and (d) $\Gamma_{PD} = 10\gamma$. Parameters used: $B = 5$ T, $g_{e(h)} = 0.5(0.3)$, $\gamma^{-1} = 1$ ns, $\epsilon = \sqrt{0.01 \times 2g^2}$.

6.4.1 Spin Readout Including Pure Dephasing

Just as when studying spin initialisation with a finite pulse, we can once again introduce pure dephasing to the system to examine its effect on the spin readout fidelity. Given the long duration of the readout pulse, it is important that the process is robust against pure dephasing as on these timescales spin decoherence mechanisms become relevant [172]. Figures 6.9 and 6.10 show the results for a single-mode and bi-modal cavity respectively. When coupled to a single-mode cavity we find the inclusion of pure dephasing has a minimal impact on the readout fidelity for all but the largest pure dephasing rate. The addition of pure dephasing increases the threshold Purcell factor for achieving a given readout fidelity. However, with the cavity parameters studied it remains possible to achieve $\mathcal{R} \geq 99\%$ regardless of the pure dephasing rate. For $\Gamma_{PD} = 10\gamma$, $\mathcal{R} = 99\%$ can be achieved with $F_P = 26$ compared to $F_P = 16$ with $\Gamma_{PD} = 0.1\gamma$. A similar behaviour is found in the bi-modal configuration. The readout process remains robust against pure dephasing for $\Gamma_{PD} \leq \gamma$. However, at the largest pure dephasing, $\Gamma_{PD} = 10\gamma$, rate studied, $\mathcal{R} > 99\%$ is no longer achievable with the cavity parameter combinations studied.

6.5 Optical Spin Control

Now we have identified the optimal cavity configurations for enhancing optical spin initialisation and readout, we now must confirm that we maintain the ability to manipulate the spin-state of the system using optical pulses when the QD is coupled to these cavities. Optical control of the spin-state of singly charged QD is achieved by directly driving the two transitions of one of the $\Lambda-$systems with two orthogonally polarised optical laser pulses (see Figure 6.11). This creates a Raman transition between the two ground states transferring the spin population [138]. We choose to again drive the $|1\rangle \rightarrow |4\rangle$ transition with an $X-$polarised laser, and therefore we must also drive the $|2\rangle \rightarrow |4\rangle$ transition with a $Y-$polarised laser to achieved the required Raman transition. We also include a common detuning (δ) between the laser pulses and the frequencies of their respective transitions such that the frequencies of the $X-$ and $Y-$polarised laser pulses are given by $\omega_l^{(X)} = \omega_0 - \delta + (\Delta_B^e + \Delta_B^h)/2$ and $\omega_l^{(Y)} = \omega_0 - \delta + (\Delta_B^h - \Delta_B^e)/2$ respectively. As we shall see, this detuning is critical to the control process as, in addition to allowing us to neglect cavity driving, it ensures the transitions are virtual, preventing any real population in the excited states which would introduce decoherence to the process.

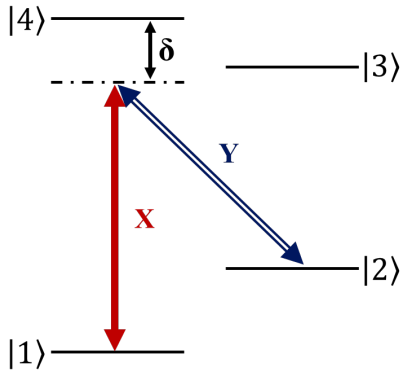

Figure 6.11: A depiction of the spin control process. The two transitions of one of the Λ−systems are simultaneously driven by two orthogonal linearly polarised Gaussian pulses with equal detuning (δ) from their respective transitions.

The difference in frequency between the two driving fields will inevitably result in the return of time-dependent exponential terms to the driving Hamiltonian. For simplicity, rather than transforming to a frame of reference rotating at one of the laser frequencies, as we did for initialisation and readout, we shall instead now move to a reference frame rotating at the QD transition frequency in the absence of an applied magnetic field, ω_0. In this reference frame the Hamiltonian is given by

$$\begin{aligned}
\tilde{H}_0 &= \frac{\Delta_B^e}{2}(\sigma_{22}-\sigma_{11}) + \frac{\Delta_B^h}{2}(\sigma_{44}-\sigma_{33}) + \sum_{\lambda=X,Y}(\nu_\lambda-\omega_0)a_\lambda^\dagger a_\lambda, \\
\tilde{H}_I &= \sum_{\lambda=X,Y} g_\lambda a_\lambda^\dagger \sigma_\lambda + g_\lambda^* a_\lambda \sigma_\lambda^\dagger, \\
\tilde{H}_D^{QD}(t) &= -\sum_{\lambda=X,Y}\frac{\Omega_\lambda(t)}{2}\left(\sigma_\lambda^\dagger e^{-i(\omega_l^{(\lambda)}-\omega_0)t} + \sigma_\lambda e^{i(\omega_l^{(\lambda)}-\omega_0)t}\right),
\end{aligned} \tag{6.19}$$

where we have neglected the cavity driving Hamiltonian as we are only interesting in direct QD driving.

Starting in the $|1\rangle$ ground state, we calculate the trace distance from the $|2\rangle$ ground state, along with the purity of the ground state manifold ($P(\rho_{12}) = \mathrm{Tr}(\rho_{12}^2)$), at a time much greater than the pulse widths ($t \gg \Delta\tau$). We choose these metrics as an optimised control process should provide access to all possible combinations of the qubit ($|\uparrow\rangle, |\downarrow\rangle$) states (indicated by $0 \leq T(\rho, \varrho) \leq 1$), and should also be coherent returning a high ground-state purity after the driving pulse. Figures 6.12 and 6.13 show the results for a QD coupled to a single-mode, and bi-modal cavity respectively.

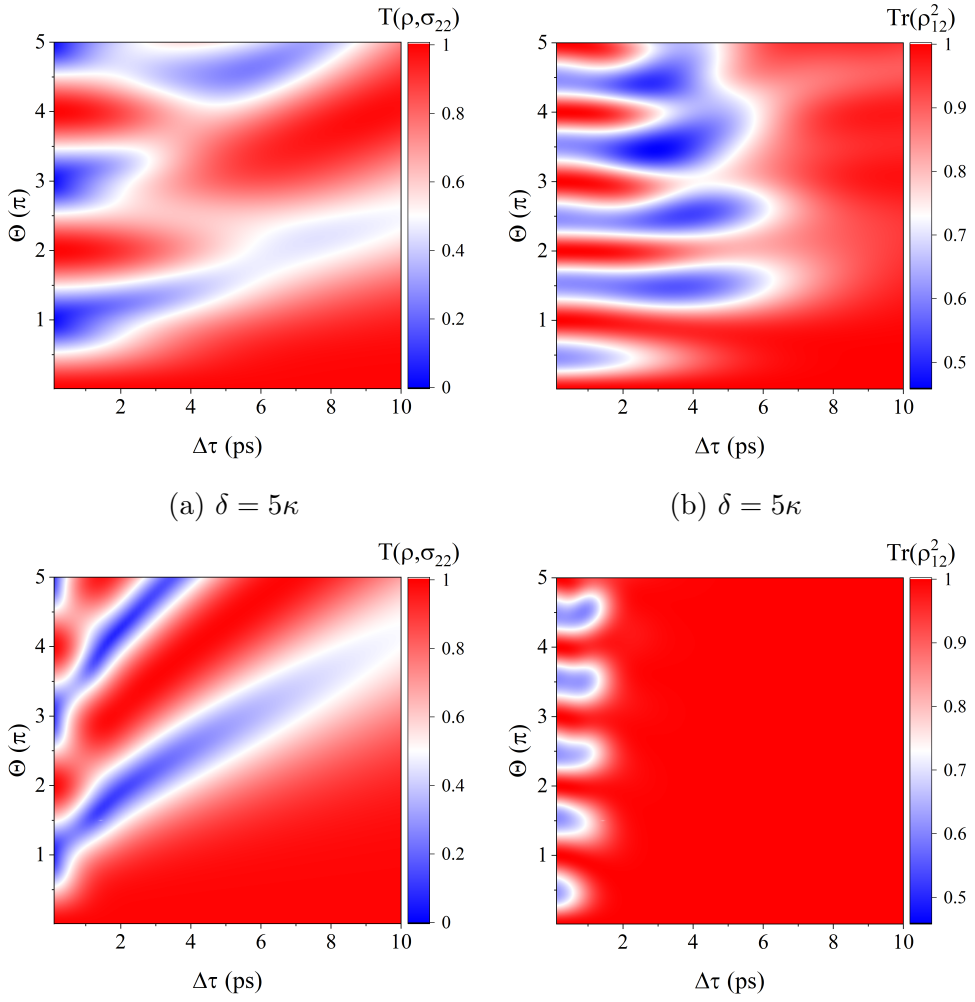

(a) $\delta = 5\kappa$ (b) $\delta = 5\kappa$

(c) $\delta = 20\kappa$ (d) $\delta = 20\kappa$

Figure 6.12: The calculated trace distances (left) and state purities (right) after the control pulses have directly driven the transitions of a Four-Level System (4LS) (initialised in the $|1\rangle$ ground state) coupled to a single-mode cavity as a function of pulse Full-Width Half Maximum (FWHM) and pulse area for a number of different laser detunings (δ). Parameters used: $F_p = 10$, $\kappa/2\pi = 21$ GHz.

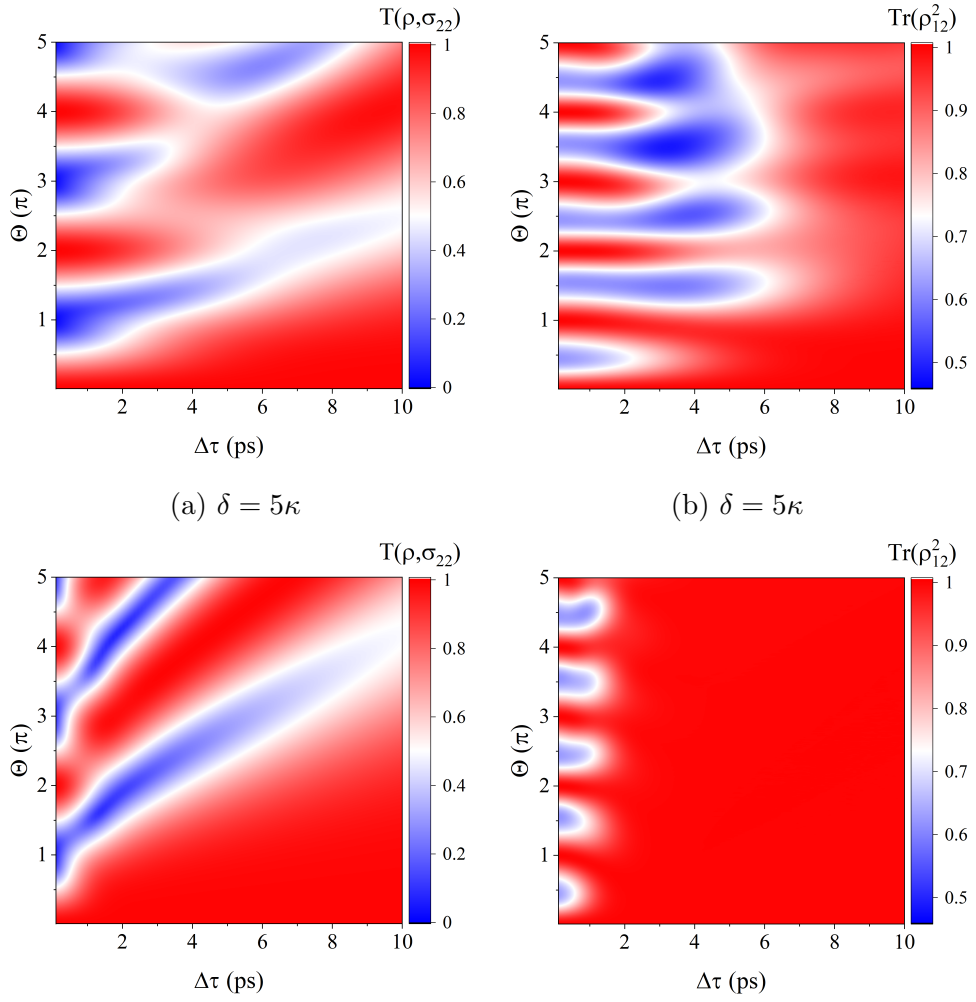

(a) $\delta = 5\kappa$ (b) $\delta = 5\kappa$

(c) $\delta = 20\kappa$ (d) $\delta = 20\kappa$

Figure 6.13: The calculated trace distances (left) and state purities (right) after the control pulses have directly driven the transitions of a Four-Level System (4LS) (initialised in the $|1\rangle$ ground state) coupled to a bi-modal cavity as a function of pulse Full-Width Half Maximum (FWHM) and pulse area for a number of different laser detunings (δ). Parameters used: $F_p = 10$, $\kappa/2\pi = 21$ GHz.

When coupled to a single-mode cavity, we find the control process is optimised for larger pulse detunings (δ). Figures 6.12a and 6.12b show the results for $\delta = 5\kappa$. We find that, when $\delta = 5\kappa$, the control process only returns states with $P(\rho_{12}) \approx 1$ when driving the system with pulses of long duration, or when the areas of the control pulses are integer multiples of π. Additionally, we find the control process is unable to simultaneously access a wide range of possible ground states, and return a pure state, when the detuning is small. On the other hand, Figures 6.12c and 6.12d show that when $\delta = 20\kappa$ the control process is able to access a wide range of qubit states, and also return a state with approximately unity purity (i.e. $P(\rho_{12}) \approx 1$). In fact, at the larger pulse detuning, we find there is a wide driving parameter regime where states with $P(\rho_{12}) \approx 1$ are returned by the control process. The larger detuning of the excitation pulses from the optical transitions of the 4LS minimises the excited state populations during the control process [173]. As a result, the trion states are predominantly virtually excited by the control pulses, ensuring the coherence of the control process by removing decoherence resulting from the fast decay of the trion states [173]. Even at the largest detuning studied, we find the $P(\rho_{12}) < 1$ for the shortest pulse durations. When $\Delta\tau < 2$ ps, even for $\delta = 20\kappa$, the spectral width of the pulses is large enough to excite a significant population in the trion states, and thus decoherence from the decay of these states becomes significant.

We find a near identical behaviour when the 4LS is coupled to a bi-modal cavity. Figure 6.13 shows that, much like in the single-mode case, the larger detuning studied returns states with a high purity for a greater range of driving pulse parameters due to the protection offered against decoherence resulting from the decay of the excited states. Similarly, we also find the large detuning enables access to a large range of qubit states while ensuring the control process remains coherent.

6.6 Summary

In this chapter we have studied the impact of cavity configuration on the optical initialisation, control, and readout of single spins in semiconductor QDs. We found that while the enhancement of undesired transitions resulting from coupling to a bi-modal cavity may be mitigated against in the optical spin initialisation and control stages, these enhanced transitions significantly limit optical spin readout with a QD coupled to a bi-modal cavity. Likewise, we

have shown that the range of cavity parameters that optimises spin initialisation with a bi-modal cavity does not overlap with the cavity parameters that optimise optical spin readout in this cavity configuration meaning there is no single set of bi-modal cavity parameters that can simultaneously optimise both the spin initialisation and spin readout fidelities.

On the other hand, our results show that optical spin initialisation and optical spin readout may be performed with near unity fidelity over a large range of cavity parameters when driving a QD coupled to a single, linearly polarised cavity mode with a square pulse. We find a spin readout fidelity of $\mathcal{R} \geq 99\%$ may be achieved across a broad range of cavity linewidths. Achieving $\mathcal{R} > 99\%$, assuming a pure dephasing rate $\Gamma_{PD} \leq \gamma$, requires a Purcell enhancement of $F_P > 19$, while of the parameters studied a cavity width $\kappa/2\pi = 20$ GHz returned the best initialisation fidelity. Moreover, when coupled to a single-mode cavity we find the spin initialisation, and readout stages are robust against pure dephasing, maintaining the potential to achieve fidelities $\geq 99\%$ at even the largest pure dephasing rates studied.

Furthermore, we have also shown that in the limit of short pulse duration a Gaussian pulse produces a smaller trace distance in the initialisation stage than a square pulse of comparable duration. However, while this does provide a significant time advantage, the best trace distances achieved using Gaussian pulses are orders of magnitude larger than those achieved with longer square pulses.

By performing driving pulse parameter sweeps, we have also shown both single-mode and bi-modal cavities allow optical spin control when directly driving the QD with two orthogonally polarised detuned Gaussian pulses. For either cavity configuration, we find this process is optimised when the control pulses are far detuned from the optical transitions of the 4LS. This detuning ensures decoherence resulting from the decay of excited state populations does not degrade the coherence of the optical control process.

This page is intentionally left otherwise blank.

Chapter 7

Crossed Nanobeam Photonic Crystal Cavities: Part I

In Chapter 6 we explored how an optical cavity may be employed to improve the fidelity with which a QD spin state may be prepared and read out using optical pulses. In this chapter we shall discuss the methods for designing, and fabricating physical structures that can be used to test the ideas set out in Chapter 6. This includes a discussion of the methods for simulating optical structures, the growth of QDs, and the optical characterisation of the resulting phononic samples. We shall begin with a brief overview of Maxwell's equations in matter, and how they are used in the Finite-Difference Time-Domain (FDTD) method for simulating the propagation of electromagnetic waves. The principles behind guiding and confining light, and the operation of diode structures is then presented. Finally the chapter closes with an overview of the growth of QDs and diodes, and the experimental methods used in the characterisation of the samples studied in Chapter 8.

7.1 Maxwell's Equations

Maxwell's equations unified the previously separate fields of electricity, magnetism, and light; bringing together Gauss' law, Gauss' law of magnetism, Faraday's law, and the Maxwell-Ampere law to form a set of four coupled differential equations. It is in this differential form that Maxwell's equations are useful for computationally simulating the propagation of light through optical media. This section shall provide a brief overview of Maxwell's equations in a material in their differential form as applies to the FDTD method. For a more in-depth discussion see [174, 175].

The first of Maxwell's equations, Gauss' law, states the divergence[1] of the displacement field, $\boldsymbol{D}$, in a medium is directly proportional to the free electric charge density, ρ_f

$$\nabla \cdot \boldsymbol{D} = \rho_f, \tag{7.1}$$

where $\boldsymbol{D}$ is related to the electric field by $\boldsymbol{D} = \epsilon_0 \epsilon_r \boldsymbol{E}$. Here ϵ_0 and ϵ_r are the permittivity of free space, and the relative permittivity of the material respectively. Physically we can interpret this law as stating that electric charges are the source of electric fields. The electric fields diverge from positive charges, and converge on negative charges. The next of Maxwell's equations, known as Gauss' law of magnetism, states that the divergence of the magnetic induction, $\boldsymbol{B}$, is equal to zero

$$\nabla \cdot \boldsymbol{B} = 0, \tag{7.2}$$

which indicates that, unlike electric monopoles, magnetic monopoles do not exist. The third of Maxwell's equations is the Faraday-Lenz law which is given by

$$\nabla \times \boldsymbol{E} = -\frac{\partial \boldsymbol{B}}{\partial t}. \tag{7.3}$$

This states the curl[2] of the electric field is directly proportional to the time derivative of the magnetic induction. The Faraday-Lenz law tells us that a time varying magnetic induction will generate vortices in the electric field. The final equation, known as the Maxwell-Ampere law, relates the curl of the magnetic field, $\boldsymbol{H}$, to the time derivative of the displacement field, and current density, $\boldsymbol{J}$, through

$$\nabla \times \boldsymbol{H} - \frac{\partial \boldsymbol{D}}{\partial t} = \boldsymbol{J}. \tag{7.4}$$

The magnetic field vector, $\boldsymbol{H}$, is related to the magnetic induction by $\boldsymbol{H} = \mu_0 \mu_r \boldsymbol{B}$, where μ_0 and μ_r are the permeability of free space and relative permeability of the material respectively. The Maxwell-Ampere equation tells us that magnetic field loops are generated by electric currents and time varying electric fields.

[1]The divergence of a vector field produces a scalar field indicating the rate at which the density of the vector source enters or exits a region of space.

[2]The curl of a vector field produces another vector field indicating the magnitude and axis of circulation of the initial vector field.

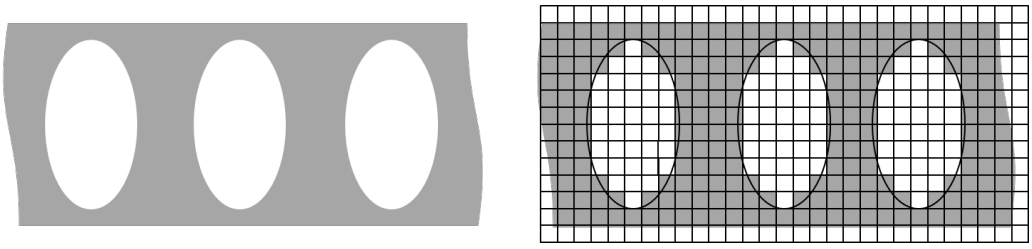

(a) (b)

Figure 7.1: A 2D depiction of a segment of a 1D Photonic Crystal (PhC) (a) approximated on a coarse mesh Yee lattice (b).

7.2 Finite-Difference Time-Domain

The work performed in Chapter 8 will require us to simulate the properties of optical nanostructures. One approach for computationally modelling the evolution of electric and magnetic fields in such optical structures is the Finite-Difference Time-Domain (FDTD) method[3]. This method uses the time-dependent Maxwell's equations in their differential form (Eqs. 7.1-7.4) to propagate electromagnetic waves through a given structure. Since the FDTD method works in the time-domain, it has the benefit of the ability to include a wide range of frequencies in a single simulation, and animate the simulated fields easily to show explicitly their temporal evolution. However, for large regions of interest, or systems with small feature sizes, the FDTD approach can be computationally expensive, requiring large amounts of memory and long simulation times. Therefore, for systems that are sufficiently small along one spatial dimension, it is usually more efficient to use either a 2.5D, 2D, or eigenmode expansion approach rather than the full 3D FDTD approach used in this thesis.

To calculate the dynamics of the electric and magnetic fields using the FDTD method we must first define a region of interest which is then approximated by a lattice, known as a Yee lattice, consisting of an array of uniform Yee cells. Structures within the simulation region are approximated on the Yee lattice as a position dependent dielectric map as shown in Figure 7.1. The FDTD method then uses Faraday's law (Eq. 7.3) with a fictitious magnetic charge current density term, $\boldsymbol{J}_B$, subtracted from the right hand side, and the Maxwell-Ampere law (Eq. 7.4) to propagate the time-dependent electric and magnetic fields. The temporal and spatial derivatives of these equations are approximated by finite differences in space (i.e. the dimensions of the Yee cell)

[3]For a more detailed discussion of the FDTD method see [176, 177].

and time (using a time step Δt). The simulation proceeds from time zero, when any sources we have included are switched on, using a so-called 'leap frog' approach. The electric field components are calculated along the vertices of the Yee cells at time t using the electric fields at time $t - \Delta t$, the magnetic fields at time $t - (\Delta t/2)$, and any sources. On the other hand, the magnetic fields are calculated at the faces of the Yee cell at time $t + (\Delta t/2)$ using the magnetic fields at time $t-(\Delta t/2)$, the electric fields at time t, and any sources. The simulation is then halted by either reaching a pre-determined time limit or by a threshold for the total energy within the simulation region (either low or high) [176].

7.2.1 Boundary Conditions

In the FDTD simulations our region of interest does not extend indefinitely, but is instead enclosed by user-defined boundaries. Choosing the correct boundary conditions is critical to ensuring the results of the simulation are accurate. The different boundary conditions may be separated into three broad categories: absorbing, metallic, and periodic. Absorbing boundaries are the most commonly implemented boundary condition, and typically use the Perfectly Matched Layer (PML) approach. This method uses a number of absorbing layers in the boundary region to absorb all incident electromagnetic waves ensuring there are no back reflections at the boundary to simulate free-space [178]. As the name suggests, periodic boundary conditions are used in the simulation of periodic structures enabling one to consider only a single unit cell of a potentially extremely large structure [179] and thus reducing the computational resources required to simulate the structure. The periodicity of the photonic structure of interest, and thus also the dimensions of a single unit cell, is then determined by the dimensions of the applied boundaries [176]. It is important to note that the electromagnetic field with which the periodic structure interacts must also be periodic for the simulation to be valid [176]. The final boundary condition, metallic, is essentially the opposite of the absorbing boundary condition. When a boundary is set to metallic any incident fields are perfectly reflected back into the simulation region, i.e. the boundary behaves as a perfect electrical conductor. This boundary type requires the least computational resources of the three boundary condition categories.

7.2.2 Symmetry

One method for reducing the memory requirements of a simulation is to take advantage of any symmetries in the structure of interest. Introducing symmetry to the simulations reduces the overall volume that needs to be simulated. It is important to note that the correct symmetry must be chosen to account not only for the structure being simulated, but also the electromagnetic waves that are also present in the simulation. The simulations of the structures we shall consider in Chapter 8 make extensive use of different symmetry conditions along all three spatial dimensions.

7.3 Guiding and Confining Light

The ability to guide light on-chip is one of the essential components for developing optical-based quantum technologies. There are two main approaches typically used to confine and guide light on-chip that are relevant here, namely Total Internal Reflection (TIR) and the engineering of photonic bands through the modulation of dielectric constants. The cavities studied in Chapter 8 make use of a combination of these approaches.

7.3.1 Total Internal Reflection

TIR refers to the phenomenon whereby light travelling in a medium may be reflected back at the interface with another medium of lower optical density. It is therefore one of the simplest methods for confining light in a dielectric medium [180]. While possibly the most well known application of TIR is in the optical fibres used extensively to carry information across the globe, TIR can also be critical for confinement of light on much smaller scales. Micro-scale structures such as those using 1D or 2D photonic crystals (discussed in section 7.3.2), as well as suspended nanobeam waveguides, all rely on TIR to confine light along one or two axes.

It is important to note that TIR will only occur when light is incident on the interface between the two media at an angle, measured from the normal of the interface, greater than the so-called critical angle θ_c. This critical angle defines the angle of incidence where the refracted light will propagate along the boundary, and is determined by the ratio of the refractive indices of the two media at the boundary such that $\theta_c = \sin^{-1}\left(n_2/n_1\right)$ where $n_{1(2)}$ are the optical densities of the two media [180]. The larger the difference in refractive

indices between the two media, the smaller the critical angle and the greater the confinement. At 4K, and in the wavelength range of typical InAs QD emission, GaAs is transparent with a low dispersion and a refractive index $n_{GaAs} \approx 3.4$. When clad with air ($n_{air} = 1$), this gives a critical angle $\theta_c \approx 17°$. In a physical system, even beyond the critical angle there will be a non-zero evanescent component of the fields that couples into the second medium.

7.3.2 Photonic Crystals

In contrast to TIR, a PhC use a periodic modulation of the dielectric constant of a medium to guide and confine light [181]. Analogous to the electronic band structure of semiconductors discussed in Sec. 3.2.1, this periodic spatial variation of the dielectric constant results in the formation of optical bands. If the modulation of the dielectric constant is great enough, and any absorption is low enough, complete band gaps will open up in the photonic band structure where no photonic states exist as a result of destructive interference caused by the periodic variation in the refractive index. Subsequently in the PhC region light in a given wavelength range will couple evanescently, with the intensity decaying rapidly within the PhC. Therefore, by engineering the periodicity and refractive index contrast, we may prevent light from propagating in a given direction using a PhC. Depending on the number of directions in which the PhC extends we may classify them as 1D, 2D, or 3D, although the latter is extremely difficult to realise experimentally. For further details about PhCs see [181].

To guide or confine light using PhCs, we may introduce defects into their periodic structure. As PhCs typically consist of an array of air holes etched into a planar semiconductor material, defects may be introduced through the omission of one or a series of these holes[4] Removing a singe period or small number of periods from a 1D or 2D PhC confines light to a small spatial region through the introduction of a defect state to the photonic band gap, creating a cavity[5]. Examples of such Photonic Crystal Cavities (PhCCs) include: H1 cavites, where a single period is removed from a 2D hexagonal PhC lattice [152, 183–187]; L3 cavities, where three periods in a line are remove from a 2D hexagonal PhC lattice [188–191]; Photonic Crystal Waveguide Cavities (PhCWGCs), combining a waveguide and cavity mode [192, 193]; and nanobeam cavities,

[4]Defects may also be introduced through the displacement, rather than omission, of the PhC holes as in, for example, the H0 cavity [182].

[5]In 1D and 2D PhCs TIR is responsible for confinement along the axes into which the PhC region does not extend.

where a single period is removed from a linear 1D PhC [155, 194–196]. As the period of a PhC is on the order of the wavelength of interest, PhCCs have the potential to give rise to large Purcell enhancements with even modest cavity quality factors [97] given the tight confinement of light to the defect region. One may also introduce a linear defect into a PhC to form a PhC waveguide. Omitting a single row of holes in a 2D PhC creates a defect mode within the photonic band gap of the PhC. Assuming this mode remains confined out-of-plane through TIR, light may propagate along this defect mode forming a so-called W1 waveguide [197–200].

7.4 Diodes: Principle of Operation

In Chapter 3 we discussed the effects resulting from applying an external DC electric field across a QD, and how this is often achieved by situating the QD in a diode structure. However, we did not discuss the details of these diodes, the principle of their operation, or how one includes QD in such structures. This section presents an overview of the structure of semiconductor diodes and their principle of operation, while the next section (7.5) outlines the growth of diodes, and epitaxial QD.

As we discussed previously, a standard approach to applying an electric field across a QD is to situate the QDs in the optically active intrinsic region of a semiconductor P-I-N diode, although other diode configurations may also be used [201, 202]. This approach not only allows an electric field to be applied across the QDs, but also gives control over the injection of charge carriers into the depletion region of the diode. A schematic of the band structure of a P-I-N diode is shown in Figure 7.2. A P-I-N diode is formed when three semiconductor layers with different dopants (or no dopants in the case of the intrinsic I region) are grown successively. In the P-type region impurities are added during the growth process with one fewer valence electrons than the bulk intrinsic semiconductor material [46]. As the energy level of this type of dopant lies just above the edge of the valence band owing to a different binding energy, the dopant is able to easily accept electrons from the valence band (or equivalently donate holes to the valance band) and thus this type of dopant is commonly known as an acceptor. Including an acceptor in the intrinsic semiconductor has the effect of increasing the density of holes in the valence band, and also shifts the Fermi level to the acceptor energy level. In the N-type region the intrinsic semiconductor is doped with electron donors,

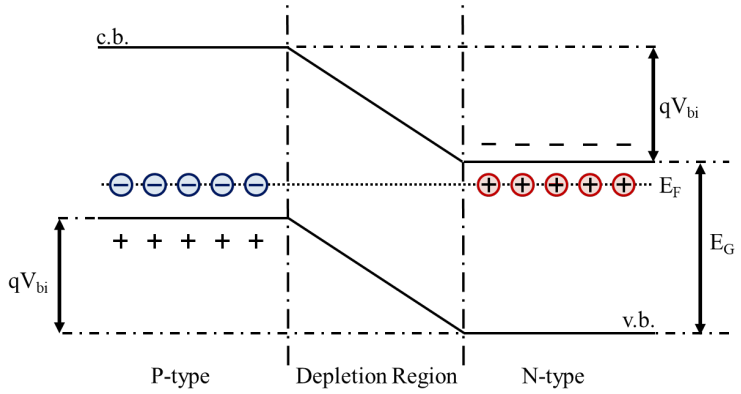

Figure 7.2: A diagram of the band structure in a P-I-N diode showing the conduction and valence bands. The built-in voltage (V_{bi}) occurs as a result of the build-up of space charge in the P-type and N-type regions, and has the effect of ensuring a uniform Fermi-level across the structure.

impurities with one additional valence electron compared to the atoms of the intrinsic semiconductor [46]. In this case the dopant level lies just below the conduction band edge, and as a result is able to increase the density electron density in the conduction band of the N-type semiconductor. Again this has the effect of shifting the Fermi level, only now up to the donor level.

When a P-type and N-type semiconductor are brought together, with an intrinsic region between them to form a P-I-N diode, there is initially a discontinuity in the Fermi level. To ensure a uniform Fermi level across the entire device, the charge carriers introduced by the doping begin to diffuse across the intrinsic region of the diode. The donors in the N-type region lose electrons to the P-type region, and the P-type region loses holes to the N-type region, until the Fermi level is equalised. This leaves a fixed space charge in the two doped regions creating a built-in electric potential across the intrinsic depletion region. The energy related to this built-in electric field is approximately equal to the band-gap energy of the intrinsic semiconductor (i.e. $E_G \approx qV_{bi}$).

In addition to the built-in voltage, we can apply an external electric bias to the diode to alter the strength of the electric field in the intrinsic region. Applying a forward bias reduces the potential difference between the P-type and N-type semiconductor regions (i.e. $V_{fb} = V_{bi} - V$). Alternatively, applying a reverse bias increases the potential difference between the doped regions (i.e. $V_{rb} = V_{bi} + V$). Hence by applying an external bias to the P-I-N diode one is able to control the magnitude of the electric field across the intrinsic region of the diode where QDs are typically situated. In Chapter 8 a reverse bias is used to study QD emission.

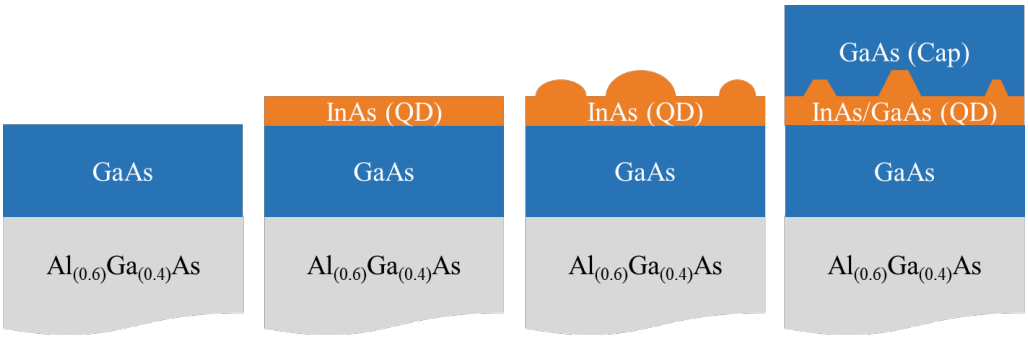

Figure 7.3: The Stranski-Krastanov (SK) growth process for Self-Assembled Quantum Dots (SAQDs). A GaAs layer is deposited on a sacrificial AlGaAs layer. An InAs Quantum Dot (QD) layer is then deposited on the GaAs layer. The difference in lattice constants between these two layers, GaAs and InAs, results in the spontaneous formation of inverted lens shaped islands on the surface of the InAs. Capping with a further GaAs layer forms the optically active QDs.

7.5 Wafer Growth

7.5.1 Stranski-Krastanov Growth

QDs embedded in bulk semiconductor layer structures are commonly grown using the Stranski-Krastanov (SK) growth mode, also known as self-assembly. The prevalence of SK growth is a result of the high optical quality of the formed Self-Assembled Quantum Dots (SAQDs). The best SAQDs have transform limited linewidths ($T_2 = 2T_1$, see Section 3.9) on the order of 1 μeV [203].

Self-assembly relies on the presence of strain in a semiconductor to form SAQDs. This strain is introduced by the consecutive deposition of semiconductor layers with differing composition and lattice constants. Thus SK growth requires the ability to control the composition of individual semiconductor monolayers throughout the growth process. Such accuracy can be achieved using now well-known crystal growth techniques such as Molecular Beam Epitaxy (MBE) or Metal-Organic Chemical Vapour Deposition (MOCVD)[6].

Figure 7.3 shows an illustration of the SK growth process for InAs SAQDs. The process begins with the deposition of GaAs layer onto any previously deposited semiconductor layers. The InAs QD layer, known as the wetting layer, is then deposited onto the substrate. There are two main reasons InAs is used as the wetting layer material on a GaAs substrate. Firstly, as mentioned

[6]Metal-Organic Chemical Vapour Deposition (MOCVD) is sometimes referred to as Organo-Metallic Vapour Phase Epitaxy (OMVPE) or Metal-Organic Vapour Phase Epitaxy (MOVPE).

previously self-assembly requires a mismatch in the lattice constant of two adjacent semiconductor layers to introduce strain. InAs and GaAs have a 7% lattice constant mismatch [204, 205] which is sufficiently large to build up the required strain in the InAs layer to form SAQDs. Secondly, InAs has a smaller band gap[7] than GaAs ensuring confinement of charge carriers to the InAs layer. Above the so-called critical thickness (one to two monolayers), it becomes energetically favourable to relieve the strain in the wetting layer through the formation of inverted lens shape islands on the surface of the 1-2 nm thick wetting layer [204, 205]. This occurs at the expense of increased surface energy [204, 205]. Self-assembly is an inherently stochastic process and thus these islands form at random spatial positions with a distribution of sizes. Deposition of a capping layer [8], a process known as overgrowth, forms optically active SAQDs by increasing the distance to any surface defects that may cause non-radiative relaxation processes [206]. Overgrowth also alters the shape of the SAQDs from inverted-lens to truncated pyramid, and diffusion of gallium from the capping layer alters the SAQD composition [206]. After overgrowth SAQDs typically extend 2-5 nm in the growth direction (out-of-plane) and approximately 20 nm in-plane [205].

Quantum Dot Registration

While SAQDs may have excellent optical properties, their random distribution sizes and positions becomes problematic when considering the scalability of on-chip quantum circuits, and yield of devices. The coupling of a QD to the mode of an optical cavity, for example, is dependent on the spatial and spectral position of the QD relative to the cavity mode (Eq. 3.54). Using a probabilistic approach to fabrication is inefficient, often resulting in optical components containing spectrally unsuitable QDs at sub-optimal spatial positions. Additionally, the size and shape of QDs affects their optical properties. Hence a probabalistic approach to fabrication ultimately limits the potential to develop complex quantum circuits as these structures require multiple identical QDs.

QD registration is a category of techniques that may be used to predetermine the spatial location of SAQDs on a sample before the fabrication of on-chip optical components. Combined with spectroscopic techniques, registration allows on-chip structures to be accurately fabricated around preselected SAQDs with pre-determined locations and suitable optical properties.

[7] The band structures of semiconductors is discussed in Section 3.2.1.

[8] The capping layer and substrate are usually formed from the same constituent semiconductor material.

Such quantum dot registration techniques include Atomic Force Microscopy (AFM) [207], Scanning Electron Microscopy (SEM) [208, 209] , Cathodo-Luminescence (CL) [210], and Micro Photoluminescence (μ-PL) [211–213]. While all of these techniques are able to determine the position of a single QD with an error below 50 nm, only CL and μ-PL are able to determine both the spectral properties and spatial locations of the SAQDs. AFM and SEM both require an additional μ-PL step to determine the spectral properties of any registered SAQDs.

The most commonly used quantum dot registration technique is μ-PL. Using a so-called two colour technique, μ-PL can be used to quickly determine the positions of SAQDs relative to a series of pre-patterned alignment markers over a large area [211, 212] (see Figure 7.4). To achieve this two LEDs are used simultaneously to illuminate the sample [211, 212]. The first LED off-resonantly excites the SAQDs to produce an intensity map which can be used to determine the spatial positions of the SAQDs by fitting 2D Gaussian point spread function [211, 212]. The second LED is used to image the alignment markers with their position being determined by a fitted Gaussian. The result is simultaneous imaging of both the SAQDs and the alignment markers. Using this technique single SAQDs have been located with an average standard deviation error of just 4.5 nm using a 1 second exposure [212]. The spectral information of the SAQDs is obtained after registration by incorporating a tunable laser into the system [211, 212] (see Section 7.6.2 for more detail).

Before the two colour μ-PL method, single-colour μ-PL spectroscopy was used either in isolation with pre-patterned alignment markers on the sample [213] or combined with photolithography to pattern alignment markers in a photoresist when a suitable SAQD was located [214]. In single-colour μ-PL a laser is scanned across the surface of the sample to locate and determine the optical properties of a SAQD [213, 214]. Photolithography can then be performed with the same laser to pattern alignment markers by simply increasing the laser power [214]. However, the drawback with the single-colour μ-PL technique is that it requires more time to complete than the two-colour method. This increase in the required time also increases the potential for misalignment in the system. Post-registration, fabrication of on-chip structures must take place in a separate step using conventional EBL techniques with the alignment markers being used to determine the positions of the on-chip structures [213].

The same basic principles that apply to single-colour μ-PL also apply to CL. However, rather than scanning a laser across the surface of the sample to

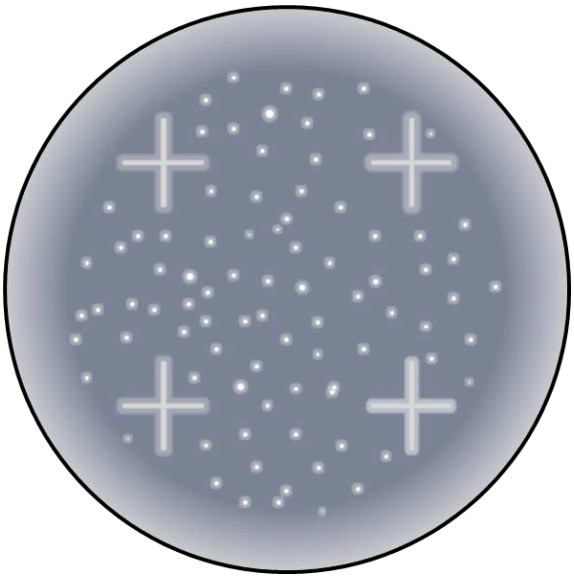

Figure 7.4: A schematic diagram of a typical image of an area of Self-Assembled Quantum Dots (SAQDs) and four alignment markers (crosses). The SAQDs appear as bright spots on in the image that can can be fit with a Gaussian function to determine their central positions. Using a filter before the camera removes QDs emitting at undesired wavelengths from the image.

excite the QDs as done in single-colour μ-PL, an electron beam is used instead. Therefore it is possible to combine CL with the lithographic fabrication of on-chip components using EBL into a single technique referred to a Cathodo-Luminescence Lithography (CLL) [210]. This removes the need for alignment markers and additional fabrication steps making CLL a potentially simpler and more accurate technique than μ-PL [210].

7.5.2 Site-Controlled Growth

QD registration goes some way to mitigating the disadvantages of self-assembly. However, developing truly scalable complex optical circuits on-chip with a high yield requires deterministic growth of QDs to control their size (and hence optical properties) and position [215]. This deterministic growth is known as Site-Controlled Quantum Dot (SCQD) growth and is currently a very active area of research.

One method of SCQD growth uses a lithographically pre-patterned array of nano-holes etched in either the bulk substrate [215–219] or on the surface of a lithographically defined mesa[9] [220–222] to act as nucleation sites when the wetting layer is deposited as in SK growth. Adjusting the size of the mesa has

[9] A mesa is a flat elevated region terminated by steep edges.

been demonstrated to enable control of the QD density at the mesa's centre, preventing the growth of interstitial QDs[10] [220]. Furthermore, the occupation of the nano-holes has been shown to be dependent on their depth [220], and diameter [219].

Unfortunately the process of etching the nano-holes introduces surface effects that significantly broaden the Zero Phonon Line (ZPL) linewidth of single SCQDs near the re-growth surface [215]. Crystal defects at the re-growth surface created by the etching of the nano-holes trap charges near the SCQDs causing spectral diffusion [215]. To overcome this the initial SCQDs may be used as a spectrally distinct or optically inactive seed layer for further SCQD growth in subsequent layers [215–217, 221, 222]. Using a seed layer to introduce a separation between the re-growth layer and optically active QDs on the order of 20 nm [219] has led to state-of-the-art observed ZPL linewidths of 43 μeV [222], 25 μeV [219] and 7 μeV [215] at cryogenic temperatures ($\leq$12K) under non-resonant excitation, although these are still much broader than the transform limit. Narrow ZPL linewidths (18-30 μeV) [223] and single photon emission [224] have also been achieved from SCQDs using inverted pyramidal recesses, rather than nano-holes, without the need for a seed layer.

Despite the typically broad ZPLs of SCQDs, Purcell enhancement of the emission from a single SCQD embedded in an L3 PhCC has been observed [225]. Using this technique a QD has been positioned within an optical cavity with an error of 50 nm [221, 225] matching the precision of QD registration techniques. Furthermore, reduced absorption within the cavity due to the presence of only a single SCQD (rather than multiple SAQDs) has been theorised to lead to an increase in the measured quality factor of the cavity [221]. Coupled with this, measurements performed on SCQDs with ZPL linewidth on the order of $\approx$ 10 μeV have shown the properties of the SCQD to be on-par with those of SAQDs [215]. Thus SCQDs with narrow ZPL linewidths show promise as triggered sources of indistinguishable single photons [215].

An alternative approach to SCQD growth that does not involve the etching of pits has also been explored. It has been shown that a buried oxide ($Al_xGa_{1-x}As/AlO_x$) stressor layer can be used to alter the strain on the surface of thick GaAs buffer layer [226, 227]. The larger lattice constant of InAs compared to the GaAs buffer results in preferential formation of InAs QDs at the points of maximum surface strain in the GaAs layer (i.e. points of

[10]The density of QDs can also be reduced by increasing the temperature of the substrate thereby increasing the diffusion length of the In adatoms, but this also has the effect of increasing the QD dimensions [219].

Figure 7.5: A schematic of the designed layer structure of the semiconductor wafer on which the cavity structures characterised for this thesis were fabricated. The layer are differentiated as follows: blue indicates a GaAs layer, grey a AlGaAs layer, and orange the InAs wetting layer. The layers form a P-I-N diode with the Quantum Dots (QDs) in the intrinsic region.

minimum strain in the InAs layer) when the wetting layer is deposited [226]. The ability to include a thick buffer layer while maintaining the surface strain field induced by the stressor layer allows the SCQDs to be formed far from the stressor layer interface where surface effects could degrade the optical quality of the QDs [227]. As a result resolution-limited ZPL linewidths as low as 40 μeV have been observed using μ-PL [227].

7.5.3 Wafer Structure

The QDs studied in Chapter 8 were grown using the SK growth mode, and embedded in a P-I-N diode structure. Figure 7.5 shows the designed layer composition and structure of the SF1520 wafer grown by the EPSRC National Epitaxy Facility at the University of Sheffield. The InAs QD layer is embedded between two 5 nm thick undoped GaAs spacer layers, with a further 30 (50) nm of undoped AlGaAs grown above (below) these layers. The asymmetric undoped AlGaAs layers act as barriers reducing the probability that a charge carrier will tunnel out of the QD layer. This not only stabilises the charge environment around the QDs, but also allows for large tuning of the QD emission wavelengths using the Quantum-Confined Stark Effect (QCSE). These undoped layers form the intrinsic region of the P-I-N diode. The top contact of the diode is formed from a 50 nm thick layer of P-doped GaAs, which in addition to the intrinsic region of the diode and an additional 30 nm thick

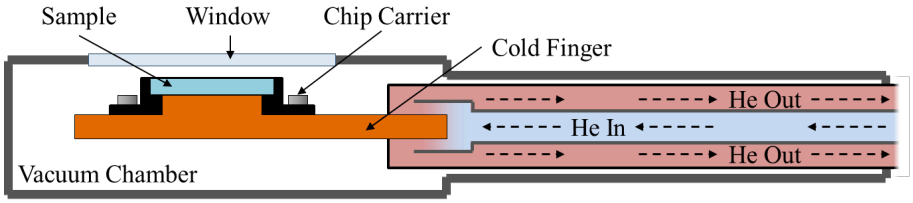

Figure 7.6: A schematic of a Continuous-Flow Cryostat with optical access.

layer of N-doped GaAs below the bottom tunnelling barrier forms the 170 nm thick membrane into which any photonic crystal devices are etched. A sacrificial layer is also included in the wafer design beneath the wafer membrane consisting of 200 nm of N-doped AlGaAs and 800 nm of undoped AlGaAs. This layer is selectively removed during the sample fabrication process to form suspended free-standing photonic structures. The last layer of the wafer is the 300 nm of N-doped GaAs that forms the bottom negative contact of the diode.

7.6 Experimental Methods

7.6.1 Cryostat

The experiments presented in Chapter 8 were all performed at cryogenic temperatures (approximately 4-5 K), and under vacuum. To achieve these conditions the samples were mounted in a Continuous-Flow Cryostat, a schematic of which is shown in Figure 7.6. The continuous-flow cryostat can be generally separated into two areas, the vacuum chamber and the transfer line. The vacuum chamber houses the sample to be studied. The sample is mounted within a chip carrier which is itself mounted to a copper cold-finger that extends into the vacuum chamber. The chip carrier enables electrical control of the diodes fabricated on the sample, and ensures the sample maintains thermal contact with the cold finger throughout the experimental characterisation process. A glass window in the top of the vacuum chamber allows optical access to the sample for this characterisation. To cool the sample to cryogenic temperatures, liquid helium is continuously pumped through the transfer line. Thermal contact between the transfer line and cold finger reduces the temperature of the cold finger, and thus also the sample mounted in the vacuum chamber. The vacuum is necessary to prevent the build-up of condensation on the surface of, and heat flow to, the sample when at the cryogenic temperatures used here. The main advantage of the continuous-flow cryostat compared to a bath cryo-

stat[11] is the speed and ease with which samples may be mounted, measured and characterised, and exchanged. However, this comes at the disadvantage of reduced optical stability owing to vibrations originating from both the pump required to maintain the flow of liquid helium, and the general environment. As a result, the continuous-flow cryostat is not suited to measurements that require long integration times or high stability.

7.6.2 Optical Characterisation

A schematic of the experimental set-up used to characterise the optical cavity devices studied in Chapter 8 is shown in Figure 7.7. Light from the excitation laser and/or white light lamp (introduced into the optical path by a pellicle beamsplitter) is focused onto the sample using an objective lens mounted above the optical window of the cryostat. This set-up allows two positioning methods to be used to adjust the alignment of the objective lens and the sample. Coarse positioning of the sample is achieved by adjusting the x-y micrometer stages to which the continuous-flow cryostat is mounted. On the other hand, fine control of the positioning and focus of the excitation and collection spots is achieved by mounting the objective lens to an x-y-z piezo stack and adjusting the alignment of other optical components within the set-up. The light emitted by, and reflected and scattered from, the sample is then collected by the same objective lens and directed to a second beamsplitter. The component reflected by this beamsplitter is used to image the surface of the sample using a standard camera set-up, while the transmitted component is passed to a spectrometer via an optical fibre. To ensure that only the emission from the sample is passed to the spectrometer, a long-pass filter is included before the optical fibre to remove the component originating from the white light lamp. The spectrometer is then used to measure the spectral properties of the cavity modes and QD emission using a liquid-nitrogen-cooled Charge-Coupled Device (CCD).

Optical Cavities

Initial characterisation of the confined modes of the cavity structures fabricated on the sample was achieved by performing low temperature μ-PL spectroscopy focusing an above-band-gap laser on the cavity centres. The above-band-gap laser excites charge carriers in the semiconductor material surrounding the

[11] In a bath cryostat the sample is cooled by immersion in liquid helium. The sample is held within an evacuated tube containing an exchange gas (often helium) at low density.

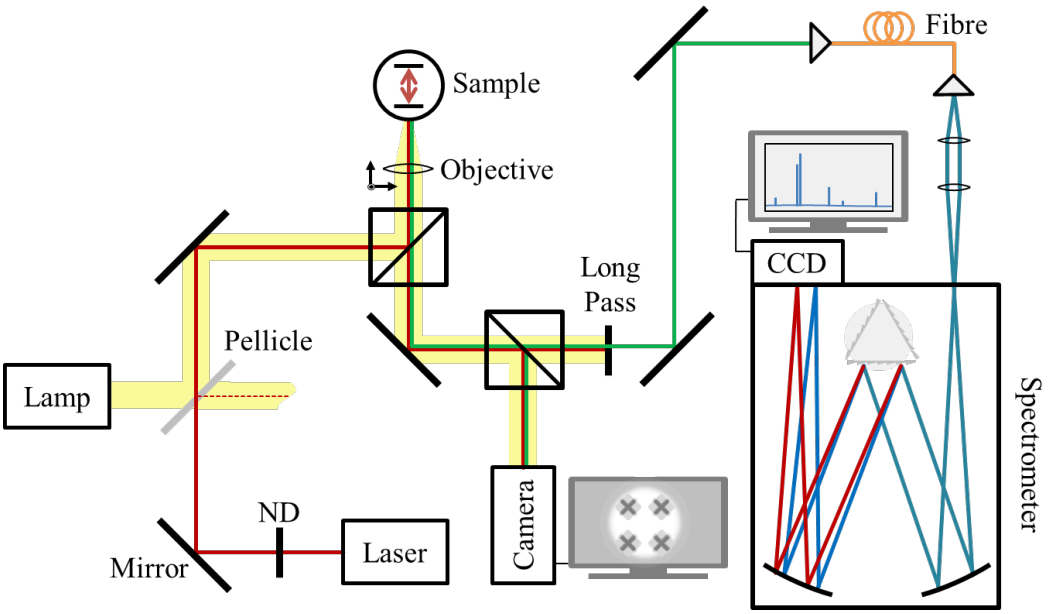

Figure 7.7: A schematic of the optical Micro Photoluminescence (μ-PL) set-up used to characterise the cavity samples. The objective lens is mounted above the flow cryostat on x-y-z piezo stages for fine control of the focus and position of the excitation spot. The spectrometer contains three gratings with: 600, 1200, and 1800 l/mm.

QD layer in the wafer. A bias across the sample, either applied or the built-in potential, sweeps some of these free charge carriers into the QDs where they decay to the energy levels closest to the InAs band edges before recombining and emitting a photon. The QDs then act as internal light sources exciting the cavity modes. Measuring the light scattered out-of-plane from the cavity centres using the experimental set-up previously discussed then allows the properties of the cavity to be determined. Fitting the observed peaks in the cavity spectra with a Lorentzian function allows the cavity mode wavelength to be determined as well as the cavity *Q-factor*, a measure of the damping due to photon loss from the cavity. This can be calculated from the spectral peaks using

$$Q = \frac{\omega_c}{\Delta\omega} = \frac{\lambda_c}{\Delta\lambda}, \tag{7.5}$$

where ω_c (λ_c) is the central frequency (wavelength) of the cavity mode and $\Delta\omega$ ($\Delta\lambda$) is the FWHM of the spectral peak in frequency (wavelength) units.

Quantum Dots

The initial characterisation of individual QDs is achieved in much the same way that the characterisation of optical cavity modes is achieved. The main

difference is that the excitation power used is a fraction of that used when characterising a cavity mode (a few μW compared to hundreds of μWs). The lower power enables individual QD emission lines to be resolved without being obscured by, for example, cavity mode lines or general background noise. Because of this reduced excitation power a longer integration time is required when characterising QDs.

7.6.3 Spectroscopy

As mentioned previously, the main method used in the characterisation of the fabricated optical cavity structures was spectroscopy. These spectroscopic measurements were performed using a grating spectrometer. Specifically, the spectrometer used in Chapter 8 was a Princeton Instruments Acton SpectraPro SP750i with a Princeton Instruments Pylon CCD. The spectrometer allows one to perform a spectral analysis of the light emitted from the sample by spatially separating the different frequencies of light before they are focused on to the CCD. This spectral separation is achieved by directing the collected light towards a diffraction grating. The turret in the spectrometer used contains three gratings with: 600 lmm^{-1}, 1200 lmm^{-1}, and 1800 lmm^{-1}. For the characterisation of the cavity structures the 600 lmm^{-1} grating was used due to the broad nature of cavity spectral lines, and the higher efficiency of the grating. The 1200 lmm^{-1} grating was used to characterise the QD emission lines measured in Chapter 8 to improve the resolution of the measurement, but also maintain a reasonable measurement time during which the drift of the sample would be minimal.

Chapter 8

Crossed Nanobeam Photonic Crystal Cavities: Part II

In Chapter 7 we outlined the methods used in the design, and characterisation of optical nanostructures, as well as the growth of QDs. In this chapter we shall describe the cavity structures that were fabricated to provide an avenue for experimentally testing the theoretical work presented in Chapter 6.

8.1 Introduction

Coupling QDs to optical cavities provides a number of significant potential benefits for realising quantum technologies. Decreasing the timescales on which optical processes occur, through a Purcell enhancement of the decay rate of the excited states of a QD, reduces the relative importance of pure dephasing mechanisms by ensuring a disparity between the timescales on which radiative and non-radiative transitions occur [82]. Furthermore, coupling QDs to optical cavities may be employed to both suppress the laser background resulting from the resonant excitation of QDs [158, 159], and ensure preferential coherent emission into the ZPL over incoherent scattering into the phonon side-band [97, 115, 228]. This suppression of any resonant laser background, and the preferential coherent emission into the ZPL, are both important for increasing the indistinguishability of the photons emitted by single-photon sources. In Chapter 6 we also studied how cavity structures may be employed to improve the fidelity of optical spin initialisation and readout, two processes required for the implementation of optical quantum technologies. However, thus far we have not discussed what the physical implementation of such a cavity structure might look like.

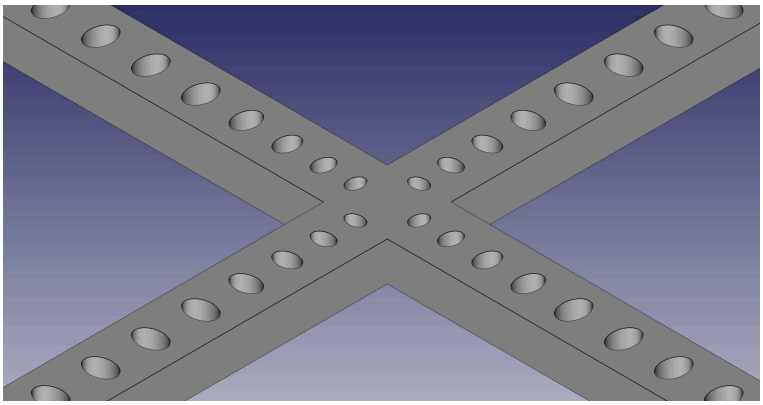

Figure 8.1: A diagram of a bi-modal Crossed-Nanobeam Photonic Crystal Cavity (XNBPhCC). The cavity is formed by four 'arms' each consisting of a nanobeam waveguide and two Photonic Crystal (PhC) Bragg mirrors, an inner modulated Bragg mirror and an outer uniform Bragg mirror.

To be used in on-chip optical quantum technologies it would be advantageous for any optical cavity structures to have a number of properties. The cavity structure must be able to support solid-state, single-photon emitters. Any cavity design must also have the potential to be integrated into scalable, on-chip optical circuits. Additionally, it would be preferable for the underlying architecture of the cavity structure to be able to support single-mode and bi-modal cavities by altering the design to allow the benefits of either configuration to be used in different scenarios as discussed in Chapter 6. The Crossed-Nanobeam Photonic Crystal Cavity (XNBPhCC) is a structure that appears to have the potential to meet all of these criteria. Previous studies of XNBPhCCs have already demonstrated that they can support two near-independent cavity modes [155], and also demonstrated their suitability for applications in non-linear frequency conversion [229]. In this chapter we shall study the properties of XNBPhCCs both theoretically using FDTD, and experimentally using the methods outlined in Chapter 7, to demonstrate additional properties of the XNBPhCC structure that make them suitable for applications in quantum technologies.

8.2 Device Design

The XNBPhCCs studied in this chapter were designed using an intuitive approach, and simulated using the three-dimensional Finite-Difference Time-Domain (FDTD) software from Lumerical Solutions, Inc. [230] (see Section 7.2 for more information on the FDTD method). The XNBPhCC structure con-

sists of two 1D nanobeam PhCCs orientated orthogonally to one another, overlapping at their cavity centres where a single PhC hole is absent. This results in a single structure composed of four 'arms' extending in the the $\pm\hat{x}$ and $\pm\hat{y}$ directions in a + configuration with each 'arm' consisting of a nanobeam waveguide containing Photonic Crystal (PhC) Bragg mirrors that may be subdivided into two distinct Bragg mirror classes (see Figure 8.1).

The first of these PhC mirror classes is the modulated Bragg mirror. These modulated mirrors lie nearest to the cavity centre and consist of n_t PhC holes of increasing radius and period moving out from the cavity centre, linearly increasing the Filling Fraction (FF) (the ratio of PhC hole area to total PhC period area). Tapering the PhC holes reduces the mode profile mismatch between the waveguide mode and PhC mirror Bloch mode by incrementally adjusting the effective refractive index of the PhC mirror [231]. This reduces scattering losses at the interface between the central cavity region and the PhC mirror improving the quality factor (Q-factor) of the cavity [231]. The design of the modulated Bragg mirrors is critical to obtaining a high Q-factor in the XNBPhCC structure. Without careful consideration, we find additional low-Q cavity modes may be introduced to the structure that are confined to the inner modulated Bragg mirrors. As these modes are not localised to the centre of the cavity they would not contribute to the Purcell enhancement of any QDs located at the cavity centre, but may degrade the fundamental cavity mode.

The second distinct PhC mirror class is the uniform Bragg mirror. These mirrors flank the inner modulated Bragg mirror with n_u identical PhC holes with a constant FF. It is these mirrors that provide a majority of the in-plane confinement of the light within the cavity structure. An optional second modulated Bragg mirror may be included after the uniform Bragg mirror identical to the inner modulated mirror, but tapering in the opposite direction. This second modulated mirror provides a smooth transition in the effective refractive index for light emitted from the cavity into the optical mode of the waveguide.

From our FDTD simulations of the XNBPhCCs, we find this design supports two nearly independent, orthogonally linearly polarised cavity modes with electric fields that decay evanescently into the modulated Bragg mirrors with significant (minimal) penetration in the axis orthogonal (parallel) to the dipole polarisation vector (see Figures 8.2a and 8.2b), agreeing with [155]. This design of the XNBPhCCs allows one to optimise the wavelength and Q-factor of the cavity modes by altering (see Figure 8.2c): n_t, n_u, the length of the central cavity region (L_c), the semi-minor radii of the initial hole of the

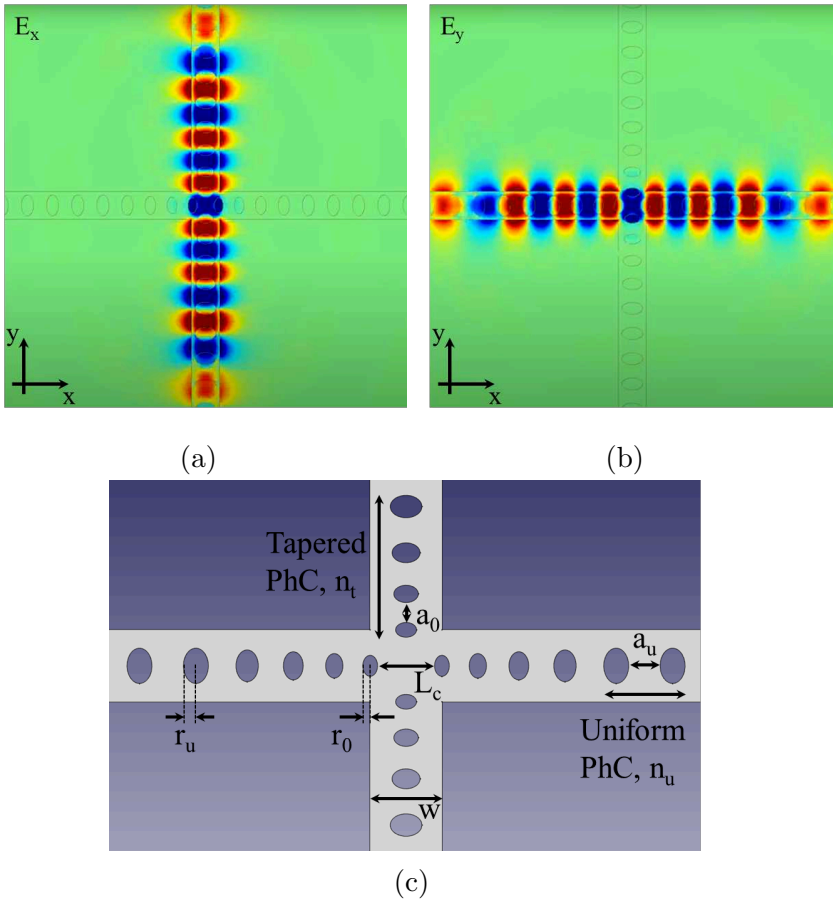

Figure 8.2: (a) and (b) The simulated electric field profiles of the two modes of a bi-modal Crossed-Nanobeam Photonic Crystal Cavity (XNBPhCC). E_x and E_y indicate the polarisation of the dipole source used to excite the cavity model in Lumerical's Finite-Difference Time-Domain (FDTD) software. The fields show anti-nodes localised to the material in between the mirror holes. (c) A labelled schematic of a bi-modal XNBPhCC structure indicating the parameters used in the device design.

modulated Bragg mirror (r_0) and uniform Bragg mirror holes (r_u), the hole eccentricity (e) such that the semi-major hole radius is related to the semi-minor radius by $r_{maj} = er_{min}$, and lastly the initial period of the modulated Bragg mirror (a_0) and the period of the uniform Bragg mirror (a_u). Maintaining the uniform mirror parameters and hole radii, we find adjusting L_c and a_0 allows the wavelength of the cavity mode to be altered within a given wavelength range without a large impact on the Q-factor. We also find the cross-sectional dimensions of the nanobeam waveguides impact the properties of the cavity modes. However, here these parameters are fixed by the requirement for single TE-mode propagation along the waveguides while remaining suitable for integration into diodes.

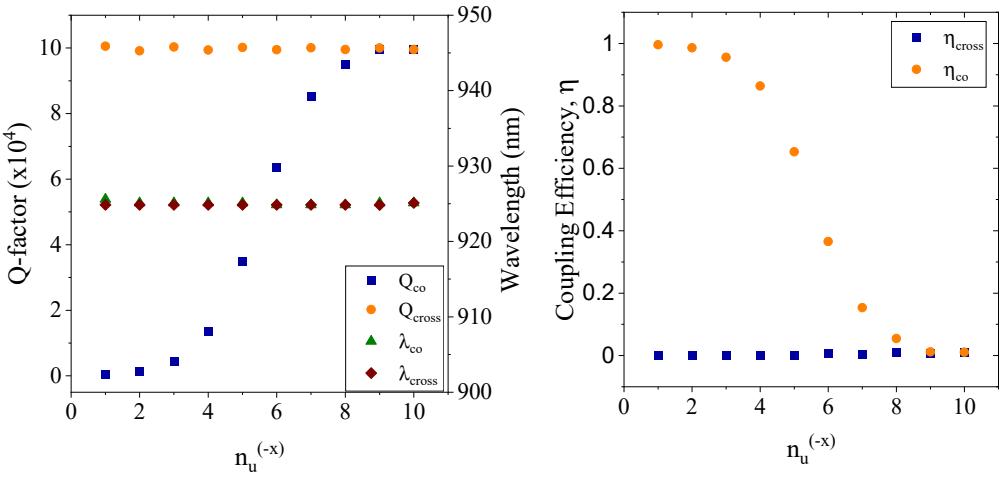

(a) (b)

Figure 8.3: The simulated (a) Q-factor and wavelength, and (b) relative coupling efficiencies, of the two cavity modes of a bi-modal Crossed-Nanobeam Photonic Crystal Cavity (XNBPhCC) as a function of the number of uniform Bragg mirror periods in the cavity arm along the $-x$ direction ($n_u^{(-x)}$). All other cavity arms have $n_u = 10$. For all cavity arms $n_t = 4$. The simulations were performed using the Finite-Difference Time-Domain (FDTD) method with software from Lumerical.

8.2.1 Asymmetric Cavity Emission

In addition to supporting symmetric cavities, our design of the XNBPhCCs also allows for asymmetric emission from the cavity modes by independently adjusting the number of uniform Bragg mirror periods in each of the four arms of the cavity structure. Reducing the number of uniform Bragg mirror periods (n_u) in one of the cavity arms reduces the reflectivity of that mirror relative to the second arm along the same axis. This results in a stronger coupling between the cavity mode and the guided modes of the nanobeam waveguide in the direction with the smallest n_u. Figure 8.3 shows the effect of altering the number of uniform mirror periods in the $-x$ arm of the cavity leaving all other cavity arms with $n_u = 10$. As one would expect, Figure 8.3a shows that reducing the mirror strength in the $-x$ cavity arm reduces the Q-factor of the co-polarised cavity mode without significantly changing the wavelength of that cavity mode. Figure 8.3a also demonstrates the near independence of the two cavity modes as both the Q-factor and wavelength of the cross-polarised cavity mode are unaffected by the change in mirror strength in the co-polarised cavity axis. The effect on the relative coupling strengths between the cavity modes and waveguide modes is shown in Figure 8.3b. We define the coupling

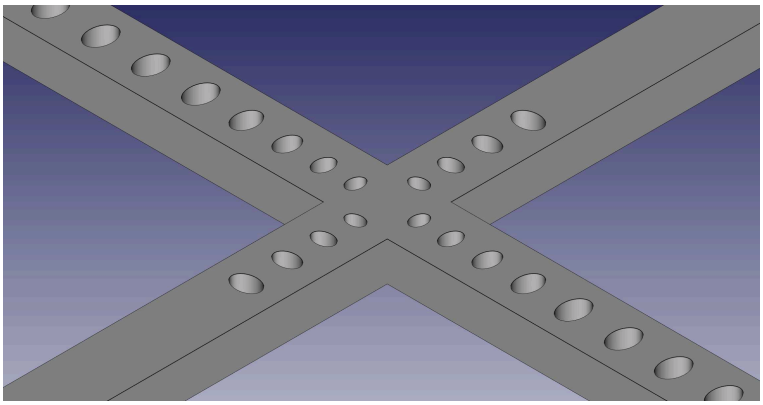

Figure 8.4: A schematic of a single-mode Crossed-Nanobeam Photonic Crystal Cavity (XNBPhCC). The uniform Bragg mirrors along a single axis are removed leaving only the modulated Bragg mirrors in that axis. The orthogonal axis maintains both the modulated and uniform Bragg mirror regions.

efficiency between the cavity and waveguide modes as [152, 190]

$$\eta_{co(cross)} = \frac{Q^{-1}_{co(cross)} - Q^{-1}_{U}}{Q^{-1}_{tot}}, \tag{8.1}$$

where

$$Q_{tot} = \left(Q^{-1}_{co} + Q^{-1}_{cross} - Q^{-1}_{U}\right)^{-1}, \tag{8.2}$$

and Q_U is the Q-factor of the cavity when un-coupled from the waveguide modes, i.e. when $n_u \to \infty$. Again, Figure 8.3b demonstrates the near independence of the two cavity modes as the coupling efficiency of the cross-polarised cavity (i.e. the unaltered cavity mode) mode remains unchanged as the coupling efficiency of the co-polarised mode increases with decreasing n_u in the $-x$ cavity arm. Such directionallity could prove useful in the construction of on-chip optical circuits, enabling information to be reliably passed on to the next node in the chain or allowing the structure to act as an optical switch.

8.2.2 Single-mode and Bi-modal Cavities

From Figure 8.3 we find that when the number of uniform Bragg mirror holes is reduced to one, the Q-factor and coupling efficiency of the co-polarised cavity mode go to zero and unity respectively, while the cross-polarised cavity mode maintains its high Q-factor, low coupling efficiency, and wavelength. Thus by removing the uniform Bragg mirrors from a single axis, the XNBPhCC structure can be made to support only a single linear cavity mode while maintaining access to the orthogonal polarisation via a waveguide mode. However,

our FDTD simulations show that to maintain the remaining cavity mode in the orthogonal axis, the modulated Bragg mirrors need to remain in all four cavity arms as can be seen in Figure 8.4. This ability to support either one or two linearly polarised cavity modes while maintaining access to both orthogonal linear polarisations independent of the cavity configuration makes these structures ideal for experimentally testing the theoretical work discussed in Chapter 6.

8.3 Optical Characterisation

8.3.1 Cavity Q-factor and Polarisation

As discussed in Chapter 7, the properties of the cavity structures were determined by performing μ-PL measurements using the set-up shown in Figure 7.7. The samples (see Figure 8.5 for SEM images of some example structures) were mounted in a continuous-flow cryostat, and held under vacuum at a temperature of approximately 4 K. An above-band CW diode laser at $\lambda = 808$ nm, with a measured power of 150 μW, was focused on the sample through the optical window of the cryostat using an objective lens to a spot size on the order of a few micrometres. To determine the mode structure and cavity Q-factor, the excitation laser spot was aligned with the cavity centre, and the light emitted vertically from the cavity centre[1] was collected using the same objective lens as in the excitation path. The properties of the cavity modes, such as Q-factor, could then be determined by directing the collected cavity emission to a spectrometer

Figure 8.6 shows a selection of emission spectra for four different cavity structures. These spectra confirm the potential for the XNBPhCC structure to support either a single-mode (Figure 8.6a) or bi-modal (Figure 8.6b) cavity by excluding or including the uniform Bragg mirrors along one of the cavity axes as demonstrated in our FDTD simulations. Furthermore, by measuring the FWHM of the spectral peaks, the Q-factor of the cavity modes could be determined. Of the cavity structures studied that showed cavity modes, the highest Q-factors measured were $3600 > Q \gtrsim 3000$.

Inserting a linear polariser into either the collection or excitation path of the set-up allowed the linear and orthogonal nature of the cavity modes to be verified. Figure 8.7 shows the polarisation dependence of the two cavity

[1]Excitation and collection of light from the cavity centre will be referred to as the C-C alignment.

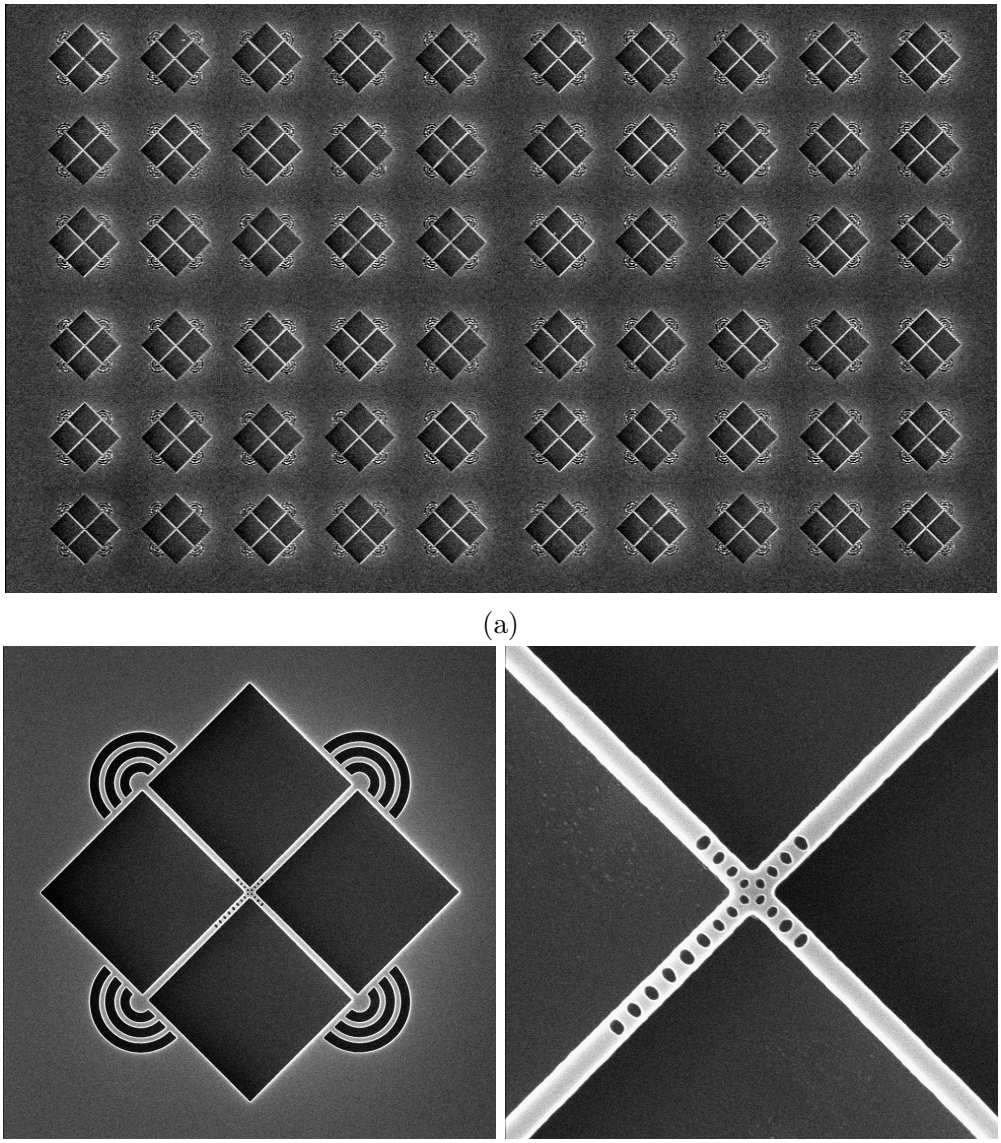

(a)

(b) (c)

Figure 8.5: Scanning Electron Microscopy (SEM) images of the Crossed-Nanobeam Photonic Crystal Cavity (XNBPhCC) devices fabricated by Dr. René Dost. Images courtesy of Dr. René Dost. (a) An overview of the array of cavity devices fabricated on a single diode. (b) A narrowed down SEM image of a singe cavity device including Bragg grating out-couplers at the ends of the nanobeam waveguides. (c) A magnified SEM image of the Photonic Crystal (PhC) holes in a cavity device designed to support a single cavity mode with directional emission. Each nanobeam waveguide is approximately 14 μm long.

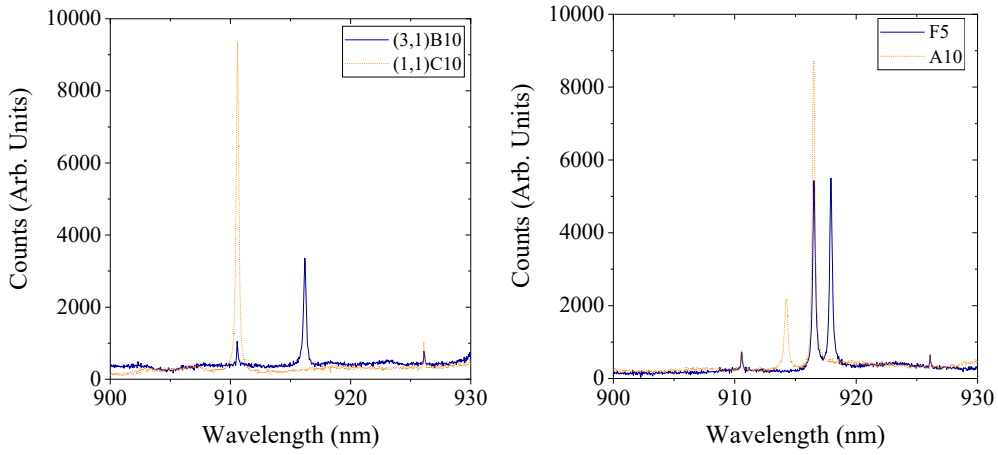

(a) (b)

Figure 8.6: Spectra showing the modes of (a) two single-mode cavity devices and (b) two bi-modal cavity devices. The spectra were taken at high power (μW) with a 1 s exposure time. All cavity modes shown have $Q \gtrsim 3000$. Small lines originating from higher order modes of the excitation laser can be seen at $\lambda \approx 911$ nm and $\lambda \approx 926$ nm.

modes of a bi-modal cavity structure when the polariser was orientated to maximise the spectral peak of each cavity mode. It can be seen that aligning the polarisation of the linear polariser and one of the cavity modes to maximise its spectral peak completely extinguishes the observed emission from the second cavity mode. Furthermore, the maximisation and minimisation of the cavity spectra occurs at orthogonal polarisations confirming the linear and orthogonal nature of the polarisation of the two cavity modes in the bi-modal configuration as expected from the FDTD simulations.

Comparing the experimentally measured Q-factors with those predicted by the FDTD simulations there is clearly a large discrepancy in the two values. There are a number of potential reasons for this difference in the theoretical and measured Q-factors. Absorption of light from the cavity by, for example, excess non-resonant QDs [221] resulting from the SK growth process or dopant impurities [232] may account for some of the losses. Additionally, imperfections in the fabrication of the PhCs such as: deviations from the design, random variations in the PhC hole sizes, side-wall roughness, or angled side-walls varying the hole radius or nanobeam width vertically through the structure, may also account for the reduced measured Q-factor. These imperfections in the fabrication also lead to the mode splitting observed in the bi-modal cavity spectra, as these structures were designed with degenerate cavity modes.

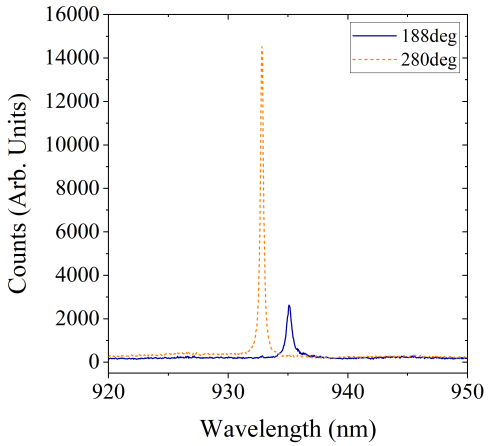

Figure 8.7: The polarisation dependence of the modes of an asymmetric bi-modal cavity structure taken with a linear polariser in the excitation/collection path orientated at orthogonal polarisations. The measured Q-factors of the two modes, $Q_{\lambda=932.8\text{ nm}} = 3100 \pm 20$ and $Q_{\lambda=935.1\text{ nm}} = 1600 \pm 30$, differ due to the asymmetric cavity design discussed in Sec. 8.3.2.

8.3.2 Directional Coupling

Having established the potential for the XNBPhCC structures to support either a single-mode or bi-modal cavity, and the nature of the polarisation of these cavity modes, we now wish to demonstrate directional emission from the cavity mode as discussed in Sec. 8.2.1. Initial evidence of this directional emission from a cavity mode can be seen in the emission spectrum of an asymmetric bi-modal cavity shown Figure 8.7. Determining the spectral linewidths of the cavity peaks using a Lorentzian fitting function, the Q-factors of the two modes were determined to be $Q = 3100 \pm 20$ for the shorter wavelength mode, and $Q = 1600 \pm 30$ for the longer wavelength mode. From the FDTD simulations presented in Sec. 8.2.1, such a difference in the Q-factors of the two cavity modes would be an expected characteristic of a bi-modal cavity with directional emission from a one of the cavity modes. This is a result of reducing the strength of the mirror in one of the cavity arms naturally reducing the Q-factor of that cavity mode.

However, to confirm the directional nature of the emission from the cavity mode we perform μ-PL measurements now exciting and collecting at different spatial positions over the cavity structure. By exciting at the grating out-couplers located at the end of the cavity arms as can be seen in Figure 8.5b, and collecting above the centre of the cavity, we can compare the direction-dependent coupling efficiency between the cavity and waveguide modes. As the excitation laser used is above-band ($\lambda = 808$ nm), it is photoluminescence

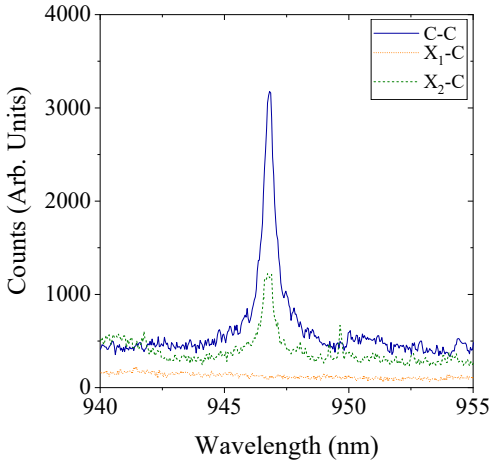

Figure 8.8: Cavity spectra showing directional emission from a single-mode cavity device. The cavity modes were excited via the out-couplers at either end of the x-axis nanobeam, and light was collected from above the centre of the cavity. The measured Q-factor of the device is $Q = 1300 \pm 40$.

emission resulting from absorption of the excitation light near the outcoupler that propagates along the waveguide and excites the cavity mode. Figure 8.8 shows an example of such a spectrum exciting and collecting above the cavity centre ($C-C$) of a single-mode cavity, and exciting either end of the nanobeam with the cavity mode and collecting above the cavity centre ($X_{1,2} - C$). Comparing the $X_{1,2} - C$ spectra it is clear than in the X_1 direction there is no coupling between the waveguide mode and cavity mode as the absence of the cavity peak in the spectrum indicates no light from the excitation laser was able to reach the centre of the structure. On the other hand, a peak in the spectrum at the cavity mode wavelength can be seen when exciting at the X_2 outcoupler, thus demonstrating the asymmetric coupling efficiency between the cavity mode and waveguide mode.

8.3.3 Quantum Dot Coupling

To be used in on-chip optical circuits the XNBPhCCs must be able to both support and couple to optically active QDs in addition to supporting high quality factor cavity modes. To identify any QDs coupled to the cavity devices we again used an above-band excitation laser exciting and collecting above the cavity centre, only now reducing the power and extending the integration time. Reducing the excitation power incident on the sample and increasing the integration time allows any individual QD emissions lines to be identified in the emission spectrum without being obscured by the cavity mode, other QD

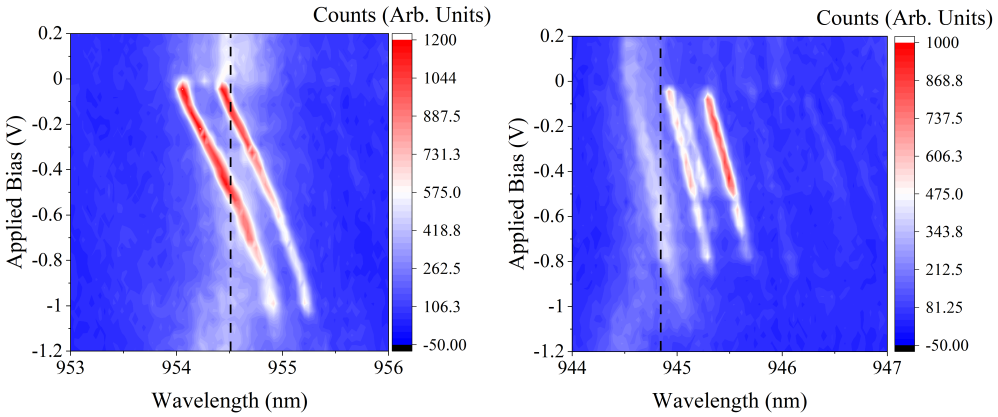

Figure 8.9: Spectra showing Quantum Dots (QDs) tuning across the cavity mode (approximately indicated by the dashed line) of two single-mode cavity devices. The spectra were taken at low power (2 μW) exciting and collecting above the centre of the cavity.

emission, emission from higher order QD states, or general background noise as discussed in Chapter 7.

As discussed in Chapter 3, the resonance of a QD can be tuned through the application of an electric field as described by the Quantum-Confined Stark Effect (QCSE). Figure 8.9 shows low power bias dependent μ-PL spectra taken by exciting and collecting above the centre of two different cavity devices. In both bias dependent spectra two QD emission lines can be seen to tune across the cavity mode of a single-mode structure as the potential difference applied across the diode was varied. The QD lines were observed to tune roughly 1 nm, increasing in intensity as they moved towards the cavity mode resonance. This increase in intensity could be due to a Purcell enhancement increasing the rate of emission from the QD. The absence of the QD spectral lines outside of the -1 V to 0 V bias range likely indicates a change in the charge state of the QDs.

8.4 Discussion

Using the optimal cavity parameters found in Chapter 6 we can calculate the Q-factor values these structures would require to be suitable for optical spin initialisation, and readout. In Chapter 6 we observed using a single-mode cavity the readout process was nearly independent of the cavity linewidth, and thus it was the spin initialisation stage that placed the bounds on the required cavity linewidths. To achieve both a spin initialisation and readout

fidelity greater than 99% a Purcell enhancement of the $|2\rangle \rightarrow |4\rangle$ transition of $F_P = 19$ and a cavity linewidth in the limits $20 \leq \kappa/2\pi \leq 40$ GHz depending on driving conditions would be required. Converting cavity linewidth to Q-factor assuming $\lambda_c = 930$ nm yields limits to the Q-factor of $16200 \gtrsim Q \gtrsim 8000$.

Realising a high-fidelity spin-photon interface would therefore require a minimum of approximately a three-fold increase in the cavity Q-factors demonstrated in this chapter. This should be achievable as nanobeam PhCC structures in the literature have demonstrated Q-factors on the order of $10^4 - 10^5$ [194, 195]. There are a number of paths that could produce such an increase in the Q-factor utilising the designs outlined in this thesis. Firstly, through multiple iterations the fabrication process could be further optimised to produce cavity structures that more faithfully reflect the design parameters. Secondly, changes to the design of the cavity structures could be made. The cavity design could be further optimised to produce a higher theoretical Q-factor value which, assuming a similar percentage decrease in the Q-factor resulting from fabrication imperfections, could also improve the measured Q-factors. Likewise, it may be possible to increase the resilience of the cavity modes against fabrication imperfections through changes in the cavity design. Finally processes such as surface passivisation may be employed to further improve the experimentally measured Q-factor, and reduce the spread of cavity wavelengths, through the suppression of surface recombination centres [169]. Additionally, fabricating the cavity structures around registered or site-controlled QD (see Chater 7 for more information) would improve the yield of devices with spectrally suitable QDs at the cavity centre, and could also lead to an improvement of the Q-factor by reducing the number of off-resonant QDs in the structures [221].

In addition to applications as a spin-photon interface, the XNBPhCC structures show promise for implementing on-demand single-photon sources in on-chip in-plane optical circuits. Previous studies have demonstrated that bimodal cavities with two orthogonal linearly polarised cavity modes may be used to develop high-brightness high-purity single photon sources [159, 233]. This has been achieved by using the cross-polarised nature of the cavity modes to suppress the excitation field in the output mode by exciting and collecting from different cavity modes, and the Purcell enhancement of the diagonal transitions present in a charged QD in a Voigt geometry magnetic field to improve the brightness [159, 233]. However, the cavity structures in which this has been demonstrated are not suited to integration in a scalable on-chip in-plane opti-

cal circuits. The XNBPhCCs present a potential solution to this, maintaining the cavity properties demonstrated in previous studies, including directional emission from the cavity mode, only in an in-plane photonic structure. Furthermore, the potential to maintain access to the orthogonal polarisation in a single-mode XNBPhCC structure gives rise to the possibility of increasing the brightness by improving the cyclicity of the driven Λ-system.

8.5 Summary

We have demonstrated the XNBPhCC structure is capable of supporting linearly polarised cavity modes with Q-factors on the order of 10^3 in either a single-mode or bi-modal configuration. Furthermore, we have also demonstrated emission from the cavity mode via the cavity mirrors can be made to be directional in either cavity configuration by individually adjusting the number of uniform Bragg mirror periods in each cavity arm. Lastly we have shown that these structures are also not only able to support and couple to individual optically active QDs, but also still allow optical tuning via the QCSE by applying an external bias despite the small area of the cavity centre.

Chapter 9

Conclusion and Outlook

The work presented in this thesis addresses a variety of important areas regarding the behaviours of open quantum systems under pulsed optical excitation, and the influence of coupling to an optical cavity or a thermal bath in such driving regimes. From this we have developed a theory that is valid beyond the limits of widely used phonon-coupling models, and demonstrated the importance of cavity configuration in optical spin initialisation and readout processes. Additionally, we have designed and characterised a photonic nano-cavity structure with properties that make it potentially suitable for applications in quantum technologies, including as a spin-photon interface, based on the theoretical calculations presented in the thesis.

9.1 Phonon Effects Under Pulsed Resonant Excitation

In Chapters 4 and 5 we studied the impact of phonon coupling on the properties of a QD under resonant pulsed excitation. Using the Markovian full polaron model with a time-dependent drive, we demonstrated that under resonant pulsed excitation coupling to a phonon-bath induces an asymmetry in the pulsed emission spectra at low temperatures. This effect is not captured by a simple pure dephasing model, further demonstrating that such an approach is not adequate for capturing the full effects of phonon-coupling. Additionally, to move beyond the limits of weak optical driving and weak system-phonon coupling, we extended the variational polaron model to derive a time-dependent variational polaron model. In doing so we provide a formalism for studying the effects of pulsed optical driving of phonon-coupled systems that remains valid

in parameter regimes where the weak-coupling and full polaron models break down. When driving a QD with short optical pulses, we have demonstrated that the QD eigenstates are only weakly coupled to the low frequency phonon bath modes during the pulse. Thus in this limit the weak-coupling model remains valid at low temperatures, while the full polaron model over-estimates the phonon induced damping. Accordingly, when driving with short optical pulses one can accurately predict the evolution of the states of a QD using the weak-coupling model which, of the three models studied, is the least computationally demanding model, and thus fastest to perform calculations with. Conversely, in the limit of long pulse duration we have shown a good agreement between the full polaron and time-dependent variational polaron models at low temperatures. On the other hand, the dynamics returned by the weak-coupling model now over-estimate the phonon-coupling effects as it samples the phonon spectral density closer to its peak owing to predicting no renormalisation of the Rabi frequency. Hence, when driving in the regime where $\Omega \ll \omega_c$, our results confirm the polaron model, the second least computationally demanding of the models, is suited to accurately predicting the dynamics of a QD under pulsed excitation at low temperatures. However, driving in the intermediate pulse FWHM regime neither the weak-coupling nor polaron models return consistently reliable results. We also find this is the case in the high temperature regime regardless of the pulse duration. In these regimes our time-dependent variational polaron model is required to provide accurate results across the range of pulse areas studied. Due to the larger number of correlation functions compared to the weak-coupling or polaron models, the time-dependent variational polaron model is the most computationally expensive of the phonon models used in the thesis. However, of the three models it also has the largest range of validity.

There are a number of approaches that could be followed to extend the work presented in Chapters 4 and 5. Taking the Markovian limits of the weak-coupling and time-dependent variational polaron models would allow spectra to be calculated from these models, and compared with the spectra presented in this thesis. Using cQED, full cavity effects could be included in the weak-coupling, full polaron, and variational polaron models to study the interplay between the impact of coupling to a phonon-bath and cavity mode. Furthermore, this work could be extended to systems beyond the epitaxial semiconductor QD with phonon-coupling defined by sub-Ohmic and Ohmic spectral densities, regimes where the full polaron model breaks down, in addition to

the super-Ohmic spectral density used in Chapters 4 and 5. Additionally, the predictions made by the time-dependent variational polaron model could be tested experimentally by measuring Rabi rotations as a function of the driving pulse area as detailed in [121, 122], only performing these sweeps for a range of different pulse parameters and temperatures.

9.2 Optical Spin Control with Cavity-Coupled Quantum Dots

In Chapter 6 we explored how an optical cavity may be employed to enhance the spin initialisation, control, and readout processes when driving a negatively charged QD with finite optical pulses, and how the inclusion of cavity effects enables all three processes to take place under a single applied magnetic field geometry. Comparing the effects of a single-mode, and bi-modal cavity configuration, we found that for the spin initialisation process both cavity configurations may be conducive to fast, high-fidelity state preparation when driving the system with either a square or Gaussian optical pulse. Furthermore, we have also shown that when directly driving the QD with two far detuned Gaussian pulses of orthogonal polarisation, both cavity configurations are compatible with complete coherent control of the prepared spin state. However, for optical spin readout, the Purcell enhancement of the linearly polarised vertical transitions resulting from coupling to a bi-modal cavity significantly limits the range of cavity parameters for which the readout success rate may be optimised. We therefore find that, unlike the single-mode configuration, there is no single set of bi-modal cavity parameters that may simultaneously optimise the spin initialisation and readout processes.

This work may naturally be extended by applying the phonon theory developed in Chapters 4 and 5 to move beyond the simple pure dephasing model presented. Applying appropriate phonon-coupling models to the optical spin initialisation, control, and readout processes would further increase the accuracy with which optimal cavity parameters could be identified by more accurately modelling the dephasing processes experienced by QDs. Furthermore, the theoretical predictions outlined in Chapter 6 could be tested using the photonic nano-cavity structures detailed in Chapter 8.

9.3 Crossed-Nanobeam Photonic Crystal Cavities

In Chapter 8 we both theoretically and experimentally studied the properties of a XNBPhCC, consisting of two orthogonal nanobeam PhCCs overlapping at their centres. Our FDTD simulations showed that such cavities may be designed support either a single linearly polarised cavity mode, or two near-independent orthogonal linearly polarised cavity modes. Furthermore, by altering the number of PhC mirror periods along a given axis or FDTD simulations demonstrated that these cavity modes could be made to couple directionally to the waveguide mode. These properties, along with the ability to support QDs at the cavity centre, were then demonstrated using low temperature μ-PL spectroscopy.

The clear extension of this work would be to improve the Q-factor of the fabricated XNBPhCC devices. A number of methods for achieving this were outlined in Chapter 8 including design optimisation, and surface passivation. The calculations performed in Chapter 6, obtaining a Q-factor on the order of 10^4 would enable a demonstration of spin control in these structure, potentially using site-controlled or registered QDs discussed in Chapter 7. Additionally, this work could be extended to demonstrating the suitability of these structures in the implementation of single-photon sources.

Appendices

Appendix A

Parity Transition Selection Rules

In this appendix we shall show how the parity operator excludes the diagonal matrix elements from the spectral decomposition of the transition dipole operator.

The dipole operator is given by

$$\hat{d} = -q\hat{r}, \tag{A.1}$$

where q is the charge. The unitary parity operator, Π, acts to change the sign of the position operator, $\hat{r}$, such that

$$\Pi\hat{r}\Pi^{\dagger} = -\hat{r}. \tag{A.2}$$

Multiplying the both sides of this equation to the right by Π, we see the anticommutation relation of the parity and position operators is then

$$\left\{\Pi, \hat{r}\right\} = \Pi r + r\Pi = \Pi r - \Pi r = 0. \tag{A.3}$$

The matrix elements of the anti-commutator are then given by

$$\langle\psi| \left\{\Pi, \hat{r}\right\} |\phi\rangle = \langle\psi| \Pi\hat{r} + \hat{r}\Pi |\phi\rangle = \left(\pi_{\psi} + \pi_{\phi}\right) \langle\psi| \hat{r} |\phi\rangle = 0, \tag{A.4}$$

where π_{ψ} and π_{ϕ} are the non-zero expectation values of the parity operator. For this relationship to hold the diagonal matrix elements must be zero and there must be a change of parity i.e. $\pi_{\psi} = -\pi_{\phi}$.

This page is intentionally left otherwise blank.

Appendix B

Correlation Functions for the Polaron Theory

In this appendix we shall derive the environment correlation functions used in the Polaron theory derived in Chapter 4.

When the linear coupling terms between the Quantum Dot (QD) and phonon bath are removed by setting $\alpha_k = g_k/\omega_k$, the non-zero bath correlation functions are

$$\begin{aligned} B_x &= \frac{1}{2}\big(B_+ + B_- - 2B\big), \\ B_y &= \frac{1}{2i}\big(B_- - B_+\big), \\ B &= \langle B_\pm \rangle, \end{aligned} \tag{B.1}$$

where $B_+ = \prod_k D(\alpha_k)$, and $B_- = \prod_k D^\dagger(\alpha_k)$, and the displacement operators act such that

$$\begin{aligned} D^\dagger(\alpha_k) b D(\alpha_k) &= (b + \alpha_k), \\ D(\alpha_k) b D^\dagger(\alpha_k) &= (b - \alpha_k). \end{aligned} \tag{B.2}$$

We shall begin with the derivation of the average displacement of the environment, $B = \langle B_\pm \rangle$. In the coherent state representation, the thermal state of the phonon bath may be written as

$$\rho_T = \bigotimes_k \int d^2\alpha_k P(\alpha_k) \left|\alpha_k\right\rangle\!\left\langle\alpha_k\right| . \tag{B.3}$$

Using this thermal state, and the relationships: $|\beta\rangle = D(\beta)|0\rangle$, $D(a)D(b) = e^{ab^* - a^*b} D(b)D(a)$, and $D^\dagger(a)D(a) = D(a)D^\dagger(a) = \mathbf{I}$ [234], we find the average

displacement of the phonon bath is given by

$$\begin{aligned}
B = \langle B_{\pm} \rangle &= \prod_k \int d^2\beta_k P(\beta_k) \langle \beta_k | \, D(\pm\alpha_k) \, | \beta_k \rangle \\
&= \prod_k \int d^2\beta_k P(\beta_k) \langle 0 | \, D^\dagger(\beta_k) D(\pm\alpha_k) D(\beta_k) \, | 0 \rangle \\
&= \prod_k \int d^2\beta_k P(\beta_k) e^{\pm\alpha_k(\beta_k^* - \beta_k)} \langle 0 | \, D(\pm\alpha_k) \, | 0 \rangle \\
&= \prod_k \int d^2\beta_k \frac{1}{\pi\bar{n}_k} e^{-\frac{\beta_k^2}{\bar{n}_k}} e^{\pm\alpha_k(\beta_k^* - \beta_k)} \langle 0 | \alpha_k \rangle \\
&= \prod_k \int d^2\beta_k \frac{1}{\pi\bar{n}_k} e^{-\frac{\beta_k^2}{\bar{n}_k}} e^{\pm\alpha_k(\beta_k^* - \beta_k)} e^{-\alpha_k} \\
&= \exp\Big\{ -\frac{1}{2} \sum_k \frac{g_k^2}{\omega_k^2} \coth\big(\frac{\beta\omega_k}{2}\big) \Big\} \\
&= \exp\Big\{ -\frac{1}{2} \int_0^\infty d\omega \frac{J(\omega)}{\omega^2} \coth\frac{\beta\omega}{2} \Big\}.
\end{aligned} \tag{B.4}$$

where $\int d^2\beta = \int d\alpha \int d\gamma$ for $\beta = \alpha + i\gamma$. To find expressions for the remaining correlation functions it will be useful to find calculate the expectation values of different combinations of $B_\pm$.

$$\begin{aligned}
\langle B_\pm(t) B_\pm(t') \rangle &= \prod \langle D(\pm\alpha_k) D(\pm\alpha_k) \rangle \\
&= \prod \langle e^{-i\omega_k \alpha_k^\dagger \alpha_k t} D(\pm\alpha_k) e^{i\omega_k \alpha_k^\dagger \alpha_k t} e^{-i\omega_k \alpha_k^\dagger \alpha_k t'} D(\pm\alpha_k) e^{i\omega_k \alpha_k^\dagger \alpha_k t'} \rangle \\
&= \prod_k e^{i\mathrm{Im}(|\alpha_k|^2 e^{i\omega_k(t-t')})} \langle D(\pm\alpha(e^{i\omega t} + e^{i\omega_k t'})) \rangle \\
&= \prod_k e^{i|\alpha_k|^2 \sin(\omega_k(t-t'))} \langle D(\pm\alpha_k(e^{i\omega t} + e^{i\omega_k t'})) \rangle \\
&= \prod_k e^{i|\alpha_k|^2 \sin(\omega_k(t-t'))} e^{-\frac{1}{2}|\pm\alpha_k e^{i\omega_k t} \pm \alpha_k e^{i\omega_k t'}|^2 \coth\left(\frac{\beta\omega_k}{2}\right)} \\
&= \prod_k e^{i|\alpha_k|^2 \sin(\omega_k(t-t'))} e^{-|\alpha_k|^2 \coth\left(\frac{\beta\omega_k}{2}\right)} e^{-|\alpha_k|^2 \left(\cos(\omega_k(t-t')) \coth\left(\frac{\beta\omega_k}{2}\right)\right)} \\
&= \prod_k e^{i\frac{g_k^2}{\omega_k^2} \sin(\omega_k(t-t'))} e^{-\frac{g_k^2}{2\omega_k^2} \coth\left(\frac{\beta\omega_k}{2}\right)} e^{-\frac{g_k^2}{\omega_k^2} \left(\cos(\omega_k(t-t')) \coth\left(\frac{\beta\omega_k}{2}\right)\right)} \\
&= B^2 e^{-\sum_k \frac{g_k^2}{\omega_k^2} \left(\left(\cos(\omega_k(t-t')) \coth\left(\frac{\beta\omega_k}{2}\right) - i \sin(\omega_k(t-t'))\right)\right)} \\
&= B^2 e^{-\phi(t,t')},
\end{aligned} \tag{B.5}$$

where we have used $D(a)D(b) = e^{i(Im)(ab^*)} D(a+b)$, $e^{-i\omega a^\dagger a t} D(a) e^{i\omega a^\dagger a t} =$

$D(ae^{i\omega t})$, $\mathrm{Im}(e^{ix}) = \sin(x)$, and where in the continuum limit the phonon propagator, $\phi(t,t')$, is given by

$$\begin{aligned}\phi(t,t') &= \sum_k \frac{g_k^2}{\omega_k^2}\Big(\cos(\omega_k(t-t'))\coth\Big(\frac{\beta\omega_k}{2}\Big) - i\sin(\omega_k(t-t'))\Big) \\ &= \int_0^\infty d\omega \frac{J(\omega)}{\omega^2}\Big(\cos(\omega(t-t'))\coth\Big(\frac{\beta\omega}{2}\Big) - i\sin(\omega(t-t'))\Big).\end{aligned} \tag{B.6}$$

Similarly

$$\langle B_\pm(t)B_\mp(t')\rangle = B^2 e^{\phi(t,t')}. \tag{B.7}$$

From these definitions we find $\langle B_x(t)B_y(t')\rangle = \langle B_y(t)B_x(t')\rangle = 0$. Furthermore, as $\langle B_+(t)B_+(t')\rangle = \langle B_-(t)B_-(t')\rangle$ and $\langle B_+(t)B_-(t')\rangle = \langle B_-(t)B_+(t')\rangle$ we find

$$\begin{aligned}\langle B_x(t)B_x(t')\rangle =& \frac{1}{2}\big(\langle B_+(t)B_+(t')\rangle + \langle B_+(t)B_-(t')\rangle - 2B^2\big), \\ \langle B_y(t)B_y(t')\rangle =& \frac{1}{2}\big(\langle B_+(t)B_+(t')\rangle - \langle B_+(t)B_-(t')\rangle\big).\end{aligned} \tag{B.8}$$

In the continuum limit (and with the substitution $\tau = t - t'$) the polaron correlation functions are thus given by

$$\begin{aligned}\Lambda_{xx}(\tau) &= \frac{B^2}{2}\big(e^{\phi(\tau)} + e^{-\phi(\tau)} - 2\big), \\ \Lambda_{yy}(\tau) &= \frac{B^2}{2}\big(e^{\phi(\tau)} - e^{-\phi(\tau)}\big), \\ \Lambda_{xy}(\tau) &= \Lambda_{yx}(\tau) = 0,\end{aligned} \tag{B.9}$$

where

$$\phi(\tau) = \int_0^\infty \frac{J(\omega)}{\omega^2}\Big(\cos(\omega\tau)\coth\Big(\frac{\beta\omega}{2}\Big) - i\sin(\omega\tau)\Big)d\omega. \tag{B.10}$$

This page is intentionally left otherwise blank.

Appendix C

Correlation Functions for the Variational Polaron Model

In this appendix we shall derive the correlation functions used in the time-dependent variational polaron model. Rather than the three bath operators in the polaron model, we now start with four non-zero bath operators as we no longer choose the coupling strength to cancel the liner coupling terms between the Quantum Dot (QD) and phonon bath. These four bath operators are given by

$$\begin{aligned} B_x(t) &= \frac{1}{2}\big(B_+(t) + B_-(t) - 2B(t)\big), \\ B_y(t) &= \frac{1}{2i}\big(B_-(t) - B_+(t)\big), \\ B_z(t) &= \sum_k h_k(t) b_k^\dagger + \text{h.c.}, \\ B(t) &= \langle B_\pm(t) \rangle. \end{aligned} \tag{C.1}$$

C.1 Polaron-Type Correlation Functions

We shall start with the polaron-type correlation functions. Making a comparison with the polaron model, we see three of the bath operators maintain a polaron form only now with the inclusion of time-dependence arising from the variational function, $F(\omega, t)$. From this we can assume some of the variational polaron correlation functions take a polaron form. Following the same derivation as in the polaron model only now with $\alpha_k(t) = f_k(t)/\omega = g_k F(\omega, t)/\omega$ we can write the average displacement of the phonon bath in the in the continuum

limit of the time-dependent variational polaron formalism as

$$B(t) = \exp\Big\{-\frac{1}{2}\int_0^\infty d\omega \frac{J(\omega)F(\omega,t)^2}{\omega^2}\coth\Big(\frac{\beta\omega}{2}\Big)\Big\}. \tag{C.2}$$

To derive the remaining polaron-type correlation functions we can follow the same procedure as set out in Appendix B, only with a different form of the coupling strength α_k. Doing so yields

$$\begin{aligned}\langle B_\pm(t)B_\pm(t')\rangle =& B(t)B(t')e^{-\phi(t,t')},\\ \langle B_\pm(t)B_\mp(t')\rangle =& B(t)B(t')e^{\phi(t,t')},\end{aligned} \tag{C.3}$$

where in the variational polaron model the phonon propagator, $\phi(t,t')$, is now given by

$$\begin{aligned}\phi(t,t') &= \sum_k \frac{g_k^2 F(\omega_k,t)F(\omega_k,t')}{\omega_k^2}\Big(\cos(\omega_k(t-t'))\coth\Big(\frac{\beta\omega_k}{2}\Big) - i\sin(\omega_k(t-t'))\Big)\\ &= \int_0^\infty d\omega \frac{J(\omega)F(\omega,t)F(\omega,t')}{\omega^2}\Big(\cos(\omega(t-t'))\coth\Big(\frac{\beta\omega}{2}\Big) - i\sin(\omega(t-t'))\Big).\end{aligned} \tag{C.4}$$

The polaron-type correlation functions in the variational polaron limit are thus given by

$$\begin{aligned}\Lambda_{xx}(t,t') =& \frac{B(t)B(t')}{2}\big(e^{\phi(t,t')} + e^{-\phi(t,t')} - 2\big),\\ \Lambda_{yy}(t,t') =& \frac{B(t)B(t')}{2}\big(e^{\phi(t,t')} - e^{-\phi(t,t')}\big),\\ \Lambda_{xy}(t,t') =& \Lambda_{yx}(t,t') = 0.\end{aligned} \tag{C.5}$$

In Chapter 4 we move the factors of the time-dependent Rabi frequency, $\Omega(t)$, into the correlation functions yielding $\Omega_r(t) = \Omega(t)B(t)$.

C.2 Cross-Term Correlation Functions

Now we have our polaron-like correlation functions, we can move on to derive the correlation functions involving both the polaronic bath operators, and the additional weak-coupling-type bath operator ($B_z(t)$) we now have in the variational polaron formalism. To do this we shall first consider only a single bath mode, and then move on to generalise for the multi-mode case. Considering the correlation between a single bath mode and the weak-coupling bath

operator yields

$$
\begin{aligned}
\langle D(\delta_k)B_z(t')\rangle &= \int d^2\beta_k P(\beta_k)\,\langle\beta_k|\,D(\delta_k)\big(h_k(t)b_k^\dagger e^{i\omega_k t'}+h_k^*(t)b_k e^{-i\omega_k t'}\big)\,|\beta_k\rangle \\
&= \int d^2\beta_k P(\beta_k)\,\langle 0|\,D^\dagger(\beta_k)D(\delta_k)\big(h_k(t)b_k^\dagger e^{i\omega_k t'}+h_k^*(t)b_k e^{-i\omega_k t'}\big)D(\beta_k)\,|0\rangle \\
&= \int d^2\beta_k P(\beta_k)\Big(\langle 0|\,D^\dagger(\beta_k)D(\delta_k)h_k(t)b_k^\dagger e^{i\omega_k t'}D(\beta_k)\,|0\rangle \\
&\qquad\qquad + \langle 0|\,D^\dagger(\beta_k)D(\delta_k)h_k^*(t)b_k e^{-i\omega_k t'}D(\beta_k)\,|0\rangle\Big) \\
&= \int d^2\beta_k P(\beta_k)\Big(h_k(t)e^{i\omega_k t'}\,\langle 0|\,D^\dagger(\beta_k)D(\delta_k)b_k^\dagger D(\beta_k)\,|0\rangle \\
&\qquad\qquad + h_k^*(t)e^{-i\omega_k t'}\,\langle 0|\,D^\dagger(\beta_k)D(\delta_k)b_k D(\beta_k)\,|0\rangle\Big) \\
&= \int d^2\beta_k P(\beta_k)\Big(h_k(t)e^{i\omega_k t'}\,\langle 0|\,D^\dagger(\beta_k)D(\delta_k)b_k^\dagger D^\dagger(\delta_k)D(\delta_k)D(\beta_k)\,|0\rangle \\
&+ h_k^*(t)e^{-i\omega_k t'}\,\langle 0|\,D^\dagger(\beta_k)D(\delta_k)D(\beta_k)D^\dagger(\beta_k)b_k D(\beta_k)\,|0\rangle\Big) \\
&= \int d^2\beta_k P(\beta_k)\Big(h_k(t)e^{i\omega_k t'}\,\langle 0|\,D^\dagger(\beta_k)(b_k^\dagger-\delta_k^*)D_k(\beta_k)D_k^\dagger(\beta_k)D(\delta_k)D(\beta_k)\,|0\rangle \\
&+ h_k^*(t)e^{-i\omega_k t'}\,\langle 0|\,D^\dagger(\beta_k)D(\delta_k)D(\beta_k)(b+\beta_k)\,|0\rangle\Big) \\
&= \int d^2\beta_k P(\beta_k)\Big(h_k(t)e^{i\omega_k t}\big(\langle 0|\,(b_k^\dagger+\beta_k^*))D^\dagger(\beta_k)D(\delta_k)D(\beta_k)\,|0\rangle \\
&- \delta_k^*\,\langle 0|\,D^\dagger(\beta_k)D(\delta_k)D(\beta_k)\,|0\rangle\big)+h_k^*(t)e^{-i\omega_k t'}\,\langle 0|\,D^\dagger(\beta_k)D(\delta_k)D(\beta_k)(b_k+\beta_k)\,|0\rangle\Big) \\
&= \int d^2\beta_k P(\beta_k)\big((\beta_k-\delta_k)^*h_k(t')e^{i\omega_k t'}+\beta_k h_k^*(t')e^{-i\omega_k t'}\big)\,\langle 0|\,D^\dagger(\beta_k)D(\delta_k)D(\beta_k)\,|0\rangle \\
&= \int d^2\beta_k P(\beta_k)\big((\beta_k-\delta_k)^*h_k(t')e^{i\omega_k t'}+\beta_k h_k^*(t')e^{-i\omega_k t'}\big)e^{\beta_k^*\delta_k-\beta_k\delta_k^*}e^{-|\delta_k|^2/2} \\
&= e^{-\frac{1}{2}|\delta_k|^2\coth\left(\frac{\beta\omega_k}{2}\right)}\int d^2\beta_k\big((\beta_k-\delta_k)^*h_k(t')e^{i\omega_k t'}+\beta_k h_k^*(t')e^{-i\omega_k t'}\big) \\
&= e^{-\frac{1}{2}|\delta_k|^2\coth\left(\frac{\beta\omega_k}{2}\right)}\big(\delta_k n_k h_k(t')e^{i\omega_k t'}-(1+n_k)\delta_k^*h_k^*(t')e^{-i\omega_k t'}\big).
\end{aligned}
\tag{C.6}
$$

In this derivation we have used the relationships: $b\,|0\rangle = \langle 0|\,b^\dagger = 0$, $D^\dagger D = DD^\dagger = \mathbf{I}$, and $D^\dagger(\alpha)aD(\alpha) = (a+\alpha)$ and $D(\alpha)aD^\dagger(\alpha) = (a-\alpha)$ [234]. From here we can move to the multi-mode case by making the substitution

$\delta_k \to \alpha_k(t)e^{i\omega_k t}$. This yields

$$\begin{aligned}
&\langle B_\pm(t)B_z(t')\rangle = B(t)\sum_k \alpha_k(t)\big(n_k h_k(t')e^{i\omega_k(t-t')} - (1+n_k)h_k^*(t')e^{-i\omega_k(t-t')}\big)\\
&= \pm B(t)\sum_k \frac{f_k(t)}{\omega_k}\Big(n_k h_k(t')e^{i\omega_k(t-t')} - h_k^*(t')e^{-i\omega_k(t-t')} - n_k h_k^*(t')e^{-i\omega_k(t-t')}\Big)\\
&= \pm B(t)\sum_k \frac{f_k(t)}{\omega_k}\Big(n_k h_k(t')e^{i\omega_k(t-t')} - h_k^*(t')e^{-i\omega_k(t-t')} - n_k h_k^*(t')e^{-i\omega_k(t-t')}\\
&\quad + \frac{1}{2}h_k(t')e^{i\omega_k(t-t')} - \frac{1}{2}h_k(t')e^{i\omega_k(t-t')} + \frac{1}{2}n_k h_k^*(t')e^{i\omega_k(t-t')}\\
&\quad - \frac{1}{2}n_k h_k^*(t')e^{i\omega_k(t-t')} + \frac{1}{2}n_k h_k(t')e^{-i\omega_k(t-t')} - \frac{1}{2}n_k h_k(t')e^{-i\omega_k(t-t')}\Big)\\
&= \pm B(t)\sum_k \frac{f_k(t)}{\omega_k}\Big\{\Big(\frac{1}{2}n_k h_k(t')\big(e^{i\omega_k(t-t')} + e^{-i\omega_k(t-t')}\big)\\
&\quad + \frac{1}{2}n_k h_k^*(t')\big(e^{i\omega_k(t-t')} + e^{-i\omega_k(t-t')}\big) - \frac{1}{2}h_k^*(t')\big(e^{i\omega_k(t-t')} + e^{-i\omega_k(t-t')}\big)\Big)\\
&\quad + \Big(\frac{1}{2}n_k h_k(t')\big(e^{i\omega_k(t-t')} - e^{-i\omega_k(t-t')}\big) + \frac{1}{2}n_k h_k^*(t')\big(e^{i\omega_k(t-t')} - e^{-i\omega_k(t-t')}\big)\\
&\quad - \frac{1}{2}h_k^*(t')\big(e^{i\omega_k(t-t')} - e^{-i\omega_k(t-t')}\big)\Big)\Big\}\\
&= \pm B(t)\sum_k \frac{f_k(t)}{\omega_k}\Big\{\cos\big(\omega_k(t-t')\big)\big[n_k h_k(t') - n_k h_k^*(t') - h_k^*(t')\big]\\
&\quad + i\sin\big(\omega_k(t-t')\big)\big[n_k h_k(t') + n_k h_k^*(t') + h_k^*(t')\big]\Big\}.
\end{aligned} \tag{C.7}$$

Remembering that $h_k(t) = \sum_k\big(g_k - \omega_k\alpha_k(t) + i\partial_t\alpha_k(t)\big) = \sum_k\big(g_k - f_k(t) + i\omega_k^{-1}\partial_t f_k(t)\big)$ and $n_k = (e^{-\beta\omega_k}-1)^{-1}$ this then becomes

$$\begin{aligned}
&\langle B_\pm(t)B_z(t')\rangle = \pm B(t)\sum_k \frac{f_k(t)}{\omega_k}\Big\{\cos\big(\omega_k(t-t')\big)\Big[\frac{i}{\omega_k}\coth\Big(\frac{\beta\omega_k}{2}\Big)\partial_{t'}f_k(t')\\
&\quad + f_k(t') - g_k\Big] + i\sin\big(\omega_k(t-t')\big)\Big[\coth\Big(\frac{\beta\omega_k}{2}\Big)\big(g_k - f_k(t')\big) - \frac{i}{\omega_k}\partial_{t'}f_k(t')\Big]\Big\},
\end{aligned} \tag{C.8}$$

as $2(n_k + 1/2) = \coth(\beta\omega_k/2)$. Rearranging this yields

$$\begin{aligned}
&\langle B_\pm(t)B_z(t')\rangle = \pm B(t)\sum_k f_k(t)\Big\{\frac{\big(g_k - f_k(t')\big)}{\omega_k}\Big[i\coth\Big(\frac{\beta\omega_k}{2}\Big)\sin\big(\omega_k(t-t')\big)\\
&- \cos\big(\omega_k(t-t')\big)\Big] + \frac{i\partial_t f_k(t')}{\omega_k^2}\Big[\coth\Big(\frac{\beta\omega_k}{2}\Big)\cos\big(\omega_k(t-t')\big) - i\sin\big(\omega_k(t-t')\big)\Big]\Big\}.
\end{aligned} \tag{C.9}$$

From this form we see that $\langle B_x(t)B_z(t')\rangle = 0$ and

$$\begin{aligned}
&\langle B_y(t)B_z(t')\rangle = \langle\frac{1}{2i}\big(B_-(t) - B_+(t)\big)B_z(t')\rangle \\
&= -\frac{1}{2i}\big(2\langle B_+(t)B_z(t')\rangle\big) = i\langle B_+(t)B_z(t')\rangle \\
&= iB(t)\sum_k \frac{f_k(t')\big(g_k - f_k(t')\big)}{\omega_k}\Big[i\coth\Big(\frac{\beta\omega_k}{2}\Big)\sin\big(\omega_k(t-t')\big) - \cos\big(\omega_k(t-t')\big)\Big] \\
&+ iB(t)\sum_k \frac{if_k(t')\partial_t f_k(t')}{\omega_k^2}\Big[\coth\Big(\frac{\beta\omega_k}{2}\Big)\cos\big(\omega_k(t-t')\big) - i\sin\big(\omega_k(t-t')\big)\Big],
\end{aligned} \tag{C.10}$$

using $\langle B_-(t)B_z(t')\rangle = -\langle B_+(t)B_z(t')\rangle$. Moving to the continuum limit yields

$$\begin{aligned}
\Lambda_{yz}(t,t') = B(t)\int_0^\infty d\omega\Big\{ \\
&-\frac{J(\omega)F(\omega,t)(1-F(\omega,t'))}{\omega}\Big[\coth\Big(\frac{\beta\omega}{2}\Big)\sin\big(\omega(t-t')\big) + i\cos\big(\omega(t-t')\big)\Big] \\
&+\frac{J(\omega)F(\omega,t)\partial_{t'}F(\omega,t')}{\omega^2}\Big[i\sin\big(\omega(t-t')\big) - \coth\Big(\frac{\beta\omega}{2}\Big)\cos\big(\omega(t-t')\big)\Big]\Big\}.
\end{aligned} \tag{C.11}$$

We redefine the cross-correlation function such that $\Lambda'_{yz}(t,t') = i\Lambda_{yz}(t,t')$ to ensure the useful relationship $\Lambda^*(t',t) = \Lambda(t,t')$ yielding

$$\begin{aligned}
\Lambda'_{yz}(t,t') = B(t)\int_0^\infty d\omega\Big\{ \\
&-\frac{J(\omega)F(\omega,t)(1-F(\omega,t')}{\omega}\Big[i\coth\Big(\frac{\beta\omega}{2}\Big)\sin\big(\omega(t-t')\big) - \cos\big(\omega(t-t')\big)\Big] \\
&-\frac{J(\omega)F(\omega,t)\partial_{t'}F(\omega,t')}{\omega^2}\Big[i\coth\Big(\frac{\beta\omega}{2}\Big)\cos\big(\omega(t-t')\big) + \sin\big(\omega(t-t')\big)\Big]\Big\}.
\end{aligned} \tag{C.12}$$

C.3 Weak-Coupling Correlation Function

The final correlation function to calculate is the weak-coupling-type correlation function arising purely from the additional bath operator, $B_z(t)$. To calculate this correlation function we shall make use of the relationships $\langle b_k^\dagger b_{k'}\rangle = \langle b_k^\dagger\rangle\langle b_{k'}\rangle = 0$, $\langle b_k^\dagger b_k^\dagger\rangle = \langle b_k b_k\rangle = 0$, $[b_k^\dagger, b_{k'}] = \delta_{k,k'}$. Calculating the correlation

between the weak-coupling-type bath operators then yields

$$
\begin{aligned}
&\langle B_z(t)B_z(t')\rangle = \\
&\quad\sum_k \big\langle \big(h_k(t)b_k^\dagger e^{i\omega_k t} + h_k^*(t)b_k e^{-i\omega_k t}\big)\big(h_k(t')b_k^\dagger e^{i\omega_k t'} + h_k^*(t')b_k e^{-i\omega_k t'}\big)\big\rangle \\
&= \sum_k \big\langle h_k(t)h_k(t')b_k^\dagger b_k^\dagger e^{i\omega_k(t+t')} + h_k(t)h_k^*(t')b_k^\dagger b_k e^{i\omega_k(t-t')} \\
&\quad + h_k^*(t)h_k(t')b_k b_k^\dagger e^{-i\omega_k(t-t')} + h_k^*(t)h_k^*(t')b_k b_k e^{-i\omega_k(t+t')}\big\rangle \\
&= \sum_k \Big[h_k(t)h_k(t')\langle b^\dagger b^\dagger\rangle e^{i\omega_k(t+t')} + h_k(t)h_k^*(t')\langle b_k^\dagger b_k\rangle e^{i\omega(t-t')} \\
&\quad + h_k^*(t)h_k(t')\langle b_k b_k^\dagger\rangle e^{-i\omega_k(t-t')} + h_k^*(t)H_k^*(t')\langle b_k b_k\rangle e^{-i\omega_k(t+t')}\Big] \\
&= \sum_k \Big[h_k(t)h_k^*(t')\langle b_k^\dagger b_k\rangle e^{i\omega(t-t')} + h_k^*(t)h_k(t')\langle b_k b_k^\dagger\rangle e^{-i\omega_k(t-t')}\Big] \\
&= \sum_k \Big[h_k(t)h_k^*(t')\langle b_k^\dagger b_k\rangle e^{i\omega(t-t')} + h_k^*(t)h_k(t')(\langle b_k^\dagger b_k\rangle + 1) e^{-i\omega_k(t-t')}\Big] \\
&= \sum_k \Big[h_k(t)h_k^*(t')n_k e^{i\omega_k(t-t')} + h_k^*(t)h_k(t')(n_k+1) e^{-i\omega_k(t-t')}\Big] \\
&= \sum_k \Big[h_k(t)h_k^*(t')n_k\big(\cos(\omega(t-t')) + i\sin(\omega(t-t'))\big) \\
&\quad + h_k^*(t)h_k(t')(n_k+1)\big(\cos(\omega_k(t-t')) - i\sin(\omega_k(t-t'))\big)\Big] \\
&= \sum_k \Big[\Big(\big(h_k(t)h_k^*(t') + h_k^*(t)h_k(t')\big)n_k + h_k^*(t)h_k(t')\Big)\cos(\omega_k(t-t')) \\
&\quad + \Big(\big(h_k(t)h_k^*(t') - h_k^*(t)h_k(t')\big)n_k - h_k^*(t)h_k(t')\Big) i\sin(\omega(t-t'))\Big] \\
&= \sum_k \Big[\Big\{ \Big((g_k - f_k(t))(g_k - f_k(t')) + \frac{\partial_t f_k(t)\partial_{t'} f_k(t')}{\omega_k^2}\Big)(2n_k+1) \\
&\quad + i(g_k - f_k(t))\frac{\partial_{t'} f_k(t')}{\omega_k} - i(g_k - f_k(t'))\frac{\partial_t f_k(t)}{\omega_k}\Big\}\cos(\omega_k(t-t')) \\
&\quad + \Big\{\frac{i}{\omega_k}\Big((g_k - f_k(t'))\partial_t f_k(t) - (g_k - f_k(t))\partial_{t'} f_k(t')\Big)(2n_k+1) \\
&\quad - (g_k - f_k(t))(g_k - f_k(t')) - \frac{\partial_t f_k(t)\partial_{t'} f_k(t')}{\omega_k^2}\Big\} i\sin(\omega_k(t-t'))\Big],
\end{aligned}
\tag{C.13}
$$

where we have again defined $h_k(t) = \sum_k\big(g_k - \omega_k\alpha_k(t) + i\partial_t\alpha_k(t)\big) = \sum_k\big(g_k - f_k(t) + i\omega_k^{-1}\partial_t f_k(t)\big)$, and $n_k = (e^{-\beta\omega_k} - 1)^{-1}$ such that $(2n_k+1) = \coth\Big(\frac{\beta\omega}{2}\Big)$.

Rearranging correlation function becomes

$$\langle B_z(t)B_z(t')\rangle = \sum_k \Big\{(g_k - f_k(t))(g_k - f_k(t'))\Big\}\Big(\cos(\omega_k(t-t'))\coth\Big(\frac{\beta\omega_k}{2}\Big) - i\sin(\omega_k(t-t'))\Big) + \frac{\partial_t f_k(t)\partial_{t'} f_k(t')}{\omega_k^2}\Big(\cos(\omega_k(t-t'))\coth\Big(\frac{\beta\omega_k}{2}\Big) - i\sin(\omega_k(t-t'))\Big) + \frac{\big((g_k - f_k(t'))\partial_t f_k(t) - (g_k - f_k(t))\partial_{t'} f_k(t')\big)}{\omega_k} \times \Big(i\cos(\omega_k(t-t')) - \sin(\omega_k(t-t'))\coth\Big(\frac{\beta\omega}{2}\Big)\Big). \tag{C.14}$$

Taking the continuum limit, the weak-coupling correlation function is given by

$$\Lambda_{zz}(t,t') = \int_0^\infty d\omega J(\omega)u(\omega,t)u^*(\omega,t')\left[\coth\left(\frac{\beta\omega}{2}\right)\cos(\omega(t-t')) - i\sin(\omega(t-t'))\right], \tag{C.15}$$

where $u(\omega,t) = 1 - F(\omega,t) + i\omega^{-1}\partial_t F(\omega,t)$.

C.4 Recovering the Polaron Model

We can recover the Polaron model from our full variational polaron model by by setting $F(\omega,t) = 1\forall t$ and $\partial_t f_k(t) = 0$. In this case the cross-terms ($\Lambda_{yz} = \Lambda_{zy}$) and weak-coupling ($\Lambda_{zz}$) type correlation functions go to zero, leaving only the polaron-type correlation functions non-zero.

C.5 Recovering the Weak-Coupling Model

By setting $F(\omega,t) = 0\forall t$ and $\alpha_k(t) = 0\forall t$ we can instead recover the weak-coupling limit from the full variational polaron model. In this case it is the polaron-type and cross-term-type correlation functions that go to zero as well as leaving $B(t) = 1\forall t$ (i.e. $\Omega_r(t) = \Omega(t)$ and $\delta_r(t) = \delta$). The only remaining non-zero correlation function is the weak-coupling correlation function given by

$$\Lambda_{zz}(t,t') = \int_0^\infty d\omega J(\omega)\Big(\coth\Big(\frac{\beta\omega}{2}\Big)\cos(\omega(t-t')) - i\sin(\omega(t-t'))\Big). \tag{C.16}$$

The non-Markovian weak-coupling master equation is then

$$\frac{\partial}{\partial t}\rho_S(t) = -i[\delta_r\sigma^\dagger\sigma + \frac{\Omega(t)}{2}\sigma_x, \rho_S(t)] - \Big([\sigma^\dagger\sigma, \theta_z(t)\rho_s(t)] + [\rho_s(t)\theta_z^\dagger(t), \sigma^\dagger\sigma]\Big), \tag{C.17}$$

where

$$\theta_z(t) = \int_0^t \sigma^\dagger\sigma(t', t)\Lambda_{zz}(t, t')dt', \tag{C.18}$$

is the non-Markovian rate operator. Under the Markov approximation we can take the upper limit of the integral in the environment rate operator to infinity to remove its time dependence.

Appendix D

Unitary Transformation of a Four-Level System Coupled to a Bi-modal Cavity

In this appendix we will transform the Hamiltonian describing a Four-Level System (4LS) in a Voigt geometry magnetic field coupled to a bi-modal cavity, and driven by a classical laser pulse from the laboratory frame to a reference frame rotating at a frequency ω_R.

D.1 Lab-Frame Hamiltonian

The lab frame Hamiltonian describing such a cavity-coupled system is given by $H = H_0 + H_I + H_D^{QD}(t) + H_D^C(t)$, where

$$\begin{aligned} H_0 &= \frac{\Delta_B^e}{2}(\sigma_{22} - \sigma_{11}) + (\omega_0 - \frac{\Delta_B^h}{2})\sigma_{33} + (\omega_0 + \frac{\Delta_B^h}{2})\sigma_{44} + \sum_{\lambda=X,Y} \nu_\lambda a_\lambda^\dagger a_\lambda, \\ H_I &= \sum_{\lambda=X,Y} g_\lambda(\boldsymbol{\sigma}_\lambda + \boldsymbol{\sigma}_\lambda^\dagger)(a_\lambda + a_\lambda^\dagger), \\ H_D^{QD}(t) &= -\sum_{\lambda=X,Y} \Omega_\lambda(t)\cos(\omega_l t)\sigma_\lambda + \text{h.c.}, \\ H_D^C(t) &= -\sum_{\lambda=X,Y} \epsilon_\lambda(t)\cos(\omega_l t)(a_\lambda + a_\lambda^\dagger). \end{aligned} \tag{D.1}$$

D.2 Rotating Frame Hamiltonian

To move to a rotating frame of reference we need to perform a unitary transformation such that the total Hamiltonian in the rotating reference frame is given by

$$\tilde{H}(t) = U(t)H(t)U^{\dagger}(t) + i\big(\frac{\partial}{\partial t}U(t)\big)U^{\dagger}(t), \tag{D.2}$$

as derived in Section 3.4.1. We perform this transformation using the unitary operator

$$U(t) = e^{i\omega_R t\left(a_X^{\dagger}a_X + a_Y^{\dagger}a_Y + \sigma_{33} + \sigma_{44}\right)}, \tag{D.3}$$

From here we can calculate the second term on the right hand side of Eq. D.2 by taking the derivative of Eq. D.3 with respect to time. Doing so produces

$$i\big(\frac{\partial}{\partial t}U(t)\big)U^{\dagger}(t) = -\omega_R(a_X^{\dagger}a_X + a_Y^{\dagger}a_Y + \sigma_{33} + \sigma_{44}). \tag{D.4}$$

To calculate the first term on the right hand side of Eq. D.2 we can make use of the individual cavity modes and 4LS being described by different Hilbert spaces. This allows the total unitary operator (Eq. D.3) to be separated into the tensor product of three separate unitary operators, each acting on one of the three Hilbert spaces, such that

$$U(t) = U_C^X(t) \otimes U_C^Y(t) \otimes U_{QD}(t) = e^{i\omega_R t\left(a_X^{\dagger}a_X\right)} \otimes e^{i\omega_R t\left(a_Y^{\dagger}a_Y\right)} \otimes e^{i\omega_R t(|3\rangle\langle 3| + |4\rangle\langle 4|)}. \tag{D.5}$$

Starting with the unitary operators acting on the cavity modes we define $a_\lambda(t) = U_C^\lambda(t)a_\lambda(U_C^\lambda(t))^\dagger$ where $U_C^\lambda(t) = e^{i\omega_R t(a_\lambda^\dagger a_\lambda)}$. Taking the derivative of $a(t)$ with respect to time yields

$$\partial_t a_\lambda(t) = (\partial_t U_C^\lambda(t))a_\lambda(U_C^\lambda(t))^\dagger + U_C^\lambda(t)a_\lambda(\partial_t(U_C^\lambda(t))^\dagger). \tag{D.6}$$

Substituting in $U_C^\lambda(t)$ yields

$$\begin{aligned}\partial_t a_\lambda(t) &= i\omega_R a_\lambda^\dagger a_\lambda U_C^\lambda(t)a_\lambda(U_C^\lambda(t))^\dagger + U_C^\lambda(t)a_\lambda(-i\omega_R a_\lambda^\dagger a_\lambda)(U_C^\lambda(t))^\dagger \\ &= i\omega_R(a_\lambda^\dagger a_\lambda U_C^\lambda(t)a_\lambda(U_C^\lambda(t))^\dagger - U_C^\lambda(t)a_\lambda a_\lambda^\dagger a_\lambda(U_C^\lambda(t))^\dagger).\end{aligned} \tag{D.7}$$

The commutator between $U_C^\lambda(t)$ and $a_\lambda^\dagger a_\lambda$ is

$$\begin{aligned}\left[U_C^\lambda(t), a_\lambda^\dagger a_\lambda\right] &= \sum_{n=0}^{\infty}\frac{(i\omega_R t)^n}{n!}\left[\left(a_\lambda^\dagger a_\lambda\right)^n, a_\lambda^\dagger a_\lambda\right] \\ &= 0,\end{aligned} \tag{D.8}$$

hence we can re-write the derivative of $a(t)$ with respect to time as

$$\partial_t a_\lambda(t) = i\omega_R U_C^\lambda(t)[a_\lambda^\dagger a_\lambda, a_\lambda](U_C^\lambda(t))^\dagger. \tag{D.9}$$

Using the commutation relation between the cavity raising and lowering operators ($[a, a^\dagger] = 1$) it can be shown that $[a_\lambda^\dagger a_\lambda, a_\lambda] = -a_\lambda$ and therefore

$$\partial_t a_\lambda(t) = -i\omega_R U_C^\lambda(t) a_\lambda (U_C^\lambda(t))^\dagger = -i\omega_R a_\lambda(t), \tag{D.10}$$

which has the formal solution

$$a_\lambda(t) = a_\lambda e^{-i\omega_R t}, \tag{D.11}$$

and therefore $a_\lambda^\dagger(t) = a_\lambda^\dagger e^{i\omega_R t}$.

We must now also apply the unitary transformation to the 4LS degrees of freedom. We can also calculate $U_{\mathrm{QD}}(t)\sigma U_{\mathrm{QD}}^\dagger(t)$ for each of the 4LS operators, as we have already done for the individual cavity modes. Taking the Taylor expansion of $U_{\mathrm{QD}}(t)$ yields

$$\begin{aligned}
U_{\mathrm{QD}}(t) = e^{i\omega_R t(\sigma_{33}+\sigma_{44})} &= \sum_n \frac{(i\omega_R t)^n}{n!}(\sigma_{33}+\sigma_{44})^n \\
&= \mathbf{I} + (i\omega_R t)(\sigma_{33}+\sigma_{44}) + \frac{(i\omega_R t)^2}{2}(\sigma_{33}+\sigma_{44})^2 + ... \\
&= \Big(\sum_{j=1}^4 \sigma_{jj}\Big) + (i\omega_R t)(\sigma_{33}+\sigma_{44}) + \frac{(i\omega_R t)^2}{2!}(\sigma_{33}+\sigma_{44})^2 + ... \\
&= \sigma_{11} + \sigma_{22} + (1 + (i\omega_R t) + \frac{(i\omega_R t)^2}{2!} + ...)(\sigma_{33}+\sigma_{44}) \\
&= \sigma_{11} + \sigma_{22} + e^{i\omega_R t}(\sigma_{33}+\sigma_{44}),
\end{aligned} \tag{D.12}$$

where $\mathbf{I} = \sum_{j=1}^4 \sigma_{jj}$ is the identity matrix. Applying the QD unitary operator in this form to the QD transition operators we find

$$\begin{aligned}
U_{\mathrm{QD}}(t)\sigma_{ij}U_{\mathrm{QD}}^\dagger(t) &= \sigma_{ij}e^{-i\omega_R t}, \\
U_{\mathrm{QD}}(t)\sigma_{ij}^\dagger U_{\mathrm{QD}}^\dagger(t) &= \sigma_{ji}^\dagger e^{i\omega_R t},
\end{aligned} \tag{D.13}$$

for $i \in \{1,2\}$ and $j \in \{3,4\}$ where $\sigma_{ij} = |i\rangle\langle j|$. The σ_{kk} with $k \in \{1,2,3,4\}$ operators remain unchanged by this unitary transformation. Applying all of

these transformations to the components of the lab frame Hamiltonian yields

$$\begin{aligned}
\tilde{H}_0 &= \frac{\Delta_B^e}{2}(\sigma_{22}-\sigma_{11}) + (\omega_0 - \omega_R - \frac{\Delta_B^h}{2})\sigma_{33} \\
&\quad + (\omega_0 - \omega_R + \frac{\Delta_B^h}{2})\sigma_{44} + \sum_{\lambda=X,Y}(\nu_\lambda - \omega_R)a_\lambda^\dagger a_\lambda, \\
\tilde{H}_I &= \sum_{\lambda=X,Y} g_\lambda\big(a_\lambda^\dagger e^{i\omega_R t} + a_\lambda e^{-i\omega_R t}\big)\big(\sigma_\lambda^\dagger e^{i\omega_R t} + \sigma_\lambda e^{-i\omega_R t}\big), \\
\tilde{H}_D^{QD}(t) &= -\sum_{\lambda=X,Y}\frac{\Omega_\lambda(t)}{2}(e^{i\omega_l t} + e^{-i\omega_l t})\big(\sigma_\lambda^\dagger e^{i\omega_R t} + \sigma_\lambda e^{-i\omega_R t}\big), \\
\tilde{H}_D^{C}(t) &= -\sum_{\lambda=X,Y}\frac{\epsilon_\lambda(t)}{2}(e^{i\omega_l t} + e^{-i\omega_l t})\big(a_\lambda e^{-i\omega_R t} + a_\lambda^\dagger e^{i\omega_R t}\big).
\end{aligned} \tag{D.14}$$

Using the Rotating Wave Approximation (RWA) we can replace the counter rotating terms (i.e. terms with $\omega_l + \omega_R$ in the exponent) with their zero time averages to find

$$\begin{aligned}
\tilde{H}_0 &= \frac{\Delta_B^e}{2}(\sigma_{22}-\sigma_{11}) + (\omega_0 - \omega_R - \frac{\Delta_B^h}{2})\sigma_{33} \\
&\quad + (\omega_0 - \omega_R + \frac{\Delta_B^h}{2})\sigma_{44} + \sum_{\lambda=X,Y}(\nu_\lambda - \omega_R)a_\lambda^\dagger a_\lambda, \\
\tilde{H}_I &= \sum_{\lambda=X,Y} g_\lambda a_\lambda^\dagger \boldsymbol{\sigma}_\lambda + g_\lambda^* a_\lambda \boldsymbol{\sigma}_\lambda^\dagger, \\
\tilde{H}_D^{QD}(t) &= -\sum_{\lambda=X,Y}\frac{\Omega_\lambda(t)}{2}\big(\sigma_\lambda^\dagger e^{-i(\omega_l-\omega_R)t} + \sigma_\lambda e^{i(\omega_l-\omega_R)t}\big) \\
\tilde{H}_D^{C}(t) &= -\sum_{\lambda=X,Y}\frac{\epsilon_\lambda(t)}{2}\big(a_\lambda^\dagger e^{-i(\omega_l-\omega_R)t} + a_\lambda e^{i(\omega_l-\omega_R)t}\big).
\end{aligned} \tag{D.15}$$

Thus in the case where $\omega_R = \omega_l$ the time dependence in the exponential terms cancel leaving the only time-dependence originating from the pulse's envelope function. Setting $\omega_R = \omega_0$ recovers the Hamiltonian used in studying optical spin control.

Bibliography

[1] Q. Zhu et al. "Quantum computational advantage via 60-qubit 24-cycle random circuit sampling". *Science Bulletin* 67 (2022), pp. 240–245. DOI: 10.1016/j.scib.2021.10.017.

[2] H. S. Zhong et al. "Quantum computational advantage using photons". *Science* 370 (2020), pp. 1460–1463. DOI: 10.1126/science.abe8770.

[3] F. Arute et al. "Quantum supremacy using a programmable superconducting processor". *Nature* 574 (2019). DOI: 10.1038/s41586-019-1666-5.

[4] R. P. Feynman. "Simulating physics with computers". *International Journal of Theoretical Physics* 21 (1982), pp. 467–488. DOI: 10.1007/BF02650179.

[5] D. Deutsch and R. Penrose. "Quantum theory, the Church-Turing principle and the universal quantum computer". *Proceedings of the Royal Society of London. A. Mathematical and Physical Sciences* 400 (1985), pp. 97–117. DOI: 10.1098/rspa.1985.0070.

[6] R. Orús, S. Mugel, and E. Lizaso. "Quantum computing for finance: Overview and prospects". *Reviews in Physics* 4 (2019). DOI: 10.1016/j.revip.2019.100028.

[7] B. P. Lanyon et al. "Universal Digital Quantum Simulation with Trapped Ions". *Science* 334 (2011), pp. 57–62.

[8] Y. Cao et al. "Quantum Chemistry in the Age of Quantum Computing". *Chemical Reviews* 119 (2019), pp. 10856–10915. DOI: 10.1021/acs.chemrev.8b00803.

[9] P. S. Emani et al. "Quantum computing at the frontiers of biological sciences". *Nature Methods* 18 (2021), pp. 701–709. DOI: 10.1038/s41592-020-01004-3.

[10] T. Koshiba. "Quantum cryptography". *Reviews of Modern Physics* 74 (2002), pp. 145–195. DOI: 10.1007/978-3-540-92910-9_45.

[11] A. M. Fox. *Quantum optics : an introduction*. eng. Oxford master series in physics ; 15. Oxford: Oxford University Press, 2006.

[12] A. Montanaro. "Quantum algorithms: An overview". *npj Quantum Information* 2 (2016), pp. 1–8. DOI: 10.1038/npjqi.2015.23.

[13] P. W. Shor. "Polynomial-time algorithms for prime factorization and discrete logarithms on a quantum computer". *SIAM Journal on Computing* 26 (1997), pp. 1484–1509.

[14] L. K. Grover. "Quantum Mechanics Helps in Searching for a Needle in a Haystack". *Phys. Rev. Lett.* 79 (1997), pp. 325–328. DOI: 10.1103/PhysRevLett.79.325.

[15] K. Nemoto and W. J. Munro. "Nearly Deterministic Linear Optical Controlled-NOT Gate". *Phys. Rev. Lett.* 93 (2004), p. 250502. DOI: 10.1103/PhysRevLett.93.250502.

[16] J. L. O'Brien et al. "Demonstration of an all-optical quantum controlled-NOT gate". *Nature* 426 (2003), pp. 264–267. DOI: 10.1038/nature02054.

[17] J. Chen et al. "Demonstration of a Quantum Controlled-NOT Gate in the Telecommunications Band". *Phys. Rev. Lett.* 100 (2008), p. 133603. DOI: 10.1103/PhysRevLett.100.133603.

[18] K. Park, P. Marek, and R. Filip. "Deterministic nonlinear phase gates induced by a single qubit". *New Journal of Physics* 20 (2018). DOI: 10.1088/1367-2630/aabb86.

[19] E. Knill, R. Laflamme, and G. J. Milburn. "A scheme for efficient quantum computation with linear optics". *Nature* 409 (2001). DOI: 10.1038/35051009.

[20] D. Loss, D. P. DiVincenzo, and P. DiVincenzo. "Quantum computation with quantum dots". *Physical Review A* 57 (1998), pp. 120–126.

[21] L. Fan and C. Cao. "Deterministic CNOT gate and complete Bell-state analyzer on quantum-dot-confined electron spins based on faithful quantum nondemolition parity detection". *Journal of the Optical Society of America B* 38 (2021), p. 1593. DOI: 10.1364/josab.415321.

[22] H-F Wang et al. "Deterministic CNOT gate and entanglement swapping for photonic qubits using a quantum-dot spin in a double-sided optical microcavity". *Physics Letters A* 377 (2013), pp. 2870–2876. DOI: https://doi.org/10.1016/j.physleta.2013.09.005.

[23] C. H. Bennett and G. Brassard. "Quantum cryptography: Public key distribution and coin tossing". *Theoretical Computer Science* 560 (2014), pp. 7–11. DOI: 10.1016/j.tcs.2014.05.025.

[24] C. H. Bennett. "Quantum cryptography using any two nonorthogonal states". *Phys. Rev. Lett.* 68 (1992), pp. 3121–3124. DOI: 10.1103/PhysRevLett.68.3121.

[25] D. Bruß. "Optimal Eavesdropping in Quantum Cryptography with Six States". *Phys. Rev. Lett.* 81 (1998), pp. 3018–3021. DOI: 10.1103/PhysRevLett.81.3018.

[26] D. S. Naik et al. "Entangled State Quantum Cryptography: Eavesdropping on the Ekert Protocol". *Phys. Rev. Lett.* 84 (2000), pp. 4733–4736. DOI: 10.1103/PhysRevLett.84.4733.

[27] E. Polino et al. "Photonic quantum metrology". *AVS Quantum Science* 2 (2020), p. 024703. DOI: 10.1116/5.0007577.

[28] M. A. Taylor and W. P. Bowen. "Quantum metrology and its application in biology". *Physics Reports* 615 (2016), pp. 1–59. DOI: 10.1016/j.physrep.2015.12.002.

[29] R. Schnabel et al. "Quantum metrology for gravitational wave astronomy". *Nature Communications* 1 (2010), pp. 1–10. DOI: 10.1038/ncomms1122.

[30] G. Tóth and I. Apellaniz. "Quantum metrology from a quantum information science perspective". *Journal of Physics A: Mathematical and Theoretical* 47 (2014). DOI: 10.1088/1751-8113/47/42/424006.

[31] V. Giovannetti, S. Lloyd, and L. MacCone. "Advances in quantum metrology". *Nature Photonics* 5 (2011), pp. 222–229. DOI: 10.1038/nphoton.2011.35.

[32] K. R. Motes et al. "Linear Optical Quantum Metrology with Single Photons: Exploiting Spontaneously Generated Entanglement to Beat the Shot-Noise Limit". *Phys. Rev. Lett.* 114 (2015), p. 170802. DOI: 10.1103/PhysRevLett.114.170802.

[33] M. W. Mitchell, J. S. Lundeen, and A. M. Steinberg. "Super-resolving phase measurements with a multiphoton entangled state". *Nature* 429 (2004), pp. 161–164. DOI: 10.1038/nature02493.

[34] S. Slussarenko et al. "Unconditional violation of the shot-noise limit in photonic quantum metrology". *Nature Photonics* 11 (2017), pp. 700–703. DOI: 10.1038/s41566-017-0011-5.

[35] J. C.F. Matthews et al. "Towards practical quantum metrology with photon counting". *npj Quantum Information* 2 (2016). DOI: 10.1038/npjqi.2016.23.

[36] C. You et al. "Scalable multiphoton quantum metrology with neither pre- nor post-selected measurements". *Applied Physics Reviews* 8 (2021). DOI: 10.1063/5.0063294.

[37] M. Müller et al. "Quantum-Dot Single-Photon Sources for Entanglement Enhanced Interferometry". *Phys. Rev. Lett.* 118 (2017), p. 257402. DOI: 10.1103/PhysRevLett.118.257402.

[38] M. Bohmann, J. Sperling, and W. Vogel. "Entanglement and phase properties of noisy NOON states". *Phys. Rev. A* 91 (2015), p. 042332. DOI: 10.1103/PhysRevA.91.042332.

[39] H.-P. Breuer, F. Petruccione, et al. *The theory of open quantum systems*. Oxford University Press on Demand, 2002.

[40] D. T. Haar. "Theory and applications of the density matrix". *Reports on Progress in Physics* 24 (1961), pp. 304–362. DOI: 10.1088/0034-4885/24/1/307.

[41] A. Galindo et al. *Quantum Mechanics I*. Quantum Mechanics. Springer-Verlag, 1990. Chap. 2.

[42] S. Nakajima. "On Quantum Theory of Transport Phenomena". *Progress of Theoretical Physics* 20 (1958), pp. 948–959. DOI: 10.1143/PTP.20.948.

[43] R. Zwanzig. "Ensemble Method in the Theory of Irreversibility". *The Journal of Chemical Physics* 33 (1960), pp. 1338–1341. DOI: 10.1063/1.1731409.

[44] D. Manzano. "A short introduction to the Lindblad master equation". *AIP Advances* 10 (2020), p. 025106. DOI: 10.1063/1.5115323.

[45] A. M. Fox. *A student's guide to atomic physics*. eng. Cambridge: Cambridge University Press, 2018.

[46] A. M. Fox. *Optical properties of solids*. eng. Second edition. Oxford master series in condensed matter physics ; v. 3. Oxford: Oxford University Press, 2010.

[47] B. D. Gerardot et al. "Manipulating exciton fine structure in quantum dots with a lateral electric field". *Applied Physics Letters* 90 (2007), pp. 88–91. DOI: 10.1063/1.2431758.

[48] R. Winik et al. "On-demand source of maximally entangled photon pairs using the biexciton-exciton radiative cascade". *Phys. Rev. B* 95 (2017), p. 235435. DOI: 10.1103/PhysRevB.95.235435.

[49] S. Savasta, G. Martino, and R. Girlanda. "Entangled photon pairs from the optical decay of biexcitons". *Solid State Communications* 111 (1999), pp. 495–500. DOI: 10.1016/S0038-1098(99)00233-1.

[50] M. Müller et al. "On-demand generation of indistinguishable polarization entangled photon pairs". *Nature Photonics* 8 (2014), pp. 224–228. DOI: 10.1038/nphoton.2013.377.

[51] T. M. Stace, G. J. Milburn, and C. H. W. Barnes. "Entangled two-photon source using biexciton emission of an asymmetric quantum dot in a cavity". *Phys. Rev. B* 67 (2003), p. 085317. DOI: 10.1103/PhysRevB.67.085317.

[52] P. K. Pathak and S. Hughes. "Cavity-assisted fast generation of entangled photon pairs through the biexciton-exciton cascade". *Phys. Rev. B* 80 (2009), p. 155325. DOI: 10.1103/PhysRevB.80.155325.

[53] P. W. Fry et al. "Inverted Electron-Hole Alignment in InAs-GaAs Self-Assembled Quantum Dots". *Phys. Rev. Lett.* 84 (2000), pp. 733–736. DOI: 10.1103/PhysRevLett.84.733.

[54] J. J. Finley et al. "Quantum-confined Stark shifts of charged exciton complexes in quantum dots". *Phys. Rev. B* 70 (2004), p. 201308. DOI: 10.1103/PhysRevB.70.201308.

[55] S. Walck and T. Reinecke. "Exciton diamagnetic shift in semiconductor nanostructures". *Physical Review B - Condensed Matter and Materials Physics* 57 (1998), pp. 9088–9096. DOI: 10.1103/PhysRevB.57.9088.

[56] D. H. Kobe. "Gauge-invariant classical Hamiltonian formulation of the electrodynamics of nonrelativistic particles". 49 (1981), pp. 581–588. DOI: 10.1119/1.12463.

[57] J. D. Jackson. "From Lorenz to Coulomb and other explicit gauge transformations". *American Journal of Physics* 70 (2002), pp. 917–928. DOI: 10.1119/1.1491265.

[58] K-H Yang. "The physics of gauge transformations". *American Journal of Physics* 73 (2005), pp. 742–751. DOI: 10.1119/1.1938949.

[59] P. Tighineanu et al. "Unraveling the Mesoscopic Character of Quantum Dots in Nanophotonics". *Physical Review Letters* 114 (2015), pp. 1–5. DOI: 10.1103/PhysRevLett.114.247401.

[60] M. L. Andersen et al. "Strongly modified plasmon-matter interaction with mesoscopic quantum emitters". *Nature Physics* 7 (2011), pp. 215–218. DOI: 10.1038/nphys1870.

[61] H. J. Carmichael. *Statistical methods in quantum optics 1: master equations and Fokker-Planck equations*. Vol. 1. Springer Science & Business Media, 1999.

[62] J. R. Johansson, P. D. Nation, and F. Nori. "QuTiP: An open-source Python framework for the dynamics of open quantum systems". *Computer Physics Communications* 183 (2012), pp. 1760–1772.

[63] M. E. Donovan et al. "Experimental observation of multiple excitonic optical Rabi oscillations in a semiconductor". *Ultrafast Phenomena in Semiconductors III* 3624 (1999), pp. 216–223. DOI: 10.1117/12.349298.

[64] S. J. Boyle et al. "Two-color two-photon Rabi oscillation of biexciton in single InAs/GaAs quantum dot". *Physica E* 42 (2010). DOI: 10.1016/j.physe.2009.11.008.

[65] S. Stufler et al. "Two-photon Rabi oscillations in a single Inx Ga1-x As GaAs quantum dot". *Physical Review B - Condensed Matter and Materials Physics* 73 (2006), pp. 1–7. DOI: 10.1103/PhysRevB.73.125304.

[66] T. H. Stievater et al. "Rabi Oscillations of Excitons in Single Quantum Dots". *Phys. Rev. Lett.* 87 (2001), p. 133603. DOI: 10.1103/PhysRevLett.87.133603.

[67] P. Borri et al. "Rabi oscillations in the excitonic ground-state transition of InGaAs quantum dots". *Physical Review B - Condensed Matter and Materials Physics* 66 (2002), pp. 1–4. DOI: 10.1103/PhysRevB.66.081306.

[68] D. Steck. *Quantum and Atom Optics*. Available online at http://steck.us/teaching (revision 0.13.4, 24 September 2020).

[69] M. Strauß et al. "Wigner Time Delay Induced by a Single Quantum Dot". *Phys. Rev. Lett.* 122 (2019), p. 107401. DOI: 10.1103/PhysRevLett.122.107401.

[70] C. Matthiesen, A. N. Vamivakas, and M. Atatüre. "Subnatural linewidth single photons from a quantum dot". *Physical Review Letters* 108 (2012), pp. 1–4. DOI: 10.1103/PhysRevLett.108.093602.

[71] D. P. S. McCutcheon. "Optical signatures of non-Markovian behavior in open quantum systems". *Physical Review A* 93 (2016), pp. 1–7. DOI: 10.1103/PhysRevA.93.022119.

[72] B. R. Mollow. "Power spectrum of light scattered by two-level systems". *Physical Review* 188 (1969).

[73] J. H. Shirley. "Solution of the schrödinger equation with a hamiltonian periodic in time". eng. *Physical review* 138 (1965), B979–B987.

[74] P. Kok and B. W. Lovett. *Introduction to optical quantum information processing*. eng. Cambridge ; New York: Cambridge University Press, 2010.

[75] J. Dalibard and C. Cohen-Tannoudji. "Atomic motion in laser light: connection between semiclassical and quantum descriptions". *Journal of Physics B: Atomic and Molecular Physics (1968-1987)* 18 (1985), p. 1661.

[76] J. H. Eberly, C. V. Kunasz, and K. Wodkiewicz. "Time-dependent spectrum of resonance fluorescence". *J. Phys. B* 13 (1980), pp. 217–239.

[77] R. Román-Ancheyta et al. "Time-dependent spectra of a three-level atom in the presence of electron shelving". *Physical Review A* 98 (2018), pp. 1–5. DOI: 10.1103/PhysRevA.98.013820.

[78] A. Moelbjerg et al. "Resonance fluorescence from semiconductor quantum dots: Beyond the Mollow triplet". *Physical Review Letters* 108 (2012), pp. 1–5. DOI: 10.1103/PhysRevLett.108.017401.

[79] J. K. Gamble et al. "Two-electron dephasing in single Si and GaAs quantum dots". *Phys. Rev. B* 86 (2012), p. 035302. DOI: 10.1103/PhysRevB.86.035302.

[80] E. A. Muljarov and R. Zimmermann. "Dephasing in Quantum Dots: Quadratic Coupling to Acoustic Phonons". *Phys. Rev. Lett.* 93 (2004), p. 237401. DOI: 10.1103/PhysRevLett.93.237401.

[81] E. Purcell. "Spontaneous emission probabilities at radio frequencies". *Phys. Rev.* 681 (1946).

[82] F. Liu et al. "High Purcell factor generation of indistinguishable on-chip single photons". *Nature Nanotechnology* 13 (2018), pp. 835–840.

[83] E. V. Denning et al. "Phonon effects in quantum dot single-photon sources". *Optical Materials Express* 10 (2020), p. 222. DOI: 10.1364/ome.380601.

[84] K. Kuruma et al. "Time-resolved vacuum Rabi oscillations in a quantum-dot-nanocavity system". *Physical Review B* 97 (2018), pp. 4–6. DOI: 10.1103/PhysRevB.97.235448.

[85] T. Yoshle et al. "Vacuum Rabi splitting with a single quantum dot in a photonic crystal nanocavity". *Nature* 432 (2004), pp. 200–203. DOI: 10.1038/nature03119.

[86] P. Lodahl, S. Mahmoodian, and S. Stobbe. "Interfacing single photons and single quantum dots with photonic nanostructures". *Reviews of Modern Physics* 87 (2015), p. 347.

[87] S. Unsleber et al. "Observation of resonance fluorescence and the Mollow triplet from a coherently driven site-controlled quantum dot". *Optica* 2 (2015), pp. 1072–1077. DOI: 10.1364/optica.2.001072.

[88] A. N. Vamivakas et al. "Spin-resolved quantum-dot resonance fluorescence". *Nature Physics* 5 (2009), pp. 198–202. DOI: 10.1038/nphys1182.

[89] R. Al-Khuzheyri et al. "Resonance fluorescence from a telecom wavelength quantum dot". *Applied Physics Letters* 109 (2016), p. 163104. DOI: 10.1063/1.4965845.

[90] E. B. Flagg et al. "Resonantly driven coherent oscillations in a solid-state quantum emitter". *Nature Physics* 5 (2009), pp. 203–207. DOI: 10.1038/nphys1184.

[91] D. Press et al. "Photon Antibunching from a Single Quantum-Dot-Microcavity System in the Strong Coupling Regime". *Phys. Rev. Lett.* 98 (2007), p. 117402. DOI: 10.1103/PhysRevLett.98.117402.

[92] A. Kiraz et al. "Photon correlation spectroscopy of a single quantum dot". *Physical Review B - Condensed Matter and Materials Physics* 65 (2002), pp. 1–4. DOI: 10.1103/PhysRevB.65.161303.

[93] S. Kimura et al. "Photon antibunching observed from an InAlAs single quantum dot". *Japanese Journal of Applied Physics, Part 2: Letters* 44 (2005), pp. L793–L796. DOI: 10.1143/JJAP.44.L793.

[94] H. Kamada et al. "Exciton Rabi Oscillation in Single Isolated Quantum Dots". *physica status solidi (a)* 190 (2002), pp. 485–490. DOI: 10.1103/PhysRevLett.87.246401.

[95] I. Favero et al. "Acoustic phonon sidebands in the emission line of single InAs/GaAs quantum dots". *Physical Review B - Condensed Matter and Materials Physics* 68 (2003), pp. 68–71. DOI: 10.1103/PhysRevB.68.233301.

[96] L. Besombes et al. "Acoustic phonon broadening mechanism in single quantum dot emission". *Phys. Rev. B* 63 (2001), p. 155307. DOI: 10.1103/PhysRevB.63.155307.

[97] A. J. Brash et al. "Light Scattering from Solid-State Quantum Emitters : Beyond the Atomic Picture". *Physical Review Letters* 123 (2019), p. 167403. DOI: 10.1103/PhysRevLett.123.167403.

[98] J. Iles-Smith et al. "Limits to coherent scattering and photon coalescence from solid-state quantum emitters". *Phys. Rev. B* 95 (2017), p. 201305. DOI: 10.1103/PhysRevB.95.201305.

[99] Z. X. Koong et al. "Fundamental Limits to Coherent Photon Generation with Solid-State Atomlike Transitions". *Phys. Rev. Lett.* 123 (2019), p. 167402. DOI: 10.1103/PhysRevLett.123.167402.

[100] D. P.S. McCutcheon et al. "A general approach to quantum dynamics using a variational master equation: Application to phonon-damped Rabi rotations in quantum dots". *Physical Review B - Condensed Matter and Materials Physics* 84 (2011), pp. 2–5. DOI: 10.1103/PhysRevB.84.081305.

[101] L. Monniello et al. "Excitation-induced dephasing in a resonantly driven InAs/GaAs quantum dot". *Physical Review Letters* 111 (2013), pp. 1–5. DOI: 10.1103/PhysRevLett.111.026403.

[102] P. Machnikowski and L. Jacak. "Damping of Rabi oscillations in quantum dots due to lattice dynamics". *Semiconductor Science and Technology* 19 (2004), S299–S300.

[103] J. Forstner et al. "Phonon-induced damping of Rabi oscillations in semiconductor quantum dots". *Phys. Stat. Sol. B* 238 (2003), pp. 419–422. DOI: DOI10.1002/pssb.200303155Phonon-induced.

[104] D. P. S. Mccutcheon and A. Nazir. "Model of the Optical Emission of a Driven Semiconductor Quantum Dot : Phonon-Enhanced Coherent Scattering and Off-Resonant Sideband Narrowing". 217401 (2013), pp. 1–5. DOI: 10.1103/PhysRevLett.110.217401.

[105] A. Vagov et al. "Nonmonotonic field dependence of damping and reappearance of rabi oscillations in quantum dots". *Physical Review Letters* 98 (2007), pp. 1–4. DOI: 10.1103/PhysRevLett.98.227403.

[106] D. P. S. McCutcheon and A. Nazir. "Quantum dot Rabi rotations beyond the weak exciton-phonon coupling regime". *New Journal of Physics* 12 (2010), pp. 1–22. DOI: 10.1088/1367-2630/12/11/113042.

[107] R. Manson, K. Roy-Choudhury, and S. Hughes. "Polaron master equation theory of pulse-driven phonon-assisted population inversion and single-photon emission from quantum-dot excitons". *Physical Review B* 93 (2016), pp. 1–12. DOI: 10.1103/PhysRevB.93.155423.

[108] A. Vagov et al. "Real-time path integrals for quantum dots: Quantum dissipative dynamics with superohmic environment coupling". *Physical Review B - Condensed Matter and Materials Physics* 83 (2011). DOI: 10.1103/PhysRevB.83.094303.

[109] B. Krummheuer, V. M. Axt, and T. Kuhn. "Theory of pure dephasing and the resulting absorption line shape in semiconductor quantum dots". *Physical Review B - Condensed Matter and Materials Physics* 65 (2002), pp. 1–12. DOI: 10.1103/PhysRevB.65.195313.

[110] D. E. Reiter et al. "The role of phonons for exciton and biexciton generation in an optically driven quantum dot". *Journal of Physics Condensed Matter* 26 (2014). DOI: 10.1088/0953-8984/26/42/423203.

[111] A. Nazir and D. P.S. McCutcheon. "Modelling exciton-phonon interactions in optically driven quantum dots". *Journal of Physics Condensed Matter* 28 (2016). DOI: 10.1088/0953-8984/28/10/103002.

[112] G. D. Mahan. *Many-particle physics*. Springer Science & Business Media, 2013.

[113] A. Reigue et al. "Probing Electron-Phonon Interaction through Two-Photon Interference in Resonantly Driven Semiconductor Quantum Dots". *Physical Review Letters* 118 (2017), pp. 1–6. DOI: 10.1103/PhysRevLett.118.233602.

[114] P. Tighineanu et al. "Phonon Decoherence of Quantum Dots in Photonic Structures: Broadening of the Zero-Phonon Line and the Role of Dimensionality". *Physical Review Letters* 120 (2018), p. 257401. DOI: 10.1103/PhysRevLett.120.257401.

[115] J. Iles-Smith et al. "Phonon scattering inhibits simultaneous near-unity efficiency and indistinguishability in semiconductor single-photon sources". *Nature Photonics* 11 (2017), pp. 521–526. DOI: 10.1038/nphoton.2017.101.

[116] A. J. Ramsay et al. "Damping of Exciton Rabi Rotations by Acoustic Phonons in Optically Excited InGaAs/GaAs Quantum Dots". *Phys. Rev. Lett.* 104 (2010), p. 017402. DOI: 10.1103/PhysRevLett.104.017402.

[117] A. J. Ramsay et al. "Phonon-Induced Rabi-Frequency Renormalization of Optically Driven Single InGaAs/GaAs Quantum Dots". *Phys. Rev. Lett.* 105 (2010), p. 177402. DOI: 10.1103/PhysRevLett.105.177402.

[118] D. P.S. McCutcheon and A. Nazir. "Consistent treatment of coherent and incoherent energy transfer dynamics using a variational master equation". *Journal of Chemical Physics* 135 (2011), p. 114501. DOI: 10.1063/1.3636081.

[119] R. Silbey and R. A. Harris. "Variational calculation of the dynamics of a two level system interacting with a bath". *The Journal of Chemical Physics* 80 (1984), pp. 2615–2617. DOI: 10.1063/1.447055.

[120] R. A. Harris and R. Silbey. "Variational calculation of the tunneling system interacting with a heat bath . II . Dynamics of an asymmetric tunneling system". *The Journal of Chemical Physics* 83 (1985), pp. 1069–1074. DOI: 10.1063/1.449469.

[121] A. J. Ramsay et al. "Damping of exciton rabi rotations by acoustic phonons in optically excited InGaAs/GaAs quantum dots". *Physical Review Letters* 104 (2010), pp. 20–23. DOI: 10.1103/PhysRevLett.104.017402.

[122] A. J. Ramsay et al. "Phonon-induced Rabi-frequency renormalization of optically driven single InGaAs/GaAs quantum dots". *Physical Review Letters* 105 (2010), pp. 1–4. DOI: 10.1103/PhysRevLett.105.177402.

[123] M. Glässl et al. "Influence of the pulse shape and the dot size on the decay and reappearance of Rabi rotations in laser driven quantum dots". *Physical Review B - Condensed Matter and Materials Physics* 84 (2011), pp. 1–7. DOI: 10.1103/PhysRevB.84.125304.

[124] R. J. Warburton. "Single spins in self-assembled quantum dots". *Nature Materials* 12 (2013), pp. 483–493. DOI: 10.1038/nmat3585.

[125] H. J. Kimble. "The quantum internet". *Nature* 453 (2008), pp. 1023–1030.

[126] M. Kroutvar et al. "Optically programmable electron spin memory using semiconductor quantum dots". *Nature* 432 (2004), pp. 81–84.

[127] G. Gillard et al. "Fundamental limits of electron and nuclear spin qubit lifetimes in an isolated self-assembled quantum dot". *NJP Quantum Information* 7 (2021), pp. 1–8.

[128] D. Press et al. "Ultrafast optical spin echo in a single quantum dot". *Nature Photonics* 4 (2010), pp. 367–370.

[129] A. Bechtold et al. "Three-stage decoherence dynamics of an electron spin qubit in an optically active quantum dot". *Nature Physics* 11 (2015), pp. 1005–1008.

[130] D. E. Chang et al. "A single-photon transistor using nanoscale surface plasmons". *Nature Physics* 3 (2007), pp. 807–812. DOI: 10.1038/nphys708.

[131] A. Javadi et al. "Single-photon non-linear optics with a quantum dot in a waveguide". *Nature Communications* 6 (2015), pp. 6–10. DOI: 10.1038/ncomms9655.

[132] S. Sun et al. "A single-photon switch and transistor enabled by a solid-state quantum memory". *Science* 361 (2018), pp. 57–60. DOI: 10.1126/science.aat3581.

[133] N. H. Lindner and T. Rudolph. "Proposal for Pulsed On-Demand Sources of Photonic Cluster State Strings". *Phys. Rev. Lett.* 103 (2009), p. 113602. DOI: 10.1103/PhysRevLett.103.113602.

[134] E. V. Denning et al. "Protocol for generating multiphoton entangled states from quantum dots in the presence of nuclear spin fluctuations". *Physical Review A* 96 (2017), p. 062329.

[135] D. Scerri et al. "Frequency-encoded linear cluster states with coherent Raman photons". *Phys. Rev. A* 98 (2018), p. 022318. DOI: 10.1103/PhysRevA.98.022318.

[136] I. Schwartz et al. "Deterministic generation of a cluster state of entangled photons". *Science* 354 (2016), pp. 434–437. DOI: 10.1126/science.aah4758.

[137] M. Atatüre et al. "Quantum-Dot Spin-State Preparation with Near-Unity Fidelity". *Science* 312 (2006), pp. 551–553. DOI: 10.1126/science.1126074.

[138] C. Emary and L. J. Sham. "Optically controlled single-qubit rotations in self-assembled InAs quantum dots". *Journal of Physics: Condensed Matter* 19 (2007), p. 056203. DOI: 10.1088/0953-8984/19/5/056203.

[139] A. Delteil et al. "Observation of Quantum Jumps of a Single Quantum Dot Spin Using Submicrosecond Single-Shot Optical Readout". *Phys. Rev. Lett.* 112 (2014), p. 116802. DOI: 10.1103/PhysRevLett.112.116802.

[140] C. Emary et al. "Fast Initialization of the Spin State of an Electron in a Quantum Dot in the Voigt Configuration". *Phys. Rev. Lett.* 98 (2007), p. 047401. DOI: 10.1103/PhysRevLett.98.047401.

[141] T. Belhadj et al. "Impact of heavy hole-light hole coupling on optical selection rules in GaAs quantum dots". *Applied Physics Letters* 97 (2010), pp. 2–5. DOI: 10.1063/1.3473824.

[142] M. Atatüre, J. Dreiser, and A. Badolato. "Quantum-Dot Spin-State Preparation with near-unity fidelity". *Science* 312 (2006), pp. 551–554.

[143] X. Xu et al. "Fast Spin State Initialization in a Singly Charged InAs-GaAs Quantum Dot by Optical Cooling". *Physical Review Letters* 99 (2007), pp. 1–4. DOI: 10.1103/PhysRevLett.99.097401.

[144] S. G. Carter et al. "Quantum control of a spin qubit coupled to a photonic crystal cavity". *Nature Photonics* 7 (2013), pp. 329–334. DOI: 10.1038/nphoton.2013.41.

[145] S. G. Carter et al. "Coherent Population Trapping Combined with Cycling Transitions for Quantum Dot Hole Spins Using Triplet Trion States". *Physical Review Letters* 126 (2021), p. 107401. DOI: 10.1103/PhysRevLett.126.107401.

[146] S. Sun and E. Waks. "Single-shot optical readout of a quantum bit using cavity quantum electrodynamics". *Phys. Rev. A* 94 (2016), p. 012307. DOI: 10.1103/PhysRevA.94.012307.

[147] S. Sun et al. "Cavity-Enhanced Optical Readout of a Single Solid-State Spin". *Physical Review Applied* 9 (2018), p. 054013. DOI: 10.1103/PhysRevApplied.9.054013.

[148] M. H. Appel et al. "Coherent Spin-Photon Interface with Waveguide Induced Cycling Transitions". *Phys. Rev. Lett.* 126 (2021), p. 013602. DOI: 10.1103/PhysRevLett.126.013602.

[149] M. Arcari et al. "Near-Unity Coupling Efficiency of a Quantum Emitter to a Photonic Crystal Waveguide". *Phys. Rev. Lett.* 113 (2014), p. 093603. DOI: 10.1103/PhysRevLett.113.093603.

[150] A. Reinhard et al. "Strongly correlated photons on a chip". *Nature Photonics* 6 (2012), pp. 93–96.

[151] R. Ohta et al. "Strong coupling between a photonic crystal nanobeam cavity and a single quantum dot". *Applied Physics Letters* 98 (2011), p. 173104. DOI: 10.1063/1.3579535.

[152] R. J. Coles et al. "Waveguide-coupled photonic crystal cavity for quantum dot spin readout". *Optics Express* 22 (2014), pp. 2376–2385. DOI: 10.1364/OE.22.002376.

[153] U. M. Gür et al. "Elliptical micropillar cavity design for highly efficient polarized emission of single photons". *Applied Physics Letters* 118 (2021). DOI: 10.1063/5.0041565.

[154] B. Gayral et al. "Optical study of GaAs/AlAs pillar microcavities with elliptical cross section". *Applied Physics Letters* 72 (1998), pp. 1421–1423. DOI: 10.1063/1.120582.

[155] K. Rivoire, S. Buckley, and J. Vučković. "Multiply resonant high quality photonic crystal nanocavities". *Applied Physics Letters* 99 (2011), p. 013114. DOI: 10.1063/1.3607281.

[156] S. Reitzenstein et al. "AlAs/GaAs micropillar cavities with quality factors exceeding 150.000". *Applied Physics Letters* 90 (2007), p. 251109. DOI: 10.1063/1.2749862.

[157] I. J. Luxmoore et al. "Restoring mode degeneracy in H1 photonic crystal cavities by uniaxial strain tuning". *Applied Physics Letters* 100 (2012), p. 121116. DOI: 10.1063/1.3696036.

[158] H. Wang et al. "Towards optimal single-photon sources from polarized microcavities". *Nature Photonics* 13 (2019), pp. 770–775.

[159] N. Tomm et al. "A bright and fast source of coherent single photons". *Nature Nanotechnology* 16 (2021), pp. 399–404. DOI: 10.1038/s41565-020-00831-x.

[160] A. Majumdar et al. "Proposed coupling of an electron spin in a semiconductor quantum dot to a nanosize optical cavity". *Physical Review Letters* 111 (2013), p. 027402. DOI: 10.1103/PhysRevLett.111.027402.

[161] V. Loo et al. "Single-shot initialization of electron spin in a quantum dot using a short optical pulse". *Physical Review B* 83 (2011), p. 033301. DOI: 10.1103/PhysRevB.83.033301.

[162] A. Gilchrist, N. K. Langford, and M. A. Nielsen. "Distance measures to compare real and ideal quantum processes". *Phys. Rev. A* 71 (2005), pp. 1–14. DOI: 10.1103/PhysRevA.71.062310.

[163] B. D. Gerardot et al. "Optical pumping of a single hole spin in a quantum dot". *Nature* 451 (2008), pp. 441–444. DOI: 10.1038/nature06472.

[164] D. Stefanatos et al. "Adiabatic control of quantum dot spin in the voigt geometry with optical pulses". *WSEAS Transactions on Systems and Control* 14 (2019), pp. 319–325.

[165] P. Kumar and T. Nakajima. "Fast and high-fidelity optical initialization of spin state of an electron in a semiconductor quantum dot using light-hole-trion states". *Optics Communications* 370 (2016), pp. 103–109. DOI: 10.1016/j.optcom.2016.03.006.

[166] E. Paspalakis, S. E. Economou, and F. Carreño. "Adiabatically preparing quantum dot spin states in the Voigt geometry". *Journal of Applied Physics* 125 (2019). DOI: 10.1063/1.5079412.

[167] M. A. Nielsen and I. L. Chuang. *Quantum computation and quantum information*. eng. Cambridge: Cambridge University Press, 2000.

[168] T. Volz et al. "Ultrafast all-optical switching by single photons". *Nature Photonics* 6 (2012), pp. 605–609.

[169] K. Kuruma et al. "Surface-passivated high-Q GaAs photonic crystal nanocavity with quantum dots". *APL Photonics* 5 (2020). DOI: 10.1063/1.5144959.

[170] T. G. Tiecke et al. "Efficient fiber-optical interface for nanophotonic devices". *Optica* 2 (2015), p. 70. DOI: 10.1364/OPTICA.2.000070.

[171] R. S. Daveau et al. "Efficient fiber-coupled single-photon source based on quantum dots in a photonic-crystal waveguide". *Optica* 4 (2017), pp. 178–184. DOI: 10.1364/OPTICA.4.000178.

[172] L. Huthmacher et al. "Coherence of a dynamically decoupled quantum-dot hole spin". *Physical Review B* 97 (2018). DOI: 10.1103/PhysRevB.97.241413.

[173] P. Chen et al. "Theory of quantum optical control of a single spin in a quantum dot". *Physical Review B - Condensed Matter and Materials Physics* 69 (2004), pp. 1–8. DOI: 10.1103/PhysRevB.69.075320.

[174] D. A. Fleisch. *A student's guide to Maxwell's equations*. eng. Cambridge: Cambridge University Press, 2008.

[175] P. G. Huray. *Maxwell's equations [electronic resource]*. eng. Wiley : IEEE Press, 2010.

[176] A. Taflove. *Computational electrodynamics : the finite-difference time-domain method*. eng. 2nd ed. Artech House antennas and propagation library. Boston, Mass. ; London: Artech House, 2000.

[177] A. Taflove. *Advances in computational electrodynamics : the finite-difference time-domain method*. eng. Artech House antenna library. Boston ; London: Artech House, 1998.

[178] B. Jean-Pierre. "A perfectly matched layer for the absorption of electromagnetic waves". *Journal of Computational Physics* 114 (1994), pp. 185–200.

[179] A. Taflove. *Computational electrodynamics : the finite-difference time-domain method*. eng. 2nd ed. Artech House antennas and propagation library. Boston, Mass. ; London: Artech House, 2000.

[180] E. Hecht. *Optics*. eng. Fourth edition.; Pearson new international edition. Pearson custom library. Harlow, Essex: Pearson, 2014.

[181] J. D. Joannopoulos et al. *Photonic crystals : molding the flow of light*. eng. 2nd ed. Princeton: Princeton University Press, 2008.

[182] R. Abe et al. "Optimization of an H0 photonic crystal nanocavity using machine learning". eng. *Optics letters* 45 (2020), pp. 319–322.

[183] H. Takagi et al. "High Q H1 photonic crystal nanocavities with efficient vertical emission". *Optics Express* 20 (2012), p. 28292. DOI: 10.1364/oe.20.028292.

[184] C. Bonato et al. "H1 photonic crystal cavities for hybrid quantum information protocols". *Optics Express* 20 (2012), pp. 24714–24726. DOI: 10.1364/OE.20.024714.

[185] A. Tandaechanurat et al. "Increase of Q-factor in photonic crystal H1-defect nanocavities after closing of photonic bandgap with optimal slab thickness". *Optics Express* 16 (2008), pp. 448–455. DOI: 10.1364/oe.16.000448.

[186] F. Ying-Jhe, L. Yi-Shan, and L. Sheng-Di. "Design and demonstration of high quality-factor H1-cavity in two-dimensional photonic crystal". *Opt. Lett.* 38 (2013), pp. 4915–4918. DOI: 10.1364/OL.38.004915.

[187] D. Hallett et al. "Engineering Chiral Light–Matter Interactions in a Waveguide-Coupled Nanocavity". *ACS Photonics* 9 (2022), pp. 706–713. DOI: 10.1021/acsphotonics.1c01806.

[188] Y. Lai et al. "Genetically designed L3 photonic crystal nanocavities with measured quality factor exceeding one million". *Applied Physics Letters* 104 (2014), pp. 1–5. DOI: 10.1063/1.4882860.

[189] A. R.A. Chalcraft et al. "Mode structure of the L3 photonic crystal cavity". *Applied Physics Letters* 90 (2007), pp. 1–4. DOI: 10.1063/1.2748310.

[190] A. Faraon et al. "Efficient photonic crystal cavity-waveguide couplers". *Applied Physics Letters* 90 (2007), pp. 88–91. DOI: 10.1063/1.2472534.

[191] S. Lam et al. "Coupled Resonant Modes of Dual L3-Defect Planar Photonic Crystal Cavities". *Conference on Lasers and Electro-Optics/Quantum Electronics and Laser Science Conference and Photonic Applications Systems Technologies*. Optica Publishing Group, 2008, QFG6.

[192] F. S. F. Brossard et al. "Strongly coupled single quantum dot in a photonic crystal waveguide cavity". *Applied Physics Letters* 97 (2010), pp. 1–4. DOI: 10.1063/1.3487937.

[193] K. Kuruma et al. "Telecommunication-wavelength two-dimensional photonic crystal cavities in a thin single-crystal diamond membrane". *Applied Physics Letters* 119 (2021). DOI: 10.1063/5.0061778.

[194] P. B. Deotare et al. "High quality factor photonic crystal nanobeam cavities". *Applied Physics Letters* 94 (2009). DOI: 10.1063/1.3107263.

[195] Q. Quan, P. B. Deotare, and M. Loncar. "Photonic crystal nanobeam cavity strongly coupled to the feeding waveguide". *Applied Physics Letters* 96 (2010), p. 203102. DOI: 10.1063/1.3429125.

[196] Q. Quan and M Loncar. "Deterministic design of wavelength scale, ultra-high Q photonic crystal nanobeam cavities". *Optics Express* 19 (2011), pp. 18529–18542. DOI: 10.1364/OE.19.018529.

[197] A. P. Foster et al. "Tunable Photon Statistics Exploiting the Fano Effect in a Waveguide". *Physical Review Letters* 122 (2019), p. 173603. DOI: 10.1103/PhysRevLett.122.173603.

[198] L. Juntao et al. "Systematic design of flat band slow light in photonic crystal waveguides". *Opt. Express* 16 (2008), pp. 6227–6232. DOI: 10.1364/OE.16.006227.

[199] B. Lang, R. Oulton, and D. M. Beggs. "Optimised photonic crystal waveguide for chiral light–matter interactions". *Journal of Optics* 19 (2017), p. 045001. DOI: 10.1088/2040-8986/aa5f5f.

[200] S. Mahmoodian et al. "Engineering chiral light-matter interaction in photonic crystal waveguides with slow light". *Opt. Mater. Express* 7 (2017), pp. 43–51. DOI: 10.1364/OME.7.000043.

[201] H. Singh et al. "Large Purcell enhancement of a quantum dot coupled to a circular grating in a charge tunable device" (2021), pp. 1–6.

[202] D. Ding et al. "Coherent Optical Control of a Quantum-Dot Spin-Qubit in a Waveguide-Based Spin-Photon Interface". *Physical Review Applied* 11 (2019), pp. 031002–1. DOI: 10.1103/PhysRevApplied.11.031002.

[203] A. V. Kuhlmann et al. "Transform-limited single photons from a single quantum dot". eng. *Nature communications* 6 (2015), pp. 8204–8204.

[204] R. Notzel. "Self-organized growth of quantum-dot structures". *Semiconductor Science and Technology* 11 (1996), pp. 1365–1379.

[205] D. J. Mowbray and M. S. Skolnick. "New physics and devices based on self-assembled semiconductor quantum dots". *Journal of Physics D: Applied Physics* 38 (2005), pp. 2059–2076. DOI: 10.1088/0022-3727/38/13/002.

[206] G. Costantini et al. "Interplay between thermodynamics and kinetics in the capping of InAs/GaAs(001) quantum dots". *Physical Review Letters* 96 (2006), pp. 1–4. DOI: 10.1103/PhysRevLett.96.226106.

[207] S. Hughes. "On the "quantum nature of a strongly coupled single quantum dot-cavity system"". *Conference on Quantum Electronics and Laser Science (QELS) - Technical Digest Series* 445 (2008), pp. 22–25. DOI: 10.1109/QELS.2008.4553269.

[208] A. Badolato. "Deterministic Coupling of Single Quantum Dots to Single Nanocavity Modes". *Science* 308 (2005), pp. 1158–1161. DOI: 10.1126/science.1109815.

[209] K. Kuruma et al. "Position dependent optical coupling between single quantum dots and photonic crystal nanocavities". *Applied Physics Letters* 109 (2016), pp. 1–5. DOI: 10.1063/1.4961389.

[210] M. Gschrey et al. "In situ electron-beam lithography of deterministic single-quantum-dot mesa-structures using low-temperature cathodoluminescence spectroscopy". *Applied Physics Letters* 102 (2013), pp. 1–4. DOI: 10.1063/1.4812343.

[211] L. Sapienza et al. "Nanoscale optical positioning of single quantum dots for bright and pure single-photon emission". *Nature Communications* 6 (2015), pp. 1–8. DOI: 10.1038/ncomms8833.

[212] J. Liu et al. "Cryogenic photoluminescence imaging system for nanoscale positioning of single quantum emitters". *Review of Scientific Instruments* 88 (2017), pp. 1–7. DOI: 10.1063/1.4976578.

[213] T. Kojima et al. "Accurate alignment of a photonic crystal nanocavity with an embedded quantum dot based on optical microscopic photoluminescence imaging". *Applied Physics Letters* 102 (2013), pp. 2011–2014. DOI: 10.1063/1.4773882.

[214] K. H. Lee et al. "Registration of single quantum dots using cryogenic laser photolithography". *Applied Physics Letters* 88 (2006), pp. 1–4. DOI: 10.1063/1.2202193.

[215] G. Juska et al. "Towards quantum-dot arrays of entangled photon emitters". *Nature Photonics* 7 (2013), pp. 527–531. DOI: 10.1038/nphoton.2013.128.

[216] A. S. Vlasov et al. "Site-Controlled Growth of Single InP QDs". *Semiconductors* 49 (2015), pp. 1095–1098. DOI: 10.1134/S1063782615080230.

[217] A. Huggenberger et al. "Site-controlled In(Ga)As/GaAs quantum dots for integration into optically and electrically operated devices". *Journal of Crystal Growth* 323 (2011), pp. 194–197. DOI: 10.1016/j.jcrysgro.2010.11.144.

[218] K. D. Jöns et al. "Triggered indistinguishable single photons with narrow line widths from site-controlled quantum dots". *Nano Letters* 13 (2013), pp. 126–130. DOI: 10.1021/nl303668z.

[219] C. Schneider et al. "In(Ga)As/GaAs site-controlled quantum dots with tailored morphology and high optical quality". *Physica Status Solidi (A) Applications and Materials Science* 209 (2012), pp. 2379–2386. DOI: 10.1002/pssa.201228373.

[220] T. Ishikawa et al. "Site-controlled InAs single quantum-dot structures on GaAs surfaces patterned by in situ electron-beam lithography". *Applied Physics Letters* 76 (2000), pp. 167–169. DOI: 10.1063/1.125691.

[221] C. Schneider et al. "Single site-controlled In(Ga)As/GaAs quantum dots: Growth, properties and device integration". *Nanotechnology* 20 (2009), pp. 1–9. DOI: 10.1088/0957-4484/20/43/434012.

[222] A. Huggenberger et al. "Narrow spectral linewidth from single site-controlled In(Ga)As quantum dots with high uniformity". *Applied Physics Letters* 98 (2011), pp. 1–3. DOI: 10.1063/1.3568890.

[223] L. O. Mereni et al. "A site-controlled quantum dot system offering both high uniformity and spectral purity". *Applied Physics Letters* 94 (2009), pp. 2009–2012. DOI: 10.1063/1.3147213.

[224] M. H. Baier et al. "Single photon emission from site-controlled pyramidal quantum dots". *Applied Physics Letters* 84 (2004), pp. 648–650. DOI: 10.1063/1.1643533.

[225] T. Sünner et al. "Scalable fabrication of optical resonators with embedded site-controlled quantum dots". *Optics Letters* 33 (2008), p. 1759. DOI: 10.1364/ol.33.001759.

[226] A. Strittmatter et al. "Lateral positioning of InGaAs quantum dots using a buried stressor". *Applied Physics Letters* 100 (2012), pp. 30–33. DOI: 10.1063/1.3691251.

[227] A. Strittmatter et al. "Site-controlled quantum dot growth on buried oxide stressor layers". *Physica Status Solidi (A) Applications and Materials Science* 209 (2012), pp. 2411–2420. DOI: 10.1002/pssa.201228407.

[228] T. Grange et al. "Reducing Phonon-Induced Decoherence in Solid-State Single-Photon Sources with Cavity Quantum Electrodynamics". *Physical Review Letters* 118 (2017), pp. 1–6. DOI: 10.1103/PhysRevLett.118.253602.

[229] K. Rivoire, S. Buckley, and J. Vučković. "Multiply resonant photonic crystal nanocavities for nonlinear frequency conversion". *Opt. Express* 19 (2011), pp. 22198–22207. DOI: 10.1364/OE.19.022198.

[230] *Lumerical Inc.* https://www.lumerical.com/products/fdtd/. Accessed: 2022-02-23.

[231] P. Lalanne and J.P. Hugonin. "Bloch-wave engineering for high-Q, small-V microcavities". *IEEE journal of quantum electronics* 39 (2003), pp. 1430–1438. DOI: 10.1109/JQE.2003.818283.

[232] H. C. Casey, D. D. Sell, and K. W. Wecht. "Concentration dependence of the absorption coefficient for n- and p-type GaAs between 1.3 and 1.6 eV". *Journal of Applied Physics* 46 (1975), pp. 250–257. DOI: 10.1063/1.321330.

[233] X. Ding et al. "On-Demand Single Photons with High Extraction Efficiency and Near-Unity Indistinguishability from a Resonantly Driven Quantum Dot in a Micropillar". *Phys. Rev. Lett.* 116 (2016), p. 020401. DOI: 10.1103/PhysRevLett.116.020401.

[234] K. E. Cahill and R. J. Glauber. "Density operators for fermions". *Physical Review A - Atomic, Molecular, and Optical Physics* 59 (1999), pp. 1538–1555. DOI: 10.1103/PhysRevA.59.1538.